MICROSTRUCTURAL CHARACTERIZATION OF HETEROEPITAXIAL LAYERS OF III-V COMPOUND SEMICONDUCTORS

Tae-Yeon Seong
Wolfson College, Oxford

A dissertation submitted for the degree of Doctor of Philosophy in the University of Oxford

Michaelmas term, 1991

ABSTRACT

MICROSTRUCTURAL CHARACTERIZATION OF HETEROEPITAXIAL LAYERS OF III-V COMPOUND SEMICONDUCTORS

A dissertation submitted for the degree of Doctor of Philosophy
in the University of Oxford

Tae-Yeon Seong, Wolfson College, Oxford
Michaelmas Term, 1991

This work describes results obtained from TEM, TED and HREM studies of MBE and MOCVD $InAs_ySb_{1-y}$, MOCVD $In_xGa_{1-x}As$, MOCVD InP_ySb_{1-y} and MOCVD GaP_ySb_{1-y} layers which were grown over a wide range of conditions. These semiconductor layers are of considerable importance for a variety of applications in optoelectronic and high-speed devices.

TEM/TED investigations showed that phase separation occurs in MBE InAsSb layers, resulting in two phases with platelet structures ~5 to ~200nm thick approximately parallel to the layer surface. Phase separation was dependent on growth temperature and layer composition. Anisotropic geometry of the platelets was observed when viewed in the [110] and [$\bar{1}$10] directions. The compositions of the two phases were derived by TED and EDX analyses. A model for the phase-separated layers was proposed based on the presence of a miscibility gap and using the lateral and island growth mechanisms.

TEM results of InGaAs, InPSb and GaPSb layers showed a fine scale modulated contrast (8-20nm in scale) which is a characteristic of alloy clustering occurring by spinodal decomposition, and a fine scale speckle contrast (4-5nm in scale). TEM/TED studies showed that [110] diffuse intensity lines in [001] TED patterns of InGaAs are not related to the fine scale modulated contrast but to the fine scale speckle contrast. It was concluded that a fine scale modulated contrast due to alloy clustering coexists with a fine scale speckle contrast associated with static atomic displacements from the average lattice in InGaAs. For InPSb and GaPSb, a fine needle-like contrast was also observed, which corresponds to diffuse streaks in the [$\bar{1}$10] patterns. This fine needle-like contrast was attributed to segregation of atoms at missing rows of atoms in the reconstructed growing surface.

TED investigations revealed CuPt-type ordering in some of the InGaAs, InAsSb and InPSb layers. Regardless of alloy systems and growth conditions, the ordering occurred on only two of the four possible {111} variants. The degree of ordering was strongly dependent on growth conditions. Two variants of the ordered regions in InGaAs nucleated separately. TED/HREM studies of the ordered structure in InGaAs revealed a direct relationship between the inclination and elongation of superlattice spots and the morphology of anti-phase boundaries present within the domains. Two competing processes of surface-induced ordering, and bulk-induced disordering within a transition region, were considered to interpret the growth condition dependence of the ordering in InGaAs. A model for the ordering observed was proposed based on the surface reconstruction mechanism.

MBE InAsSb strained layer superlattices (SLSs) were examined by TEM and HREM techniques. Defect configuration and the atomic structure of tetragonal distortion of the SLSs were directly imaged. Defect behaviour was dependent on the geometry of the SLSs. Possible relaxation mechanisms for the SLSs were proposed.

The Lord your God in your midst, the Mighty One, will save; He will rejoice over you with gladness, He will quiet you in His love, He will rejoice over you with singing.
-Zephaniah 3:17-

Preface

This dissertation is an account of work carried out by the author in the Department of Materials, Oxford University from Michaelmas term 1988 to Trinity term 1991 under the supervision of Dr. G.R. Booker. The work was supported by the British Council and the LINK DTI/SERC project 'MOCVD of III-V Materials for Integration'.

No part of this work has been submitted for a degree of any other university. Any studies mentioned in the text carried out by other workers are duly acknowledged, and a list of references is given at the end of each chapter.

I would like to thank Prof. Sir Peter Hirsch, F.R.S. for the provision of laboratory facilities. I am extremely grateful to Dr. G.R. Booker for his constant encouragement, invaluable advice, guidance and support at all stages of the work. I am also deeply indebted to Dr. A.G. Norman for his invaluable advice and comprehensive discussions.

To others, who have provided assistance during this work, I would like to express sincere thanks. I am particularly grateful to:

Dr. A.G. Norman, Dr. I.T. Ferguson, Prof. R.A. Stradling and Prof. B.A. Joyce of Imperial College, London, Dr. A.G. Cullis and Dr. S.J. Bass of the Royal Signals and Radar Establishment, Malvern, and Prof. G.B. Stringfellow of Utah University, U.S.A., for provision of the epitaxially grown samples and electrical and optical data, and for helpful discussions.

Mr. E.J. Thrush, BNR Europe Ltd, Harlow, and Dr. A. Wood, GEC-Marconi Materials Technology Ltd, Caswell for useful discussions.

Dr. J.L. Hutchison, who introduced me to the art of HREM, and for his help in teaching me and obtaining some of the lattice images.

Dr. M.L. Jenkins for his help in teaching me the convergent beam and weak beam techniques.

Dr. N.J. Long for performing computer image simulation using SEMPER as described in chapter 5.

Dr. F. Glas for performing the TED pattern computer simulation described on page 80, chapter 5.

Dr. P.R. Wilshaw, Prof. S. Mahajan and Dr. P.J. Dobson for valuable discussions on spinodal decomposition, atomic ordering, surface reconstruction and defect structures.

Dr. R.E. Mallard for discussions and help with proof-reading the thesis.

All members of the Semiconductor Group at Oxford not only for their practical help, but also their encouragement and good humour which have contributed much to the author's enjoyment while working in Oxford.

Mr. G. Dixon-Brown, Mr. R. Doole and Mr. P. Hambridge for the maintenance of the electron microscopes and Mr. A. McKnight and Mr. M. Taheri for photographic work.

Special thanks are due to my wife for her devoted love and my father- and mother-in-law for their love and support.

Finally, I should like to express my sincere thanks to my father and mother and family for their love and support.

Praise the Lord my God, who walks along with me at all times.

He must deserve all the glory !!!

Tae-Yeon Seong.

Wolfson College, Oxford.

Some of the work presented in this thesis has already been published or will be published very soon. These are as follows:

"Atomic ordering and alloy clustering in MBE $InAs_ySb_{1-y}$ layers", T-Y. Seong, A.G. Norman, G.R. Booker, R. Droopad, R.L. Williams, S.D. Parker, P.D. Wang and R.A. Stradling, Mat. Res. Soc. Symp. Proc. **163** (1990) 907.

"Spontaneous formation of strained layers in MBE grown $InAs_ySb_{1-y}$ due to phase separation", T-Y. Seong, A.G. Norman, G.R. Booker, I.G. Ferguson and R.A. Stradling, presented at the Strained Layers Conference - Growth, Characterization and Devices, Oxford,1990.

"TEM, TED/HREM studies of ordering and associated domain structures in MOCVD InGaAs layers", T-Y. Seong, A.G. Norman, J.L. Hutchison, G.R. Booker, A.G. Cullis, S.J. Bass and L.L. Taylor, Inst. Phys. Conf. Ser. **117** (1991) 463.

"Phase separation and associated defects in MBE $InAs_ySb_{1-y}$ layers", T-Y. Seong, A.G. Norman, J.L. Hutchison, G.R. Booker, I.T. Ferguson and R.A. Stradling, Inst. Phys. Conf. Ser. **117** (1991) 485.

"Growth and optical properties of natural $InAs_XSb_{1-X}$ SLSs", I.T. Ferguson, A.G. Norman, T-Y. Seong, R.H. Thomas, C.C. Phillips, R.A. Stradling, G.R. Booker and B.A. Joyce, presented at International Symp. of GaAs and Related Compounds, Seattle, U.S.A., 1991, accepted for publication in Inst. Phys. Conf. Ser. (Adam Hilger, Bristol).

"MBE Growth of $InAs_xSb_{1-x}$ strained layer superlattices; can nature do it better?", I.T. Ferguson, T-Y. Seong, R.H. Thomas, A.G. Norman, C.C. Philips, R.A. Stradling, G.R. Booker and B.A. Joyce, accepted for publication in Appl. Phys. Lett.

"A mechanism for the CuPt-type ordering in ternary III-V compund semiconductors", A.G. Norman, B.A. Philips, T-Y. Seong, S. Mahajan and G.R. Booker, to be submitted to J. Cryst. Growth.

"TEM/TED studies of fine scale contrasts in InGaAs MOCVD layers", T-Y. Seong, G.R. Booker and A.G. Norman, in preparation.

"Surface-induced ordering in $InAs_ySb_{1-y}$ MBE layers", T-Y. Seong, A.G. Norman, G.R. Booker and I.T. Ferguson, in preparation.

"TEM, TED/HREM studies of surface-induced ordering in MOCVD InGaAs layers", T-Y. Seong, A.G. Norman, J.L. Hutchison, G.R. Booker and A.G. Cullis, in preparation.

PATENT

"British patent application on novel growth of strained layers of MBE $InAs_ySb_{1-y}$ semiconductors", G.R. Booker, A.G. Norman, T-Y. Seong, I.G. Ferguson, R.A. Stradling and B.A. Joyce, filed on March, 1991.

CONTENTS

CHAPTER 1

INTRODUCTION AND PROPERTIES AND APPLICATIONS OF III-V COMPOUND SEMICONDUCTORS

1-1 Introduction

Heteroepitaxial layers of III-V semiconductor alloys, e.g. InAsSb/GaAs, InGaAs/InP, InPSb/InAs and GaPSb/InAs, are of considerable importance because of their use for a wide range of semiconductor devices such as infrared emitters and detectors, field effect transistors, solar cells, etc. Growth of such layers has been achieved by the techniques of liquid phase epitaxy (LPE), vapour phase epitaxy (VPE), metalorganic chemical vapour deposition (MOCVD) and molecular beam epitaxy (MBE). Thermodynamical and structural stability of the layers is an important factor for obtaining reliable devices. Regarding the thermodynamical stability, considerable efforts have been made to study two kinds of phenomena occurring in III-V semiconductor alloys, i.e. spinodal decomposition and atomic ordering.

Calculations based upon the bulk thermodynamic properties of these materials have indicated the presence of a miscibility gap in some ternary and most quarternary alloy systems at temperatures of practical importance (1-7), and such a gap can give rise to either alloy clustering or 'phase' separation (or perhaps more correctly 'composition' separation) by spinodal decomposition. Calculated spinodal decomposition curves for III-V quarternary solid solutions by Onabe (1) are shown in the diagram of Fig. 1.1. The continuous curves are isotherms corresponding to the 400°C-1000°C temperature range. Dashed lines represent the compositions for lattice matching to GaAs, InP, InAs and GaSb. If on inserting the point corresponding to the particular alloy composition in the appropriate diagram, it is found to lie within the particular temperature curve, then the alloy should be unstable and phase separation should occur by spinodal decomposition. Inspection of the diagrams shows that when epitaxial layers of some of these semiconductor alloys are grown below a critical temperature, phase separation may occur by spinodal decomposition during epitaxial growth. TEM studies of a number of ternary and quarternary alloy layers have revealed both a coarse scale tweed-like contrast (~150nm) and a fine scale modulated contrast (~10-20nm) aligned along the <100> directions parallel to the layer surface (8-12). The coarse scale tweed-like contrast was directly shown to correspond to compositional variations (9,10) and was

Figure 1.1

Calculated spinodal isotherms for III-V compound semiconductor alloys at 400°C - 1000°C (solid lines). Temperatures indicated as 4 for 400°C etc. Dashed lines represent the compositions for lattice matching to GaAs, InP, InAs and GaSb (1).

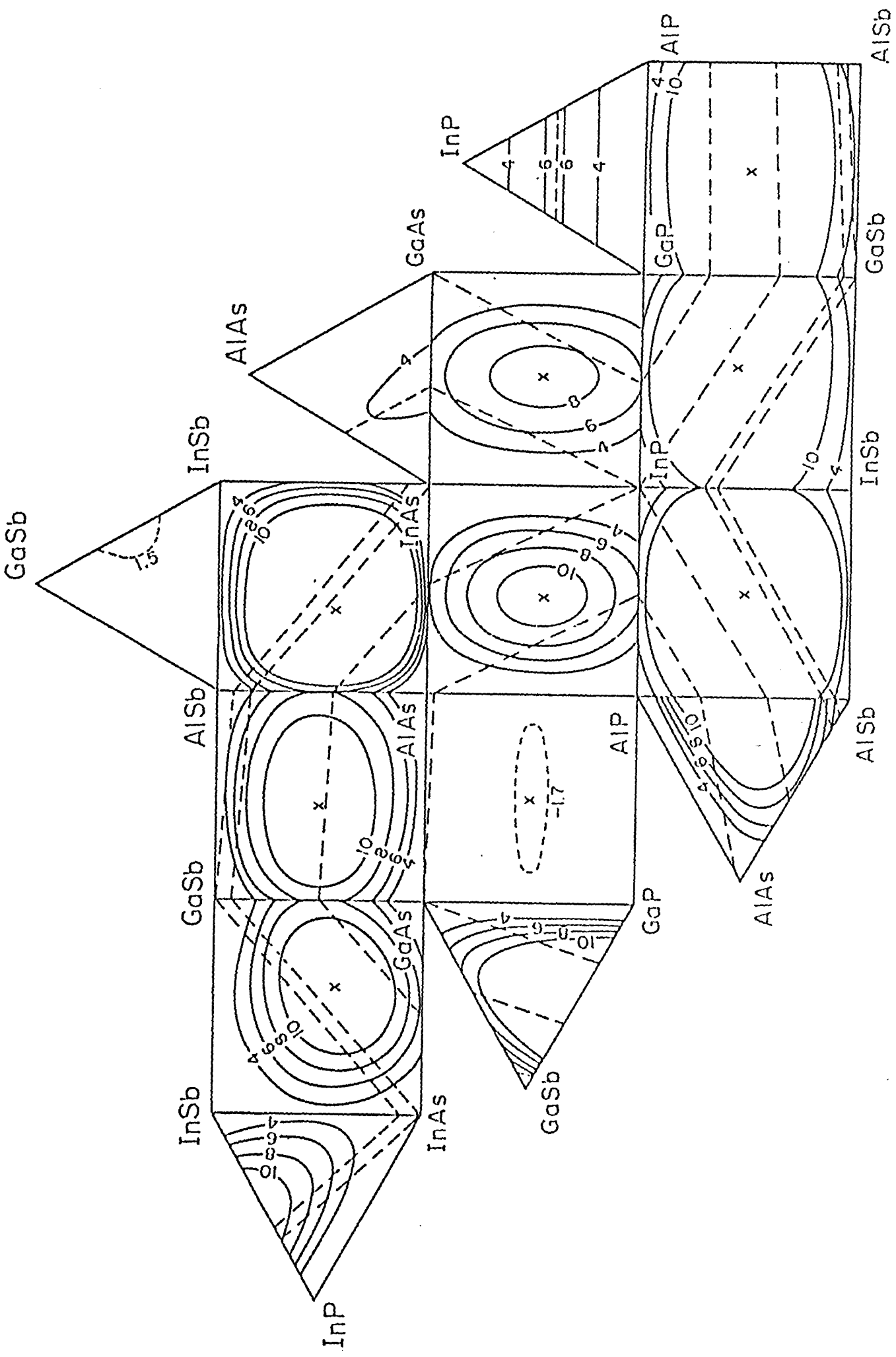
GaSb
InSb
AlSb
AlAs
GaAs
InP
AlP
GaP
InAs
GaAs
GaSb
InSb
InP
AlP
GaP
InAs
GaSb
InSb
AlSb
AlAs
GaSb
InP
GaSb
AlAs
AlSb

Fig. 1.1

attributed to alloy clustering resulting from spinodal decomposition occurring at the surface of the growing layer. The fine scale modulated contrast was also considered to be a form of alloy clustering (11-13), but the mechanism by which it arises has not yet been definitely established (11-13).

Theoretical calculations carried out by Bernard et al.(14) based on the first-principles total-minimization and cluster-variation methods have indicated that atomically ordered structure can be unstable in bulk layers. In spite of the expectation of instability, however, TEM and TED studies have revealed evidence for atomic ordering of various types such as CuAu-I, famatinite, CuPt and chalcopyrite in III-V compound semiconductor alloy layers grown by LPE, VPE, MOCVD and MBE (13). The type and amount of ordering depend on the growth conditions including the alloy system and layer composition, the growth method, temperature and rate, and the substrate crystallographic orientation. The most commonly observed ordering has been the CuPt-type and this was shown to arise at the surface of the growing layer (15). The presence of such alloy clustering and atomic ordering in ternary and quarternary III-V alloy layers can have significant effects on the electrical and optical properties of the layers (16,17).

Heteroepitaxial growth of III-V alloy layers involves several problems including lattice mismatch and thermal expansion coefficient differences. These effects can introduce crystallographic defects such as threading dislocations, stacking faults and microtwins to accommodate the induced strain. In order to obtain good quality layers, it is important to understand the nature and origin of these defect structures and their properties.

In this thesis, detailed TEM, TED and HREM studies have been performed to characterise the structures and growth behaviour of heteroepitaxial layers of MOCVD $In_xGa_{1-x}As$, MOCVD and MBE $InAs_ySb_{1-y}$, MOCVD InP_ySb_{1-y}, MOCVD GaP_ySb_{1-y} and MBE $InAs_{y1}Sb_{1-y1}/InAs_{y2}Sb_{1-y2}$ strained layer superlattices.

In chapter 2, the basic theories of spinodal decomposition and atomic ordering are briefly reviewed, followed by the experimental evidence for these effects. In chapter 3, experimental techniques are described including the non-equilibrium growth techniques of MBE and MOCVD, crystallographic polarity determinations, sample preparation methods,

and TEM and TED techniques. In chapter 4, TEM and TED examinations of phase separation in heteroepitaxial $InAs_ySb_{1-y}$ MBE layers are described. We show for the first time that such phase separation occurs at the surface during layer growth. A possible growth mechanism based on island and lateral growth is presented. In chapter 5, we present the results obtained from TEM, TED and HREM examinations of $In_xGa_{1-x}As$, InP_ySb_{1-y} and GaP_ySb_{1-y} MOCVD layers, which showed the occurrence of fine scale contrast, but no coarse scale tweed-like contrast. We present results which we interpret as the coexistence of a fine scale modulated contrast due to alloy clustering and a fine scale mottled contrast associated with static atomic displacements in $In_xGa_{1-x}As$ layers. In addition to a fine scale modulated contrast, a fine needle-like contrast occurred in InP_ySb_{1-y} and GaP_ySb_{1-y} layers, which may be associated with surface reconstruction present during layer growth. In chapter 6, the results obtained from the TED and TEM studies of MOCVD $In_xGa_{1-x}As$, MOCVD and MBE $InAs_ySb_{1-y}$ and MOCVD InP_ySb_{1-y} layers are presented, which reveal CuPt-type ordering. In order to interpret the growth dependence of the ordering in InGaAs, a model based on the two competing processes of surface-induced ordering and bulk diffusion-induced disordering is proposed. A possible model is proposed to describe the formation of the CuPt-type ordering in both the mixed Group III and mixed Group V compound semiconductors. In chapter 7, a brief review of strain relaxation is presented, followed by results obtained from TEM and HREM studies of MBE $InAs_ySb_{1-y}$ SLSs. Possible relaxation mechanisms are discussed. Finally, in chapter 8, conclusions and suggestions for further work are given.

1-2 Properties and applications of III-V compound semiconductors

1-2-1 Introduction

Once binary III-V alloys were recognised as being semiconductors, it was realized that these alloys could provide the basis for the practical engineering of specific semiconductors to achieve certain device requirements. The group III-V semiconductors have energy band gaps spanning the range 0.18-2.42 eV. Much effort has been invested in studying the properties of

these semiconductors and developing growth processes for new material systems. These efforts led to the availability of samples of sufficiently good quality for characterization of the basic properties of these new semiconductor alloys, for example, the composition dependence of band structure and lattice parameter. Practical heterojunction device development could then be achieved by selecting suitable III-V semiconductor alloys. However, a major drawback for device development is evident from Fig. 1.2, which shows the variation of lattice constant as a function of band gap for a large family of ternary III-V semiconductors. The monotonic relationship between band gap and lattice parameter for each ternary alloy system means that only a few ternary alloy compositions can be grown if they are to be lattice-matched to available binary substrates (18). In order to overcome lattice mismatch limitations, compositional grading between the substrate and the device material was introduced to minimize the incorporation of a high concentration of line defects that would adversely affect device performance. The alloy systems InAsSb, InGaAs, InPSb and GaPSb are now briefly reviewed.

1-2-2 $InAs_ySb_{1-y}$ semiconductors

$InAs_ySb_{1-y}$ has attracted great interest because of its potential for the fabrication of infrared emitters and detectors operating at wavelengths in the 8-12μm spectral range, where the atmospheric absorption is minimum (19-23). $InAs_ySb_{1-y}$ (y=0.35) has the smallest energy band gap (E_g = 0.10eV at room temperature) among III-V semiconductors and offers the possibility for replacing HgCdTe, which is not easy to grow and is difficult to work with. However, this material system is faced with two problems that are detrimental to the growth as well as to the optical properties of the alloy. First, there is no suitable binary substrate available which is lattice matched to $InAs_ySb_{1-y}$ alloys with a band gap corresponding to a wavelength of 8-12μm. Second, the miscibility gap in the middle region of the composition range makes the growth difficult by the near equilibrium technique of LPE. Recently, Yen et al.(24) reported a systematic study of the MBE growth and the optical absorption properties of $InAs_ySb_{1-y}$ covering the composition range (0<y<1) and the results showed promise for

Figure 1.2

Relationship between band gap energy, photon wavelength and lattice parameter for a number of ternary Group III-V semiconductors. Ternary layers of only a few compositions can be lattice-matched to binary substrates.

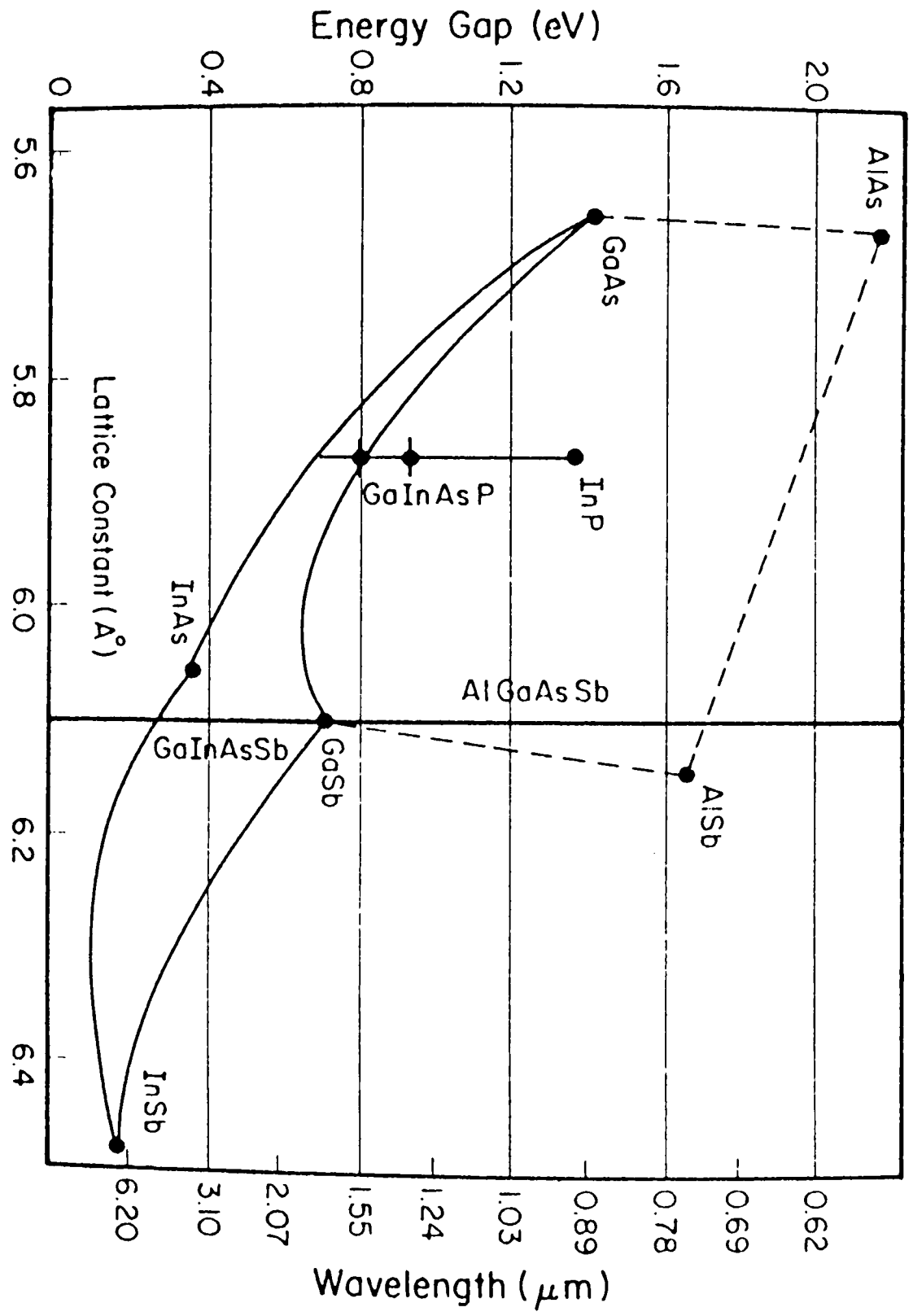
Energy Gap (eV)
0
0.4
0.8
1.2
1.6
2.0
5.6
5.8
6.0
6.2
6.4
Lattice Constant (Å)
AlAs
GaAs
GaInAsP
InP
InAs
AlGaAsSb
GaInAsSb
GaSb
AlSb
InSb
6.20
3.10
2.07
1.55
1.24
1.03
0.89
0.78
0.69
0.62
Wavelength (μm)

Fig. 1.2

this material to function as a detector to absorb light in the desired long wavelength spectral range. Heteroepitaxial layer growth of $InAs_ySb_{1-y}$ on GaAs has been performed using different deposition techniques such as MBE (24-26), MOCVD (27) and metalorganic magnetron sputtering (MOMS) (28).

1-2-3 $In_xGa_{1-x}As$ semiconductors

The III-V semiconductor alloy, $In_xGa_{1-x}As$, lattice matched to InP at x=0.53, is emerging as an important material because of its large potential for a number of novel optoelectronic (29-32) and electronic (33-35) devices. The room temperature band gap of 0.75eV of $In_{0.47}Ga_{0.53}As$ coincides with a range of low attenuation in optical silica fibres, thus making this alloy very suitable for optical communication systems operating at wavelengths between 1.1 and 1.7 μm. Ultrafast photoconductive detectors with a response of 28ps have been built (36). The presence of a two-dimensional electron gas at the interface of n-$In_xGa_{1-x}As/n^+$-InP (34) suggests that this hetero-structure might be suitable for a new type of field effect transistor, the TEGFET (two-dimensional electron gas field effect transistor), and present an alternative to $GaAs/Ga_xAl_{1-x}As$. Large efforts have been made to improve the quality of the InGaAs layer grown by different epitaxial techniques. Control of impurity incorporation, in particular in the low doping range, and control of composition including suppression of any depth or lateral variation are two of the most important prerequisites for reproducible device fabrication and good performance. The growth of InGaAs alloy has been achieved using a variety of growth techniques such as LPE, VPE, MOCVD (37,38) and MBE (39).

1-2-4 InP_ySb_{1-y} and GaP_ySb_{1-y} semiconductors

The metastable III-V ternary alloys, InPSb and GaPSb, are of scientific interest because of the extremely large miscibility gaps in both systems. The delta lattice parameter (DLP) model has predicted that all such alloys have a positive deviation from ideality. The

magnitude of the positive enthalpy of mixing is roughly proportional to the square of the difference in lattice constant for the two binary end components of the system (39). This means that the epitaxial layer growth over most of the alloy range will be prohibited for the near equilibrium technique of LPE (40). The DLP model also predicted a miscibility gap extending from y=0.01 to 0.99 at 530°C for GaP_ySb_{1-y} and from y=0.03 to 0.98 at 460°C for InP_ySb_{1-y} (41).

InP_ySb_{1-y} is a fundamentally interesting material because its band gap covers 1.35eV (InP) to 0.17eV (InSb) at 300K. It may have applications in optoelectronic devices at wavelengths between 0.9 and 7 μm. Moreover, superlattice structures combining InP_ySb_{1-y} and InAs are potentially useful for quantum well lasers (42,43), detectors and two-dimensional electron gas devices (44). The conduction band discontinuity of this type I superlattice is predicted to be 0.35eV, which is nearly equal to the band gap difference (44,45). This, coupled with the extremely small effective mass of InAs, makes the quantum size effect extremely large in this system. In addition, avalanche photodiodes are most effective when the conduction band discontinuity introduces the new superlattice concepts developed by Capasso (46). Thus, the combination of InP_ySb_{1-y} and InAs is promising for injection lasers and detectors operating at 2.0-3.5μm spectral range.

GaP_ySb_{1-y} layers have been grown by MOCVD in the temperature range 530 to 600°C over the full composition range (47). The layers showed good surface morphology and gave strong luminescence covering the energy range 0.79 to 1.61 eV. Although the properties of this material look promising, no TEM structural studies have yet been reported.

REFERENCES-CHAPTER 1

1. K. Onabe, NEC Research and Development **72** (1984) 1.
2. B. de Cremoux, J. de Physique coll. C5, suppl. **no12**, (1982) C5-19.
3. K. Onabe, Jpn. J. Appl. Phys. **21** (1982) 964.
4. G.B. Stringfellow, J. Cryst. Growth **62** (1983) 225.
5. G.B. Stringfellow, J. Cryst. Growth **65** (1983) 454.
6. G.B. Stringfellow, J. Appl. Phys. **54** (1983) 404.
7. K. Onabe, Jpn. J. Appl. Phys. **21** (1982) 964.
8. J.S. Roberts, G.B. Scott and J.P. Gowers, J. Appl. Phys. **52** (1981) 4018.
9. H. Launois, M. Quillec, F. Glas and M.J. Treacy, Inst. Phys. Conf. Ser. No. **65** (1982) 537.
10. P. Henoc, A. Izrael, M. Quillec and H. Launois, Appl. Phys. Lett. **40** (1982) 963.
11. J.P. Gowers, Appl. Phys. **A31** (1983) 23.
12. A.G. Norman and G.R. Booker, J. Appl. Phys. **57** (1985) 4715.
13. S. Mahajan, M.A. Shahid and D.E. Laughlin, Inst. Phys. Conf. Ser. No. **100** (1989) 143.
14. J.E. Bernard, L.G. Ferreira, S.-H. Wei and A. Zunger, Phys. Rev. **B38** (1988) 6338.
15. A.G. Norman, D.Phil. Thesis, Oxford University, (1987).
16. P. Blood and A.D.C. Grassie, J. Appl. Phys. **56** (1984) 866.
17. J. Goral, S. Kurtz, J. Olson and A. Kibbler, J. Electr. Mater. **19** (1990) 95.
18. J.C. Woolley and J. Warner, Can. J. Phys. **42** (1964) 1879.
19. T.H. Chiu and W.T. Tsang, J. Appl. Phys. **57** (1985) 4572.
20. G.C. Osbourn, J. Vac. Sci. Technol. **B2** (1984) 176.
21. G.B. Stringfellow and P.E. Greene, J. Electrochem. Soc. **118** (1971) 805.
22. L.R. Dawson, J. Vac. Sci. Technol. **B4** (1986) 598.
23. R.M. Biefeld, J. Cryst. Growth **75** (1986) 255.
24. M.Y. Yen, B.F. Levine, L.G. Bethea, K.K. Choi and A.Y. Cho, Appl. Phys. Lett. **50** (1987) 927.
25. M.Y. Yen, J. Appl. Phys. **64** (1988) 3306.

26. J.I. Chyi, S. kalem, N.S. Kumar, C.W. Litton and H. Morkoc, Appl. Phys. Lett. **53** (1988) 1092.

27. P.K. Chiang and S.M. Bedair, Appl. Phys. Lett. **46** (1985) 383.

28. J.B. Webb and C. Halpin, Appl. Phys. Lett. **47** (1985) 831.

29. T.P. Pearsall, IEEE J. Quamtum Electron. **QE-16** (1980) 709.

30. J. Degani, R.F. Leheny, R.E. Nahory, M.A. Pollack, J.P. Heritage and J.C. Rewinter, Appl. Phys. Lett. **38** (1981) 27.

31. O.K. Kim, S.K. Forrest, W.A. Bonner and R.G. Smith, Appl. Phys. Lett. **39** (1981) 402.

32. T.P. Lee, C.A. Burrus, A.G. Dentai and K. Ogawa, Electron. Lett. **16** (1980) 155.

33. S.Y. Narayan, J.P. Paczkowski, S.T. Jolly, E.P. Bertin and R.T. Smith, RCA Rev. **42** (1981) 491.

34. P.D. Gardner, S.Y. Narayan, S. Colvin and Yong-hoon Yun, RCA Rev. **42** (1981) 543.

35. Y. Guldner, J.P. Vieren, P. Voisin, M. Voos, M. Razeghi and M.A. Posson, Appl. Phys. Lett. **40** (1982) 877.

36. H.J. Klein, R. Kaumans and H. Beneking, Electron. Lett. **17** (1981) 421.

37. K.H. Goetz, D. Bimberg, H. Jurgensen, T. Selders, A.V. Solomonov, G.F. Glinski and M. Razeghi, J. Appl. Phys. **54** (1983) 4543.

38. S.J. Bass, S.J. Barnett, G.T. Brown, N.G. Chew, A.G. Cullis, A.D. Pitt and M.S. Skolnick, J. Cryst. Growth **79** (1986) 378.

39. G.B. Stringfellow, J. Cryst. Growth **27** (1974) 21.

40. J. Pessetto and G.B. Stringfellow, J. Cryst. Growth **62** (1983) 1.

41. M.J. Jou, Y.T. Cherng, H.R. Jen and G.B. Stringfellow, J. Cryst. Growth **93** (1988) 62.

42. N. Kobayashi, Y. Horikoshi and C. Hemura, Jpn. J. Appl. Phys. Suppl. **19-3** (1980) 333.

43. T. Fukui and Y. Horikoshi, Jpn. J. Appl. Phys. **19** (1980) L55.

44. T. Fukui and Y. Horikoshi, Jpn. J. Appl. Phys. **20** (1981) 587.

45. G.B. Stringfellow, J. Electron. Mater. **10** (1981) 919.

46. T. Capasso, in Gallium Arsenide Tech, edited by D.K. Ferry (Sams, Indianapolis, IN 1985) p303.

47. M.J. Jou, Y.T. Cherng, H.R. Jen and G.B. Stringfellow, Appl. Phys. Lett. **52** (1988) 549.

CHAPTER 2

SPINODAL DECOMPOSITION AND ATOMIC ORDERING IN III-V COMPOUND SEMICONDUCTORS

2-1 Introduction

Epitaxial layers of III-V compound semiconductor alloys have attracted extensive interest, because of the important applications associated with a wide range of semiconductor devices, i.e. infrared emitters and detectors, field effect transistors, solar cells, etc. Theoretical calculations based upon the bulk thermodynamic properties of these semiconductors have predicted that a miscibility gap exists for some ternary and quaternary alloy systems which are of practical interest (1-10). Some of these semiconductors, therefore, might be unstable below a critical temperature and so initially alloy clustering and subsequently phase separation may take place by a process such as spinodal decomposition during epitaxial layer growth. Difficulty has been experienced in growing heteroepitaxial layers of these semiconductors across the full composition range by the near equilibrium growth technique of liquid phase epitaxy (LPE) (11). Successful growth of these layers, however, has been performed by the non-equilibrium growth techniques of metalorganic chemical vapour deposition (MOCVD) and molecular beam epitaxy (MBE). Thermal stability in these materials is an important factor for obtaining highly reliable devices having good optical and electrical properties. Regarding the thermal stability, considerable efforts have been made in the study of two kinds of phenomena occurring in III-V semiconductors: alloy clustering, possibly due to spinodal decomposition, and atomic ordering. The composition fluctuations and associated lattice strains caused by alloy clustering may have significant effects on the electrical and optical properties of III-V semiconductors and the existence of an ordered structure could modify the band gap and electrical properties.

In section 2-2, simple thermodynamic theories describing solid solutions are briefly reviewed. The regular solution model has previously been successfully employed to derive the phase diagrams of III-V semiconductor alloys. In section 2-3, the basic theories and models of spinodal decomposition are presented to describe the thermodynamic properties of these alloys. These concepts are important in the discussion of the results presented in chapters 4 and 5. The experimental evidence for the existence of miscibility gaps is briefly reviewed. Following this, published experimental results for effects of spinodal

decomposition on optical and electrical properties of III-V layers are presented. In section 2-4, a brief review of the literature concerning theoretical studies of the occurrence of ordered structures is given, and the experimental evidence for the occurrence of ordering in III-V layers is surveyed. Several models, which were presented to interpret the occurrence and anisotropy of ordering, are discussed. Finally, published results describing the effects of ordering on optical properties of III-V layers are presented.

2-2 Solid solution

In the mixing of a binary solid solution at fixed values of temperature and pressure, the Gibbs free energy change due to mixing, ΔG^m, is:

$$\Delta G^m = \Delta H^m - T\Delta S^m \qquad (2\text{-}1)$$

where ΔH^m is the enthalpy of mixing, ΔS^m is the entropy of mixing and T is the temperature (K).

For an ideal binary A-B solution, the heat of formation $\Delta H^{m,id}$ is zero. The entropy increase due to the formation of an ideal solution is a measure of the increase in the number of spatial configurations which become available to the system as a result of the solution process, in that the entropy of formation of an ideal binary solution is independent of the temperature of the solution (12). The configurational entropy change of mixing per mole is represented as:

$$\Delta S^m = -R\{X_A \ln X_A + (1-X_A)\ln(1-X_A)\} \qquad (2\text{-}2)$$

where R is the gas constant, X_A is the fraction of A, X_B is the fraction of B, and $X_A+X_B=1$. For an ideal solution,

$$\Delta G^m = -T\Delta S^m \qquad (2\text{-}3)$$

$$\Delta G^m = RT\{X_A \ln X_A + (1-X_A)\ln(1-X_A)\} \qquad (2\text{-}4)$$

and for non-ideal solutions, $\Delta H^m \neq 0$. The simplest of these mathematical formalisms is that which generates what is known as "regular solution behaviour". Hilderbrand (13) defined a regular solution as one which has a non-zero heat of formation and an ideal entropy of formation, i.e. for a regular solution,

$$\Delta H^m \neq 0 \quad \text{and} \quad \Delta S^m = \Delta S^{m,id}.$$

The quasi-chemical model of solutions is applied to solutions of components which are considered to have equal molar volumes in the unmixed state and which have zero-volume change on mixing. Furthermore, the inter-atomic forces are only significant over short distances, such that only nearest neighbour interactions need be considered. Thus the energy of the solution is calculated by summing the atom-atom bond energies. As random mixing is assumed, then the quasi-chemical model corresponds to the regular solution model:

$$\Delta H^m = \Omega X_A X_B \qquad (2\text{-}5)$$

where the interaction parameter $\Omega = \mathbf{a}Z\varepsilon$, $\mathbf{a}$ is Avogadro's number, Z is the number of bonds per atom and ε indicates the difference between the A-B bond energy and the average of the A-A and B-B bond energies given by:

$$\varepsilon = \varepsilon_{AB} - {}^1/_2(\varepsilon_{AA} + \varepsilon_{BB}). \qquad (2\text{-}6)$$

The free energy of mixing, ΔG^m, is expressed as:

$$\Delta G^m = \Omega X_A X_A - RT\{X_A \ln X_A + (1-X_A)\ln(1-X_A)\} \qquad (2\text{-}7)$$

In an ideal solution, $\varepsilon = 0$, since the internal energy of the crystal is independent of the atomic arrangement. (The bond energies ε_{AA}, ε_{BB} and ε_{AB} are, by convention, negative quantities.) If $^1/_2(\varepsilon_{AA} + \varepsilon_{BB}) > \varepsilon_{AB}$, the attractive forces between like atoms are weaker than those between unlike atoms, and there will be a tendency for each atom to surround itself with as many atoms of the opposite kind as possible. This ordering tendency may produce an atomic superlattice at low temperatures. If $^1/_2(\varepsilon_{AA} + \varepsilon_{BB}) < \varepsilon_{AB}$, it is energetically preferable for atoms to surround themselves with like nearest neighbours, i.e. a tendency for a random solid solution to experience clustering due to spinodal decomposition. Fig. 2.1 shows a free energy diagram for these three cases.

Consider an alloy system showing a miscibility gap. The free energy vs composition curve at a temperature for which such a gap occurs (Fig 2.2) is characteristic of an alloy where there is a tendency for clustering, i.e. $\varepsilon > 0$, as discussed previously. This state is unstable since the alloy can lower its free energy by the occurrence of small compositional fluctuations. As a result the alloy decomposes spontaneously at a rate limited only by the rate of atomic migration. For example, consider alloy x. ΔG^m is lowered when it dissociates into two solutions having compositions d and e. Thus, the value of ΔG^m of the whole system is :

$$\Delta G^m = B\frac{e - x}{e - d} + C\frac{x - d}{e - d} = D$$

The value of D is lower than A, the initial value of ΔG^m before dissociation, but ΔG^m will be lowered still further by making the solutions of compositions d and e, respectively. The lowest stable value of ΔG^m which can be attained by the decomposition is G at compositions y and z, respectively. This process is known as spinodal decomposition. The process occurs spontaneously and does not require nucleation in the classical sense when the composition lies within a domain defined by $d^2G/dx^2 < 0$, where G is the free energy and x is the composition (12).

Figure 2.1

Typical free energy curves of a binary alloy for a simple solution and regular solution which gives rise to either spinodal decomposition or atomic ordering.

Figure 2.2

Typical free energy curves of a binary alloy, A_xB_{1-x}, which undergoes spinodal decomposition at a temperature $< T_c$. A homogeneous alloy of composition, x, is thermodynamically unstable to composition fluctuations developing over the region d to e, because $d^2G/dx^2 < 0$. The extreme composition fluctuations are given by the common tangent construction at y and z.

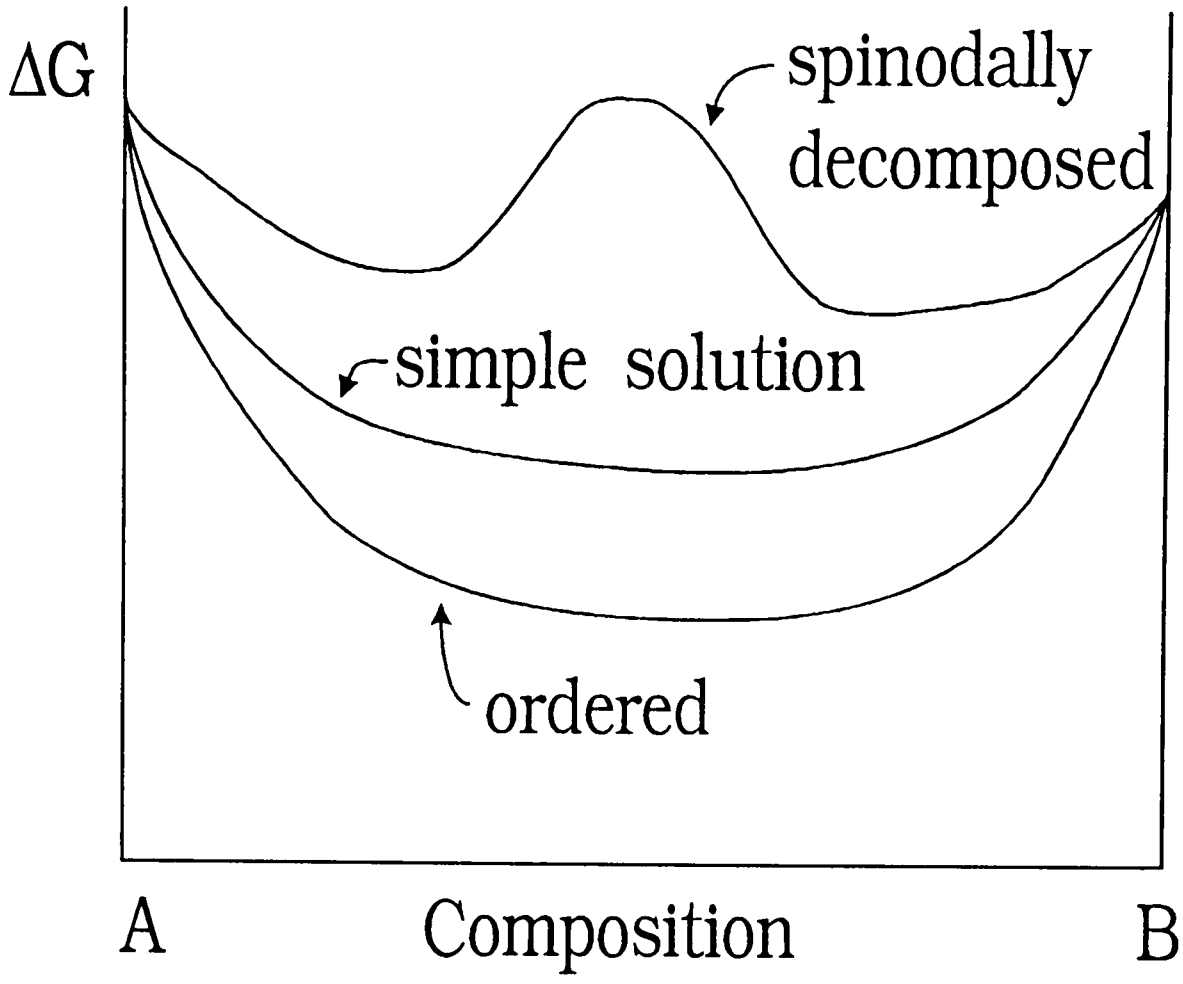
ΔG
spinodally
decomposed
simple solution
ordered
A
Composition
B

Fig. 2.1

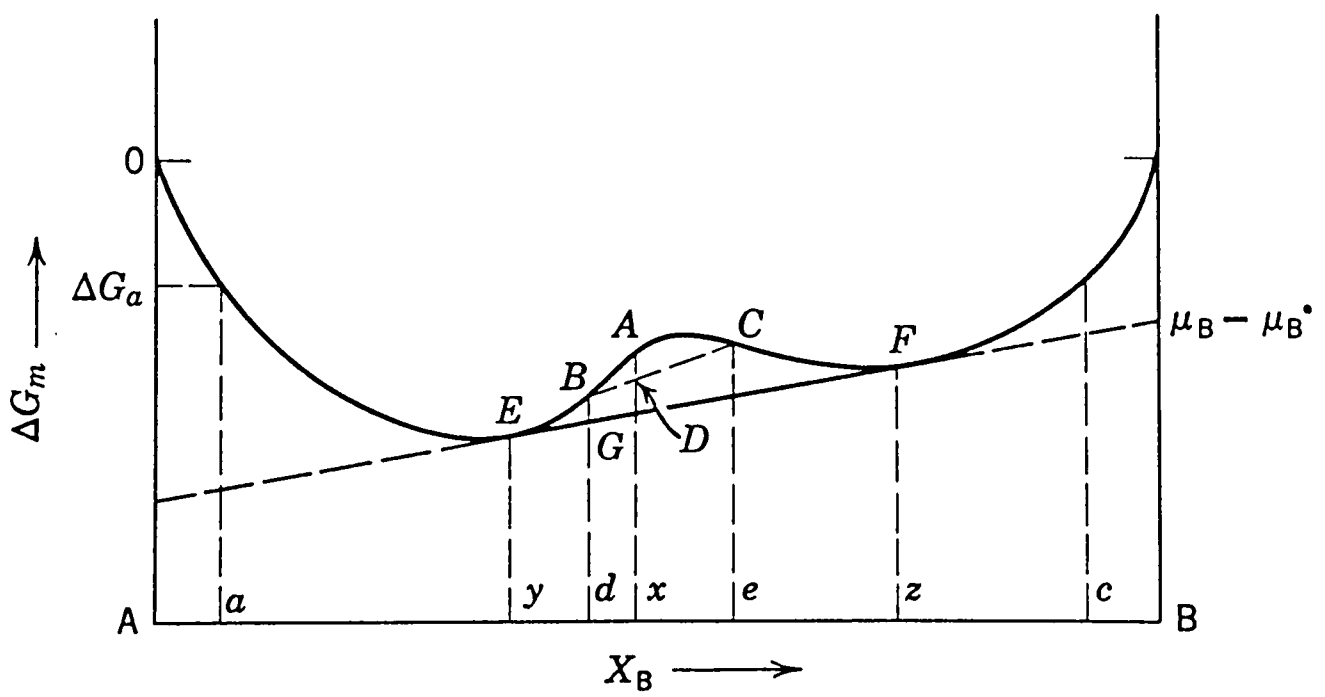
0
ΔG_a
ΔG_m
A
B
C
D
E
F
G
a
y
d
x
e
z
c
$\mu_B - \mu_B^\circ$
X_B
A
B

Fig. 2.2

2-3 Spinodal decomposition in III-V compound semiconductors

2-3-1 Review of theoretical studies

The phase diagram and thermodynamic properties of ternary and quaternary III-V semiconductor alloys can be described reasonably by a regular solution model. In this model, the enthalpy of mixing of a ternary alloy, $A_xB_{1-x}C$, is $\Omega x(1-x)$, where Ω is the interaction parameter and x is alloy composition, as given equation (2-7). The alloy is immiscible below some critical temperature T_c if the interaction parameter is positive. Similarly, the quaternary alloys are immiscible if the interaction parameters related to the pairs of constituent binaries are positive. The interaction parameter, Ω, has been estimated for most ternary alloys and it is found that $\Omega > 0$ (1-10, 14).

The band gap has long been regarded as a measure of bonding energy in semiconductors (15-17). Phillips (18) empirically found that this energy band gap (E_h) in covalent or homopolar semiconductors depends only on lattice constant,a_o,

$$E_h \alpha a_o^{-2.5} \tag{2-8}$$

Since it varies as $a_o^{-2.5}$ in III-V semiconductor alloys, the enthalpy of atomization (ΔH^{at}), which is used as a measure of bonding energy, may be written as:

$$\Delta H^{at} = K a_o^{-2.5} \tag{2-9}$$

where K is a constant. Following this observation, Stringfellow (6) suggested the delta lattice parameter (DLP) model. For a ternary alloy $A_{1-x}B_xC$, the interaction parameter (Ω^i) for the system AC and BC may be expressed as:

$$\Omega^i \approx 4.375K \alpha_o^2/\alpha^{4.5} \tag{2-10}$$

where a_{AC} and a_{BC} are the lattice parameters of binary alloys AC and BC composing the ternary alloy $A_{1-x}B_xC$, and $\alpha_o=a_{AC}-a_{BC}$ and $\alpha=1/2(a_{AC}+a_{BC})$. The value of K may be obtained by mainly fitting equation (2-9) to available experimental values for III-V pseudo-binary systems. This DLP model (6-9,19) has predicted that the interaction parameter, and hence the enthalpy of mixing, is always positive.

Fedders and Muller (20) described the mixing enthalpy of ternary tetrahedral semiconductors with a thermodynamic interaction parameter that is sensitive to the lattice spacing of the binary constituents. Their predictions agreed with experiment and were consistent with those of the DLP model.

Extended X-ray absorption fine structure (EXAFS) studies on $In_xGa_{1-x}As$ (21,22) have shown that over the full range of ternary alloy compositions, In-Ga and In-As bond lengths are maintained close to those of binary alloys. Thus, two different bond lengths are present in a ternary alloy, indicating a considerable amount of internal stress. Fukui (23,24) showed that the presence of two different bond types and lengths in a ternary alloy would give rise to a positive enthalpy of mixing, in turn giving rise to spinodal decomposition. The interactions between atoms are considered to be due entirely to strain, i.e. the stretching and bending of the bonds. Recently, Chen and Sher (25) have demonstrated that bond lengths and enthalpy of mixing could be accurately calculated by considering both strain and chemical effects.

Curves of free energy against composition have been derived for a wide range of the ternary and quaternary III-V semiconductor alloys by De Cremoux (3), Stringfellow (1,2,6-9) and Onabe (4,5,10). They calculated a critical temperature, T_C, using the regular solution approximation and the DLP model. As discussed above, in the regular solution model, the total free energy consists of nearest neighbour chemical bonding energy and entropy terms. In the DLP model, the total free energy consists of chemical free energy and elastic energy terms. In this model, interatomic interaction free energy, F_{INTER}, depends only on the lattice parameter 'a' for a given composition. Their calculations (1-10) have predicted that many III-V alloys have compositions for which the free energy curve has negative values of d^2G/dx^2. Alloys with composition within these regions would be unstable and so should

show a tendency for alloy clustering due to spinodal decomposition. The existence of miscibility gaps is predicted for GaInAsP, GaInP, GaInAsSb, InAsSb, InPSb and GaPSb (1-10).

The free energy of a lattice-mismatched layer is increased due to strain induced by the substrate. The free energy change due to strain (ΔG^E) in a solid solution can be expressed using the regular solution formation (1-4,26) as:

$$\Delta G^E = \Omega x(1-x) + RT\{(1-x)\ln(1-x) + x\ln x\} + \sigma\{(a - a_s)/a_s\}^2 \qquad (2\text{-}11)$$

where the third term on the right hand side of equation (2-11) corresponds to the elastic energy density stored in the layer derived from classical elasticity theory, and 'a_s' is the substrate lattice parameter, 'a' is the unstrained lattice parameter of the layer and σ is a function of the elastic stiffness constant which depends on substrate orientation. This increase in the free energy of the layer caused by substrate-induced strain stabilizes the alloy against spinodal decomposition (6). De Cremoux (3) showed that for nearly lattice-matched ternary alloys the negative curvature of the Gibbs free energy curve arising from the positive enthalpy of mixing of the alloys was almost exactly cancelled by a positive curvature of the free energy curve produced from the elastic strain energy term of equation (2-11). He concluded that ternary alloys expected to be unstable in the bulk form for a certain temperature and composition would actually become metastable when grown as coherent near lattice-matched layers due to the effect of substrate-induced strain stabilisation. This is further discussed by Quillec et al.(27) and Launois et al.(28) who reported the successful LPE growth of GaAsSb layers inside a miscibility gap. If a miscibility gap in the alloy is present at the growth temperature, their epitaxial growth by a near equilibrium technique such as LPE and VPE may be prevented, as observed in LPE $GaAs_ySb_{1-y}$ layers (29). However, growth of these alloys inside a miscibility gap has been accomplished using "non-equilibrium" techniques such as MOCVD and MBE.

In a binary alloy A_xB_{1-x} having a miscibility gap, the alloy spontaneously separates into two phases at a certain temperature by "uphill diffusion". Cahn (30) proposed a modified diffusion equation to describe spinodally decomposed phenomena, taking surface tension and elastic energy into account. The modified equation is written as:

$$\partial x/\partial t = M\{ \partial^2 G/ \partial x^2 + 2\eta^2 E/(1-\nu)\} \nabla^2 x - 2Mk\nabla^4 x \qquad (2\text{-}12)$$

The quantity $M\{ \partial^2 G/ \partial x^2 + 2\eta^2 E/(1-\nu)\}$ is identified with the interdiffusion coefficient, where M is the diffusion mobility, η is the linear strain per unit composition difference, E is Young's modulus, ν is Poisson's ratio and $\nabla = \partial/\partial l$, where 'l' represents a unit of distance. $2Mk\nabla^4 x$ results from a modification of the classical diffusion equation which arises from the existence of a diffuse interface between regions of varying composition, where k is known as the gradient energy coefficient. The composition variations occurring within the immiscible domain result in the generation of associated strain.

There is considerable evidence obtained by different experimental approaches for the occurrence of spinodal decomposition in III-V semiconductor layers. TEM studies have demonstrated the existence of two different typical strain contrasts, for example, a coarse scale tweed-like contrast (~150nm in scale) and a fine scale modulated contrast (~15nm in scale) in layers of III-V semiconductors, as the evidence of the occurrence of spinodal decomposition.

2-3-2 Experimental observations

Hénoc et al.(31), Launois et al.(32) and Glas et al.(33) examined LPE InGaAsP layers grown lattice matched to <100> InP at temperatures in the range 630 to 650°C by TEM and scanning transmission electron microscope (STEM). For these layers with compositions lying within a miscibility gap (1-9,26), they demonstrated the presence of quasi-periodic variations of strain contrast oriented along the <100> directions, with the pseudo-periodicity of ~100nm. STEM/EDX analysis revealed a direct relationship between the strain contrast of the quasi-

periodic structure and large composition variations; these composition variations were oriented along the elastically soft [100] and [010] directions. It was suggested that for the observed composition variations, the anisotropic existence of strain contrast could be such that the strain contribution to the free energy in the InGaAsP layers is minimized. For a growth temperature above the critical temperature for the miscibility gap, the same composition layers did not show these compositional modulations and the solid solution was homogeneous. It was concluded that the periodic structure arose by spinodal decomposition.

The fine scale granular contrast observed in TEM images of Ga-In containing III-V layers was investigated by Gowers (34). This contrast was observed in VPE, LPE or MBE grown Ga-In containing layers, but was absent in binary III-V layers and $Ga_{0.7}Al_{0.3}As$, and very weak in $GaAs_{0.6}P_{0.4}$ layers. It was interpreted in terms of a simple model whereby alloy clustering modulates the average lattice spacing, and the phase variation of the modulation down the diffracting planes relative to the upper crystal surface gives rise to strong contrast in the image by dynamic diffraction.

Chu et al.(35) reported the observation of a compositional modulation due to spinodal decomposition in $In_xGa_{1-x}As_yP_{1-y}$ and $In_xGa_{1-x}As$ layers grown by hydride transport vapour phase epitaxy at 700°C on (001) InP substrates. TEM examination of these layers revealed a fine scale modulated contrast oriented along [100] and [010] directions for all samples over a composition range of $0.2<x<0.53$ and $0.37<y<1$. The observation of the composition modulation in the layers was ascribed to spinodal decomposition occurring by surface diffusion during vapour phase deposition. TEM diffraction contrast experiments on (110) cross-section specimens of planar and nonplanar layers revealed a granular structure oriented along the growth direction, which was consistent with a surface spinodal formation mechanism.

Norman and Booker (36) observed a coarse scale tweed-like contrast (~150nm) and a fine scale granular contrast (~15nm) in TEM images of LPE GaInAsP layers grown on (001) InP substrates at growth temperatures in the range 590°C to 660°C. It was suggested that the coarse scale tweed contrast was due to spinodal decomposition occurring between the liquid and the growing solid solution, while the fine scale granular contrast arose from

spinodal decomposition occurring in the solid phase during cooling down from the growth temperature. TED patterns of such layers revealed <100> satellite spots associated with each of the main spots, corresponding to a periodic variation in lattice parameter correlating with the size of the fine scale granular contrast observed. Epitaxial layers with compositions outside the unstable region, as defined by de Cremoux et al.(3), showed only a weak fine scale granular contrast with very faint or no <100> satellite spots. Norman and Booker (37) showed that for layers with compositions inside the unstable region, the fine scale <100> strain contrast was weak or not present. Periodic strain contrast attributed to spinodal decomposition was observed in the [100] and [010] directions parallel to the layer surface, but not in the [001] direction perpendicular to the layer surface, indicating that spinodal decomposition in these layers was 2-dimensional. They observed this behaviour for a number of LPE, VPE, MOCVD and MBE-grown layers.

The origin of the coarse scale (100-300nm) strain contrast observed in TEM studies of spinodally decomposed $In_xGa_{1-x}As_yP_{1-y}$ layers was investigated by Treacy et al.(38). The observed contrast was explained as due to diffraction effects arising from lattice plane bending near the surface of the thinned specimens, such as would be induced by elastic relaxation of shear stresses accompanying a quasi-periodic lattice strain modulation with an amplitude on the order of 10^{-3}. Qualitative agreement between experimental and simulated images was obtained, strongly suggesting that these features are associated with spinodal decomposition. It was suggested that the fine scale modulated contrast (5-15nm) in this material might also be related to compositional variations.

Some work has been reported on the stability of alloy clustering (39,40). Kuwano et al (39) described TEM studies on the heterointerface and modulated structure in LPE GaInAsP layers lattice matched to GaAs. A strong-dependence of the planarity of the heterointerface on the composition of the layers was observed. This dependence was described in terms of a competition between the melt-back of the substrate and the crystallization of the layer. It was demonstrated that the modulation disappeared when the sample was annealed at high temperatures followed by fast quenching and reappeared if the sample was slowly cooled after annealing. McDevitt et al.(40) reported TEM studies

concerning effects of substrate orientations on alloy clustering in LPE InGaAsP and MBE InGaAs layers grown on (001) and (111) InP substrates. The fine scale contrast modulations were observed to be two-dimensional regardless of substrate orientation, thereby supporting the view that spinodal decomposition occurs at the growth interface.

Many authors have tried to explain the origin of the fine scale modulated contrast observed in III-V semiconductors. Glas (41) reported a detailed investigation of the origin of the diffuse streaks in the TED patterns of InGaAsP layers grown on (001) InP substrates. He used a valence force field (VFF) model (42,43) to compute the atomic displacement field in the material and the kinematical approximation describing the electron diffraction in the TEM. It was shown that totally uncorrelated occupational probabilities of the sites of the mixed sublattices were sufficient to produce the experimental patterns. Recently, Liddle et al.(44) investigated composition fluctuations in GaInAs, AlInAs and GaAlInAs layers using pulsed laser atom probe microanalysis. In one InGaAs layer a significant composition variation was observed (11%), but in two other layers the variations were not statistically significant. The AlInAs studies also revealed significant composition variations (11.4%). For the GaAlInAs, the Ga variation was insignificant, but the Al and In distributions showed significant deviations from random. It was not definitely established whether these compositional variations were associated with the spinodally decomposed structures observed by TEM.

2-3-3 Effects of spinodal decomposition on optical and electrical properties of III-V compound semiconductors

A coarse scale tweed-like contrast and a fine scale granular contrast occurring possibly as a result of spinodal decomposition have been observed by TEM in many III-V semiconductors. Roberts et al.(45) have investigated structural and photoluminescent (PL) properties of MBE $Ga_xIn_{1-x}P$ (x~0.5) grown on (001) GaAs. They reported fine scale grainy structure on the scale of ~10nm. It was proposed that this contrast may arise from local fluctuations in the average Ga-In ratio. The PL efficiency remained relatively unchanged across typical wafer widths of 2.5cm having a composition range of 0.02 in x.

They attributed the absence of PL linewidth broadening to carrier recombination in the regions of lower band gap, which were associated with the composition fluctuation.

Much work has been carried out to investigate PL and electrical properties of InGaAsP layers (46-49). Quillec and co-workers (46) examined LPE InGaAsP/InP grown at temperatures far above the commonly used temperature range. They suggested that a contribution to carrier mobility limitation might be related to the composition modulations present in layers grown in the usual temperature range. Mukai (48) investigated PL spectra and Hall mobility of LPE InGaAsP/GaAs grown at 785 and 815°C as a function of layer composition. He reported a local variation of energy gap and a composition dependence of electron mobility. The composition dependence of PL and X-ray diffraction spectra was more pronounced in the layers grown at 785°C than in the layers grown at 815°C. The local variations of energy gap and lattice constant were attributed to local variations in composition caused by a miscibility gap. Blood and Grassie (49) reviewed the influence of clustering on the mobility of InGaAsP/InP layers using published experimental data. The results showed that the energy of the conduction band in the GaInAsP layer had a spatial variation with an amplitude of about 0.08eV as a result of partial compositional segregation into clusters. They suggested that the electrons might be located in isolated "lakes" and that since the conduction band fluctuation is larger than kT at room temperature and below, current flow might be inhomogeneous and restricted to "percolation paths".

Chiu et al.(50) investigated $GaAs_ySb_{1-y}$ and $Al_xGa_{1-x}As_ySb_{1-y}$ layers having compositions within a miscibility gap. The layers were grown on (100) InP at 500 - 560°C. TEM showed a fine scale contrast indicating a compositional modulation due to spinodal decomposition. The layers exhibited PL spectra with narrow line widths, and good crystallinity. Since these alloys covered the emission wavelength range of 0.65 -1.5μm, they are possible alternative materials for emitters and detectors in fibre optic communication systems operating at 1.3 and 1.55μm.

2-4 Atomic ordering in III-V compound semiconductors

2-4-1 Review of theoretical studies

The ternary and quaternary III-V semiconductor alloys are substitutional solid solutions having the zinc-blende structure. This structure can be thought of as two interpenetrating FCC sublattices: one consists of group V atoms, that is displaced with respect to the other consisting of Group III atoms by one quarter of the unit cell body diagonal.

Phase diagram calculations for the ternary and quaternary III-V semiconductor alloys, using the regular solution approach (1-4,51) or DLP model (6-9,19), have predicted the presence of miscibility gaps in many alloy systems at low temperature and also the possibility that some of these alloys may be unstable with respect to alloy clustering by spinodal decomposition. Atomic ordering in these alloys was not predicted from the bulk thermodynamic calculations since ordered phases are only stable if Ω and $H^m < 0$. However, the theoretical calculation carried out by Srivastava et al.(52), based upon first-principles local-energy self-consistent total-energy minimisation methods, have indicated that the thermodynamically stable low temperature state might be as ordered phases. The total energy minimisation calculations revealed that the stability of the ordered structures arose from the fact that they are strain-reducing, as their structure is such that the two dissimilar bond lengths are accommodated in a coherent fashion (53).

A simple valence force field (VFF) approach and harmonic elasticity theory were also employed by Mbaye et al.(54,55) to investigate the relative stability of the disordered $Ga_xIn_{1-x}P$ alloy and ordered intermediate phases $Ga_nIn_{4-n}P_4$ (n=0-4) in both the bulk and epitaxial layer form. The results illustrated that the availability of structural degrees of freedom in various ternary $A_nB_{4-n}C_4$ alloys could lead to the energy stabilisation of ordered phases when grown epitaxially, and that the substrate strain can preferentially stabilise one structure over another, even when the two are equally stable (or unstable) in the bulk form.

Ichimura and Sasaki (56) have developed a thermodynamical analysis using the virtual crystal approximation (VCA) to estimate the non-randomness of the atom arrangement in III-

V ternary semiconductors. The interactions between atoms are considered to be due entirely to strain, i.e. the stretching and bending of the bonds. The bond lengths are calculated by assuming that the structure of the sublattice on which mixing occurs is uniform, as in the VCA model. Each atom on the other sublattice is allowed to relax to its lowest energy position. The final relaxed lattice consists of an array of tetrahedra, of 5 distinct types, with each containing from 0 to 4 "A" atoms (in an alloy $A_xB_{1-x}C$) at the corners of the tetrahedra and 1 C atom within. The results showed that there was a preference for ordering but not for clustering in III-V ternary alloys. However, Ciraci and Batra (57) investigated the theoretical stability of order and segregation in semiconductor superlattices with a different result. Self-consistent energy-minimization calculations provided some evidence that the ordered phases in epitaxially grown $Ga_{1-x}Al_xAs$ were only metastable. They attributed the reduction of the ordering during prolonged annealing to the onset of segregation. Recently, Boguslawski (58) has estimated the surface formation enthalpies of ordered $Ga_{0.5}In_{0.5}P$ and $GaAs_{0.5}Sb_{0.5}$ using the VFF model. (001) surfaces of {100} and {111} monolayer superlattices (MLSs) and of {110} bilayer superlattices (BLSs) were considered. It was found that a surface of the observed variants which was chemically ordered was stable against segregation at T = 0K.

TEM investigations have demonstrated the existence of ordered phases in epitaxial layers of III-V semiconductor alloys, as discussed in section 2-4-1-2. Ordered structures observed so far are: simple tetragonal CuAu-I type P4m2 structure in MBE and MOCVD $Al_xGa_{1-x}As$; famatinite structure, I42m, in LPE $In_xGa_{1-x}As$ layers; chalcopyrite structure, I42d, in MOCVD $GaAs_{0.5}Sb_{0.5}$ and CuPt-type structure, $R\bar{3}m$, in MBE $GaAs_{0.5}Sb_{0.5}$. Fig 2.3 describes these atomic superlattice structures and their characteristic reciprocal lattices. The simple tetragonal, Ll_0 CuAu-I type structure, with an ideal composition AB, consists of alternating (001) planes of A atoms and B atoms. In the fully ordered CuAu-I type structure each atom has 8 unlike nearest neighbour atoms and 4 like nearest neighbour atoms in comparison to the random solid solution where on average each atom has 6 like and 6 unlike nearest neighbours. The Al_3Ti-type superlattice, with an ideal composition A_3B, has a centred tetragonal lattice. The CuPt-type Ll_1 superlattice, with an ideal composition AB, consists of alternating {111} planes of Cu and Pt atoms, which leads to a distortion of the

Figure 2.3

Atomic superlattice structures and their characteristic reciprocal lattices. The simple tetragonal, Ll_0 CuAu-I type structure, having an ideal composition AB, consists of alternating (001) planes of A atoms and B atoms. In the CuAu-I type structure each atom has 8 unlike nearest neighbour atoms and 4 like nearest neighbour atoms in comparison to the random solid solution where on average each atom has 6 like and 6 unlike nearest neighbour atoms. The Al_3Ti-type superlattice, of ideal composition A_3B, has a centred tetragonal lattice. The CuPt-type Ll_1 superlattice, of ideal composition AB, consists of alternating {111} planes of Cu and Pt atoms, which leads to a distortion of the unit cell from cubic to rhombohedral. The El_1 superlattice, of ideal composition AB, is centred tetragonal with ordering occurring on {210} planes.

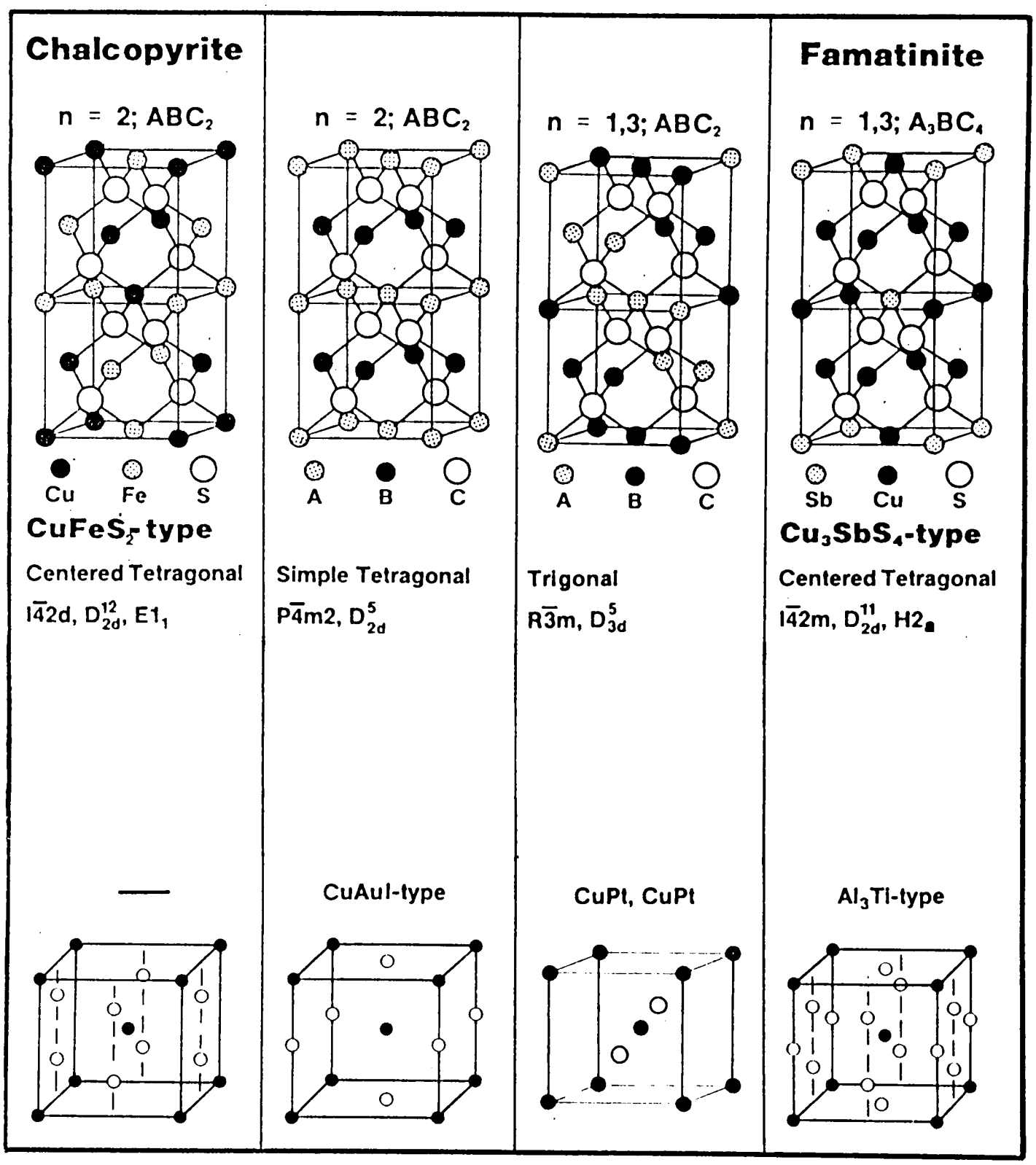
Chalcopyrite
n = 2; ABC2
Cu Fe S
CuFeS2-type
Centered Tetragonal
I4̄2d, D12 2d, E1 1
—
n = 2; ABC2
A B C
Simple Tetragonal
P4̄m2, D5 2d
CuAuI-type
n = 1,3; ABC2
A B C
Trigonal
R3̄m, D5 3d
CuPt, CuPt
Famatinite
n = 1,3; A3BC4
Sb Cu S
Cu3SbS4-type
Centered Tetragonal
I4̄2m, D11 2d, H2a
Al3Ti-type

Fig. 2.3

unit cell from cubic to rhombohedral. The El_1 superlattice, with an ideal composition AB, is centred tetragonal with ordering occurring on {210} planes.

2-4-2 Experimental observations

The first experimental observation of ordering in the ternary III-V semiconductors was reported by Kuan et al.(59). TED patterns showed the existence of CuAu-I type ordering in MOCVD and MBE AlGaAs layers. Thus, 1/2[220] and 1/2[002] extra spots were observed in the [110] TED pattern, corresponding to ordering of the (220) and (002) planes of the Group III sublattice. The intensity of these extra spots observed from $Al_xGa_{1-x}As$ layers grown on (110) GaAs was dependent on both growth temperature and Al content (x) and the ordered spots were strongest for x=0.75 and at a growth temperature of 700°C. The extra spots were streaked in the [110] growth direction and this was attributed to the presence of a high density of planar antiphase boundaries normal to the growth direction. It was suggested that the formation of the ordered state in $Al_xGa_{1-x}As$ layers depended on the surface diffusion of Ga and Al atoms during high temperature growth and that this ordered structure was the equilibrium state for AlGaAs layers. Wang (60) proposed a charge transfer dipole stabilisation model to explain the observed long range ordering in the AlGaAs layers. Kuan et al.(61) also reported TEM evidence for CuAu-I type sublattice ordering in MBE InGaAs layers grown on (110) InP at 530°C, showing identical long range ordering to that observed in the AlGaAs layer. TEM diffraction results indicated the existence of a high density of antiphase domain boundaries in the ordered InGaAs phase.

Nakayama et al.(62) reported the existence of an ordered phase in $In_{1-x}Ga_xAs$ layers grown on (001) InP at 630°C. TED patterns displayed extra spots at $\pm$1/2<200> and $\pm$1/2<210> positions corresponding to ordering in {200} and {210} planes. They interpreted this as evidence for the formation of the ordered phase having the famatinite structure with space group I42m, corresponding to a chemical composition of $InGa_3As_4$ or In_3GaAs_4. TEM images showed a strong modulated contrast due to compositional modulated structure.

The work of Jen et al (64) concerns the kinetic aspects of the formation of CuAu-I and chalcopyrite type ordering in MOCVD GaAsSb layers, i.e. the effects of growth temperature and rate, and substrate orientation. They examined $GaAs_{0.5}Sb_{0.5}$ layers grown on (001) InP at 580°C-600°C and observed [001] TED patterns similar to those described by Nakayama et al.(62). The TED patterns revealed superstructure spots at {100} and {1,1/2,0} positions. Their layer contained two ordered phases: a simple tetragonal CuAu-I type Ll_0 structure consisting of alternating {100} oriented GaAs and GaSb layers, and the chalcopyrite El_1 structure with alternating {210} oriented GaAs and GaSb layers. The ordered phases were predicted to occur if the surface mobility during epitaxial growth is high enough, and the growth temperature is lower than the critical temperature for a disordering transformation. The layers grown at 550°C on (100) InP were observed to have only the Ll_0 ordered structure at the high growth rate of 0.02μm/min and principally the Ll_0 ordered structure with a very small amount of El_1 at the low growth rate of 0.01μm/min. Photoluminescence measurements for the layers grown on (221) and (311) substrates revealed much stronger intensities and narrower half-widths than for those grown on (100) and (110) InP substrates, due probably to the absence of ordered phases.

The first observation of CuPt-type sublattice ordering in ternary III-V layers was reported by Murgatroyd et al.(65-67). The ordering on {111} planes was observed in MBE $GaAs_ySb_{1-y}$ grown lattice-mismatched on (001) GaAs and lattice-matched on (001) InP at 520°C. A spinodally decomposed structure was also observed in these layers. Only two variants of the CuPt-type structure, corresponding to ordering on $(\bar{1}11)$ and $(1\bar{1}1)$ planes, were observed in these layers. [110] cross-sectional TED patterns showed that all the 1/2{111} extra spots were streaked in the [001] growth direction, the streaks connecting extra spots. This was attributed to the presence of an abrupt breakdown of ordering occurring in the [001] growth direction. Streaking of the fundamental diffracted spots was observed along the [110] direction parallel to the interface between substrate and layer. Since the first observation of the CuPt-type ordered structure by Murgatroyd, Norman and Booker (65), CuPt-type ordering has been reported in wide variety of III-V layers such as AlInAs, InGaAs, InGaAsP, GaInP, AlGaInP, GaAsSb and InAsSb (68-77).

The stability of different ordered structures could be thermodynamically and kinetically dependant on the experimental parameters such as growth technique, growth temperature, growth direction, substrate, etc. The CuPt-type ordered structure affords less of a reduction in strain energy in bulk material for an alloy composed of binary materials with differences in lattice parameter, and so is considerably less stable than CuAu I-type and chalcopyrite structures (61). Several authors have proposed models to explain the occurrence of CuPt-type ordering in III-V layers. Suzuki et al.(78) introduced a model for InGaP layers involving both surface energy and kinetics considerations. This mechanism was based on the experimental results for the substrate orientation dependence of the apparent asymmetry of the four equivalent {111} ordered variants. Their arguments involve the participation of two kinds of mechanisms, i.e. ordering within each (001) plane and ordering for successive (001) ordered planes. The first mechanism was attributed to, in the case of InGaP, the anisotropic site occupation affinity for the Group III atoms, Ga and In, due to both a bond length difference between Ga-P and In-P, and a dangling bond direction asymmetry on the P-stabilized (001) surface (78). The second mechanism was ascribed to the presence of $\{111\}_B$ microfacets. Augarde et al.(79) also suggested simple rules controlling the growth process at the atomic level which explained the absence of the (111) and $(11\bar{1})$ variants and the selection effect of the misorientation toward $[1\bar{1}0]$ as well as the absence of ordering on $(111)_B$ substrates. They assumed that the following rules apply during crystal growth: i) growth was controlled by the deposition of Group III atoms to the surface, their migration and incorporation to steps; ii) once a Group III atom terrace had grown, it was immediately covered by Group V atoms; iii) the lowest internal energy configurations for a Group V centred tetrahedron at the surface corresponded to a tetrahedron with either a base of three Ga atoms and a summit of one In atom or a base of three In atoms and a summit of one Ga atom. Murgatroyd, Norman and Booker (80) have described a possible relationship between surface reconstruction and atomic ordering, based on MBE GaAsSb layer growth. They proposed a model to interpret the observed experimental results in terms of ordered atomic arrangements of the Group V atoms, which resulted from the surface reconstruction being incorporated into the bulk layers. This is described more fully in chapter 6.

A number of studies on the stability of CuPt-type ordering in III-V layers has been carried out. Gavrilovic et al (81) and Plano et al (82) reported disordering of the ordered structure in MOCVD GaInP and AlGaInP layers by Zn diffusion and thermal annealing. GaInP and $(Al_xGa_{1-x})_{0.5}In_{0.5}P$ layers grown at temperatures below 700°C showed an ordered arrangement of the Group III atoms and a periodic compositional modulation along the growth direction under certain growth conditions. They presented data showing that epitaxial layers of both GaInP and $(Al_xGa_{1-x})_yIn_{1-y}P$ grown on (001) GaAs and containing the ordered phase could be converted to a disordered alloy by thermal annealing under a variety of conditions at temperatures not exceeding the growth temperature. Recently, Goral and co-workers (83) investigated the effect of selenium doping on the ordering of $GaInP_2$. They showed that ordering disappeared when carrier concentrations exceeded the order of $10^{18}cm^{-3}$ for samples grown at 670°C and 740°C and that at each growth temperature, the ordering decreased and the bandgap increased with increasing Se doping. It was reported that Zn and Mn doping elements affect the ordering in a similar manner. Ueda et al.(84) investigated the effect of the rotation of the substrates during growth on ordering in MOCVD InGaP layers grown on (001) GaAs. For layers grown with substrate rotation, ordering occurred for the Group III atoms on only one set of {111} planes and the ordered regions consisted of plate-like microdomains lying close to the (001) plane. For layers grown without substrate rotation, ordering occurred on two set of {111} planes, the ordered domains were larger and the relative volume of the ordered regions was increased.

In addition to experimental evidence obtained from TED and TEM studies for ordering in III-V layers, X-ray investigations have been performed to evaluate ordered structures. Kurtz et al (85) presented X-ray diffraction studies on the nature of the ordering in $GaInP_2$, and discussed the relationship between anomalous changes in the band gap and ordering of the Group III sublattice of $GaInP_2$. It was shown that the X-ray and electron diffraction data disagreed as to which of these four possible {111} ordered variants were observed and as to the direction of the streaks through superlattice spots. They reported no correlation between the long-range order parameters and the band gap anomalies. Okuda et al (86) also examined the ordered structure occurring in MOCVD AlGaInP grown on (100)

GaAs substrates using X-ray diffraction measurements. The results showed that the ordered spot became strong as the Al content increased and was observed only for the 1/2(111) diffraction, corresponding to CuPt-type $\{111\}_B$ ordering.

2-4-3 Effects of atomic ordering on optical and electrical properties of III-V compound semiconductors

Ordering into CuAu-I, CuPt-type, famatinite and chalcopyrite structures has been recently reported in many disordered III-V semiconductor layers. Gomyo and co-workers (87,88) examined $Ga_XIn_{1-X}P$ layers grown by MOCVD at various V/III ratios and growth temperatures. They reported a shift of the PL peak energy from 1.90 to 1.85eV due to the different growth conditions. The shift was attributed to an energy band structure difference due to atomic scale arrangement differences on the Group III element sublattice. It was suggested that atomic ordering decreased the PL peak energy. Kondow et al (89,90), Nishino (91) and Fouquet et al.(92) examined abnormal properties of $Ga_{0.5}In_{0.5}P$ layers. Kondow and co-workers (89,90) investigated the relationship between growth temperature and ordering in MOCVD GaInP using TEM, electroreflectance (ER) and Raman scattering measurements. An anomalous bandgap observed was attributed to a variation in the atomic arrangement of neighbouring atoms. Nishino (91) reported on an electroreflectance (ER) study of ordered GaInP, dealing with the effects of variations in growth temperature, V/III ratio and substrate orientation. The results showed that the ER structures observed at 2.2 and 2.4eV were closely related to the ordered structure of this alloy and could be described by ordering induced pseudo-direct transitions made possible by folding the L_1 conduction band into the π point.

Gavrilovic et al (81) reported disordering of the ordered structure in MOCVD GaInP and AlGaInP layers by Zn diffusion and thermal annealing. The disappearance of the ordered phase was accompanied by a shift of the band gap to higher energy by 90meV. Nozaki et al (93) investigated the atomic arrangements and their effect on the band gap (E_g) of InGaAlP grown with a wide range of growth temperatures (570-770°C) using TEM, PL and

photoacoustic spectroscopy (PAS). It was concluded that E_g changed due to ordering and this was influenced by the Al composition in InGaAlP layers. For $In_{0.5}(Ga_{1-x}Al_x)_{0.5}P$ ($x \approx 0.5$), E_g was dependent on the degree of ordering. However, the change in E_g for $In_{0.5}(Ga_{1-x}Al_x)_{0.5}P$ ($x \approx 0.5$) was smaller than that for $In_{0.5}Ga_{0.5}P$ by 50meV. As x increased, E_g for the ordered structure approached and finally reached the value for the disordered structure at $x \approx 0.5$.

Bernard et al.(94) demonstrated ordering induced changes in the optical spectra of semiconductors. It was shown that the spontaneous ordering of ternary $A_{0.5}B_{0.5}C$ semiconductors into the $(AC)_1(BC)_1$ superlattice structure gives rise to characteristic changes in the optical and photoemission spectra. They predicted new direct transitions and substantial splittings of transitions which are absent in the disordered alloy. Recent theoretical work by Wei and Zunger (95) predicted that spontaneous ordering of semiconductors results in a reduction in the average value of the bandgap relative to the binaries. They identified the mechanism for band gap narrowing as band folding followed by repulsion between the folded states.

REFERENCES-CHAPTER 2

1. G.B. Stringfellow, J. Phys. Chem. Solids **34** (1973) 1749.
2. G.B. Stringfellow, J. Cryst. Growth **27** (1974) 21.
3. B. de Cremoux, J. de Physique coll. C5, suppl. **no12**, (1982) C5.
4. K. Onabe, Jpn. J. Appl. Phys. **21** (1982) 964.
5. K. Onabe, Jpn. J. Appl. Phys. **21** (1982) 2323.
6. G.B. Stringfellow, J. Cryst. Growth **58** (1982) 194.
7. G.B. Stringfellow, J. Electron Mater. **11** (1982) 903.
8. G.B. Stringfellow, J. Cryst. Growth **65** (1983) 454.
9. G.B. Stringfellow, J. Appl. Phys. **54** (1983) 404.
10. K. Onabe, NEC Research and Development **72** (1984) 1.
11. M. Quillec, C. Dagnet, J.L. Benchimol and H. Launois, Appl. Phys. Lett. **40** (1982) 325.
12. J.W. Christian, "The Theory of Transformations in Metals and Alloys Part 1", (Pergamon Press, 1975).
13. J.H. Hiderbrand, J. Ameri. Chem. Soc. **51** (1926) 66.
14. M.B. Panish and M. Ilegems, Prog. in Solid State Chemistry vol **7**, Eds H. Reiss and J.O. McCaldin (Pergamon, New York), (1972) p39.
15. J.P. Suchet, "Chemical Physics of Semiconductors" (New York, 1965).
16. J.C. Phillips and J.A. Van Vechten, Phys. Rev. **B2** (1970) 2147.
17. J.A. Van Vechten, Phys. Rev. **170** (1968) 773.
18. J.C. Phillips, Phys. Rev. Lett. **20** (1968) 550.
19. G.B. Stringfellow, J. Cryst. Growth **62** (1983) 225.
20. P.A. Fedders and M.W. Muller, J. Phys. Chem. Solids **45** (1984) 685.
21. J.C. Mikkelsen Jr. and J.B. Boyce, Phys. Rev. Lett. **49** (1982) 1412.
22. J. Bellessa, C. Gors, P. Launois, M. Quillec and H. Launois, Inst. Phys. Conf. Ser. **65** (1982) 529.
23. T. Fukui, Jpn. J. Appl. Phys. **23** (1984) L208.
24. T. Fukui, J. Appl. Phys. **57** (1985) 5188.

25. A.B. Chen and A. Sher, Phys. Rev. **B32** (1985) 3695.

26. B. de Cremoux, P. Hirtz and J. Ricciardi, Inst. Phys. Conf. Ser. **56** (1981) 115.

27. M. Quillec, H. Launois and M.C. Joncour, J. Vac. Sci. Tech. **B1** (1983) 238.

28. H. Launois and M. Quillec, GaAs and related compounds, Biarritz, Inst. Phys. Conf. Ser. **74** (1984) 167.

29. J.R. Pessetto and G.B. Stringfellow, J. Cryst. Growth **62** (1983) 1.

30. J.W. Cahn, Acta metall. **9** (1961) 795.

31. H. Hénoc, A. Izrael, M. Quillec and H. Launois, Appl. Phys. Lett. **40** (1982) 963.

32. H. Launois, M. Quillec, F. Glas and M.J. Treacy, Inst. Phys. Conf. Ser. **65** (1982) 537.

33. F. Glas, M.M.J. Treacy, M. Quillec and H. Launois, J. de Phys. coll. C5, suppl. **No12**, (1982) C1-11.

34. J.P. Gowers, Appl. Phys. **A31** (1983) 23.

35. S.N.G. Chu, S. Nakahara, K.E. Strege and W.D. Johnston, J. Appl. Phys. **57** (1985) 4610.

36. A.G. Norman and G.R. Booker, J. Appl. Phys. **57** (1985) 4715.

37. A.G. Norman and G.R. Booker, Inst. Phys. Conf. Ser. **76** (1985) 257.

38. M.M.J. Treacy, J.M. Gibson and A. Howie, Phil. Mag. **A51** (1985) 389.

39. N. Kuwano, K. Fukada, K. Oki, S. Tanaka, K. Hiramatsu and I. Akasaki, J. Cryst. Growth **98** (1989) 82.

40. T.L. McDevitt, F.S. Turco, M.G. Tamargo, S. Mahajan, D.E. Laughlin, V.G. Keramidas and W.A. Bonner, Inst. Phys. Conf. Ser. **100** (1989) 173.

41. F. Glas, Inst. Phys. Conf. Ser. **100** (1989) 107.

42. P.N. Keating, Phys. Rev. **145** (1966) 637.

43. R.M. Martin, Phys. Rev **B1** (1970) 4005.

44. J.A. Liddle, R.A.D. Mackenzie, C.R.M. Grovenor and A. Cerezo, Inst. Phys. Conf. Ser. **100** (1989) 81.

45. J.S. Roberts, G.B. Scott and J.P. Gowers, J. Appl. Phys. **52** (1981) 4018.

46. J.L. Benchimol, M. Quillec and S. Slempkes, J. Cryst. Growth **64** (1984) 96.

47. M. Quillec, J.L. Benchimol, S. Slempkes and H. Launois, Appl. Phys. Lett. **42** (1983) 886.

48. S. Mukai, J. Appl. Phys. **54** (1983) 2635.

49. P. Blood and A.D.C. Grassie, J. Appl. Phys. **56** (1984) 1866.

50. T.H. Chiu, W.T. Tsang, S.N.G. Chu, J. Shah and J.A. Ditzenberger, Appl. Phys. Lett. **46** (1985) 408.

51. K. Onabe, Jpn. J. Appl. Phys. **21** (1982) L323.

52. G.P. Srivastava, J.L. Martins and A. Zunger, Phys. Rev. **B31** (1985) 2561.

53. J.E. Jaffe and A. Zunger, Phys. Rev. Lett. **51** (1983) 662.

54. A.A. Mbaye, Appl. Phys. Lett. **49** (1986) 782.

55. A.A. Mbaye, Phys. Rev. **B37** (1988) 3008.

56. M. Ichimura and A. Sasaki, J. Appl. Phys. **60** (1986) 3850.

57. S. Ciraci and I.P. Batra, Phys. Rev. Lett. **58** (1987) 2914.

58. P. Boguslawski, Phys. Rev. **B42** (1990) 3737.

59. T.S. Kuan, T.F. Kuech, W.I. Wang and E.L. Wilkie, Phys. Rev. Lett. **54** (1985) 201.

60. W.I. Wang, J. Appl. Phys. **58** (1985) 3244.

61. T.S. Kuan, W.I. Wang and E.L. Wilkie, Appl. Phys. Lett. **51** (1987) 51.

62. H. Nakayama and H. Fujita, Inst. Phys. Conf. Ser. No **79** (1985) 289.

63. H.R. Jen, M.J. Cherng and G.B. Stringfellow, Appl. Phys. Lett. **48** (1986) 1603.

64. H.R. Jen, M.J. Jou, Y.T. Cherng and G.B. Stringfellow, J. Cryst. Growth **85** (1987) 175.

65. I.J. Murgatroyd, A.G. Norman and G.R. Booker, presented at Inst. Phys. Solid State Phys. Conf., University of Reading, Dec. 1985.

66. I.J. Murgatroyd, A.G. Norman and G.R. Booker, presented at MRS Spring meeting, Palo Alto, U.S.A., April, 1986.

67. I.J. Murgatroyd, A.G. Norman, G.R. Booker and T.M. Kerr, Proc. the XI Inter. Congress on Electron Microscopy, Kyoto, Japan, (1986) p1497.

68. A.G. Norman, R.M. Mallard, I.J. Murgatroyd, G.R. Booker, A. H. Moore and M.D. Scott, Inst. Phys. Conf. Ser. **87** (1987) 77.

69. M.A. Shahid, S. Mahajan, D.E. Laughlin and H.M. Cox, Phys. Rev. Lett. **58** (1987) 2567.

70. P. Bellon, J.P. Chevalier, G.P. Martin, E. Dupont-Nivet, C. Thiebaut and J.P. André, Appl. Phys. Lett. **52** (1988) 567.

71. Y.-E. Ihm, N. Otsuka, J. Klem and H. Morkoc, Appl. Phys. Lett. **51** (1987) 2013.

72. H.R. Jen, K.Y. Ma and G.B. Stringfellow, Appl. Phys. Lett. **54** (1989) 1154.

73. H.R. Jen, D.S. Cao and G.B. Stringfellow, Appl. Phys. Lett. **54** (1989) 1890.

74. O. Ueda, M. Hoshino, K. Kodama, H. Yamada and M. Ozeki, J. Cryst. Growth **99** (1990) 560.

75. O. Ueda, M. Takechi and J. Komeno, Appl. Phys. Lett. **54** (1989) 2312.

76. M. Kondow, H. Kakibayashi, T. Tanaka and S. Minagawa, Phys. Rev. Lett. **63** (1989) 884.

77. O. Ueda, M. Takechi and J. Komeno, J. Appl. Phys. **64** (1990) 312.

78. T. Suzuki, A. Gomyo and S. Iijima, J. Cryst. Growth **93** (1988) 396.

79. E. Augarde, M. Mpaskoutas, P. Bellon, J.P. Chevalier and G.P. Martin, Inst. Phys. Conf. Ser. No. **100** (1989) 155.

80. I.J. Murgatroyd, A.G. Norman and G.R. Booker, J. Appl. Phys. **67** (1990) 2310.

81. P. Gavrilovic, F.P. Dabkowski, K. Meehan, J.E. Williams, W. Stutins, K.C. Hsieh, N. Holoyak, M.A. Shahid and S. Mahajan, J. Cryst. Growth **93** (1988) 418.

82. W.E. Plano, D.W. Nam, J.S. Major, K.C. Hsieh and N. Holoyak, Appl. Phys. Lett. **53** (1988) 2537.

83. J.P. Goral, S.R. Kurtz, J.M. Olson and A. Kibbler, J. Electronic Mater. **19** (1990) 95.

84. O. Ueda, M. Takikawa, M. Takechi, J. Komeno and I. Umebu, J. Cryst. Growth **93** (1988) 418.

85. S.R. Kurtz, J.M. Olson and A. Kibbler, Appl. Phys. Lett. **54** (1989) 718.

86. H. Okuda, C. Anayama, T. Tanahashi and K. Nakajima, Appl. Phys. Lett. **53** (1988) 2537.

87. A. Gomyo, T. Suzuki, K. Kobayashi, S. Kawata, I.Hino and T. Yuasa, Appl. Phys. Lett. **58** (1987) 637.

88. A. Gomyo, T. Suzuki and S. Iijima, Phys. Rev. Lett. **60** (1988) 2645.

89. M. Kondow, H. Kakibayashi, S. Minagawa, Y. Inoue, T. Nishino and Y. Hamakawa, J. Cryst. Growth **88** (1988) 291.

90. M. Kondow, H. Kakibayashi, S. Minagawa, Y. Inoue, T. Nishino and Y. Hamakawa, Appl. Phys. Lett. **53** (1988) 2053.

91. T. Nishino, J. Cryst. Growth **98** (1989) 44.

92. J.E. Fouquet, V.M. Robbins, J. Rosner and O. Blum, Appl. Phys. Lett. **57** (1990) 1566.

93. C. Nozaki, Y. Ohba, H. Sugawara, S. Yasuami and T. Nakanisi, J. Cryst. Growth **93** (1988) 406.

94. J.E. Bernard, S.H. Wei and A. Zunger, Appl. Phys. Lett. **52** (1988) 311.

95. S.H. Wei and A. Zunger, Appl. Phys. Lett. **56** (1990) 662.

CHAPTER 3

EXPERIMENTAL METHODS FOR GROWTH AND ASSESSMENT OF HETEROEPITAXIAL LAYERS OF III-V COMPOUND SEMICONDUCTORS

3-1 Nonequilibrium epitaxial growth techniques

3-1-1 Introduction

Theoretical calculations have predicted the existence of immiscible regions for most ternary III-V compound semiconductors and difficulty has been experienced in growing epitaxial layers of these semiconductors. However, successful growth of epitaxial layers has been achieved using nonequilibrium epitaxial growth techniques such as metalorganic chemical vapour deposition (MOCVD) and molecular beam epitaxy (MBE). The heteroepitaxial layers of III-V compound semiconductor alloys investigated in this work were grown on (001) crystalline substrates by using non-equilibrium epitaxial growth techniques such as MOCVD and MBE. All of the epitaxial layers are listed in Table 4.1, Table 5.1, Table 5.2, Table 5.3 and Table 6.3 with MBE-InAsSb, MOCVD-InAsSb, MOCVD-InGaAs, MOCVD-InPSb and MOCVD-GaPSb systems. Now these growth techniques will be briefly described.

3-1-2 Metalorganic chemical vapour deposition

MOCVD is an established production technique yielding novel electronic and opto-electronic devices (1,2). Epitaxial growth using this technique can be accomplished by transporting individual components in the vapour form to a heated substrate, where the formation of the compound semiconductor occurs after chemical reactions in the gas phase and/or on the substrate surface. The Group III elements are transported by volatile metalorganic (MO) compounds such as trimethylgallium and trimethylindium (3,4), while the more volatile species such as As and P are transported in the form of their hydrides, such as AsH_3 and PH_3 (5). Reactors for MOCVD growth are of welded construction and utilize stainless steel plumbing for handling reactants. Palladium-purified hydrogen (99.9999% purity) is commonly used as the carrier gas to transport MO compound vapours to the reaction chamber. All gases are metered through mass flow controllers with a flow accuracy

of 1% of full scale. Hydrides, MOs and carrier gas are all delivered through a gas handling system to the reaction chamber. In its simplest form, the reaction chamber consists of an rf heated graphite susceptor, on which the substrate is positioned, in a quartz chamber. The temperature of the susceptor is usually monitored by means of a thermocouple embedded in it, and approximates the temperature of the substrate. The epitaxial growth occurs as a result of the mass transport of species to the substrate, surface processes such as adsorption and desorption, and kinetic factors such as the decomposition rate of the MO and the hydride. Since the growth mechanism of MOCVD is pyrolysis, a cold wall reactor is used to avoid deposition on surfaces other than the substrate. Growth is performed in the presence of an excess of the Group V species, with the Group III species serving as the rate controller. Growth may be carried out with the reaction chamber at atmospheric pressure or low pressure. There are two different reactor systems, i.e. a typical horizontal reaction chamber suitable for the growth of one to two substrates at a time, and a vertical reaction chamber capable of growing many substrates at a time. In both cases, careful control of the fluid flow conditions - involving adjustments of susceptor angle, height above the susceptor, entry distances and gas flow conditions - allows uniform growth over the substrate. The main advantages of this growth technique are: 1) the great versatility and the applicability to the preparation of a wide range of important material alloy systems; 2) thin epitaxial layer structures with widely varying but controlled compositions and thicknesses, consistently produced; 3) thin layers with extremely abrupt interfaces as required for low dimensional structures. Disadvantages include possible carbon contamination, the use of pyrophoric and hazardous chemicals and the non-availability of in-situ monitoring of the deposition reactions.

3-1-3 Molecular beam epitaxy

The MBE growth technique is a thin film deposition process in which a thermal beam of atoms or molecules reacts at the clean surface of a single crystal substrate, held at high temperatures under ultrahigh vacuum conditions, to form an epitaxial film (6). The

requirement of maintaining an ultrahigh vacuum environment throughout the growth apparatus is achieved by using multiple chambers, separated by gate valves. The first chamber serves for sample insertion (10^{-6} to 10^{-7} Torr). The second chamber acts principally as a buffer between the insertion and growth chambers. The final chamber, i.e. the growth chamber, is capable of UHV ($<10^{-10}$ Torr). The primary pumping of the growth chamber is accomplished with a combination of either storage pumps (ion, titanium sublimation or cryopumps) or throughput pumps (diffusion or turbomolecular pumps), depending on the nature of the evaporants. The most common method for producing molecular beams is the use of Knudsen effusion cells (7). The crucible employed in Knudsen cells is generally made from pyrolytic boron nitride (BN). The beam fluxes are monitored with an ionization gauge, placed close to the substrate. Control over the layer composition and doping profile is attained by incorporating a mechanical shutter in front of each source. Since the flow of molecules or atoms from the source to the substrate is in the molecular rather than the hydrodynamic flow regime, positioning a shutter in front of a source will effectively stop the beam from reaching the substrate. The ability to start and stop a molecular beam in less than the time taken to grow a single atomic or molecular layer has led to the required abruptness to produce complex multilayer structures. The use of UHV conditions has enabled the physical and chemical properties of the layers to be measured in-situ using reflection high energy diffraction (RHEED) and Auger electron spectroscopy (AES). RHEED can be used to study thermal desorption of surface oxides prior to growth, to control the initial stages of epitaxial growth, and to investigate surface reconstruction as a function of growth parameters (8,9). Another application is the study of surface topology (10). The development of the RHEED intensity oscillation technique (11-13) can be used to calibrate beam fluxes, control alloy composition, and control the thickness of quantum wells and superlattice layers (14). The advantages of MBE are as follows: 1) the low growth rate allows compositional and doping profile changes to occur within atomic dimensions by the operation of mechanical shutters; 2) the growth temperature is relatively low and so interface diffusion between layers of different compositions can be negligibly small; 3) in-situ surface analysis techniques can be used. Disadvantages include the

extremely high cost of the equipment, the low growth rate and hence long growth times, and problems in growing P-containing compounds.

3-2 Determination of crystal polarity

3-2-1 Introduction

Most semiconductor systems studied in this work have shown the presence of the CuPt-type ordered structure, as will be described in chapter 6. Anisotropy associated with the formation of this ordered structure, for example, the observation of two of the four possible {111} plane variants, was demonstrated to occur. In order to understand how this ordering occurs, it is important to be able to determine experimentally the polarity of these Group III-V epitaxial layers, so that the sense of the anisotropy can be established.

3-2-2 Chemical etching technique

It is often possible to distinguish between the opposite polar faces of sphalerite materials by the use of various chemical etches. Chemical etching is simply the preferential removal of surface material and depends on the chemical activity of different crystallographic planes and hence sample orientation, and the nature of the chemical etchant used. Due to the polar nature of crystals of Group III-V semiconductor alloys, the [110] and the $[1\bar{1}0]$ directions in the surface of an (001) wafer are not equivalent and can be distinguished by the orientation of etch pits. In the present work, polarity between [110] and $[1\bar{1}0]$ directions was determined by etching the $(00\bar{1})$ surface of the GaAs substrate upon which epitaxial layers had been grown. The $(\bar{1}11)$ and $(1\bar{1}1)$ planes, whose intersection is the [110] direction, can thus be distinguished from the (111) and $(11\bar{1})$ planes, whose intersection is the $[1\bar{1}0]$ direction. However, the $(\bar{1}11)$ and the $(1\bar{1}1)$ planes are not explicitly distinguished. We have used the convention that an exposed $(\bar{1}\,\bar{1}\,\bar{1})$ surface in a GaAs crystal is assumed to be As atom-rich. Prior to etching, the sample was polished using 6μm

diamond paste and finally syton chemically/mechanically polished to remove any remaining mechanical damage. The $(00\bar{1})$ surface of the GaAs substrate was then etched in a solution of 10:1 H_2O_2:H_2SO_4 for 1-3 min. at room temperature. Rhombohedral etch pits elongated along the [110] direction are produced (15) (Fig. 3.1(a)). This direction corresponds to the $[1\bar{1}0]$ direction for the (001) surface of epitaxial layers. The orientation of these etch pits, which were visible under an optical microscope at X1000, was determined from a piece of single crystal bulk GaAs, cut and polished so that (001), $(00\bar{1})$, (111) and $(\bar{1}\,\bar{1}\,\bar{1})$ surfaces were exposed (Fig. 3.1(b)). The orientation of this bulk crystal had been previously determined by etching in concentrated nitride acid for 30 sec, with all the faces blackening except for the slow reacting (111) Ga face (16). This etching result has confirmed the orientation of the epitaxial layers supplied by the manufacturer.

3-2-3 Convergent beam electron diffraction technique

Convergent beam electron diffraction (CBED) has become a technique of increasing interest for the determination of crystal symmetries and the phases of structure factors (17,18). Attention has mainly been given to systematic row orientations or directions exactly along or close to low-index zone axes. In order to determine the polarity of <110> cross-section thin foil specimens, we have used the coupling between the weak 002 reflection and two weak odd-index reflections. In the present work, CBEDs were obtained using a Philips CM12 electron microscope operating at 120kV. It is assumed that the polarity of a Group III-V ternary or quarternary layer is the same as that of the underlying substrate, i.e., there is no discontinuity of the Group III sublattices at the interface between the GaAs substrate and the epitaxial layer. The diffraction results with the 002 and $00\bar{2}$ reflections respectively at the Bragg condition were compared (19). The specimen was tilted about 10° or more in the (002) plane, so that two weak odd-index reflections were at the Bragg reflection position. Fig. 3.2(a) is a schematic diagram showing the important reflections and the scattering paths from the central beam to the 002 reflection. In Fig. 3.2(b), the Bragg condition is fulfilled for the 002, $1\bar{1}11$ and $1\bar{1}\,\bar{9}$ reflections, and in Fig. 3.2(c), the Bragg

Figure 3.1

(a) Optical micrograph of a rhombohedral etch pit elongated along the [110] direction on the surface of a $(00\bar{1})$ GaAs wafer. (b) Schematic drawing of stereogram showing $(111)_{Ga}$ and $(\bar{1}\,\bar{1}\,\bar{1})_{As}$ faces and orientation of etch pits (etch of 10:1 H_2O_2:H_2SO_4 for 3 min) on the $(00\bar{1})$ surface of GaAs substrate.

a)

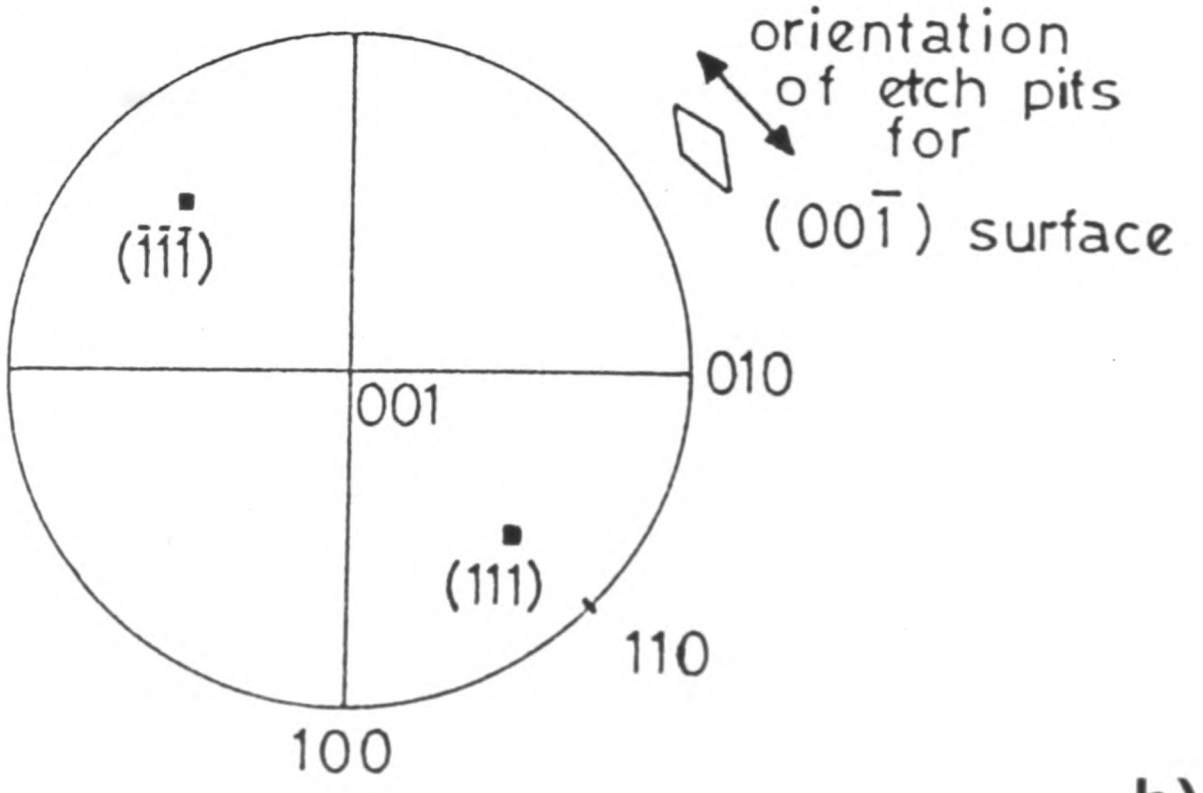
orientation
of etch pits
for
(00$\bar{1}$) surface
($\bar{1}\bar{1}\bar{1}$)
001
010
(11$\bar{1}$)
110
100

b)

Fig. 3.1

Figure 3.2

(a) Schematic drawing showing the important reflections and the scattering paths from the central beam to the (002) reflection in TED patterns from a <110> cross-section thin foil specimen. (b) and (c) GaAs with the (002) and $(00\bar{2})$ reflections, respectively. Note bright cross contrast within the (002) reflection and dark cross contrast within the $(00\bar{2})$ reflection.

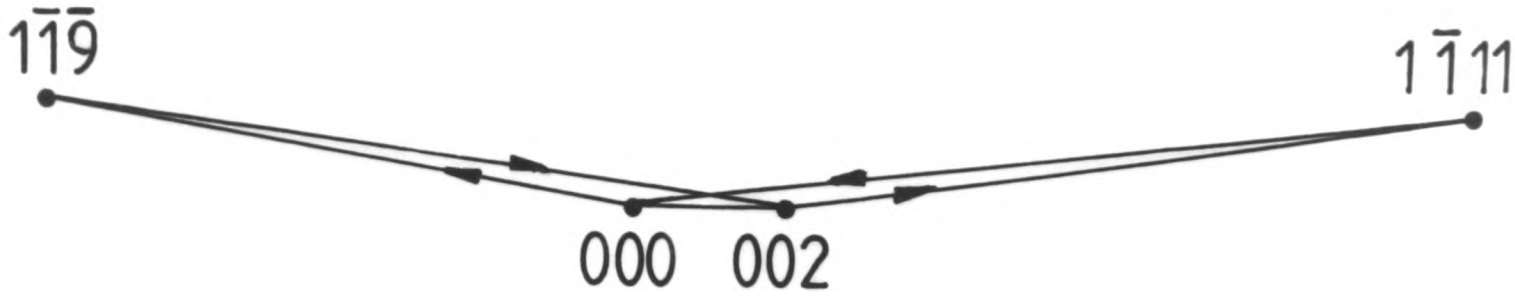

a)

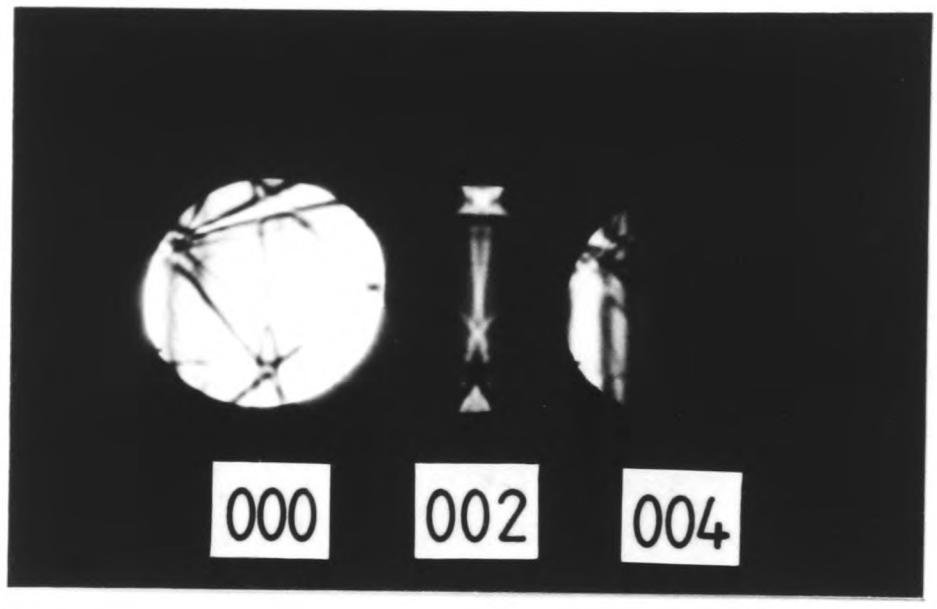

b)

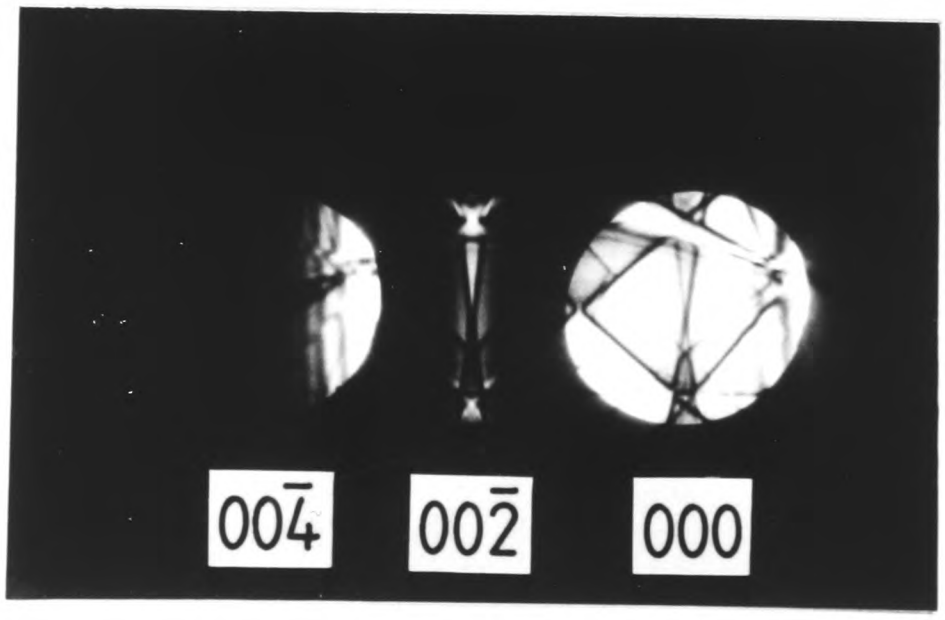

c)

Fig. 3.2

condition is fulfilled for the $00\bar{2}$, $1\bar{1}9$ and $1\bar{1}\bar{1}1$ reflections. In the first case, the three reflections scatter constructively into the 002 reflection, with particularly high intensity where the two sharp lines cross each other, whereas in the latter case, there is reduced intensity along the lines corresponding to the Bragg reflecting position for $1\bar{1}9$ and $1\bar{1}\bar{1}1$. This indicates that the scattering from those two reflections interferes destructively with the $00\bar{2}$ reflection. Indexing of the CBED patterns is possible using this interference effect; the cross contrasts inside the 002 and the $00\bar{2}$ beams in Fig. 3.2(b) and 3.2(c), respectively, enable this cross-section to be indexed as [110]. For the $[1\bar{1}0]$ cross-section, the cross contrasts would be reversed.

3-3 TEM specimen preparation

The Group III-V compound semiconductor alloys examined in this work were in the form of thin single crystal epitaxial layers grown on single crystal binary III-V semiconductor substrates. In order to examine such an epitaxial layer using TEM, an electron transparent specimen needs to be prepared. This foil can be obtained by thinning with either an ion beam or chemical etchant. Two types of specimen were prepared, namely cross-sections and plan-views.

For the cross-sectional specimens (20), 3mmx1mm bars of the as-grown epitaxial layer were obtained by cleaving along <110> directions. Two bars were glued together, epitaxial layer surface to epitaxial layer surface, using a quick setting epoxy. Pressure was applied during bonding in order to obtain as thin a glue film as possible between the two bars. This sample was mounted onto a Pyrex disc between two Si backing pieces using melted Crystal Bond wax. The sample was mechanically ground using SiC papers until it was about 40μm thick and mechanical damage removed using a 6μm diamond polish for 10 min. The sample was dissolved-off the Pyrex disc using dimethylformamide and glued to a Cu TEM grid. The mounted sample was placed in a Gatan dual ion beam mill. The sample was rotated and thinned from both sides using Ar^+ ion beams until a hole appeared in the centre of the bar giving electron transparent material in the region of the epitaxial layers. A liquid

N_2 cold stage was used to cool the sample during the ion beam milling. The milling conditions used were, ion beam energy 4kV, gun current 0.4mA and angle of beam to sample surface 15°. On obtaining a hole, the beam energy, gun current and angle of thinning were reduced to 2kV, 0.2mA and 12°, respectively, for 30 minutes to minimise any beam damage to the material. Prior to HREM examinations, the surface amorphous layer present on the thinned specimen was reduced by a brief etch in very dilute Cl_2/CH_3OH solution, so allowing better lattice images to be obtained. This technique produced TEM samples with a <110> foil normal.

For plan-view specimens (21), a 2-3mm square sample with edges parallel to <110> directions was cleaved from the epitaxial layer. This sample was mounted epitaxial layer side down, between two Si backing pieces, on a Pyrex disc using Crystal Bond. The sample was mechanically ground down from the substrate side using SiC papers until it was about 70μm thick. The SiC grinding damage was removed by a 6μm diamond polish. The square sample was dissolved-off the Pyrex disc using dimethylformamide and stuck with the epitaxial layer side down onto a PTFE stub using Lacomit lacquer. An area around the edges of the substrate side of the sample was coated with Lacomit lacquer. The unmasked area of the sample was chemically dished by rotating the PTFE stub and the sample under a jet of Cl_2/CH_3OH solution. After dishing, the plan-view sample was chemically thinned to perforation by dipping in a Cl_2/CH3OH solution. The perforated sample was then dissolved off the PTFE stub using acetone. After cleaning in acetone and methanol, the sample was stuck onto a Cu TEM grid. The (001) plan-view sample was then ready for TEM.

3-4 Transmission electron microscopy techniques.

The theory of electron microscopy and associated imaging techniques have been comprehensively described in several excellent reference books (22-24), and no attempt has been made here to duplicate such a coverage. The micrographs presented in the present work were taken on a variety of electron microscopes, i.e. a Philips CM12 operating at 120kV, a Philips CM20, a JEOL 200CX, and an Akashi 002B, all operating at 200kV, and a

JEOL 4000EX operating at 400kV. The JEOL 4000EX was mainly used for high resolution electron microscopy (HREM). Standard 2-beam diffraction contrast dark-field techniques were mainly used to take the TEM micrographs presented in chapters 4, 5, 6 and 7. Selected area TED was extensively used to investigate pseudobinary epitaxial layers. HREM was also employed to investigate atomic ordering, atomic structure and defect structures. For details of the HREM technique, the reader is referred to the comprehensive book by Spence (25).

REFERENCES-CHAPTER 3

1. P.D. Dapkus, J. Cryst. Growth **68** (1984) 345.
2. P.H. Manuel, M. Defour, C. Grattepain, F. Omnes, O. Archer, G. Timms and M. Razeghi, Chemtronics **4** (1984) 40.
3. H.M. Manasevit, Appl. Phys. Lett. **12** (1968) 158.
4. H.M. Manasevit and W.I. Simpson, J. Electrochem. Soc. **116** (1969) 1725.
5. G.B. Stringfellow, J. Electron. Mater. **17** (1988) 327.
6. A.Y. Cho and J.R. Arthur, Prog. Sol. State Chem. **10** (1975) 157.
7. M. Knudsen, Ann. Phys. **4** (28) (1909) 999.
8. K. Ploog, in Crystal Growth, Properties and Application, Vol.3, edited by H.C. Frayhard (Springer-Verlag, Berlin, Heidelberg), (1980) 73.
9. A.Y. Cho, Thin Solid Films **100** (1983) 291.
10. A.Y. Cho, J. Vac. Sci. Technol. **8** (1971) 531.
11. J.H. Neave, B.A. Joyce, P.J. Dobson and N. Norton, Appl. Phys. **A31** (1983) 1.
12. J.M. Van Hove, C.S. Lent, P.R. Pukite and P.I. Cohen, J. Vac. Sci. Technol. **B1** (1983) 741.
13. B.A. Joyce, J.H. Neave, J. Zhang and P.J. Dobson, RHEED and Reflection Electron Imaging of Surfaces ed. P.K. Larson and P.J. Dobson, Plemun (1988) 397.
14. B.A. Joyce, P.J. Dobson, J.H. Neave and J. Zhang, Surface Sci. **174** (1986) 1.
15. H. Booyens, M.B. Small, R.M. Potenski and J.H. Basson, J. Appl. Phys. **52** (1981) 4328.
16. D.F. Kyers and M.F. Miller, J. Electrochem. Soc. **111** (1964) 1102.
17. P. Goodman and W.S. Jokson, Acta Cryst. **A33** (1977) 997.
18. M. Tanaka, R. Saito and D. Watanabe, Acta Cryst. **A36** (1980) 350.
19. J. Taftϕ and J. C. H. Spence, J. Appl. Cryst. **15** (1982) 60.
20. H.R. Pettit and G.R. Booker, Proc. 25th Ann. Meeting of EMAG, Cambridge, Inst. Phys. Conf. Ser. No **10** (London-Bristol 1971) 290.
21. G.R. Booker and R. Stickler, Brit. J. Appl. Phys. **13** (1962) 446.

22. P.B. Hirsch, A. Howie, R.B. Nicholson, D.W Pashley. and M.J. Whelan, "Electron Microscopy of Thin Crystals" (Butterworths, London 1965).

23. J.W. Edington, "Practical Electron Microscopy in Materials Science" (MacMillan, London 1975) monogragh 2.

24. G. Thomas and M.J. Goringe, "Electron Microscopy of Materials" (John Wiley and Sons, Chichester-New York-Brisbane-Toronto-Singapore 1979).

25. J.L.H. Spence, "Experimental High Resolution Electron Microscopy" (Oxford University Press 1980).

CHAPTER 4

PHASE SEPARATION IN MBE $InAs_ySb_{1-y}$ COMPOUND SEMICONDUCTORS

4-1 Introduction

The ternary alloy $InAs_ySb_{1-y}$ is of increasing interest for infrared detectors because it covers wavelengths in the 3-5μm and 8-12μm ranges, where the atmospheric absorption is small. Growth of $InAs_ySb_{1-y}$ in the composition range $0.3<y<0.5$ has proved difficult by near-equilibrium growth techniques such as liquid phase epitaxy (LPE) due to the presence of a miscibility gap in the InAsSb system (1-3). Spinodal isotherms calculated using the bulk thermodynamic properties of AlAs, AlSb, InAs and InSb for the AlInAsSb system (2) are given in Fig. 4.1. The continuous curves are isotherms corresponding to the 400°C-1000°C temperature range. Dashed lines, a, b, c, represent the AlInAsSb compositions for lattice matching to InP, InAs and GaSb, respectively. Spinodal isotherms corresponding to the 600-1000°C temperature range do not intersect the horizontal axis for the InAs-InSb alloy system, but the spinodal isotherm corresponding to 400°C does intersect the axis. This indicates that at low temperatures $\leq$400°C there exists a miscibility gap for $InAs_ySb_{1-y}$ alloys. Therefore, it is predicted that if $InAs_ySb_{1-y}$ alloy layers are grown when the composition and temperature are associated with a miscibility gap, e.g. at 400°C, $0.3<y<0.7$, then spinodal decomposition and phase separation may occur within the layers. The precise temperatures and compositions for the miscibility gap are difficult to calculate, the predictions by other workers (1,3) being slightly different from those of Fig. 4.1. A direct experimental determination of the occurrence of a miscibility gap for bulk $InAs_ySb_{1-y}$ specimens has been reported by Ishida et al.(4). In order to determine the miscibility gap, the compositions of $InAs_ySb_{1-y}$ alloys were designed to have three-phase structures of two solids and one liquid at equilibrated temperatures. After equilibration at 400-700°C for 1-2 months, the microstructures of the specimens were observed by optical and scanning electron microscopy. The equilibrium compositions of the compound phases were determined using electron probe microanalysis (EPMA). Their reported phase diagram for the InAs-InSb alloy system indicated a miscibility gap below ~500°C.

Despite the presence of the miscibility gap, however, $InAs_ySb_{1-y}$ alloy layers in the composition range $0<y<0.5$ have now been successfully grown at temperatures down to

Figure 4.1

Spinodal decomposition diagram calculated by Onabe (2) using the bulk thermodynamic properties of AlAs, AlSb, InAs and InSb for the AlInAsSb system, showing isothermal curves corresponding to temperature range from 400°C to 1350°C. Dashed lines, a, b, c, represent the AlInAsSb compositions for lattice matching to InP, InAs and GaSb, respectively.

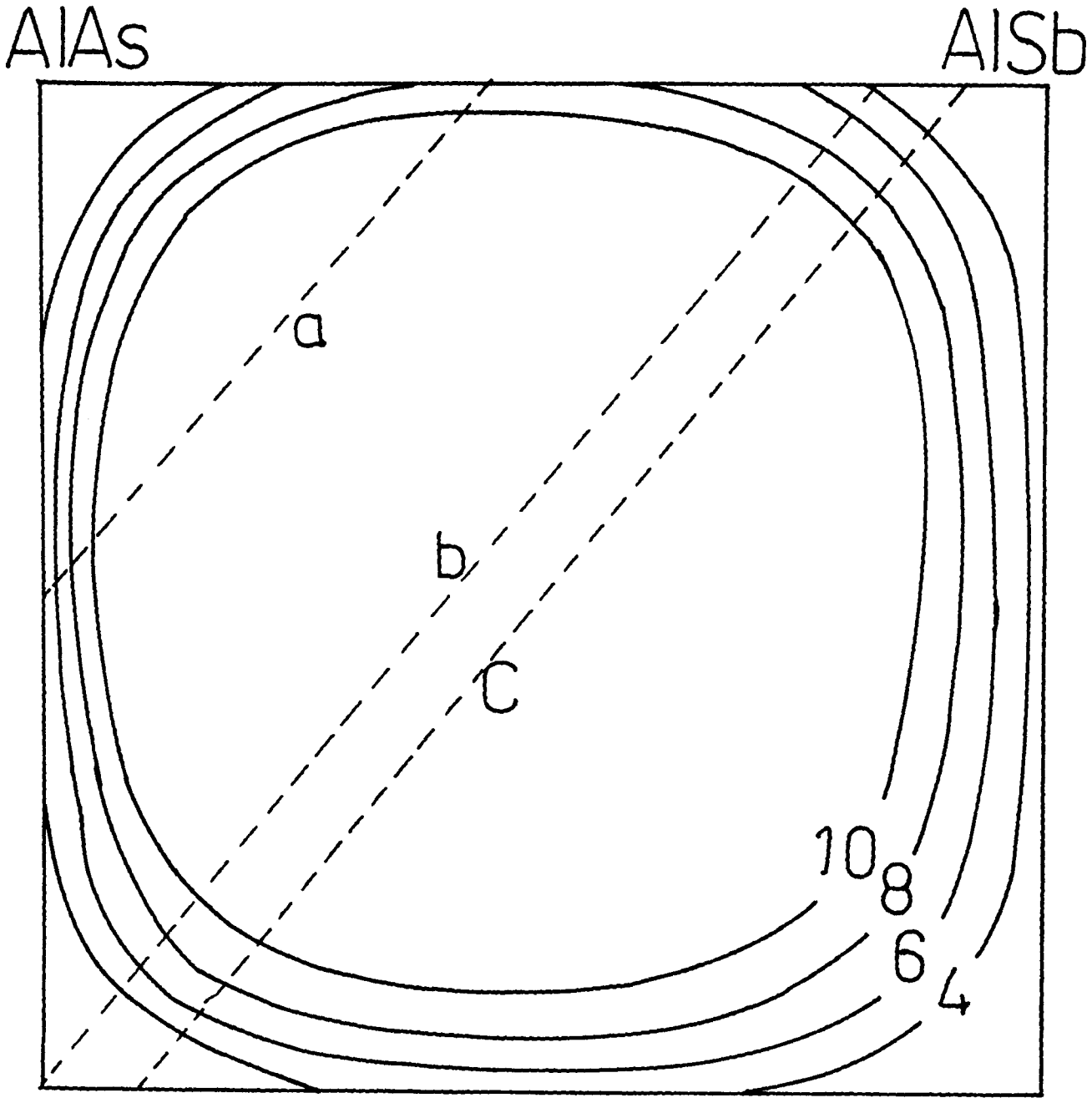

Fig. 4.1

380°C by the non-equilibrium techniques of metal-organic chemical vapour deposition (MOCVD) (5,6), molecular beam epitaxy (MBE) (7-9) and metalorganic magnetron sputtering (MOMS) (10). Detailed structural characterizations of such $InAs_ySb_{1-y}$ alloy layers have not been previously performed and no observations of phase separation in these layers grown by MBE and MOCVD have been hitherto reported. In the present work phase separation was observed in MBE $InAs_ySb_{1-y}$ layers grown in the range 295 to 400°C. A possible reason for the apparent absence of phase separation in $InAs_ySb_{1-y}$ alloy layers grown by previous workers is that their growth temperatures were higher than ours and so a miscibility gap occurred with our layers, but not with their layers. Another possible reason is that although phase separation did sometimes occur in their layers, it was not detected because no detailed structural studies were carried out.

In this chapter we present results obtained from TEM and TED studies of MBE $InAs_ySb_{1-y}$ layers. These results show for the first time that phase separation in $InAs_ySb_{1-y}$ alloy layers can occur. Systematic investigations were carried out with layers grown at different temperatures and at different compositions. The results are discussed and a possible mechanism for the phase separation is suggested.

4-2 Experimental

The substrates used were liquid encapsulated Czochralski (LEC), Cr-doped semi-insulating (SI), (001) GaAs wafers, and on to these substrates MBE InAs buffer layers ~100nm thick were grown at 490°C. MBE $InAs_ySb_{1-y}$ layers ~4μm thick were then grown at ~0.85 monolayer/s with temperatures in the range 295 to 470°C and compositions in the range y=0.2 to 0.8 (Table 4.1). In some cases, InSb was used for the substrate, and either GaAs or InSb for the buffer layer. For one specimen (IC267), an $InAs_{0.5}Sb_{0.5}$ layer ~2μm thick was grown at 430°C, and this was followed by a similar layer grown at 370°C. In order to investigate the stability of the grown layers, two specimens were annealed at 296°C and 350°C in quartz ampoules evacuated to < 10^{-6} Torr and one specimen (IC267) was annealed at 370°C in the growth kit. All the samples except IC 237 were grown using a

Table 4.1 MBE grown $InAs_ySb_{1-y}$ epitaxial layers.

Sample No.	$InAs_ySb_{1-y}$ (y)	Growth temp. (°C)	Substrate	Buffer layer	Doping
IC 247	0.5	295	GaAs	GaAs	no
IC 249	0.5	320	InSb	InSb	no
IC 262	0.5	340	GaAs	InAs	no
IC 237	0.5	340	GaAs	InAs	no
IC 121	0.2	370	GaAs	InAs	no
IC 118	0.4	370	GaAs	InAs	no
IC 264	0.5	370	GaAs	InAs	no
IC 124	0.6	370	GaAs	InAs	no
IC 119	0.8	370	GaAs	InAs	no
IC 265	0.5	400	GaAs	InAs	no
IC 209	0.56	430	GaAs	InAs	no
IC 213	0.56	430	GaAs	GaAs	no
IC 219	0.56	430	GaAs	InAs	Si
IC 267	0.5	430	GaAs	InAs	no
	0.5	370	GaAs	InAs	no
IC 248	0.5	470	GaAs	GaAs	no

calibrated antimony flux and with the arsenic flux ~3 times that required for the aimed composition. Optical response spectra were obtained (by Mr. R. Thomas) using an infra-red Fourier transform spectrometer from samples of dimensions 3x10mm which were mounted in a cryo-cooler operating at 10K.

4-3 TEM and TED results

4-3-1 Defects

In order to investigate defect behaviours of lattice-mismatched $InAs_ySb_{1-y}$ (y=0.2 to 0.8) layers grown at temperatures in the range 295 to 470°C, cross-section strain sensitive (220) TEM DF micrographs were obtained. It was found that defect structures in the layers depend on the growth temperatures used. For $InAs_ySb_{1-y}$ (y=0.4 to 0.8) layers grown at and below 400°C, the main defects are 'short'-stacking faults and 'short'-microtwins. The stacking faults and microtwins, which were formed on inclined {111} planes, often started and stopped at interfaces between the platelets (which will be described later). For $InAs_{0.5}Sb_{0.5}$ layers grown at and above 430°C, which is a critical temperature for phase separation, as discussed in section 4-3-2, and an $InAs_{0.2}Sb_{0.8}$ layer (IC121) grown at 370°C, the main defects are threading dislocations with a few 'short'-microtwins. The main defects in an $InAs_{0.5}Sb_{0.5}$ layer (IC237) grown at 340°C are 'long'-microtwins, propagating through the whole layer.

Fig. 4.2 shows cross-section TEM (220) DF micrographs obtained from the typical non-phase-separated layer (IC121) and phase-separated layer (IC124) (which will be described in section 4-3-2). There is a significant difference in defect behaviours between the non-phase-separated and phase-separated layers. For the $InAs_{0.2}Sb_{0.8}$ layer (IC121), a TEM micrograph from the region including the InAs buffer and the GaAs substrate showed a dense array of dislocations and moire fringes at the GaAs/InAs interface, and threading dislocations in the InAs layer. There is a dense array of Lomer dislocations (which were identified by high resolution electron microscopy (HREM)) and moiré fringes at the

Figure 4.2

(a) Cross-section **g**(220) TEM DF micrograph taken from the region consisting of $InAs_{0.2}Sb_{0.8}$, InAs and GaAs. (b) Cross-section **g**(220) TEM DF of the middle region of an $InAs_{0.6}Sb_{0.4}$ layer.

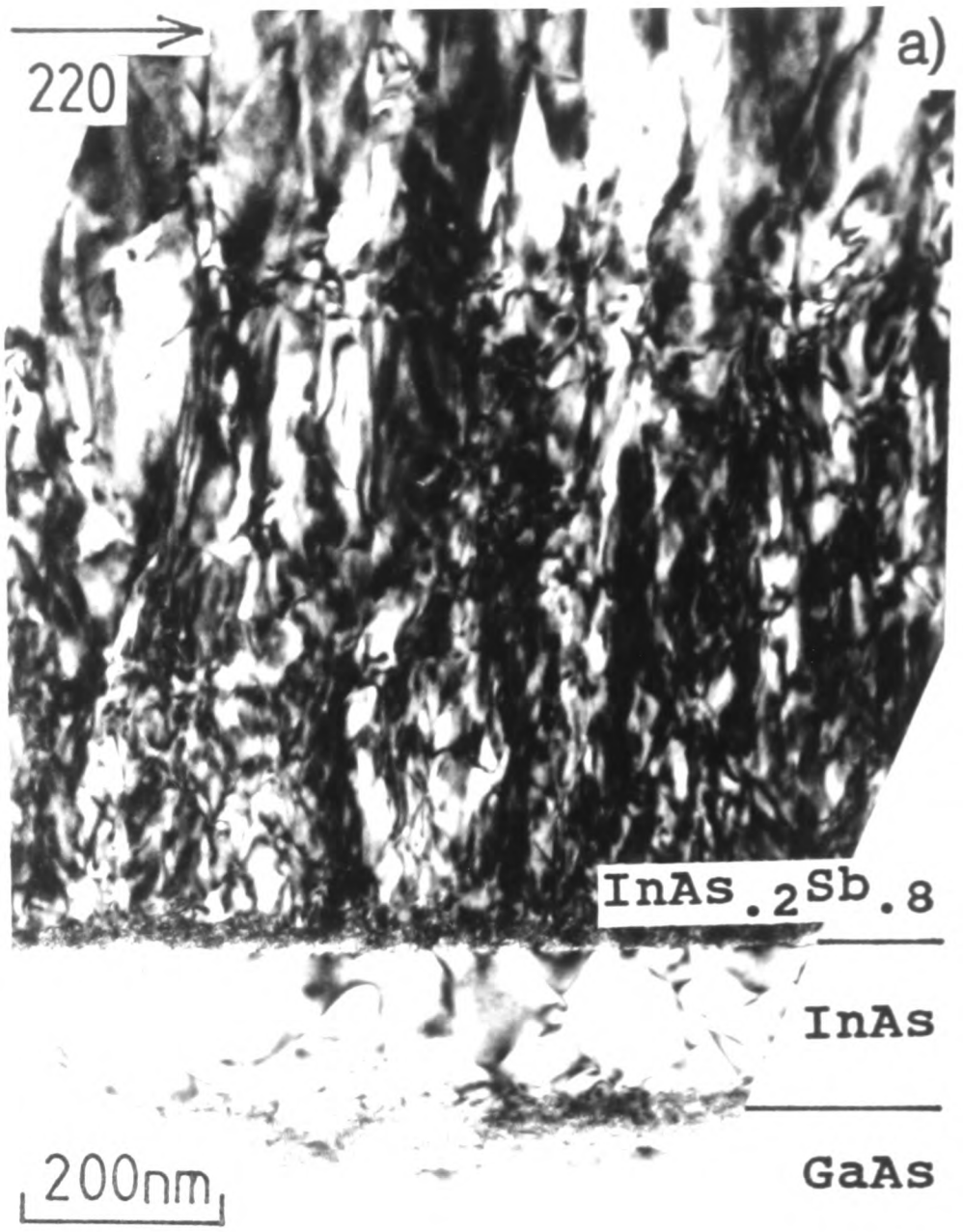

Fig. 4.2

$InAs/InAs_{0.2}Sb_{0.8}$ interface, and threading dislocations and 'short'-microtwins in the $InAs_{0.2}Sb_{0.8}$ layer. Threading dislocations in the $InAs_{0.2}Sb_{0.8}$ layer decreased in number on going away from the interface, i.e. the density of threading dislocations was ~$2x10^{10}cm^{-2}$ at the interface region, ~$1.5x10^{10}cm^{-2}$ in the middle region and ~$5x10^{9}cm^{-2}$ near the layer surface. TED examinations were performed to determine lattice parameters of the nominal $InAs_{0.2}Sb_{0.8}$ layer (IC 121). Results showed that the InAs is virtually fully relaxed with respect to GaAs and that the $InAs_{0.2}Sb_{0.8}$ layer is tetragonally distorted, although significantly relaxed with respect to the InAs layer. High resolution lattice images taken from the interface region between the InAs and $InAs_{0.2}Sb_{0.8}$ layer showed an array of Lomer dislocations of average spacing ~91Å corresponding to 93% relaxation.

For the $InAs_{0.6}Sb_{0.4}$ layer (IC124) grown at 370°C, a TEM (220) DF micrograph obtained from the middle region of the layer (Fig. 4.2 (b)) showed defect features quite different from those of the $InAs_{0.2}Sb_{0.8}$ layer (IC 121). As mentioned above, the main defects are 'short'-stacking faults and 'short'-microtwins. Line contrasts of strain are visible running approximately parallel to the interface, which are associated with interfaces between the two phase-separated materials, as will be discussed later. A few dislocations at such line contrasts were also observed, (which were identified as 60° and Lomer dislocations by HREM). These crystallographic defects are described in more detail, and mechanisms proposed for their formation, in chapter 7.

4-3-2 Phase separation

The growth behaviour of nominal $InAs_{0.5}Sb_{0.5}$ alloy layers grown at temperatures in the range 295 to 470°C were examined by two orthogonal cross-section <110> TEM DF imaging conditions taken with the (002) reflection, which is sensitive to the variation of alloy layer compositions (11).

Two orthogonal cross-section micrographs obtained from the middle regions of an $InAs_{0.5}Sb_{0.5}$ layer grown at 295°C are given in Fig. 4.3. It should be emphasised that there was no modulation of the Knudsen sources or variation of the cell temperatures during

Figure 4.3

Composition sensitive **g**(002) TEM DF micrographs taken from (a) [110] and (b) [$\bar{1}$10] cross-section samples of an $InAs_{0.5}Sb_{0.5}$ layer grown at 295°C. The layer exhibits a non-uniform island-type bright phase embedded in a dark phase.

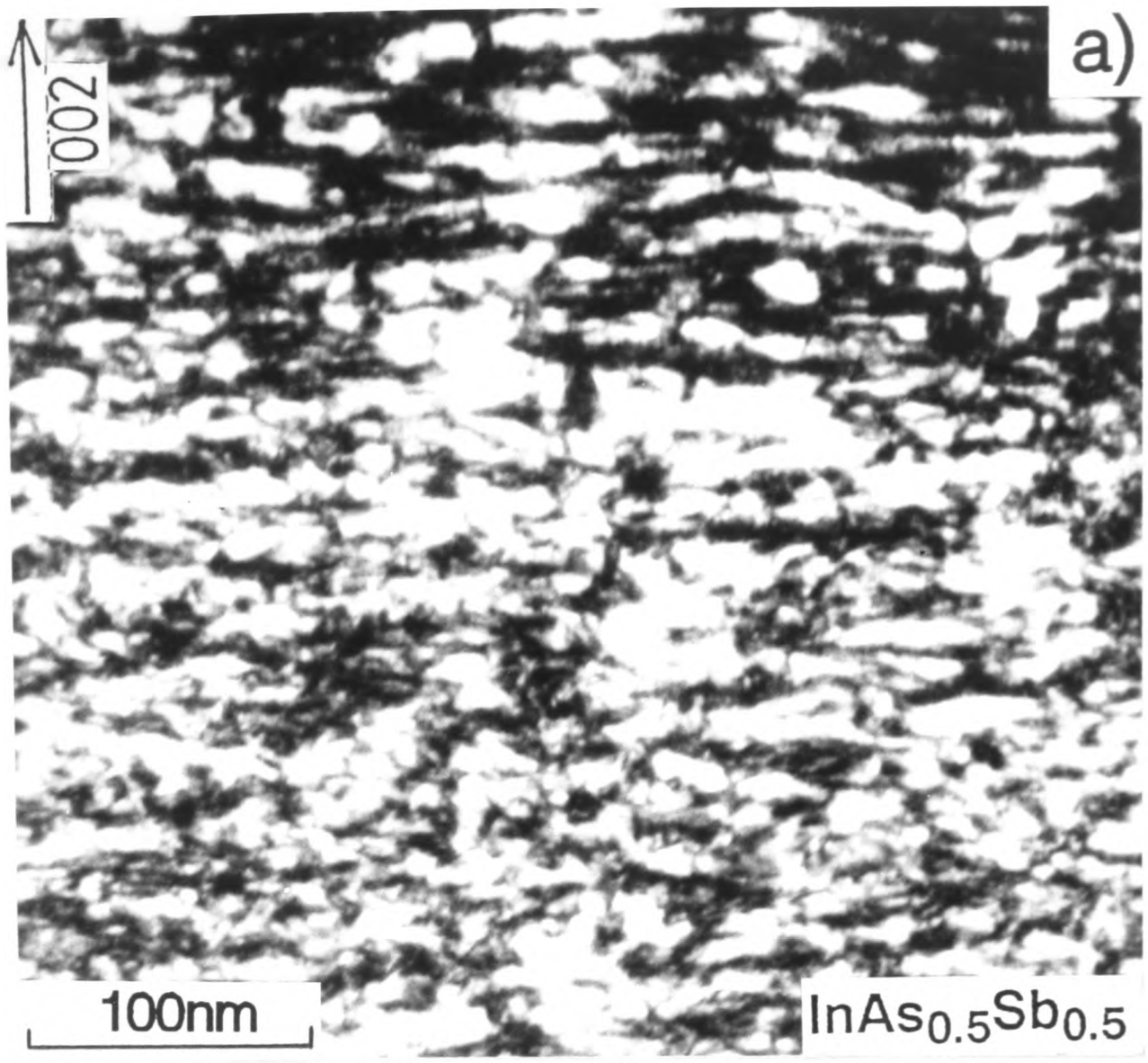

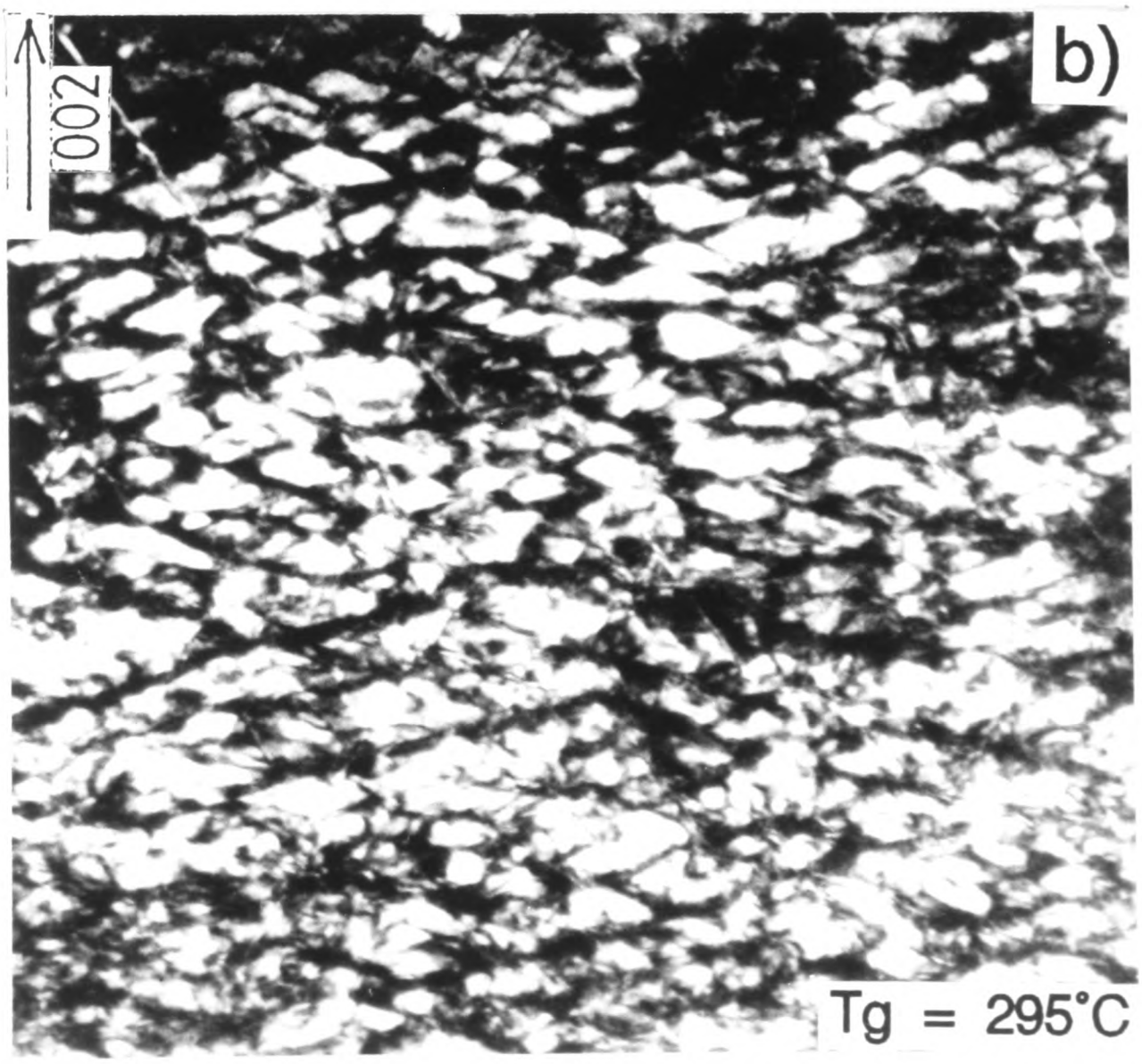

Fig. 4.3

growth. The layers showed strong non-uniform contrast, ~12 nm thick bright phases and ~5 nm thick dark phases (Table 4.2). The lateral sizes of the bright phase were ~120nm and ~50nm in the $[\bar{1}10]$ and [110] directions, respectively. The bright phases represented a volume fraction of ~80% of the layer. The morphologies of the phases are different in the (110) and $(\bar{1}10)$ cross-section specimens. The (110) cross-section micrograph of Fig. 4.3(a) shows the phases to be aligned approximately parallel to the layer surface, although the bright/dark phase interface is irregular. The $(\bar{1}10)$ cross-section micrograph of Fig.4.3(b) shows irregular phases, with wavy interfaces. These results are given in Table 4.2.

Similar micrographs of an $InAs_{0.5}Sb_{0.5}$ layer grown at 320°C are given in Fig. 4.4. The layers again showed two phases but now in the form of an ill-defined plate-like structure approximately parallel to the layer surface in the (110) cross-section specimen (Fig. 4.4(a)), but the morphology of the plate-like structure when viewed in the $[\bar{1}10]$ direction was irregular and wavy (Fig. 4.4(b)). The plate-like structure alternated in contrast from bright to dark, and ranged in thicknesses from ~10 to ~25nm. The lateral sizes of the plate-like structure were ~500nm and ~200nm in the $[\bar{1}10]$ and [110] directions, respectively. The bright phases represented a volume fraction of ~80% of the layer. The irregular interface between the bright and dark phases was approximately parallel to {511} planes.

Fig. 4.5 shows similar micrographs of an $InAs_{0.5}Sb_{0.5}$ layer grown at 340°C. Anisotropy of morphology of the plate-like structures in two orthogonal cross-section specimens is evident. The plate-like structures approximately parallel to the layer surface ranged in thickness from ~24 to ~30nm. The lateral sizes of the plate-like structures were ~600nm and ~250nm in the $[\bar{1}10]$ and [110] directions, respectively. The bright phases represented a volume fraction of ~55% of the layer.

Fig. 4.6 shows similar micrographs of an $InAs_{0.5}Sb_{0.5}$ layer grown at 370°C. The layer shows the plate-like structure approximately parallel to the layer surface. Anisotropy of morphology of the plate-like structure in two orthogonal cross-section specimens is still evident. The plate-like structure approximately parallel to the layer surface ranged in thicknesses from ~30 to ~40nm. The lateral sizes of the plate-like structure were ~1.3μm

Table 4-2 Lateral size, thickness and volume fraction of As-rich phase of plate-like structure.

Sample No.	y	Growth temp. (°C)	Lateral size (nm) [110]	[î10]	T (nm)
IC 247	0.5	295	~50	~120	5 - 12
IC 249	0.5	320	~150	~350	10 - 25
IC 262	0.5	340	~250	~600	24 - 30
IC 264	0.5	370	~500	~1300	30 - 40
IC 265	0.5	400	~900	~2600	42 - 50
IC 121	0.2	370	-	-	-
IC 118	0.4	370	~900	~1500	20 - 200
IC 124	0.6	370	~500	~1100	20 - 50
IC 119	0.8	370	~900	~1500	15 - 120

y = nominal composition in $InAs_ySb_{1-y}$, T = thickness of plate-like structure.

Figure 4.4

g(002) DF micrographs taken from (a) [110] and (b) [$\bar{1}$10] cross-section samples of an $InAs_{0.5}Sb_{0.5}$ layer grown at 320°C. The layer shows different morphology of the phase separated materials in the two micrographs.

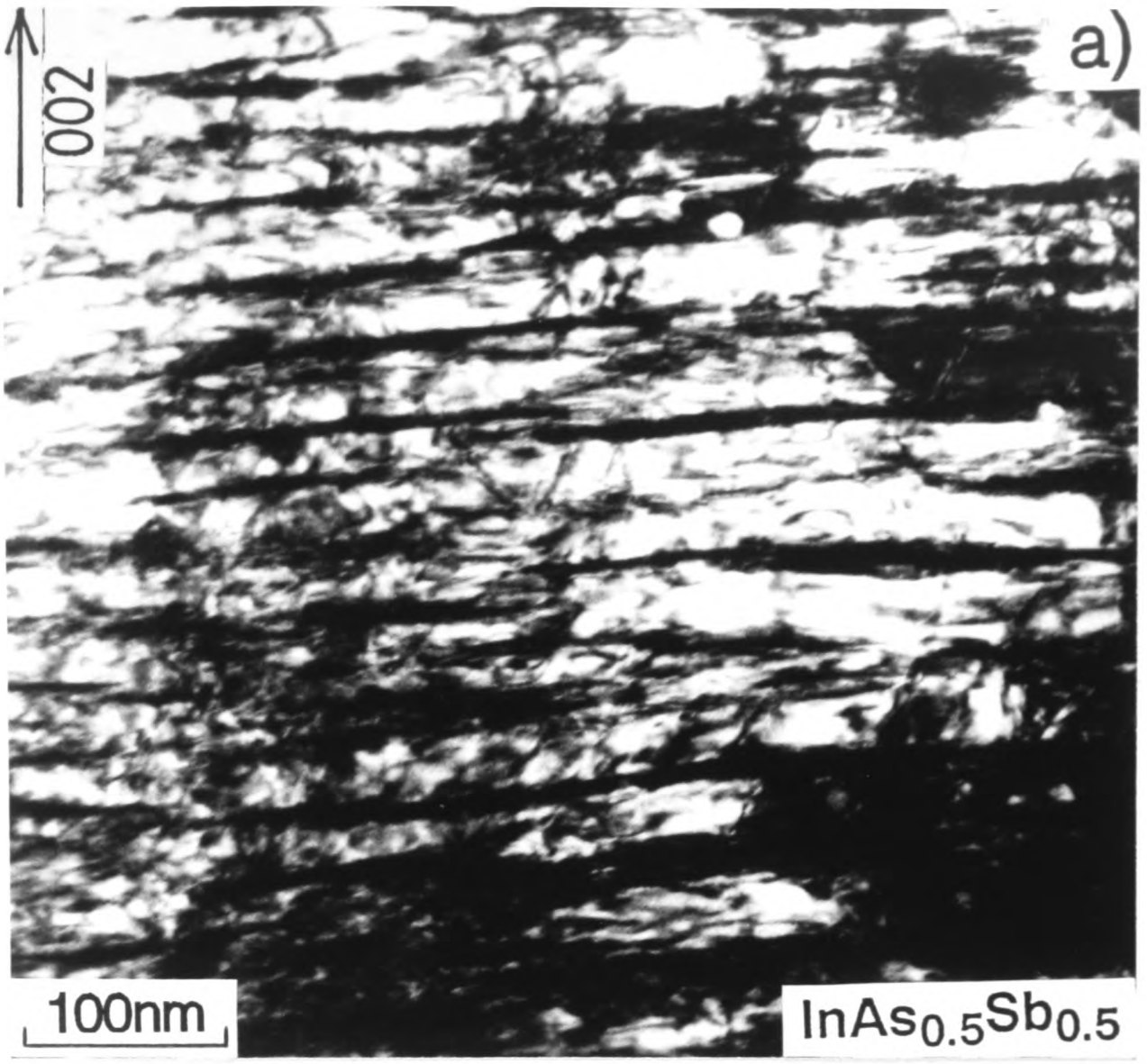

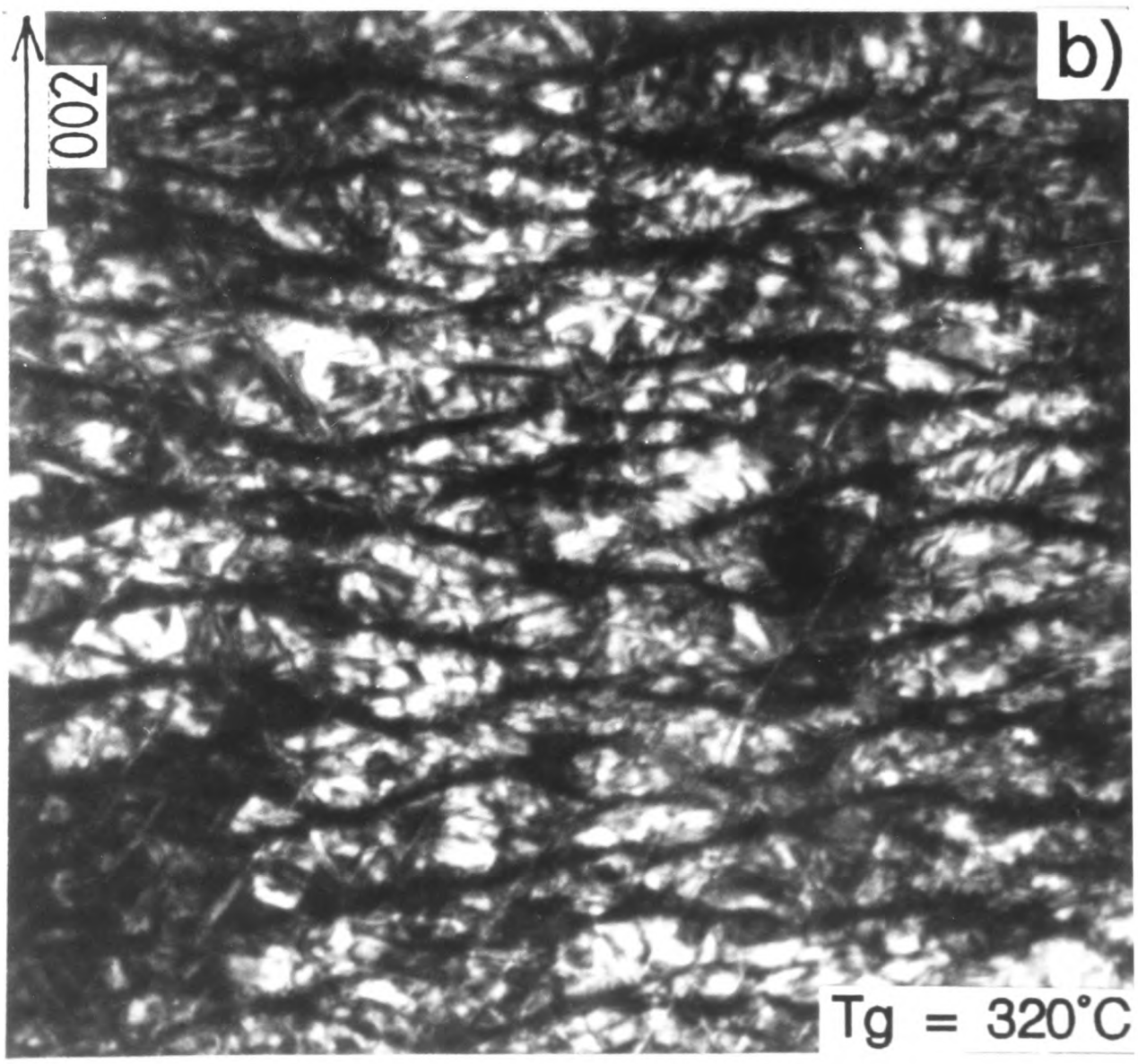

Fig. 4.4

Figure 4.5

g(002) TEM DF micrographs taken from (a) [110] and (b) [$\bar{1}$10] cross-section samples of an $InAs_{0.5}Sb_{0.5}$ layer grown at 340°C.

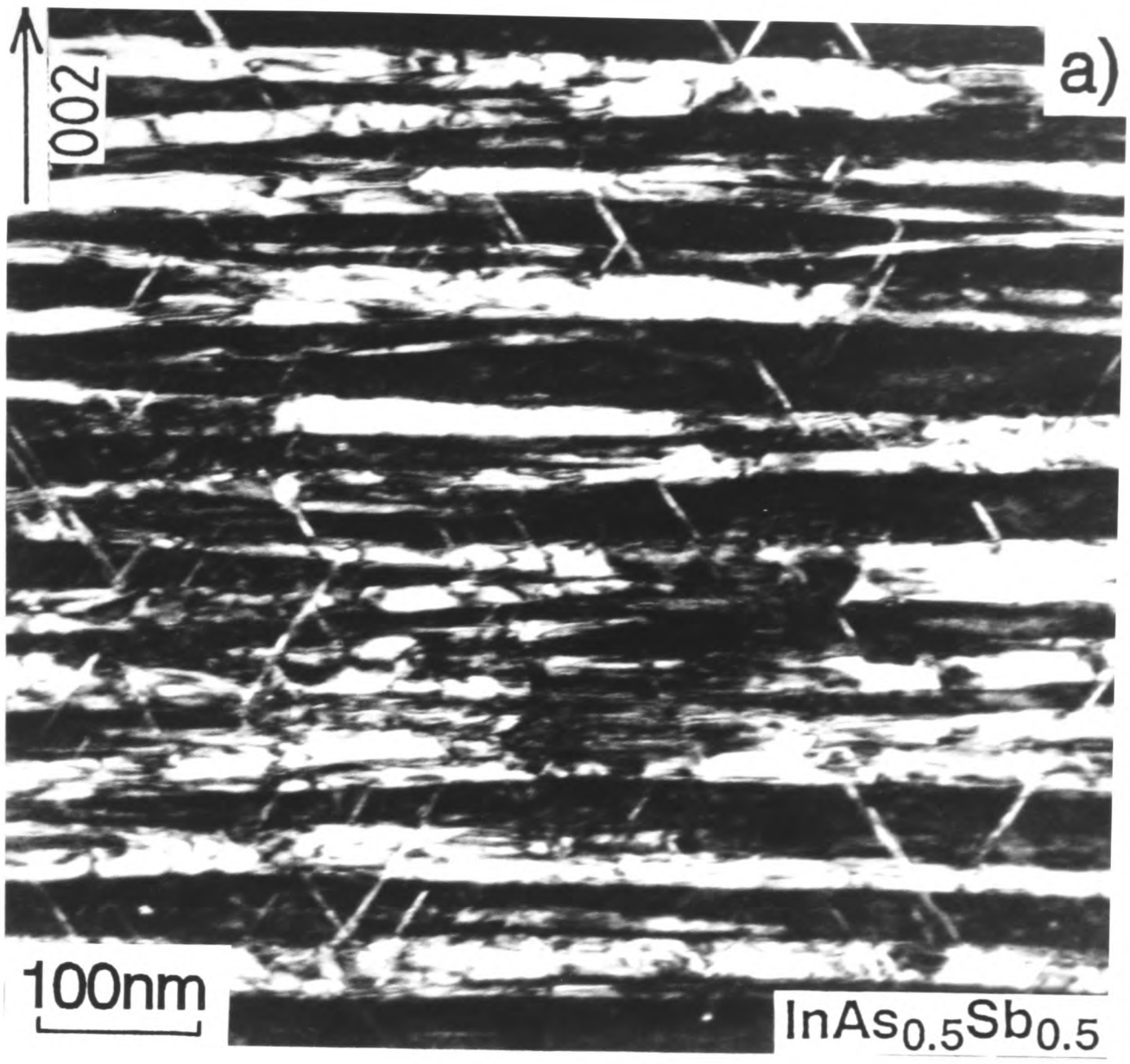

Fig. 4.5

Figure 4.6

g(002) TEM DF micrographs taken from (a) [110] and (b) [$\bar{1}$10] cross-section samples of an $InAs_{0.5}Sb_{0.5}$ layer grown at 370°C.

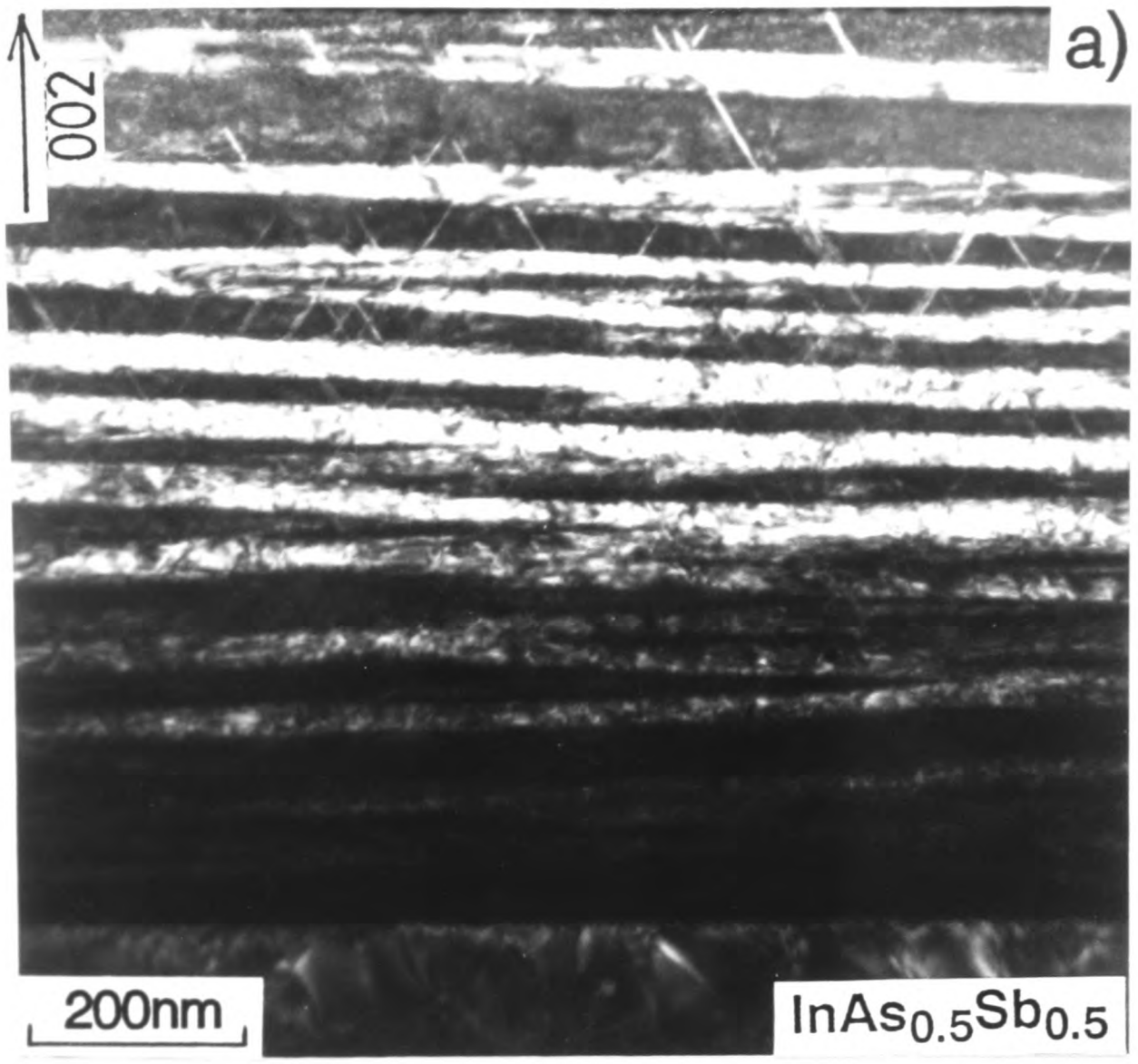

Fig. 4.6

and ~500nm in the [$\bar{1}$10] and [110] directions, respectively. The bright phases represented a volume fraction of ~55% of the layer.

Fig. 4.7 shows similar micrographs of an $InAs_{0.5}Sb_{0.5}$ layer grown at 400°C. The strong plate-like contrast is visible with the plates lying approximately parallel to the layer surface and ranged in thicknesses from ~40 to ~50nm. The lateral sizes of the plate-like structure were ~2.6μm and ~900nm in the [$\bar{1}$10] and [110] directions, respectively. The bright phases represented a volume fraction of ~55% of the layer.

Similar micrographs of an $InAs_{0.56}Sb_{0.44}$ layer grown at 430°C and an $InAs_{0.5}Sb_{0.5}$ layer grown at 470°C showed that both layers are homogeneous in both cross-section specimens, with threading dislocations providing the main contrast (Fig. 4.8), indicating the absence of the plate-like structures and different growth behaviours in these layers.

As the growth temperature increased from 295 to 400°C, the plate-like structures progressively increased in lateral size in both <110> directions. An anisotropy of the plate-like structure was observed in all the layers grown below 400°C. RHEED patterns of $InAs_ySb_{1-y}$ layers during growth indicated a weak/medium strength (2x3) reconstructed surface whose quality improved as the growth temperature increased. An anisotropy was visible in the RHEED pattern in that the integral order rods were more spotty in the [$\bar{1}$10] direction.

The contrast of (002) TEM DF micrographs obtained from $InAs_ySb_{1-y}$ alloy layers depends on the structure factors of the mixed Group V elements (11). The intensity of (002) DF micrographs of $InAs_ySb_{1-y}$ (y=0.2 to 0.8) alloy layers was determined by calculating the structure factors. The results indicated that the dark contrast in Fig. 4.3 to 4.7 corresponds to an Sb-rich phase and the bright contrast corresponds to an As-rich phase (e.g. see Appendix I).

In order to characterise the layer composition dependence of growth behaviour, four $InAs_ySb_{1-y}$ layers were grown at 370°C with y=0.2, 0.4, 0.6 and 0.8. (002) DF micrographs of the layers are given in Fig. 4.9 and Fig. 4.10. The layers with y=0.4, 0.6 and 0.8 showed the two phase-separated materials. Like previously examined samples, the plate-like

Figure 4.7

g(002) DF micrographs taken from (a) [110] and (b) [$\bar{1}$10] cross-section samples of an $InAs_{0.5}Sb_{0.5}$ layer grown at 400°C.

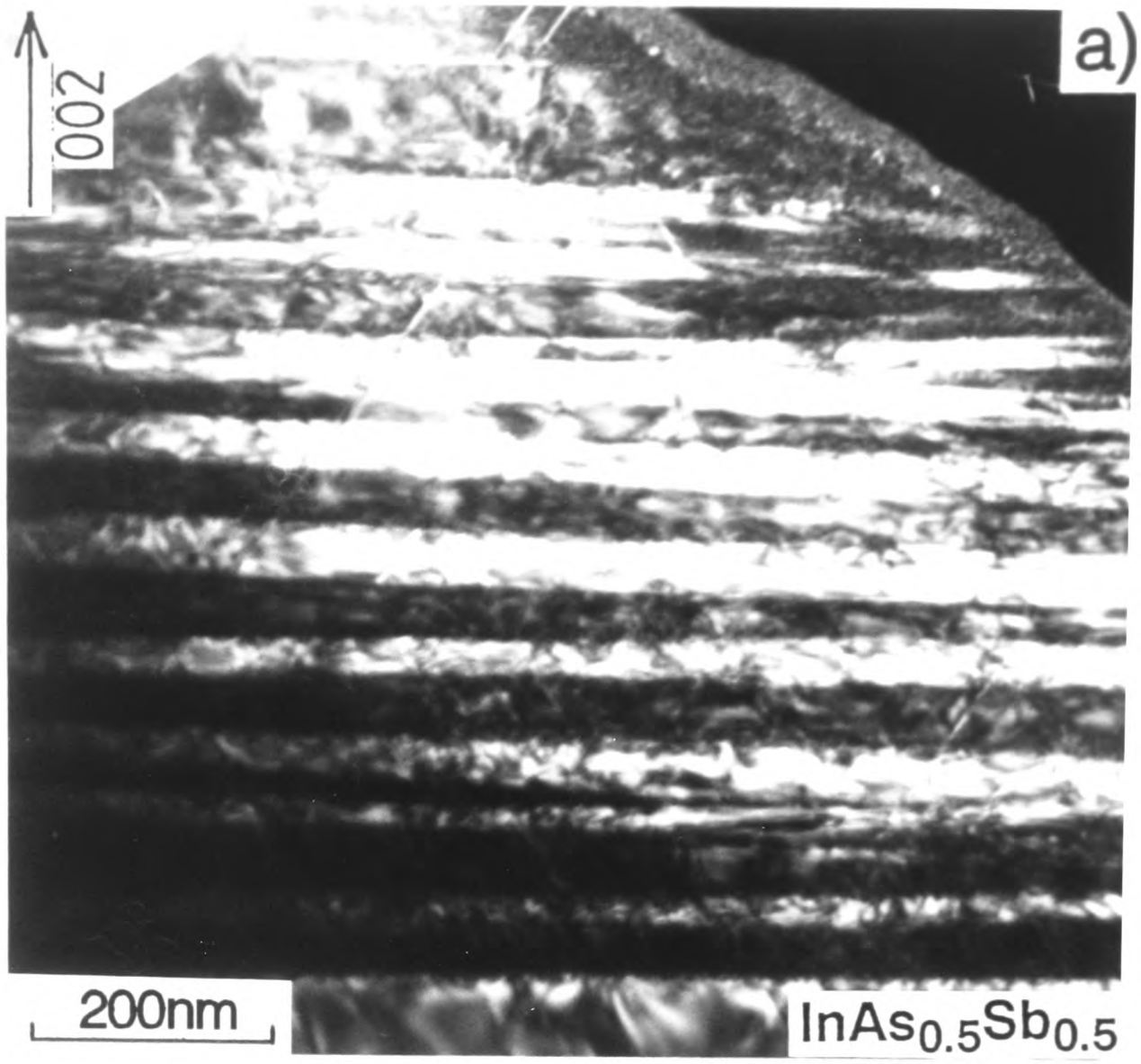

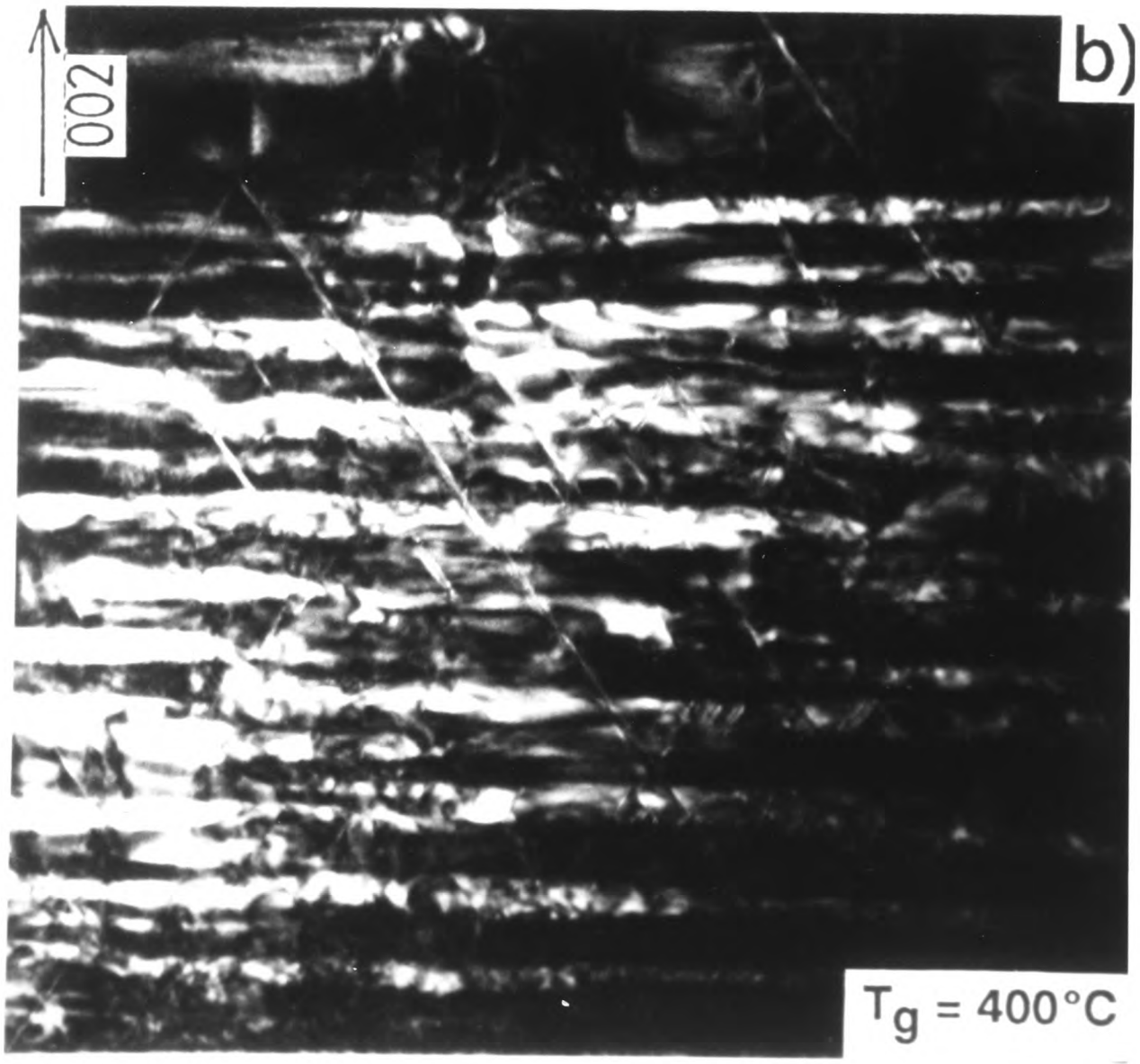

Fig. 4.7

Figure 4.8

g(002) DF micrographs of an $InAs_{0.56}Sb_{0.44}$ layer grown at 430°C. The layer is homogeneous, indicating that phase separation does not occur at this growth temperature.

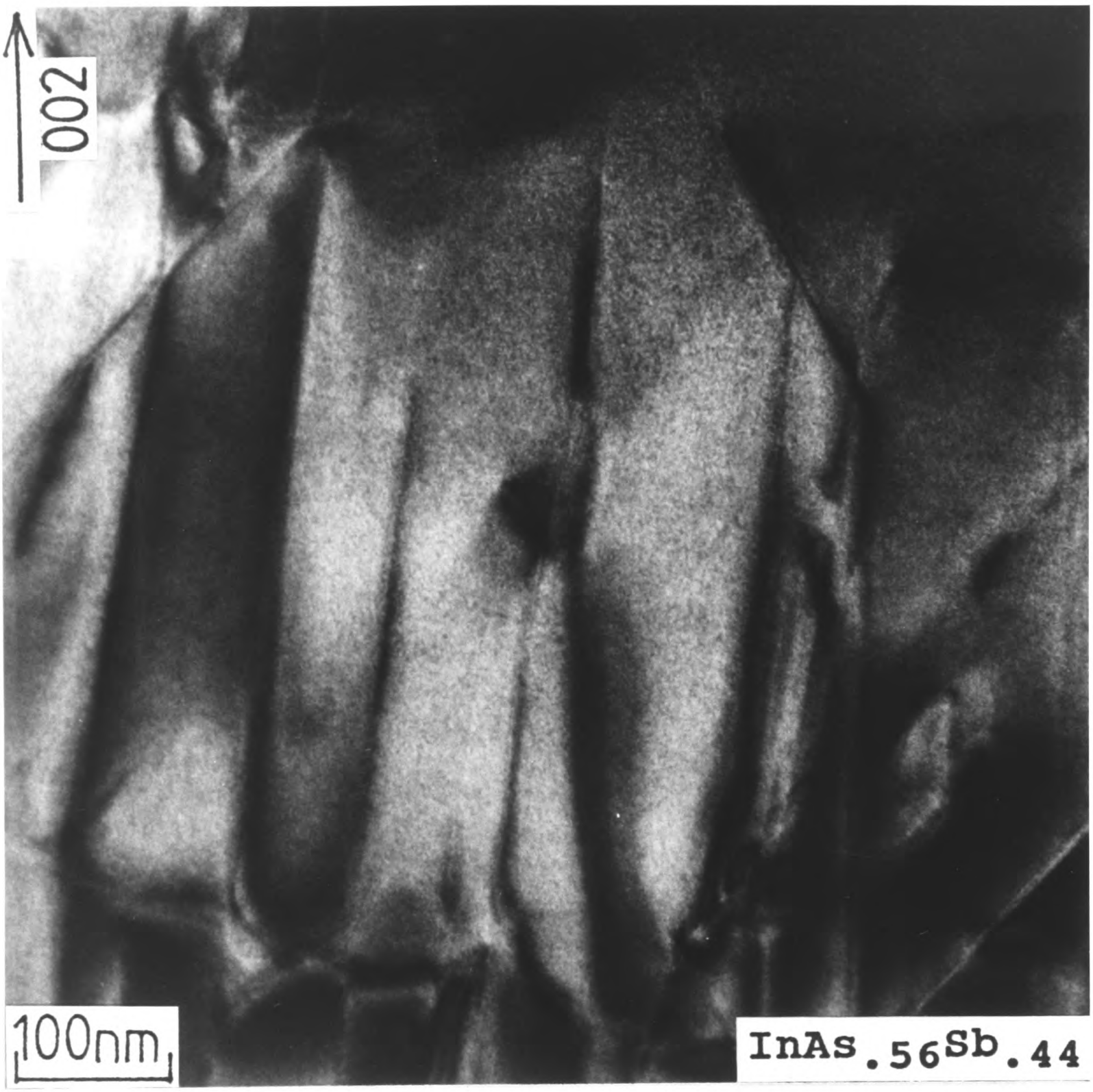

Fig. 4.8

structure appears more irregular and wavy when viewed along the [$\bar{1}$10] orientation. The As-rich phase exists in the form of elongated, lenticular cross-section platelets oriented with their longer axis along the [$\bar{1}$10] direction, surrounded by a matrix of the Sb-rich phase. The thicknesses of either the As-rich or Sb-rich plate-like structures were dependent on layer composition. For example, the thicknesses of bright contrast platelets varied from ~15nm to ~80nm with increasing y values in $InAs_ySb_{1-y}$ layers. The volume fraction of Sb-rich phase increased with decreasing As.

For the $InAs_{0.2}Sb_{0.8}$ layer, Fig. 4.9(a) and Fig. 4.10(a), the layer was homogeneous, indicating the existence of a single phase. However, for $InAs_ySb_{1-y}$ (y=0.4, 0.6, and 0.8) layers, the dark and bright plate-like structures were visible in both (110) and ($\bar{1}$10) cross-section specimens. For the $InAs_{0.4}Sb_{0.6}$ layer, Fig. 4.9(b) and Fig. 4.10(b), the plate-like structures ranged in thickness from ~20 to ~50nm. The bright platelets represented a volume fraction of ~30% of the layer (Table 4.2). For the $InAs_{0.6}Sb_{0.4}$ layer, Fig. 4.9(c) and Fig. 4.10(c), the plate-like structures ranged in thickness from ~20 to ~50nm. The bright platelets represented a volume fraction of ~60% of the layer. For the $InAs_{0.8}Sb_{0.2}$ layer, Fig. 4.9(d) and Fig. 4.10(d), the plate-like structures ranged in thickness from ~15 to ~80nm. The bright platelets now represented a volume fraction of ~85% of the layer. The results obtained from (002) DF examinations showed strong nominal composition dependence of layer growth behaviour, implying the existence of a composition range for the occurrence of the plate-like structures.

In order to measure a volume fraction of the first-grown phases of the phase-separated layers, an (002) TEM DF investigation was carried out. The results obtained showed that for all the layers, Sb-rich phases showed a larger volume fraction of the first-grown layer than As-rich phases which will be discussed in section 4-4.

In order to investigate the effect of the fluxes of As and Sb on growth behaviour, an $InAs_ySb_{1-y}$ layer was grown at 340°C using equally balanced fluxes of Sb_4 and As_4 to give a nominal alloy composition of $InAs_{0.5}Sb_{0.5}$ and was examined by a similar cross-section TEM (002) DF technique. The $InAs_{0.5}Sb_{0.5}$ layer described in Fig. 4.5 was grown using a calibrated antimony flux with the arsenic flux ~3 times that required for the aimed

Figure 4.9

[110] cross-section **g**(002) DF micrographs of (a) $InAs_{0.2}Sb_{0.8}$ and (b) $InAs_{0.4}Sb_{0.6}$ layers grown at 370°C. The $InAs_{0.2}Sb_{0.8}$ layer is homogeneous, while the $InAs_{0.4}Sb_{0.6}$ layer contains plate-like structures.

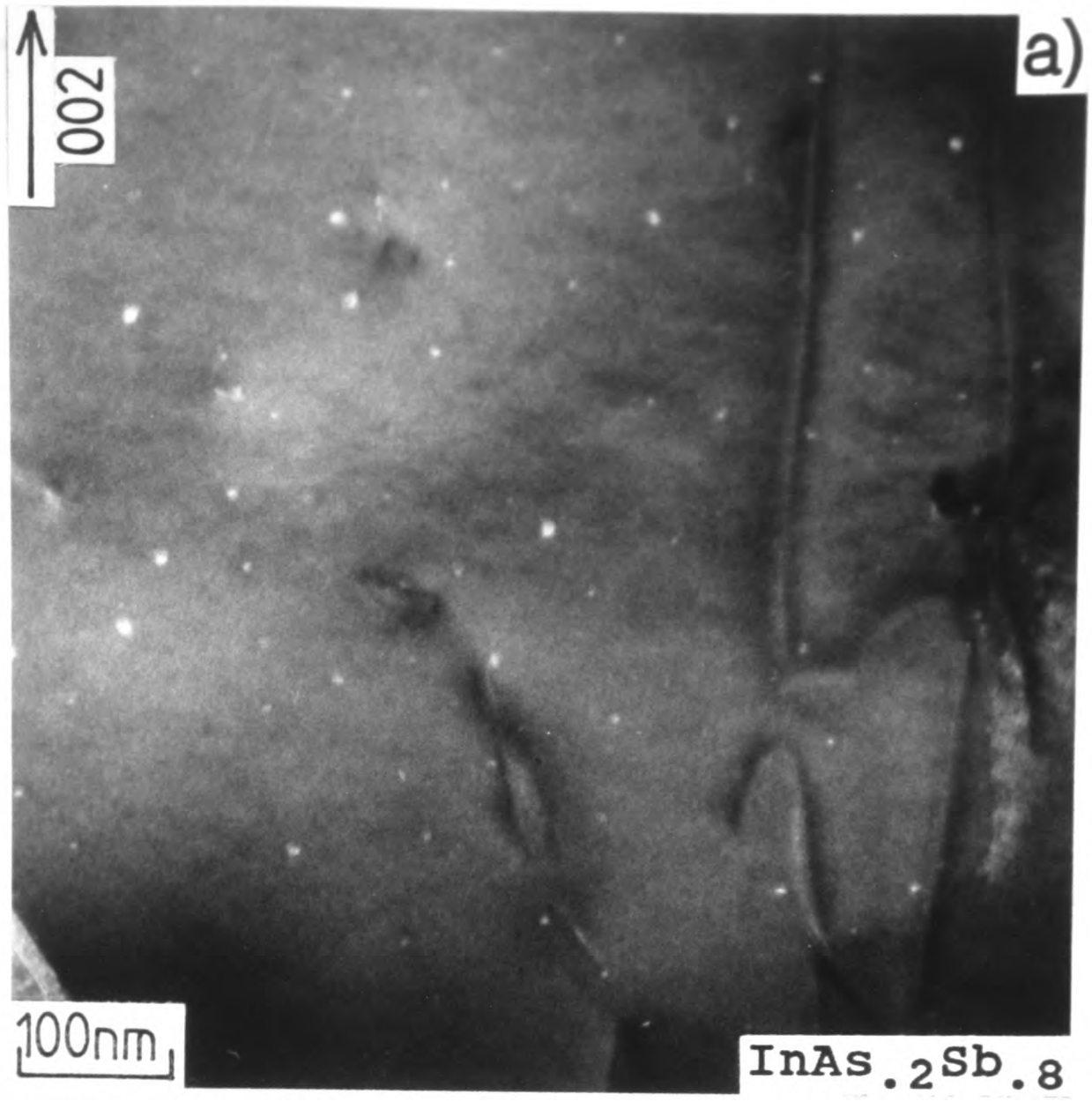

Fig. 4.9a)

Figure 4.9

[110] cross-section **g**(002) DF micrographs of (c) $InAs_{0.6}Sb_{0.4}$ and (d) $InAs_{0.8}Sb_{0.2}$ layers grown at 370°C. Both layers contain plate-like structures.

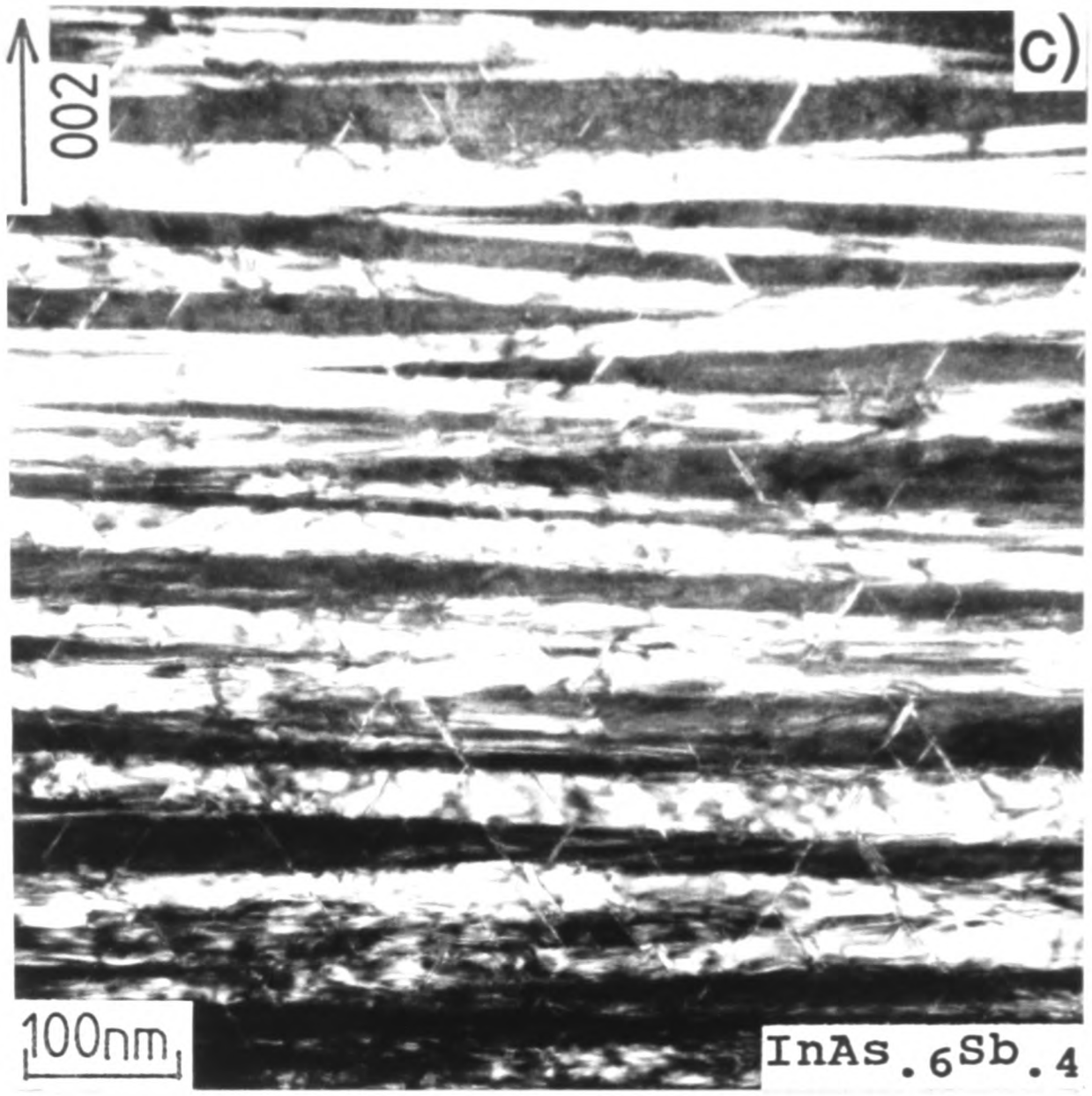

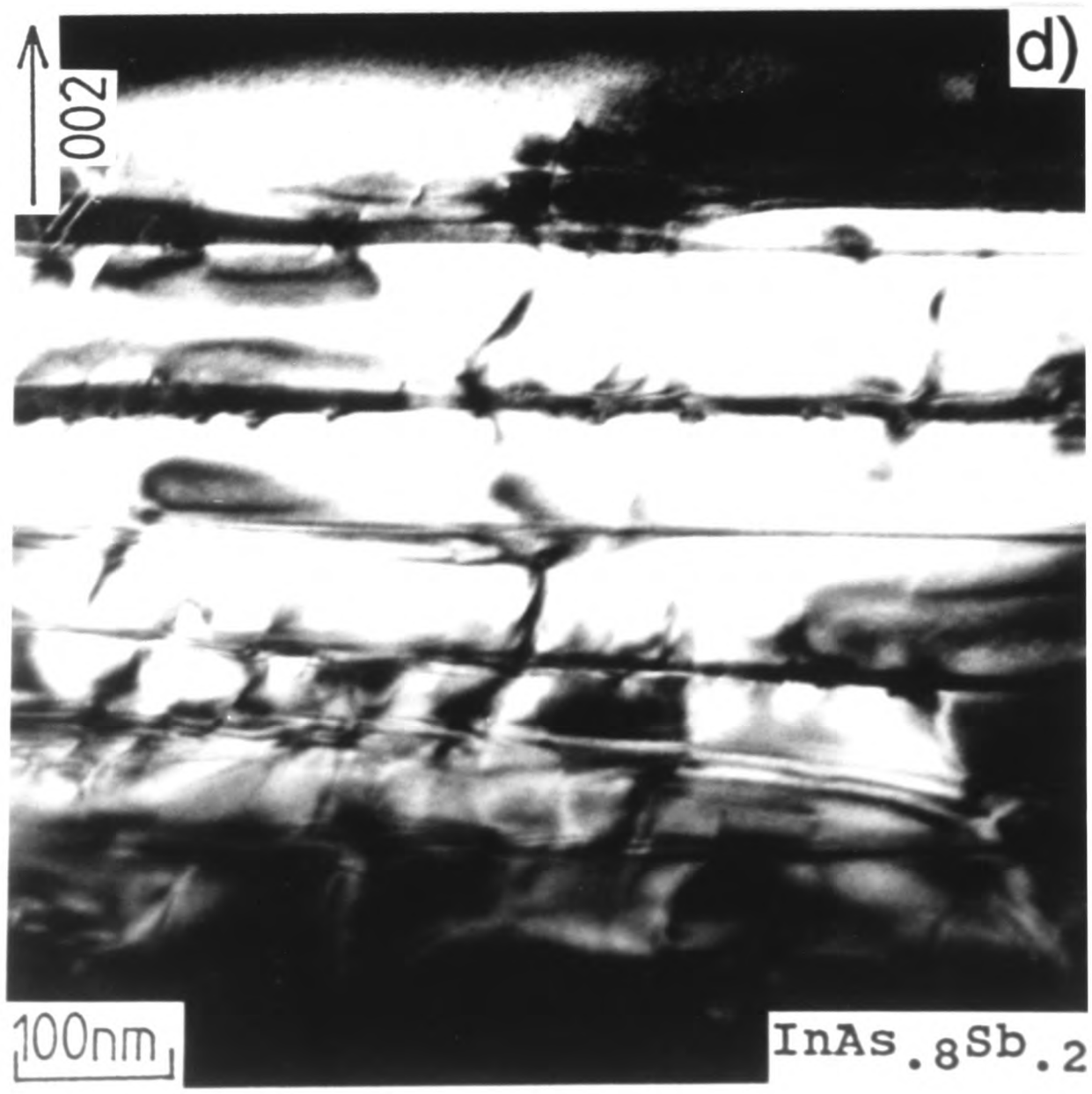

Fig. 4.9b)

Figure 4.10

[$\bar{1}$10] cross-section **g**(002) DF micrographs of (a) $InAs_{0.2}Sb_{0.8}$ and (b) $InAs_{0.4}Sb_{0.6}$ layers grown at 370°C. The $InAs_{0.2}Sb_{0.8}$ layer is homogeneous, while the $InAs_{0.4}Sb_{0.6}$ layer contains the elongated disc type plates.

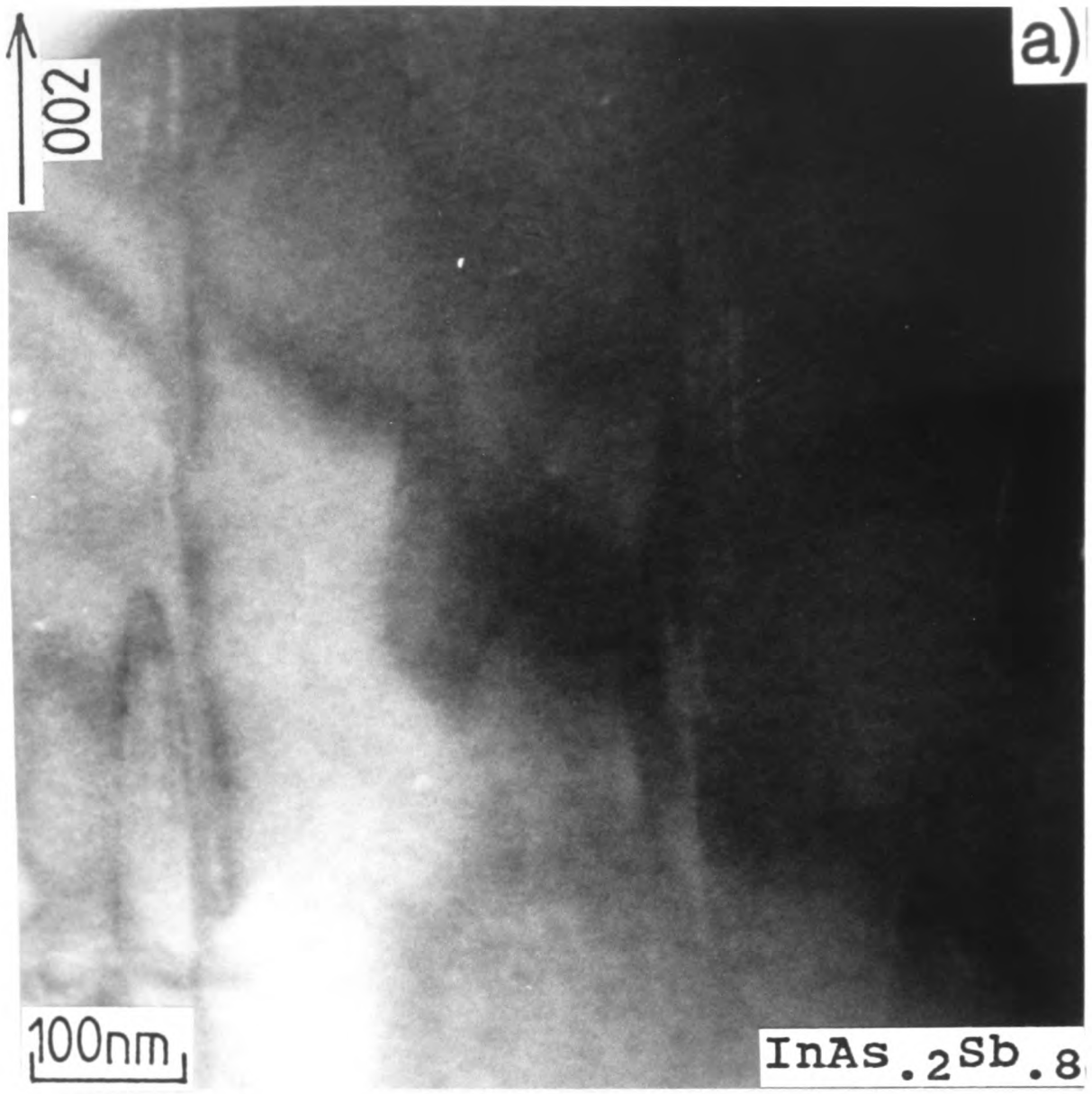

Fig 4.10a)

Figure 4.10

[$\bar{1}$10] cross-section **g**(002) DF micrographs of (c) $InAs_{0.4}Sb_{0.6}$ and (d) $InAs_{0.8}Sb_{0.2}$ layers grown at 370°C. Both layers contains elongated disc type plates.

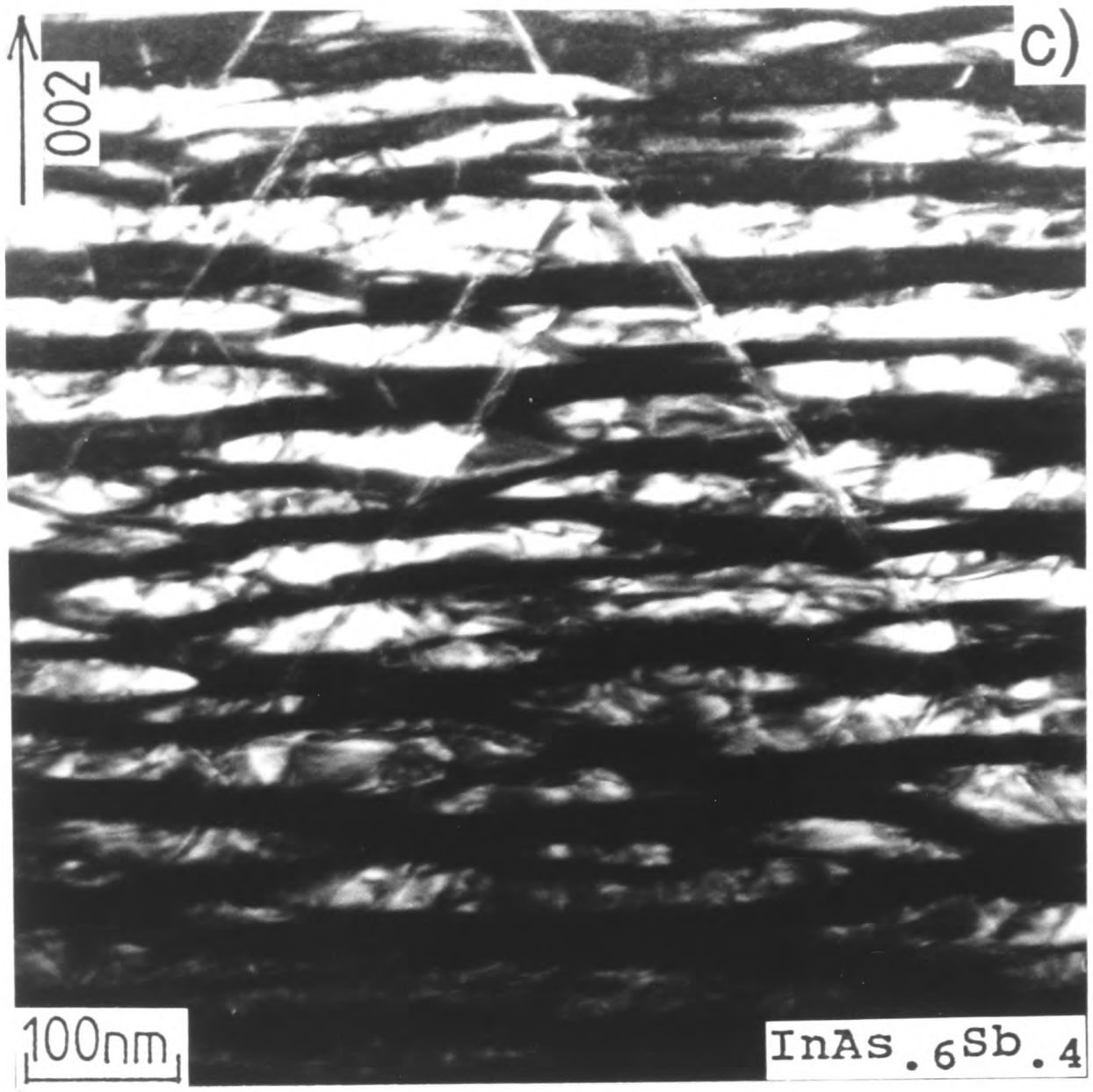

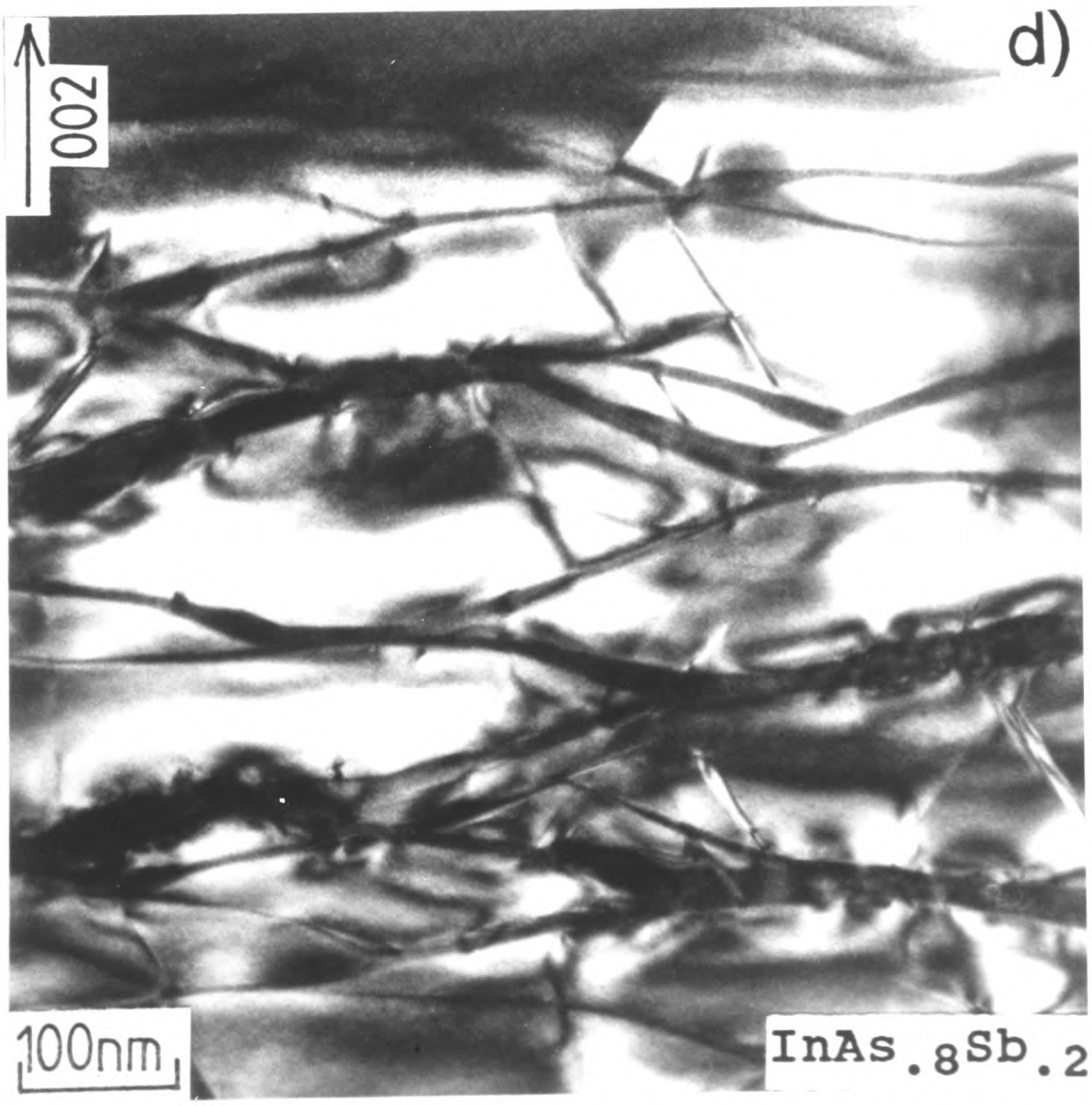

Fig. 4.10b)

composition. (002) DF micrographs, Fig. 4.11 (a) and (b), again showed plate-like structures in both (110) and ($\bar{1}$10) cross-section specimens, but with a different morphology compared to Fig. 4.5 (a) and (b). The morphology of the plate-like structure, with plates of thickness ~28nm, when viewed in the [110] orientation appeared extremely regular, but in the [$\bar{1}$10] orientation appeared slightly less regular (Fig.4.11(b)). The abrupt change in contrast between the plate-like structures indicates sharp and clearly defined interfaces.

In summary, cross-section chemically composition sensitive (002) TEM DF techniques were successfully used to characterize $InAs_ySb_{1-y}$ (y=0.2 to 0.8) layers grown at temperatures in the range 295 to 470°C. There exists a critical temperature at ~400°C, below which the formation of the non-uniform plate-like structure occurs. As the growth temperature increased from 295 to 400°C, the plate-like structure progressively extended in lateral size in both <110> directions and in thickness (e.g. see Table 4.2). The relative thicknesses of the plate-like structures were dependent on the nominal layer composition. The TEM results showed strong nominal composition dependence of layer growth behaviour, and a specific composition range for the occurrence of the plate-like structures. Different fluxes of As and Sb had strong effects on the morphology of the plate-like structures. TEM (220) DF micrographs taken from the same area of $InAs_ySb_{1-y}$ layers, which showed the plate-like structure in (002) DF images, exhibited no evidence for the plate-like structures, although many defects such as threading dislocations and microtwins, and line contrast of strains were visible, e.g. see Fig. 4.2(b). This suggests that the dark and bright contrast plate-like structures correspond to materials with two different alloy compositions and that phase separation has occurred in these alloy layers.

4-3-3 Layer lattice parameters and compositions

Selected area [110] TED patterns taken from $InAs_{0.5}Sb_{0.5}$ layers grown at temperatures of either 295, 320 and 340°C are shown in Fig. 4.12. The patterns were obtained from the middle regions of the layers. The higher order spots were split into two spots in the [002] direction, but not split in the [220] direction. This splitting indicates the

Figure 4.11

g(002) DF micrographs taken from (a) [110] and (b) [$\bar{1}$10] cross-section samples of a layer grown at 340°C using equally balanced fluxes of Sb_4 and As_4 to give a nominal alloy composition of $InAs_{0.5}Sb_{0.5}$. The plates are more regular in this layer.

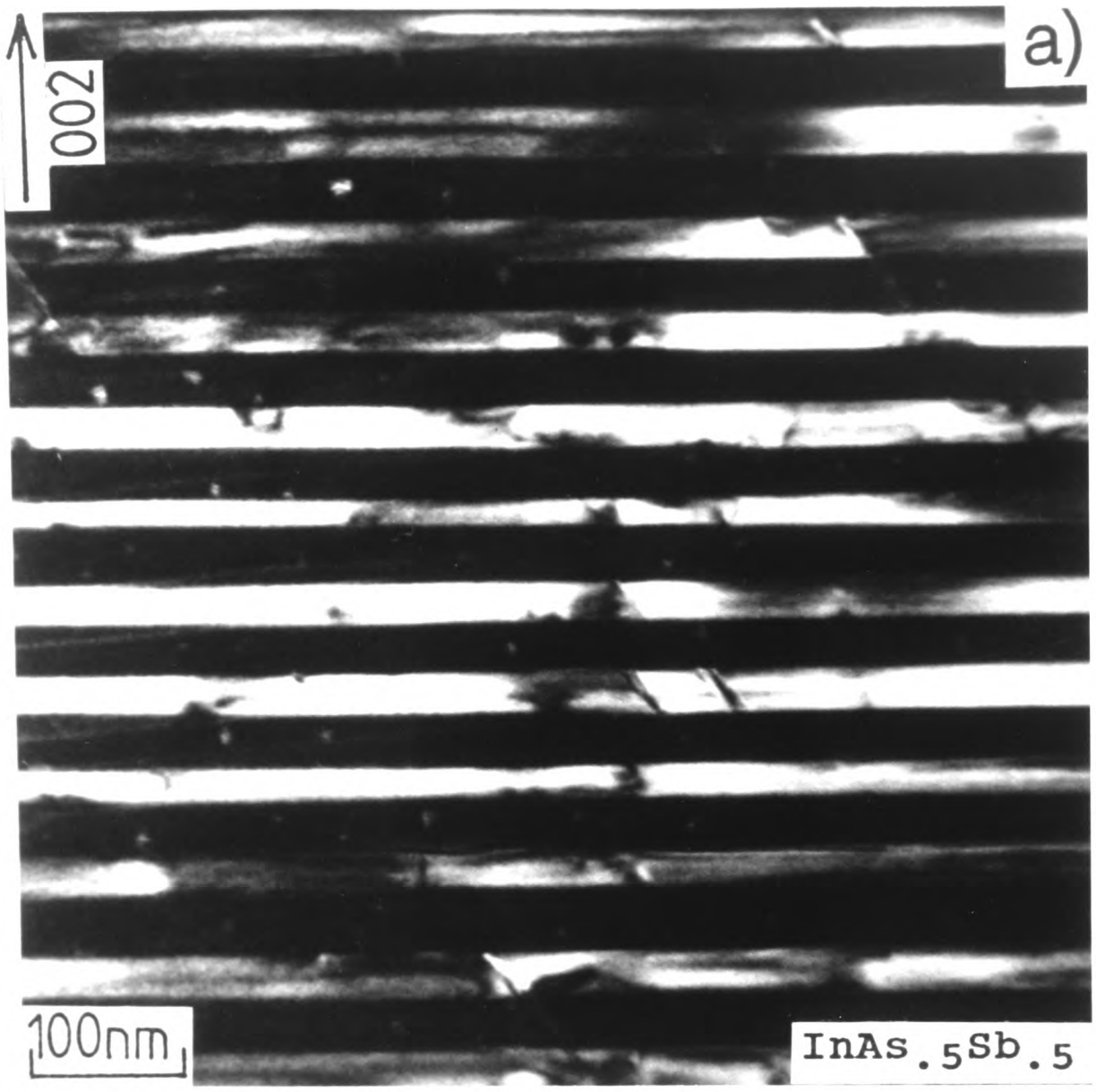
a)
002
100nm
InAs.5Sb.5

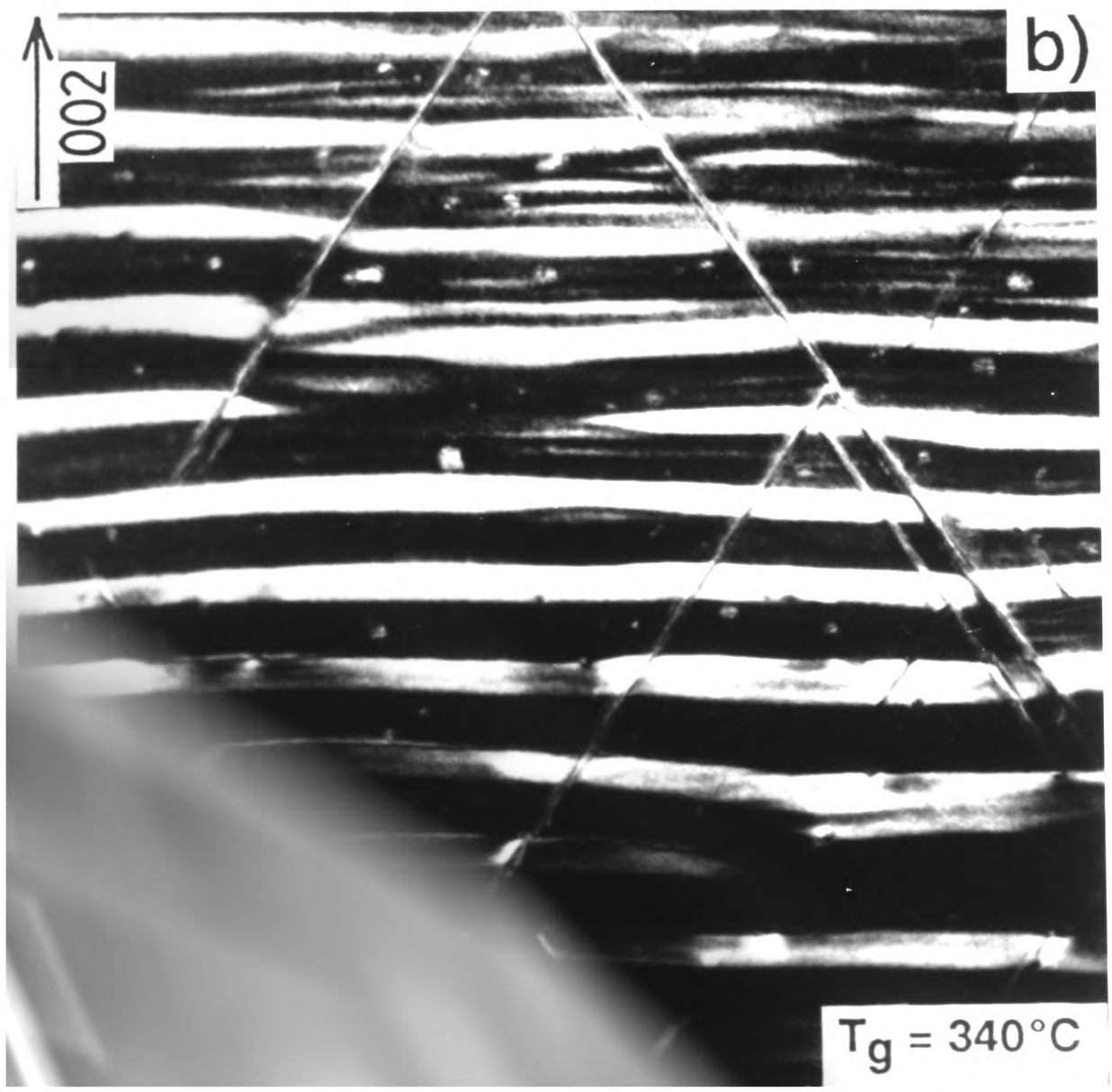
b)
002
T_g = 340°C

Figure 4.12

Selected area [110] TED patterns of $InAs_{0.5}Sb_{0.5}$ layers grown at (a) 295°C, (b) 320°C and (c) 340°C. The splitting of higher order spots become clearer as the growth temperature increases from 295 to 340°C.

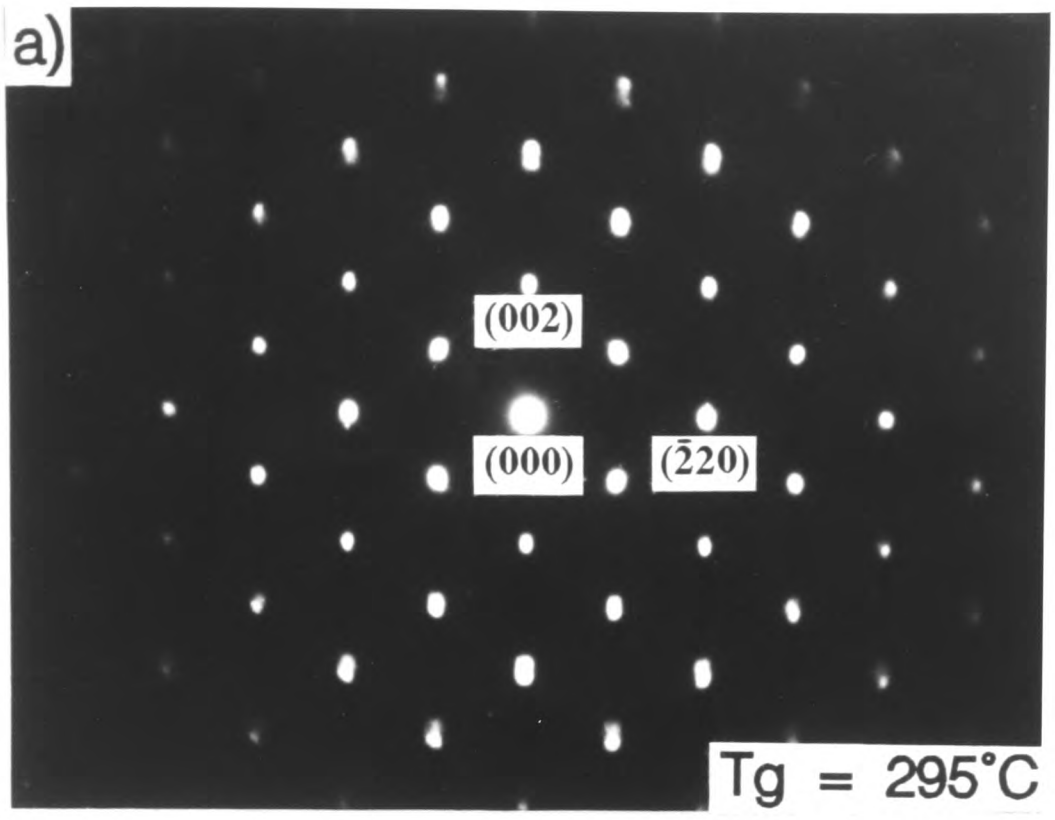

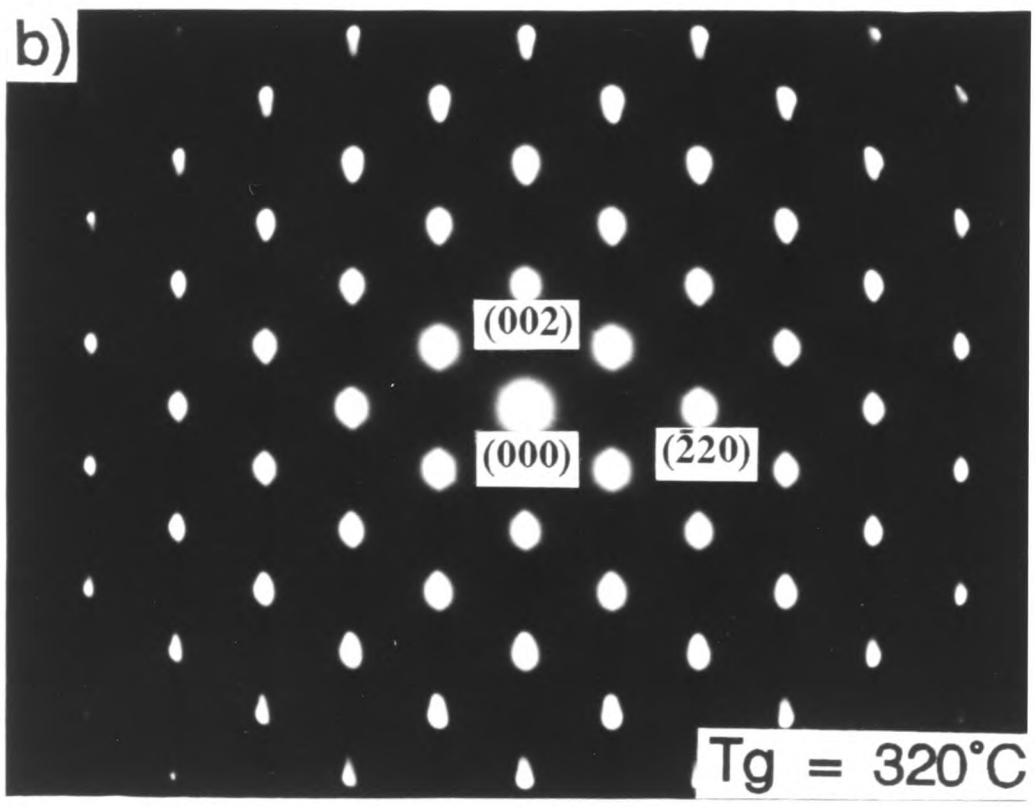

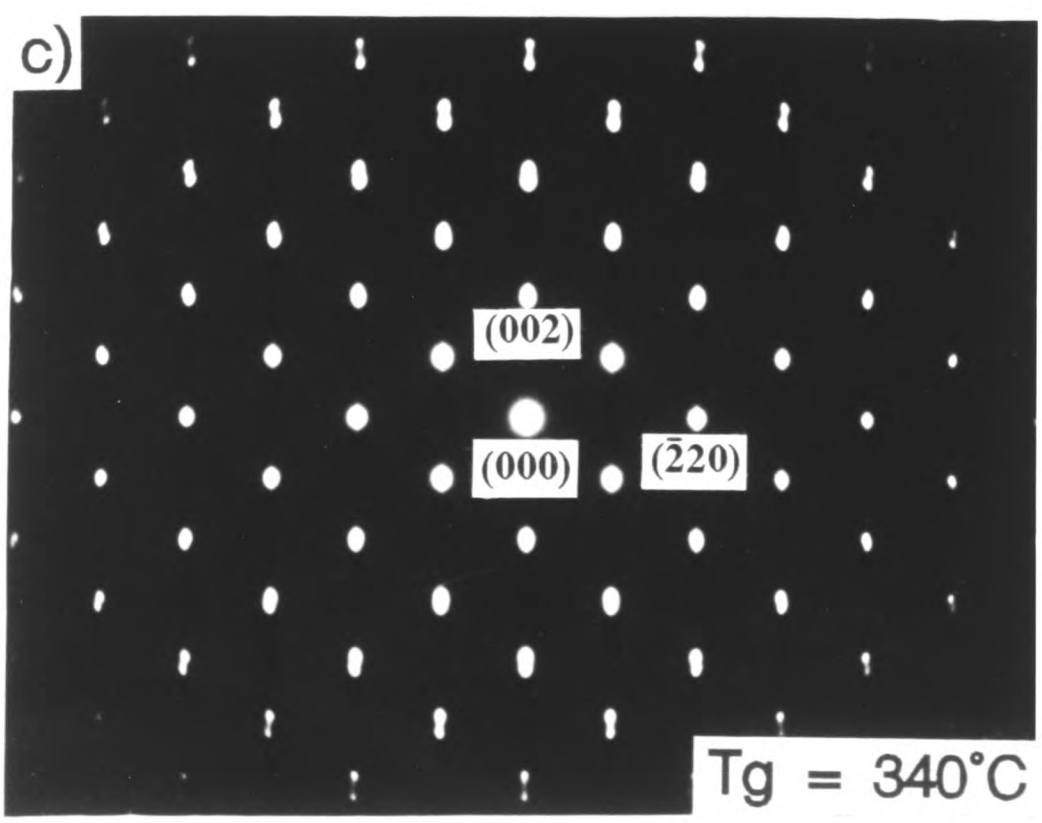

Fig. 4.12

existence of two different lattice parameters perpendicular to the layer surface of the $InAs_{0.5}Sb_{0.5}$ layers. The splitting into two spots became clearer with increasing substrate temperature, in agreement with the results obtained from TEM examinations of these layers which showed that the plate-like structure gradually became more well-defined with increasing the substrate temperature.

A similar [110] TED pattern taken from the middle region of the $InAs_{0.2}Sb_{0.8}$ layer grown at 370°C is shown in Fig. 4.13(a). Only single spots from the $InAs_{0.2}Sb_{0.8}$ layer are now visible. The corresponding pattern from the $InAs_{0.6}Sb_{0.4}$ layer grown at 370°C is shown in Fig. 4.13(b). The spots further away from the central 000 spots were split into two spots in the [002] direction, but not in the [220] direction. [110] TED patterns taken from the middle regions of $InAs_{0.5}Sb_{0.5}$ grown at 430°C and 470°C showed no splitting. All of these TED results are consistent with whether phase separation had or had not occurred as revealed by TEM.

To obtain quantitative data concerning the lattice parameters of the various layers, selected-area TED patterns were obtained from specimen regions ~1μm across. A typical [110] pattern of the $InAs_{0.2}Sb_{0.8}$ layer is given in Fig. 4.14. It arose from a region which included the GaAs substrate, the InAs buffer layer and the $InAs_{0.2}Sb_{0.8}$ layer. All the 'spots' further away from the central 000 spot were split into three spots, these corresponding to each of the three materials. On the assumption that the GaAs substrate spots corresponded to undistorted material with the bulk GaAs lattice parameter, the lattice parameters of the InAs and $InAs_{0.2}Sb_{0.8}$ layers could be calculated from the measured spacings of the spots. Moreover, this could be done for both the (004) and (440) spots (the latter not shown on the print of Fig. 4.14), i.e. in the directions perpendicular and parallel respectively to the layer surface. The results showed that the InAs had closely the bulk InAs lattice parameter of 6.06Å in both of these directions, indicating that the InAs layer was virtually fully relaxed with respect to the GaAs substrate. The results also showed that the $InAs_{0.2}Sb_{0.8}$ layer had a lattice parameter of 6.44Å perpendicular to the surface and 6.36Å parallel to the surface, i.e. although significantly relaxed (~93%) with respect to the underlying InAs layer, was tetragonally distorted.

Figure 4.13

Selected area [110] TED patterns of (a) $InAs_{0.2}Sb_{0.8}$ and (b) $InAs_{0.6}Sb_{0.4}$ layers grown at 370°C. Note single spots for the $InAs_{0.2}Sb_{0.8}$ layer, but the splitting of higher order spots for the $InAs_{0.6}Sb_{0.4}$ layer.

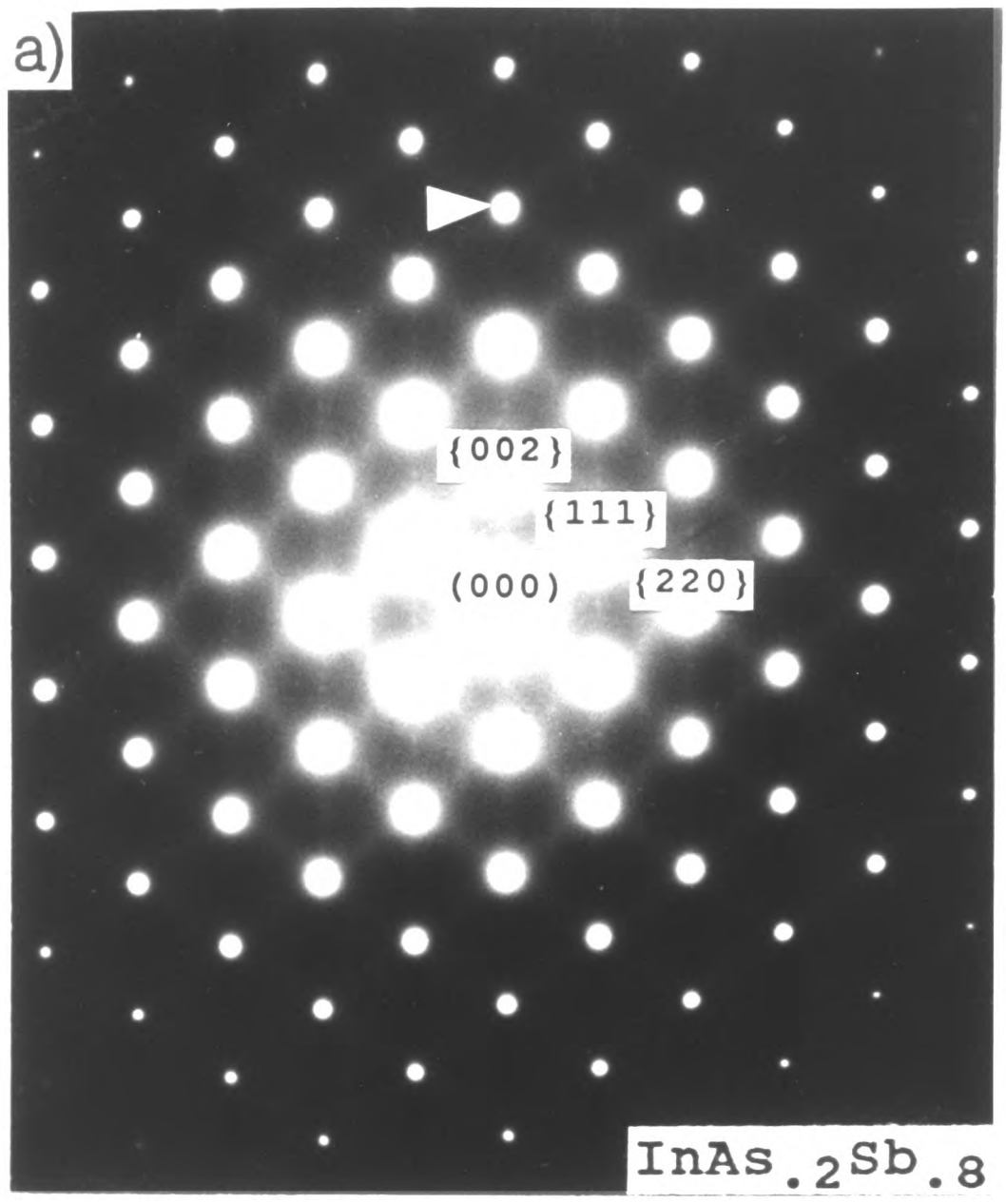

Fig. 4.13

Figure 4.14

Selected area [110] TED pattern from region consisting of $InAs_{0.2}Sb_{0.8}$ layer, InAs layer and GaAs substrate in specimen IC 121. The three spots for each (hkl) reflection correspond to each of the three materials.

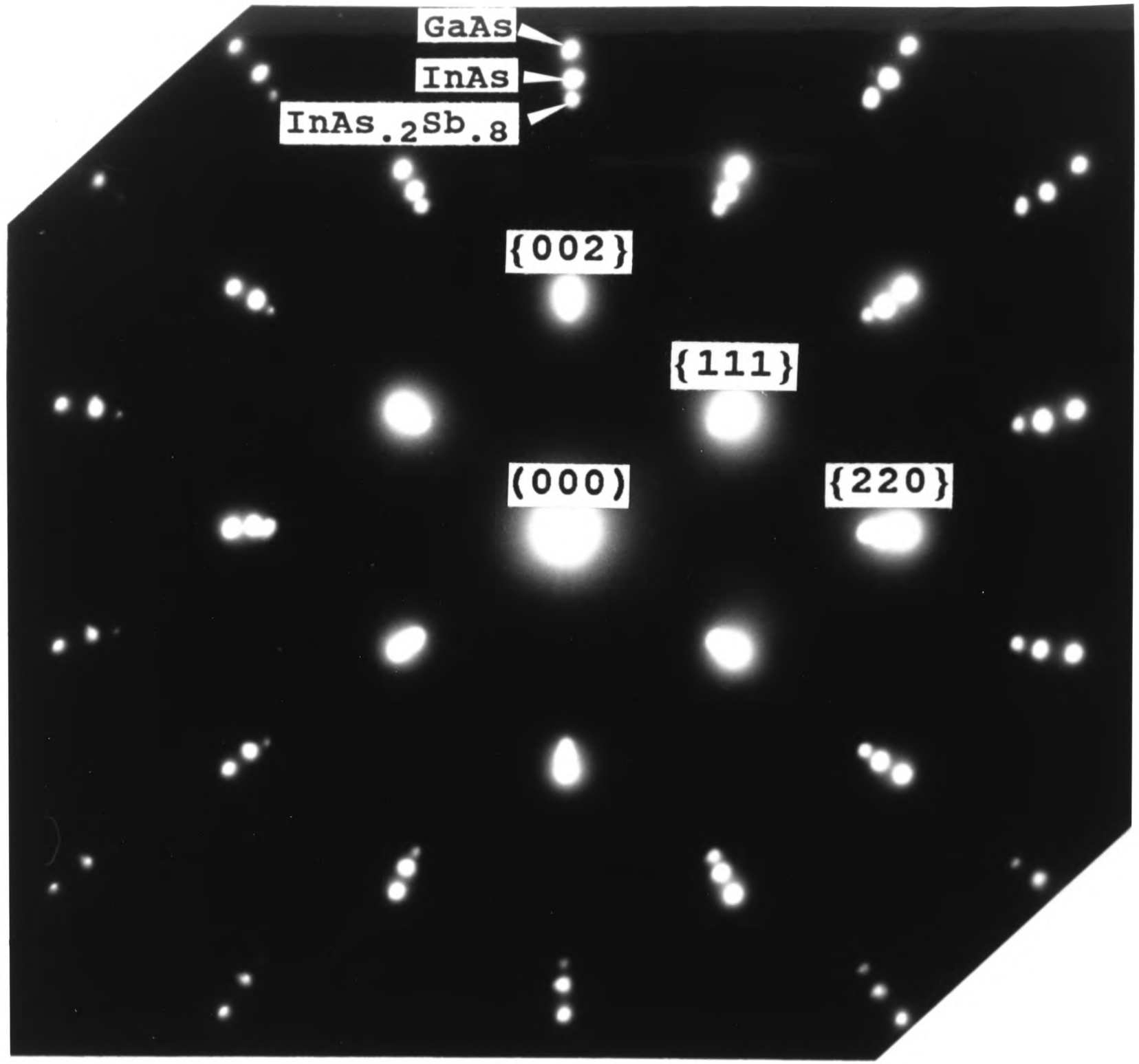

Fig. 4.14

TED patterns taken from $InAs_ySb_{1-y}$ (y=0.2 to 0.8) layers grown at temperatures ranging from 295 to 400°C were obtained, similar to that of Fig. 4.14, and lattice parameters were deduced from the (006) and (440) spots, i.e. in the directions perpendicular and parallel to the layer surface respectively. Results obtained from the middle region of the layers showed that they were all phase separated, except for y=0.2, and the individual phases were all tetragonally distorted (Table 4.3).

The results calculated from the $InAs_{0.5}Sb_{0.5}$ layers grown at temperatures ranging from 295 to 400°C were as follows. For the 295°C layer (IC 247) , there are two lattice parameters perpendicular to the layer surface of 6.40Å and 6.11Å, and one lattice parameter parallel to the surface of 6.24Å, i.e. there are two tetragonally distorted cubic lattices, one with c/a>1 and other with c/a<1. For tetragonal distortion, the corresponding relaxed lattice parameter (a_r) (12) is given by:

$$a_r = 2\,\mathbf{a}\,\frac{\upsilon}{1+\upsilon} + \mathbf{c}\,\frac{1-\upsilon}{1+\upsilon} \qquad (4\text{-}1)$$

where υ, Poisson's ratio, is ~1/3 for most materials, and **a** and **c** are lattice parameters parallel and perpendicular to the interface, respectively. Therefore, the completely relaxed cubic lattice parameters of the two phases were calculated to be a_{r1}=6.32Å and a_{r2}=6.18Å, assuming $\upsilon \cong 1/3$, which correspond to alloy layer compositions of $InAs_{0.38}Sb_{0.62}$ and $InAs_{0.72}Sb_{0.28}$ respectively, deduced using Vegard's law. For $InAs_{0.5}Sb_{0.5}$ layers grown at 320°C, 340°C, 370°C, 400°C and 430°C, the lattice parameters similarly deduced are given in Table 4.3. There are no significant changes of the compositions of the two phase-separated materials as the substrate temperature increases from 295°C to 400°C. All the nominal $InAs_ySb_{1-y}$ layers grown below 400°C resulted in the two phase-separated materials $InAs_{y1}Sb_{1-y1}$ and $InAs_{y2}Sb_{1-y2}$, i.e. the nominal composition y was decomposed into two compositions y1 and y2. For most of the layers, the nominal composition y lies between y1 and y2, i.e. y1<y< y2. However, for IC 119, the nominal composition y is larger than both y1 and y2.

Table 4-3 Electron diffraction results

No.	y	a(Å)	m(%)	a_p	c_1	c_2	a_{r1}	a_{r2}	y_1	y_2
IC 247	0.5	6.26	10.33	6.24	6.40	6.11	6.32	6.18	0.38	0.72
IC 249	0.5	6.26	3.30	6.22	6.44	6.17	6.33	6.19	0.36	0.69
IC 237	0.5	6.26	3.42	6.28	6.40	6.11	6.34	6.19	0.33	0.69
IC 262	0.5	6.26	3.42	6.25	6.40	6.04	6.32	6.14	0.38	0.80
IC 121	0.2	6.39	5.41	6.36	6.44	-	6.40	-	0.19	-
IC 118	0.4	6.31	4.08	6 .31	6.37	6.02	6.34	6.17	0.33	0.74
IC 264	0.5	6.26	3.42	6.25	6.35	6.03	6.30	6.14	0.42	0.80
IC 124	0.6	6.22	2.74	6.26	6.44	6.08	6.35	6.17	0.31	0.74
IC 119	0.8	6.14	1.38	6.20	6.44	6.15	6.32	6.17	0.38	0.74
IC 265	0.5	6.26	3.42	6.24	6.39	6.10	6.31	6.17	0.40	0.74
IC 209	0.56	6.24	3.82	6.29	6.25	-	6.27	-	0.49	-

y = nominal composition in $InAs_ySb_{1-y}$; a(Å)=relaxed cubic lattice parameter as deduced by Vegard's law; m = lattice mismatch with respect to buffer layer; a_p = measured lattice parameter parallel to interface; c_1 = measured lattice parameter in the [001] direction of phase 1; c_2 = measured lattice parameter in the [001] direction of phase 2; a_{r1} = relaxed lattice parameter of phase 1; a_{r2} = relaxed lattice parameter of phase 2; y_1 = composition of phase 1; y_2 = composition of phase 2.

In order to characterise the compositions of the plate-like structures more directly, chemical compositional analysis by EDX was carried out on the $InAs_{0.6}Sb_{0.4}$ layer using a (110) cross-section specimen and the VG HB 501 STEM (Fig. 4.15). Compositions were measured from several points across two adjacent platelets and were plotted versus distances between the points. The EDX results show that the two platelets have compositions $InAs_{0.32}Sb_{0.68}$ and $InAs_{0.80}Sb_{0.20}$, in reasonable agreement with the TED results for this layer of $InAs_{0.31}Sb_{0.69}$ and $InAs_{0.74}Sb_{0.26}$.

4-3-4 Annealed layers

The TEM and TED investigations showed that phase separation can occur in $InAs_ySb_{1-y}$ layers, resulting in plate-like phase-separated materials. The phase separation is considered to occur at the growing surface, and is not related to a bulk diffusion process (see below). In order to investigate the stability of the plate-like structure and the possibility of its generation by solid state bulk diffusion, post-growth annealing experiments were carried out. Since there is no anisotropy of the <110> directions in the bulk material, if phase separation was due to a bulk diffusion process, the plate-like structures should show similar morphology in both <110> cross-section specimens.

For this study, two samples were examined. The $InAs_{0.56}Sb_{0.44}$ layer (IC 209) grown at 430°C was annealed for 95 hours at 350°C in a quartz ampoule evacuated to less than 10^{-6} Torr. The $InAs_{0.5}Sb_{0.5}$ layer (IC267) grown at 430°C was in-situ annealed at 370°C for 3 hours under an arsenic flux in the growth kit. TEM/TED results obtained from the annealed $InAs_{0.56}Sb_{0.44}$ layer were compared with those of the as-grown sample of the same layer. As described earlier, no phase separation occurs in the as-grown $InAs_{0.56}Sb_{0.44}$ layer, and the annealed $InAs_{0.56}Sb_{0.44}$ layer showed no the plate-like structures, indicating that phase separation does not occur by a bulk diffusion process during annealing at 350°C.

Fig. 4.16 shows a (002) DF micrograph taken from a (110) cross-section of the step-growth layer of a nominal composition $InAs_{0.5}Sb_{0.5}$ alloy layer. The first layer grown at 430°C is reasonably homogeneous with no significant phase separation even after being

Figure 4.15

EDX chemical composition profile obtained from adjacent phase separated platelets in $InAs_{0.6}Sb_{0.4}$ layer (IC 124) using VG HB 501 STEM. Platelets have compositions $InAs_{0.32}Sb_{0.68}$ and $InAs_{0.80}Sb_{0.20}$.

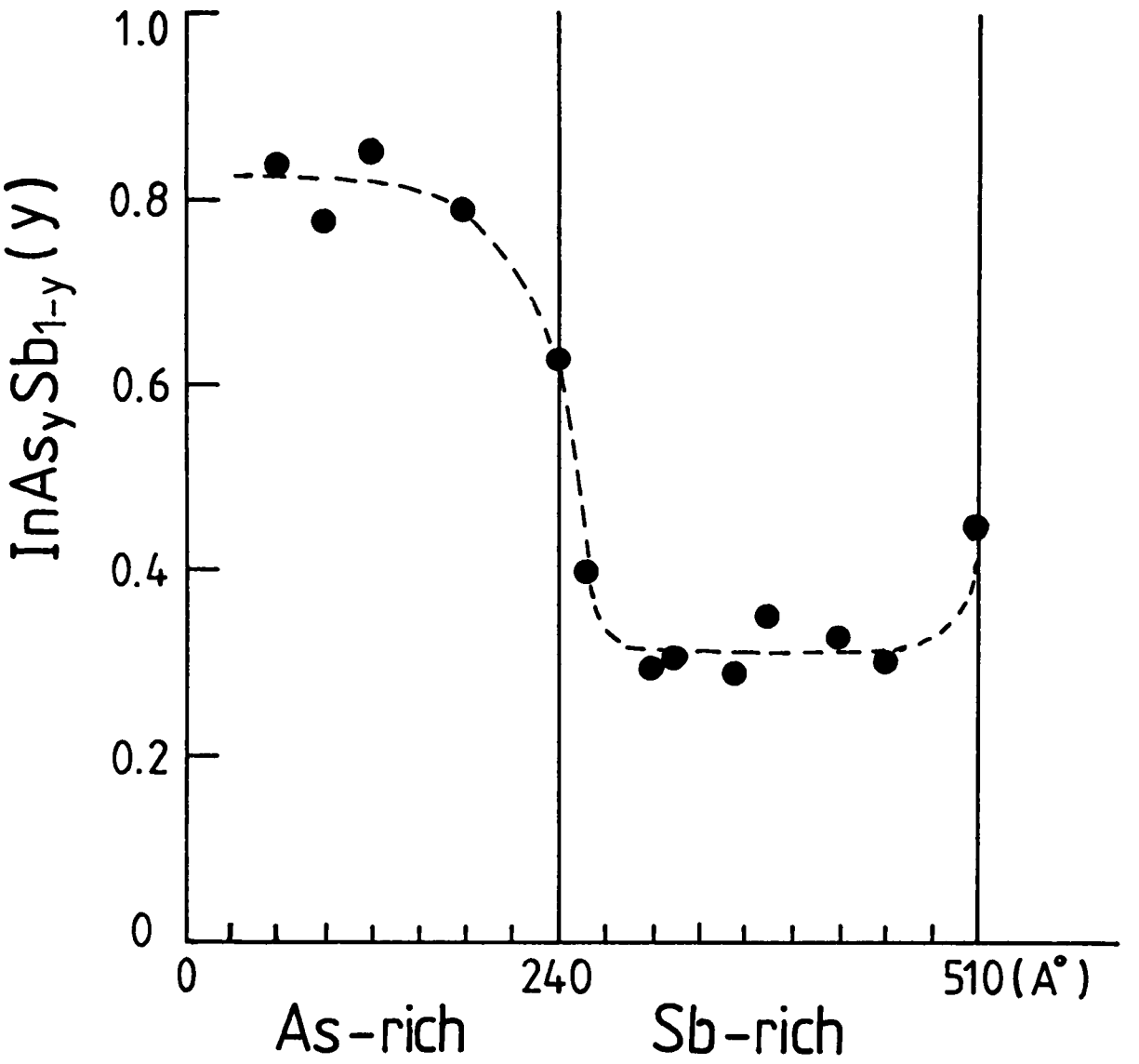

Fig. 4.15

Figure 4.16

[110] cross-section **g**(002) DF micrograph of $InAs_{0.5}Sb_{0.5}$ layer grown at 430°C for 1 hour and then grown at 370°C for 1 hour. This layer was then in-situ annealed for 2 hours in the same growth kit. The layer grown at 430°C shows no phase separation, while the layer grown at 370°C exhibits plate-like structure.

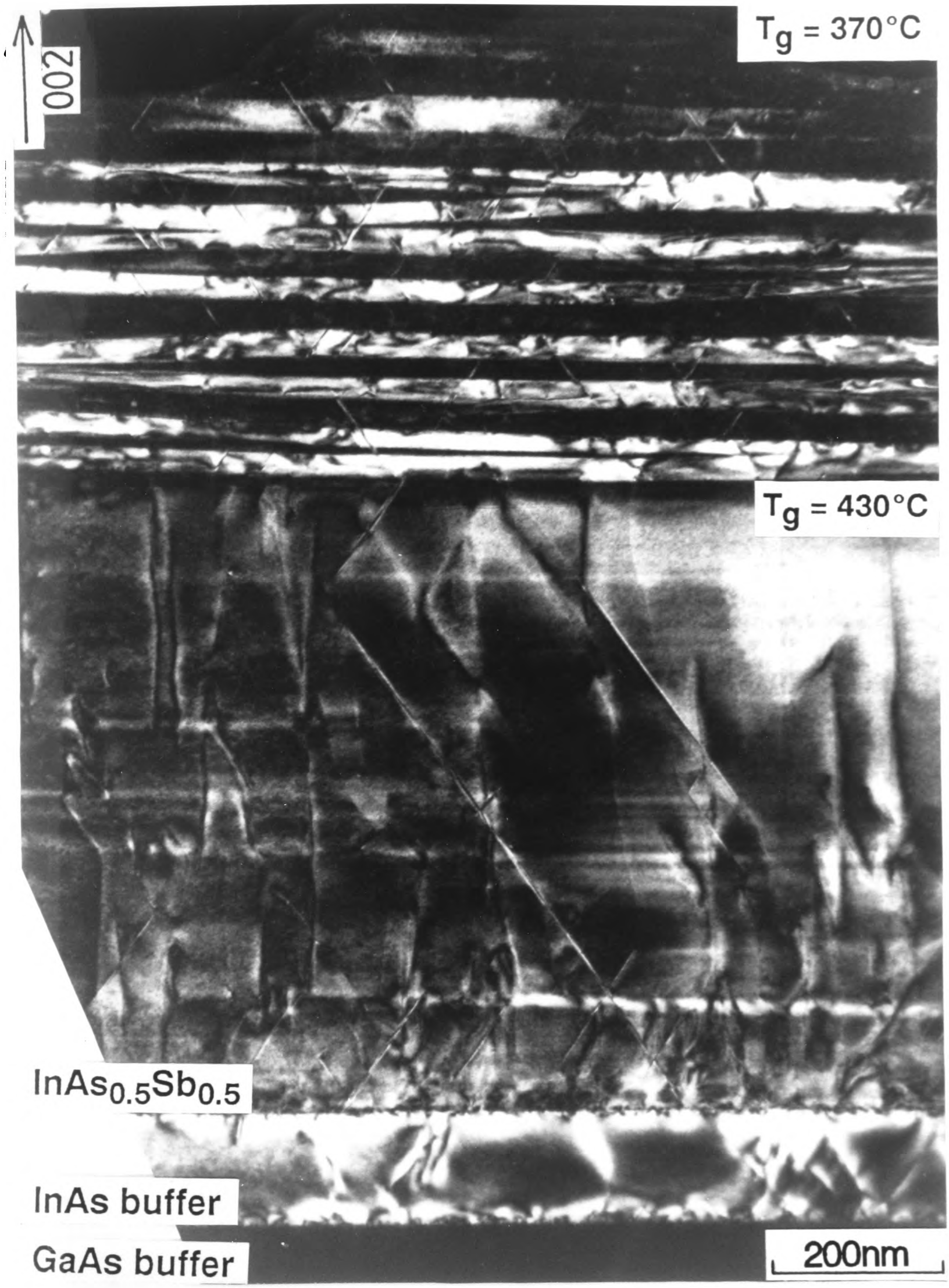
002
T_g = 370°C
T_g = 430°C
$InAs_{0.5}Sb_{0.5}$
InAs buffer
GaAs buffer
200nm

Fig. 4.16

annealed for 3 hours at 370°C, while the layer grown at 370°C is phase-separated and is stable even after being annealed for 2 hours at 370°C. This confirms the previous TEM/TED results which showed that there is a critical growth temperature at ~400°C and that the phase separation observed in the layers grown below 400°C is not a result of a bulk diffusion process, the latter indicating that there may be a kinetic barrier for phase separation because of low diffusivity below 400°C in the bulk phase. These post-growth annealing experiments together with the anisotropy of the plate-like structures strongly suggest that the phase separation observed in the layers occurred at the growing surface.

4-4 Suggested mechanism for phase-separated layers

TEM examinations showed that the plate-like structures increase in lateral size in both the [110] and [$\bar{1}$10] directions, and in thickness, as the growth temperature was increased from 295 to 400°C. Fig. 4.17(a) shows a schematic drawing corresponding to a ($\bar{1}$10) cross-section of progressive stages of formation of the plate-like structures grown at 320°C deduced from the micrographs. The first-grown material consisted of platelets of the Sb-rich phase together with islands of the As-rich phase. The growth continued by islands of the As-rich phase continuously forming on platelets of the Sb-rich phase and then being subsequently overgrown by further platelets of the Sb-rich phase. A higher volume fraction of the Sb-rich phase of the first grown material could be attributed to two main properties (13): i) the higher sublimation energy of Sb_4 molecules (49.45 kcal/mol vs 36.6 kcal/mol for As_4); ii) the low atomization energy (203kcal/mol vs 252kcal/mole for As_4). Experimentally it is observed that antimony atoms are more easily incorporated into growing InAsSb layer than arsenic. However, as the growth temperature increases, this preferential incorporation of Sb atoms over As atoms is reduced due to increasing desorption of Sb atoms from the growing layer. This is consistent with our experimental TEM results.

Fig. 4.17(b) shows a schematic drawing corresponding to a ($\bar{1}$10) cross-section of progressive stages of formation of the plate-like structures grown at 370°C. The growth

Figure 4.17 (a)

Schematic drawing corresponding to a $(\bar{1}10)$ cross-section of progressive stages of formation of the plate-like structures grown at 320°C deduced from the micrographs. The first-grown material consists of platelets of the Sb-rich phase together with islands of the As-rich phase. The growth continues by islands of the As-rich phase continuously forming on platelets of the Sb-rich phase and then being subsequently overgrown by further platelets of the Sb-rich phase.

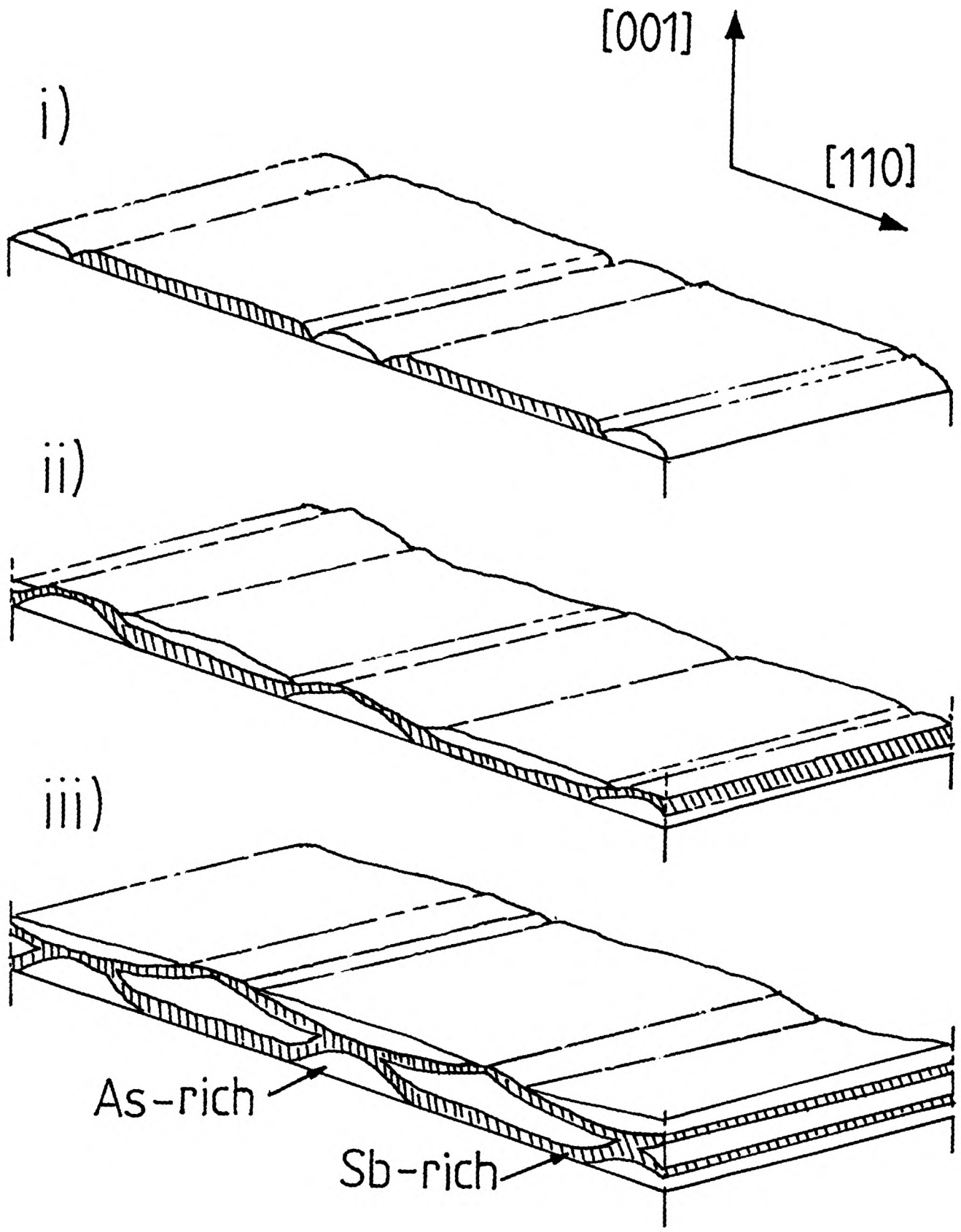

Fig. 4.17(a)

Figure 4.17 (b)

Schematic drawing corresponding to a $(\bar{1}10)$ cross-section of progressive stages of formation of the plate-like structures grown at 370°C. The growth behaviour is similar to that of the 320°C layer but the lateral sizes and thicknesses of the plate-like structures are larger.

behaviour is similar to that of the 320°C layer but the lateral size and thicknesses of the plate-like structure are larger, which will be discussed later.

The formation of the plate-like structures can be postulated as follows. Below a growth temperature of 400°C, phase separation can occur because of a miscibility gap (e.g. see Fig. 4.1). The growth behaviour depends on the nominal composition of the layers. For example, at a growth temperature of 370°C, when $InAs_{0.2}Sb_{0.8}$ layers are grown, the nominal composition is outside the gap range, and so single phase material occurs. When $InAs_ySb_{1-y}$ (y=0.4 to 0.8) layers are grown, the compositions are within the gap range, and so two phase materials occur.

The more detailed mechanism is illustrated in Fig. 4.18. Let us consider the layer grown at 295°C. The basis of this model is the nucleation of the islands of $InAs_{0.72}Sb_{0.28}$ on $InAs_{0.38}Sb_{0.62}$ layers and the converse growth of $InAs_{0.38}Sb_{0.62}$ over either $InAs_{0.72}Sb_{0.28}$ or $InAs_{0.38}Sb_{0.62}$ layers. We assume that the growth behaviours of the $InAs_{0.72}Sb_{0.28}$ islands and $InAs_{0.38}Sb_{0.62}$ layers depend on γ_A, γ_B and γ_{AB}, where γ_A and γ_B are the surface free energies of $InAs_{0.72}Sb_{0.28}$ and $InAs_{0.38}Sb_{0.62}$, respectively, and γ_{AB} is the interfacial free energy of $InAs_{0.72}Sb_{0.28}/InAs_{0.38}Sb_{0.62}$ (which may affect the sticking coefficients of As and Sb atoms). When a nominal composition $InAs_{0.5}Sb_{0.5}$ layer is grown on the (001) surface, the In, As and Sb atoms rearrange rapidly to form the thermodynamically stable As-rich and Sb-rich phases (Fig. 4.18). Unfortunately, there are no available data concerning the values of surface free energies and interfacial energy in the InAs-InSb systems. We assume that the growth velocity of $InAs_{0.38}Sb_{0.62}$ on $InAs_{0.72}Sb_{0.28}$, V_{BA}, is faster than that of $InAs_{0.38}Sb_{0.62}$ on $InAs_{0.38}Sb_{0.62}$, V_{BB}, if $\gamma_{AB} < \gamma_A$ or γ_B. During layer growth, vacancies are injected from the surface and into the islands (14), which help the As and Sb atoms to move easily from the transition region beneath the surface into the surface. As atoms desorbed from Sb-rich phase materials are redeposited on the As-rich islands and vice versa (Fig. 4.18).

We now consider the growth of $InAs_{0.38}Sb_{0.62}$ on $InAs_{0.72}Sb_{0.28}$. Fig. 4.19 shows a schematic drawing of the lateral growth behaviours. When the first monolayer is deposited on the (001) surface, atoms rearrange to reach a thermodynamically stable state,

Figure 4.18

Schematic drawing of suggested growth mechanism of Sb-rich and As-rich phases during epitaxial growth.

Figure 4.19

Schematic drawing of suggested lateral growth for an 'A' alloy ($InAs_{0.72}Sb_{0.28}$) on a 'B' alloy ($InAs_{0.38}Sb_{0.62}$).

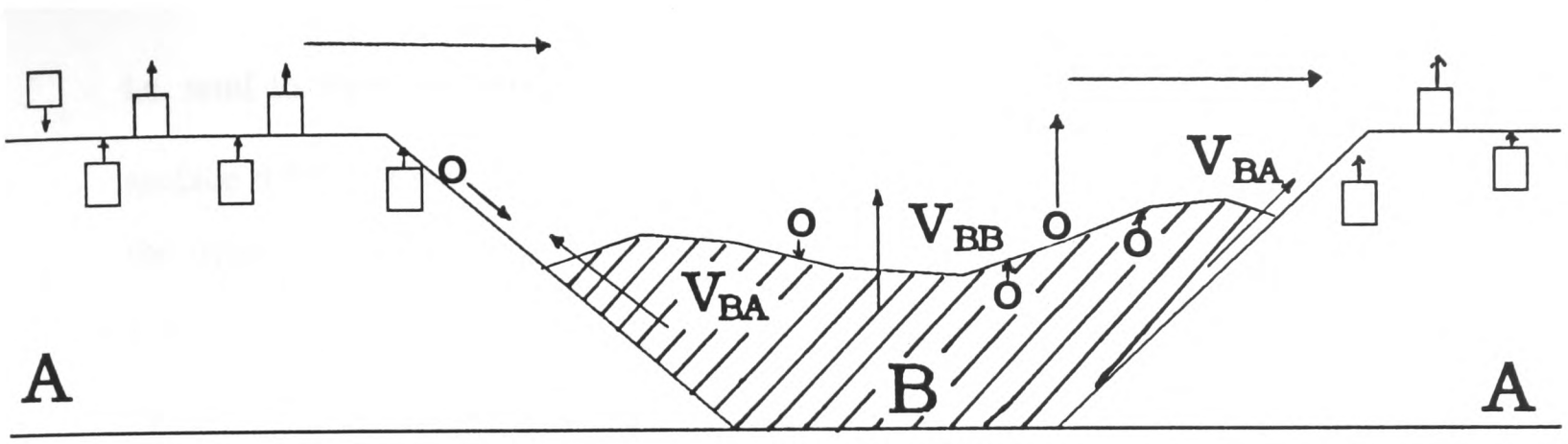

□ : Sb atoms

o : As atoms

A : As-rich phase

B : Sb-rich phase

Fig. 4.18

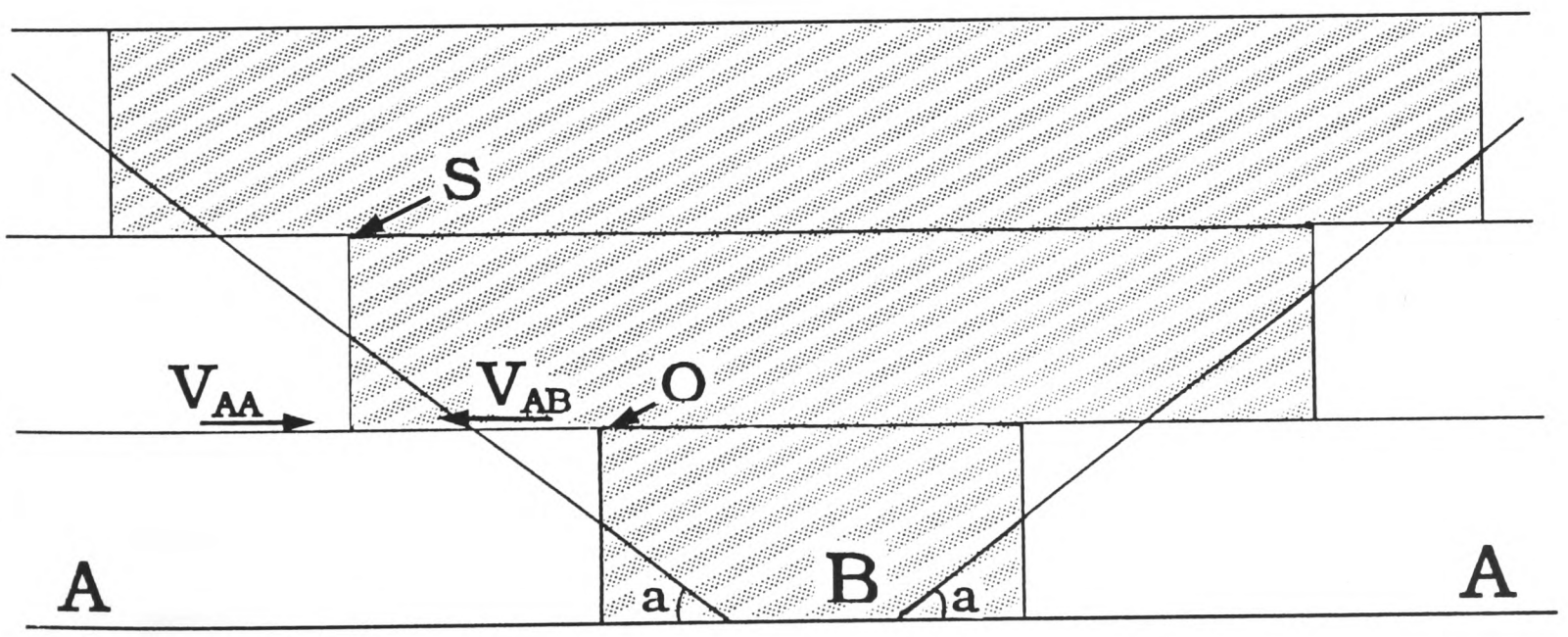

Fig. 4.19

i.e. tend to form preferential phases such as $InAs_{0.38}Sb_{0.62}$ and $InAs_{0.72}Sb_{0.28}$ through surface diffusion processes. Let us consider the deposition of the next monolayer. When the upper $InAs_{0.38}Sb_{0.62}$ layer passes over the edge (indexed by 'o' in Fig. 4.19) of the lower $InAs_{0.38}Sb_{0.62}$ layer, the growth velocity of the upper $InAs_{0.38}Sb_{0.62}$ layer speeds up from V_{BB} to V_{BA}. The growth continues until it is stopped by the $InAs_{0.72}Sb_{0.28}$ layer (indexed by 's' in Fig. 4.19). When this process is repeated for many monolayers, it creates inclined interfaces at an angle (a) with respect to the (001) plane, e.g. for growth at 295°C, a = ~15°. Hence, the lateral sizes and morphology of the islands depend on surface diffusion, nucleation and monolayer lateral growth, together with the values of the sticking coefficients.

The angle (a) between the plate-like structures was dependent on the growth temperature, i.e. this angle decreased from ~15° to ~0°, as the growth temperature increased from 295°C to 400°C. At a low temperature, the diffusion coefficients of As and Sb are low, resulting in the small lateral size of the first-grown plate-like structures on the InAs buffer layer. As suggested in Fig. 4.19, this results in the edges of the plate-like structures with the angles of ~15°. Because of the small lateral size of the plate-like structures, the angled edges are connected to one another, and this can give rise to a preferred crystallographic orientation (e.g. parallel to {511} planes) in order to lower the energy. As the growth temperature increases, the diffusion coefficients of As and Sb are higher, and so the lateral size increases. Owing to the increased lateral size, the plate-like structures appear to have a less preferred orientation, although the angled edges are still present. The predictions of this model are consistent with the experimental results, Figs. 4.3 to 4.10.

The anisotropy observed for the InAsSb plate-like structures in layers grown below 400°C is explained as follows. The long axis of the As- rich phase platelets lies along the $[\bar{1}10]$ direction, in which a much higher growth rate of GaAs by MBE has been reported in comparison with the [110] direction (15). This growth anisotropy may be a result of anisotropic cation diffusion rates (16) or more likely due to the different atomic structure of steps along the <110> directions (17). It was shown by Ohta et al.(16) from a RHEED study during MBE growth that the diffusion coefficient of isolated Ga atoms on the GaAs (001) surface in the $[\bar{1}10]$ direction is four times as large as in the [110] direction. Islands with

edges elongated parallel to [$\bar{1}$10] have been directly revealed on GaAs (001)-2x4 surfaces by scanning tunnelling microscopy (18,19). The increase in the lateral size of the InAsSb plate-like structures with increase in growth temperature is also indicative of a surface diffusion process.

The reason for the more regular plate-like structure of $InAs_{0.5}Sb_{0.5}$ layers when grown using equally balanced fluxes of Sb_4 and As_4 may be attributed to several factors, i.e. the different volume fraction of the fluxes over the growing layer may affect i) distributions of As and Sb atoms over the substrate; ii) diffusion of As and Sb atoms on the growing surface; iii) sticking coefficients of As and Sb atoms. Such factors are likely to influence the growth behaviour of the plate-like structures, although it is not yet clear why with balanced fluxes a more regular structure should occur.

4-5 Discussion

A non-uniform plate-like structure in MBE $Ga_xAl_{1-x}As$ alloy layers was reported by Petroff et al.(21), although thermodynamic calculations have not predicted the existence of a miscibility gap in the phase diagram of $Ga_xAl_{1-x}As$ alloy layers (21). They reported a substrate-orientation dependence of the occurrence of the plate-like structures after using the (002) reflection DF imaging technique to examine cross-section samples grown on [110] and [100]-oriented GaAs substrates under identical conditions. A $Ga_{0.75}Al_{0.25}As$ layer grown on [110]-oriented GaAs exhibited plate-like structures (approximately parallel to the (110) layer surface) alternately rich in GaAs and in AlAs. The plate-like structures ranged in thickness from 1.5 to 30 nm and extended over distances of 1μm. Selected area TED patterns of $Ga_{0.75}Al_{0.25}As$/(110) GaAs indicated the single crystal character of the layer. They suggested that changes in Gibbs free energy introduced by an exchange reaction could result in a miscibility gap in the $Ga_xAl_{1-x}As$ phase diagram. However, they reported that LPE $Ga_xAl_{1-x}As$ layers deposited on (100) GaAs did not exhibit the plate-like structure and suggested that its absence was due to the LPE growth rates being 10 to 100 times higher than the MBE growth rates. It is known that surface diffusion coefficients during LPE growth are

several orders of magnitude higher than solid state bulk diffusion coefficients and several orders of magnitude lower than the diffusion rates of ~10^{-5} cm^2/s expected for atomic species in the liquid phase (22). However, Wang et al.(23) reported that such plate-like structures could be greatly reduced or eliminated by reducing the MBE growth rate from 1 to 0.3 μm/h.

The presence of an orientation-dependent surface phase diagram for $Ga_xAl_{1-x}As$ alloy layer has been discussed by Madhukar (24) and Van Vechten (25). Madhukar suggested that the formation of the plate-like structure is a result of a kinetic effect driven by the geometry of sites on the {110} surface and that one should consider the local energy release during bond formations. Van Vechten also introduced the concept of kink site saturation to explain a growth rate dependent plate-like structure during MBE growth of AlGaAs layers. It was predicted that homogeneous alloys could be grown on the {110} surfaces if either the growth rate was kept low enough or sufficient kink sites were nucleated so that kink site saturation is avoided. The concept of kinetic segregations employed by Madhukar (24) and Van Vechten (25) indicate that the plate-like structure observed in $Ga_{0.75}Al_{0.25}As$ layers is not associated with the thermodynamical intrinsic properties of the epitaxial layers, i.e. surface spinodal decomposition, but due to a composition modulation, which could be related to instabilities in growth conditions.

In the present work TEM and TED results indicated that the plate-like structure observed in $InAs_ySb_{1-y}$ is different from the cases described above. A large composition variation occurs along the [001] growth direction of the layers, with tetragonally distorted, anisotropic geometry platelets, of two very different composition cubic phases, possessing abrupt interfaces. These results suggest that the phenomena arising in $InAs_ySb_{1-y}$ can be attributed to the thermodynamical intrinsic properties of the layers.

Recently, Ipatova et al.(26) predicted that the formation of a modulated two-phase structure with a macroscopic period could occur in quaternary alloys by a process of spontaneous coherent phase separation. Their theoretical calculations were performed on the basis of the regular solution approximation, i.e the total free energy of the two phases is:

$$F_{TOTAL} = F_{CHEM} + F_{ELASTIC} \qquad (4\text{-}2)$$

where F_{CHEM} is the chemical free energy and $F_{ELASTIC}$ is the elastic free energy. They assumed that the chemical free energy term consists of the entropy of the ideal mixing (NTS_{MIX}) and the interatomic interaction (F_{INTER}). The main difference between the DLP model by Stringfellow (3) and their model is the following. In the DLP model, F_{INTER} depends only on the lattice parameter 'a' for a given composition and hence on the composition x and y. In their model, F_{INTER} depends on the chemical potential and the formation enthalpy. As compared to the DLP model, their model suggests that coherent phase separation must take place for all III-V quaternary alloys and also that the critical temperature is lower than the corresponding temperature for the bulk phase separation where $F_{ELASTIC} = 0$. They calculated the phase-separation diagram for $In_xGa_{1-x}As_yP_{1-y}$, but their determined critical temperature of 1275K is higher than that of Stringfellow (~1150K) (3) and comparable with those of de Cremoux (~1320K) (1) and Onabe (~1275K) (2). They considered that the phase separation occurs in the bulk layer starting at an 'inclusion', and develops to give a series of coherent phase-separated plates in the form of a superlattice, following the earlier treatment of Khachaturyan (27). They calculated the period d_{ps} of the superlattice using the equation derived by Khachaturyan (27):

$$d_{ps} = \sqrt{(\gamma_s L_x/(\varepsilon(\Delta a/a)^2))} \qquad (4\text{-}3)$$

where γ_s is surface tension, ε is the elastic modulus, $\Delta a/a$ is the elastic strain between platelets and L_x is the size of the inclusion at the boundary. For each growth temperature of 900, 1000, 1100 and 1200K, two possible sets of phase-separated alloy compositions were determined, e.g. at 1000K, either $In_{.19}Ga_{.81}As_{.46}P_{.54}$ and $In_{.49}Ga_{.51}As_{.15}P_{.85}$ or $In_{.60}Ga_{.40}As_{.84}P_{.16}$ and $In_{.90}Ga_{.10}As_{.48}P_{.52}$. The phase-separated plates formed a SLS and over the 900 to 1200K range the calculated strains ranged from 0.88 to 1.22. The periodicity d_{ps} calculated from the above equation and over the 900 to 1200K range gave

values of 330 to 510Å. However, in order to calculate d_{ps}, a value for L_x of 0.1μm was arbitrarily assumed.

The theory of Ipatova et al.(26) is based on the phase separation occurring in the bulk, but does not consider whether at these temperatures sufficient diffusion can occur for the separation to be completed. They term the separation 'spontaneous' because it occurs without changing the growth conditions to produce the individual phase-separated plates. However, it is not spontaneous in the sense of the present work on InAsSb epitaxial layers, where the separation does occur spontaneously at the growing layer surface. None of the decomposition theories reported so far (de Cremoux (1), Onabe (2), Stringfellow (3) and Ipatova et al.(26)) consider the thermodynamics or kinetics of the processes occurring at the layer surface. Hence, although these theories may be able to predict trends, they can not be expected to predict the details of the processes, e.g. dependence on growth temperature, rate and flux ratio, or to explain the complicated microstructures that arise as shown, for example, for InAsSb in Fig. 4. 17.

Self-diffusion coefficients have been measured for binary III-V compound semiconductors such as InAs and InSb in the bulk form at high temperatures (>500°C) using radioactive tracer techniques (28-30). For the present systems, in which the growth temperature lies between 295 and 400°C, values of the self-diffusion coefficients (D_O) of As and Sb in bulk InAsSb were extrapolated from the high temperature measurements for bulk InAs and InSb, and found to lie in the range $4x10^{-19}$ - $5x10^{-29}$ cm^2/s for a temperature of 296°C, i.e. extremely low values. The extrapolation may give rise to significant errors. Nonetheless, we apply these values to diffusion in the InAsSb layers. The diffusion distance χ can be expressed as (31):

$$\chi^2 = 2|D|t \qquad (4\text{-}4)$$

For an anneal time of 95 hours, this gives a diffusion distance of As and Sb in InAsSb of less than ~0.4Å. These values are too small for the platelets to be formed in the bulk InAsSb by diffusion occurring during growth or subsequent annealing. This is consistent with the phase

separation occurring at the growing surface. Furthermore, such a diffusion distance is insufficient to give rise to platelet interface broadening during post-growth annealing.

4-6 Optical properties of $InAs_ySb_{1-y}$ natural SLSs

Strained layer superlattices (SLSs) of $InAs_ySb_{1-y}$ are suitable for the fabrication of tunable infrared detector structures which operate at wavelengths of 8-12μm, a region of minimum atmospheric absorption (32). SLSs of $InAs_ySb_{1-y}$ have been successfully grown by MBE (32,33) and MOCVD(34), although structures reported to date have been limited to antimony rich alloys ($0<y<0.4$) with comparatively small interlayer strains.

TEM and TED investigations carried out in the present work revealed the occurrence of two phase-separated materials in $InAs_ySb_{1-y}$ layers, which have tetragonally distorted cubic structures, one with $c/a<1$ and other with $c/a>1$, as described in section 4-3-3. Conventionally grown SLSs have similar structures and we have therefore termed the present plate-like structure arising from phase separation a 'natural' SLS (n-SLS). The compositions of the n-SLS phases were typically $InAs_{0.33}Sb_{0.67}$ and $InAs_{0.69}Sb_{0.31}$ (IC237, Fig. 4.11), as given in Table 4.2. As y decreases from 1 to 0, the energy band gap of bulk $InAs_ySb_{1-y}$ progressively decreases, reaches a minimum at y~0.39, and then increases, i.e varies from ~0.36eV to ~0.18eV (Fig. 1.2). The band gap of InAsSb varies relatively slowly with composition (35), so that any lateral compositional variations across the plate-like structures will not result in large variations in wavelength response. Bulk $InAs_{0.69}Sb_{0.31}$ and $InAs_{0.33}Sb_{0.67}$ have wavelength cutoffs of ~7μm and ~9μm at room temperature, respectively.

Both SLSs and n-SLSs exhibit quantum confinement, causing the so-called wavelength blue-shift which moves the cut-off to higher energies and smaller wavelengths. Conversely, the strain associated with both SLSs and n-SLSs can cause the cut-off to move to lower energies and longer wavelengths. The cut-off that occurs in practice is a combination of these two effects.

The n-SLS structures contain biaxial tensile strain in the $InAs_{0.69}Sb_{0.31}$ layer and biaxial compressive strain in the $InAs_{0.33}Sb_{0.67}$ layer. The $InAs_{0.69}Sb_{0.31}$ layer under biaxial tensile stress exhibits a reduction of the bulk conduction band minimum energy and a splitting of the bulk light- and heavy-hole bands. The $InAs_{0.33}Sb_{0.67}$ layer under biaxial compressive stress exhibits an increase in the bulk conduction band minimum energy and a splitting (with opposite sign from the tensile case) of the bulk light- and heavy-hole bands. These strain-shifts lower the electron quantum well energy ($InAs_{0.33}Sb_{0.67}$) and raise the heavy-hole quantum well energy. Both effects tend to decrease the band gap of the SLS structure with respect to the unstrained case.

The $InAs_ySb_{1-y}$ SLS system has been developed by the international leading group of Sandia, U.S.A. (36,37), as the one with the capability of covering long-wavelength response due to built-in strain effects. Their theoretical work showed that strain effects were sufficient to achieve wavelength cut-offs of 12μm at 77K independent of the band offsets. Subsequent experimental work showed that $InAs_{0.13}Sb_{0.87}$ (260Å) /InSb (260Å) SLSs exhibit a cut-off corresponding to an absorption edge of ~114meV and a wavelength length of ~11μm, Fig. 4.20 (38). It was concluded that a range of structures with different InAs alloy contents in the layers and different layer thicknesses should exhibit 12μm cut-offs.

For comparison, SLSs of $InAs_{0.2}Sb_{0.8}$/InSb with equal well and barrier thicknesses of 105Å (IC258) and 270Å(IC273) were intentionally grown at Imperial College. The SLS growth parameters used here and optical response obtained were similar to those reported by Sandia (39). The photoresponse spectra showed cut-offs of ~144meV (IC258) and ~133meV (IC273). The larger of these two values is probably due to a larger blue-shift associated with the smaller width of the wells. However, the cut-off energies are higher and the wavelengths smaller than for the above Sandia SLSs.

The n-SLS structure (IC237) exhibits a 10K photoresponse at wavelengths out to 12.5μm, considerably longer than the measured cut-off of a homogeneous $InAs_{0.5}Sb_{0.5}$ control sample grown at Imperial College and also the Sandia SLSs, Fig. 4.20. The cut-off of our control sample is in good agreement with the expected cut-off of 7.85μm calculated using the previously reported 77K absorption data (40) from homogeneous $InAs_{0.5}Sb_{0.5}$

Figure 4.20

Optical response spectra of the n-SLSs, the Sandia SLSs and a homogeneous control layer. The n-SLSs exhibits a 10K photoresponse at wavelengths out to 12.5μm, considerably longer than the measured cut-off of a homogeneous $InAs_{0.5}Sb_{0.5}$ control layer and also the Sandia SLSs. The arrows mark the expected bandedge position of the homogeneous alloy (i) and (ii) from photoluminescence measured by Fang et al.(39).

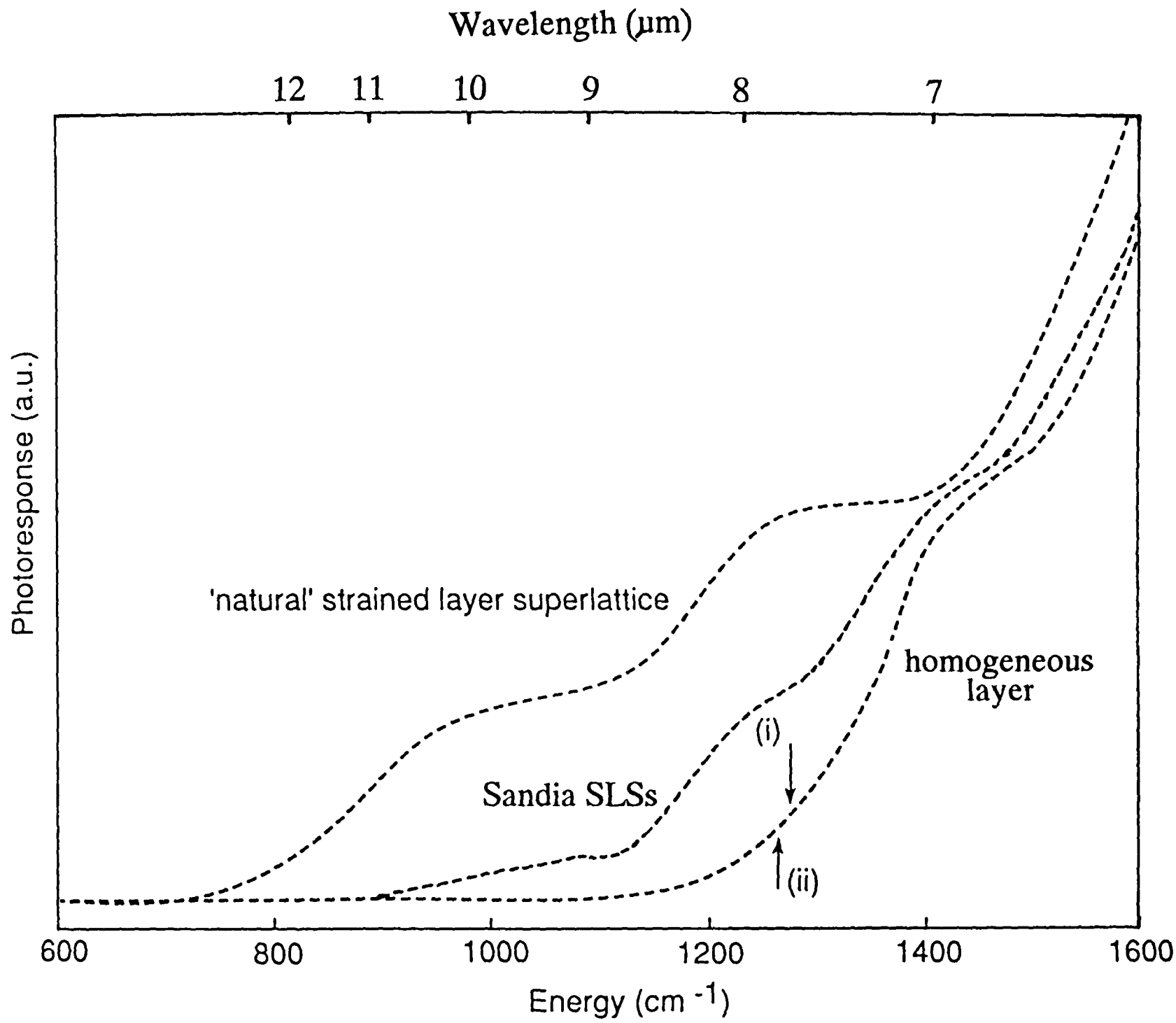
Wavelength (μm)
12
11
10
9
8
7
Photoresponse (a.u.)
'natural' strained layer superlattice
homogeneous layer
(i)
Sandia SLSs
(ii)
600
800
1000
1200
1400
1600
Energy (cm -1)

Fig. 4.20

alloy layers shifted by the known temperature dependencies of the InAs and InSb bandgap (41) (arrow (i) in Fig. 4.20), and the 10K cut-off of 7.90μm recently reported in photoluminescence studies (41) of a homogeneous $InAs_{0.5}Sb_{0.5}$ layer grown by MOCVD (arrow (ii) in Fig. 4.20). The longer wavelength cut-off for the n-SLS suggests that this may be a simple means of producing photodetector structures for use in the technologically important 8-14μm region.

Comparison of the SLSs conventionally grown by Sandia and our n-SLSs shows the following. For the Sandia specimens the composition changes on going from individual layer to individual layer (Δy) were less than 0.2. However, for the n-SLSs, the corresponding change of $\Delta y \sim 0.4$ is much greater. Furthermore, the amount of tetragonal distortion of the individual layers is also much larger than that of the Sandia SLSs. The Sandia $InAs_{0.2}Sb_{0.8}$/InSb SLSs have equal well and barrier thicknesses of ~100-200Å. Our n-SLSs have well and barrier thicknesses of ~300-500Å. The individual layer thicknesses of the n-SLSs are much larger than those of the Sandia SLSs, and so the former have a smaller quantum confinement effect, i.e. a smaller blue-shift. An important feature of the n-SLSs is that although the individual layers are relatively thick, few interface dislocations form and so the tetragonal distortion is largely maintained, and this is considered to contribute to the extended wavelength response. This indicates that our n-SLSs could provide a much greater range of optical properties, leading to wider applications of practical devices. In addition, the n-SLSs can be obtained without mechanical switching procedures for the source elements during layer growth.

4-7 Conclusion

From the detailed TEM and TED examinations described in this chapter, it is concluded that phase separation occurs at the growing surface of MBE $InAs_ySb_{1-y}$ layers grown on (001) GaAs substrates at temperatures <400°C. Phase separation resulted in two tetragonally distorted plate-like structures having approximate compositions $InAs_{0.3}Sb_{0.7}$ and $InAs_{0.7}Sb_{0.3}$. Phase separation was dependent on the growth temperature and

composition. The plate-like structure progressively increased in size as the growth temperature increased from 295 to 400°C. A particularly good quality plate-like structure was obtained when grown at 340°C using equally balanced fluxes of As and Sb atoms. These plate-like structures were termed 'natural' strained layer superlattices (n-SLSs). In order to interpret the phase separation behaviour, a model based on the presence of a miscibility gap was proposed using island and lateral growth mechanisms. Optical properties of the n-SLSs were good with wavelength cut-offs greater than 12μm, better than analogous conventional SLSs. It is suggested that the growth of these n-SLSs is important because the growth technique is simple and the n-SLSs have potential application to improved performance infra-red detectors and high-speed opto-electronic devices.

REFERENCES-CHAPTER 4

1. B. de Cremoux, J. de Physique Colleg. C5, Suppl. **No12**, (1982) C5.
2. K.Onabe, Jpn. J. Appl. Phys. **21**, (1982) 964.
3. G.B. Stringfellow, J. Appl. Phys. **54**, (1983) 404.
4. K. Ishida, T. Nomura, H. Tokunaga, H. Ohtani and T. Nishizawa, J. Less-Common Matals, **155** (1989) 193.
5. R.M. Biefeld, J. Cryst. Growth **75**, (1986) 255.
6. P.K. Chiang and S.M. Bedair, Appl. Phys. Lett. **46** (1985) 383.
7. M.Y. Yen, B.F. Levine, L.G. Bethea, K.K. Choi and A.Y. Cho, Appl. Phys. Lett. **50** (1987) 927.
8. J.H. Kim, D. Yang, Y-C. Chen and P. Bhattacharya, J. Cryst. Growth **111** (1991) 633.
9. J.I. Chyi, S. kalem, N.S. Kumar, C.W. Litton and H. Morkoc, Appl. Phys. Lett. **53** (1988) 1092.
10. J.B. Webb and C. Halpin, Appl. Phys. Lett. **47** (1985) 831.
11. P. M, Petroff, J. Vac. Sci. Technol. **14** (1977) 473.
12. M. Hockly, D.Phil. Thesis, Oxford University, 1983.
13. C-A Chang, D. Rudeke, L.L. Chang and L. Esaki, Appl. Phy. Lett. **31** (1974) 4435.
14. Y. Kim, A. Ourmazd, R. Malik and J. Rentschler, MRS symp. Proc. **159** (1990) 351.
15. M. Kawabe and T. Sugaya, Jpn. J. Appl. Phys. **28** (1989) L1077
16. K. Ohta, T. Kojima and T. Nakagawa, J. Crystal Growth **95** (1989) 71.
17. Y. Horikoshi, H. Yamaguchi, F. Briones and M. Kawashima, J. Crsyt. Growth **105** (1990) 326.
18. M.D. Pashley, Phys. Rev. B **40** (1989) 10481.
19. T. Isu, M. Hata, A. Watanabe and Y. Katayama, J. Vac. Sci. Technol. **B7** (1989) 714.
20. P.M. Petroff, A.Y. Cho, F.K. Reinhart, A.C. Gossard and W.Wiegmann, Phys. Rev. Lett. **48** (1982) 170.
21. H.C. Casey Jr. and M.B. Panish, Heterostructure lasers (Academic, New York, 1978) p71.

22. G.B. Stringfellow, Rep. Prog. Phys. **45** (1982) 469.

23 W.I. Wang, T.S. Kuan, J.S. Tsang, L.L. Chang and E. Esaki, Bull. Am. Phys. Soc. **29** (1984) 239.

24. A. Madhukar, Surf. Sci. **132** (1983) 344.

25. J.A. Van Vechten, J. Cryst. Growth **71** (1985) 326.

26. I.P. Ipatova, V.A. Shchukin, V.G. Malyshkin, A. Yu. Maslov and E. Anastassakis, Solid State Comm. **78** (1991) 19.

27. A.G. Khachaturyan, Theory of structural transformations in solids, John Wiley and Sons, N.Y. (1983).

28. F.H. Eisen and C.E. Birchenall, Acta met. **5** (1957) 265.

29. Measurement quoted by V.M. Vorob'ev, V.A. Murov'ev and V.A. Panteleev, Sov. Phys. - Solid State **23** (1981) 653.

30. D.L. Kendall and R.A. Huggins, J. Appl. Phys. **40** (1969) 2750.

31. J.W. Cahn, Trans. of the Metall. Soc. of AIME, **242** (1968) 166.

32. G.C. Osbourn, Semicon. Sci. Technol. **5** (1990) S5.

33. L.R. Dawson, J. Vac. Sci. Technol. **B4** (1986) 598.

34. S.R. Kurtz, R.M. Biefield and T.E. Zipperian, Semicon. Sci. Technol. **5** (1990) S24.

35. D.L. Smith, T.C. McGill and J.N. Schulman, Appl. Phys. Lett. **43** (1983) 14.

36. G.C. Osbourn, J. Vac. Sci. Technol. **B2** (1984) 176.

37. G.C. Osbourn, J. Appl. Phys. **53** (1982) 1586.

38. S.R. Kurtz, L.R. Dawson, R.M. Biefeld and G.C. Osbourn, Proc. SPIE **930** (1988) 101.

39. S.R. Kurtz, G.C. Osbourn, R.M. Biefeld and S.R. Lee, Appl. Phys. Lett. **53** (1988) 216.

40. S.R. Kurtz, G.C. Osbourn, R.M. Biefeld, L.R. Dawson and H.J. Stein, Appl. Phys. Lett. **52** (1988) 831.

41. Z.M. Fang, K.Y. Ma, D.H. Jaw, R.H. Cohen and G.B. Stringfellow, J. Appl. Phys. **67** (1982) 7038.

CHAPTER 5

ALLOY CLUSTERING IN $In_xGa_{1-x}As$, InP_ySb_{1-y} and GaP_ySb_{1-y} COMPOUND SEMICONDUCTORS

5-1 Introduction

Epitaxial layers of III-V compound semiconductors are of considerable importance for a wide range of applications in optoelectronic devices such as laser diodes and photodetectors. Growth of uniform single crystal epitaxial layers of ternary and quaternary III-V semiconductors is sometimes difficult for certain alloy compositions and temperatures, owing to the presence of miscibility gaps (1-4). However, non-equilibrium growth techniques such as MBE and MOCVD have been successfully employed to grow good quality epitaxial layers of such semiconductors. Many authors (5-15) using electron microscopy have observed a fine scale modulated contrast attributed to alloy clustering possibly occurring as a result of spinodal decomposition in epitaxial III-V semiconductor layers. It was reported that there are two different kinds of modulated structures, one giving a coarse scale tweed-like contrast with a periodicity of 100-200nm, and the other a quasi-periodic fine scale contrast with a periodicity of the order of 10nm. Considerable experimental and theoretical evidence (13, 16-19) has shown that such alloy clustering can significantly affect both the electrical and luminescent properties of these materials, as described in chapter 2. For example, Blood and Grassie (19) reported calculations based on previously published structural data, showing that the conduction band in GaInAsP alloys has a spatial variation with an amplitude of ~0.08 eV, and that such a variation could result from partial segregation into clusters. The effect of alloy clustering on the photoluminescence properties of GaInP was also addressed and it was argued that alloy clustering due to spinodal decomposition during the growth process may have an adverse effect on both the electrical and optical properties of the layers (13,19). Therefore, it is important to understand the structures associated with alloy clustering in III-V semiconductor layers.

In this chapter, we present the results obtained from detailed TEM, TED and HREM examinations of MOCVD $In_xGa_{1-x}As$, InP_ySb_{1-y} and GaP_ySb_{1-y} epitaxial layers, which showed the occurrence of fine scale contrast, but no coarse scale tweed-like contrast. We present for the first time results which we interpret as the coexistence of a fine scale modulated contrast due to alloy clustering and a fine scale mottled contrast associated with

static atomic displacements in $In_xGa_{1-x}As$ layers. In addition to a fine scale modulated contrast, a fine needle-like contrast occurred in InP_ySb_{1-y} and GaP_ySb_{1-y} layers, which may be associated with surface reconstruction present during layer growth. For GaP_ySb_{1-y} layers, characteristic diffuse scattering features observed in TED patterns are described and compared with computer simulated results.

5-2 Alloy clustering in $In_xGa_{1-x}As$ layers

5-2-1 Experimental

$In_{0.53}Ga_{0.47}As$ epitaxial layers were grown on (001) InP substrates by atmospheric pressure MOCVD, using trimethylgallium (TMG), trimethylindium (TMI), arsine and phosphine as sources. The horizontal MOCVD reactor and growth conditions have previously been described (14). Single layers were grown of thickness 0.3μm-2μm. The growth temperature range investigated was 500-717°C and the growth rates were 0.2 nm/s, 0.95 nm/s and 2.0 nm/s. A layer grown at 550°C was annealed for 91 hours at 550°C and a layer grown at 717°C was annealed for 744 hours at 600°C. The annealing treatment was carried out with the specimens in sealed quartz ampoules evacuated to $< 10^{-6}$ Torr. X-ray diffraction was used to determine the lattice parameters and hence the composition of the layers. Details of all the samples are given in Table 5.1.

5-2-2 TEM and TED analyses

(001) plan-view TEM examinations were carried out using standard two-beam DF conditions with the strain sensitive {220} and {400} reflections. Such micrographs of the layer grown at 596°C with 0.95nm/s are shown in Fig. 5.1, which reveal a fine scale modulated contrast on a scale of ~8-20nm, but the absence of a coarse scale tweed-like contrast. Two sets of a fine scale modulated contrast consisting of elongated nodules oriented along the [100] and [010] directions occur when using either the (220) or ($\bar{2}$20)

Table 5.1 Epitaxial $In_xGa_{1-x}As$ MOCVD layers

Sample number ($In_{0.53}Ga_{0.47}As$)	Growth temp. (°C)	Growth rate (nm/sec)	annealing treatment (°C)/hour
6460	500	0.2	-
6462	550	0.2	-
6461	600	0.2	-
6464	650	0.2	-
6459	700	0.2	-
6316	500	0.95	-
6313	550	0.95	-
6313	550	0.95	550/91
5489	596	0.95	-
6315	600	0.95	-
6312	650	0.95	-
6317	700	0.95	-
5488	717	0.95	-
5488	717	0.95	600/744
6466	550	2.0	-
6467	600	2.0	-
6468	650	2.0	-

Figure 5.1

Plan-view {220} and {400} TEM DF micrographs from $In_xGa_{1-x}As$ (x=0.53) MOCVD layer grown at 596°C using 0.95nm/s, showing a fine scale modulated contrast on a scale of ~8-20nm, which is elongated along the <100> directions.

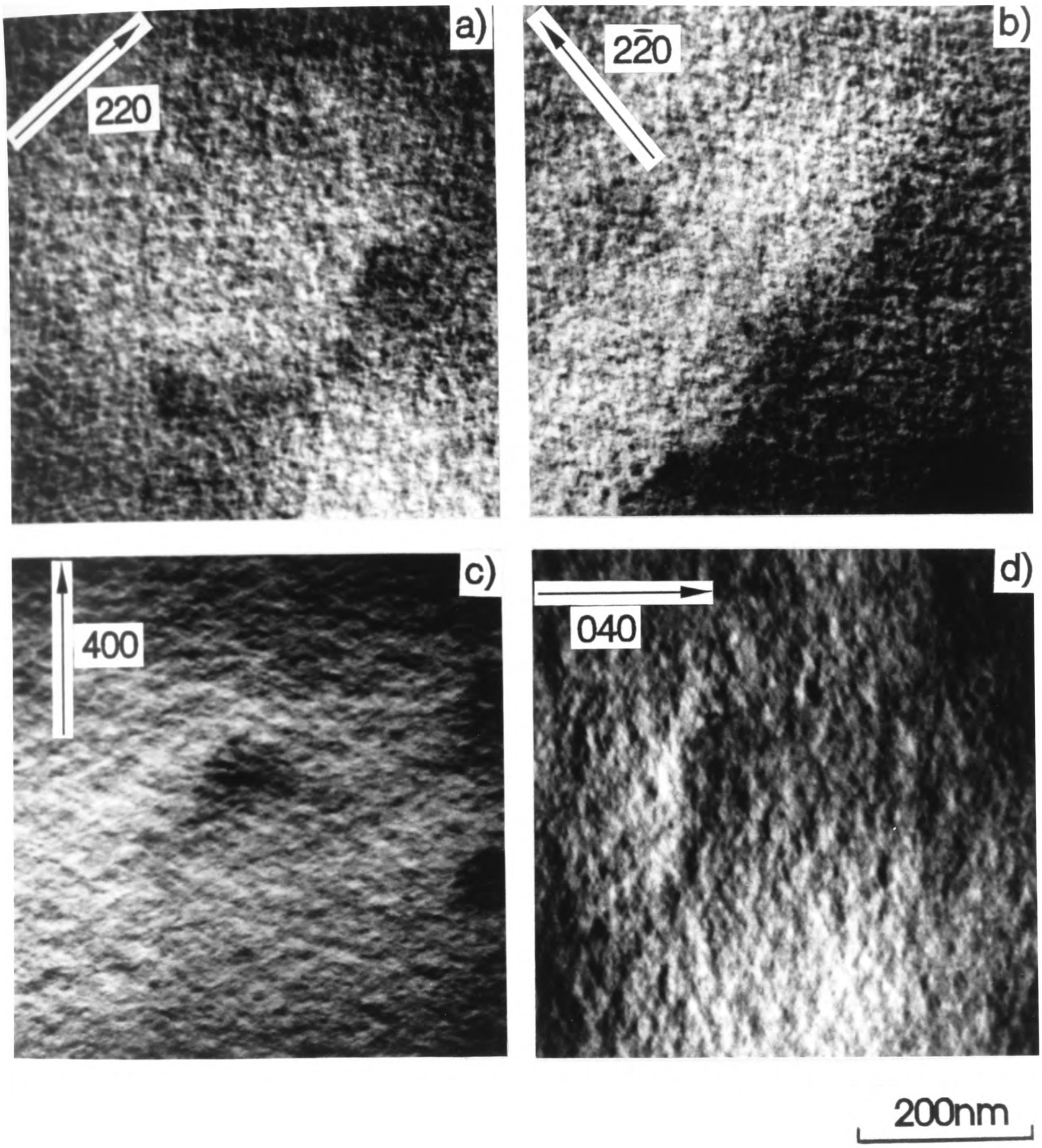

Fig. 5.1

reflections. For the (400) reflection, only a fine scale modulated contrast elongated perpendicular to the **g** vector occurred, and for the (040) reflection, a similar behaviour occurred. These results indicate that the directions of principal strain associated with the fine scale modulated contrast are along the [100] and [010] directions. However, for the {220} and {400} reflections, all the micrographs showed in addition a fine scale mottled (speckle) contrast on a scale of ~4-5nm. This fine scale mottled contrast showed no preferred orientations such as <100> directions, which will be discussed in detail in section 5-2-4.

The absence of a coarse scale tweed-like contrast in an InGaAs layer grown at 596°C is expected. Thus, Norman and Booker (9,10) and Norman (15), examining InGaAs layers, observed the coarse scale tweed-like contrast for MBE layers grown at 560°C and LPE layers grown at 585°C, but not for VPE or MOCVD layers grown at 650°C. Growth at 560 and 585°C for $In_{0.53}Ga_{0.47}As$ is within the spinodal decomposition region, while growth at 650°C is outside. The coarse scale tweed-like contrast observed was aligned along the [100] and [010] directions on a scale of ~150nm. From the TEM results, they suggested that the coarse scale tweed-like contrast originates from the presence of quasi-periodic strain fields present along the [100] and [010] directions of the crystal due to spinodal decomposition (5,9). Hénoc et al.(5) have employed combined STEM/EDX analysis to directly link the coarse scale tweed-like contrast to a compositional variation in LPE $In_xGa_{1-x}As_yP_{1-y}$. They attributed the coarse scale tweed-like contrast to a compositional modulation associated with spinodal decomposition, which is developed by the rapid diffusion of elements along the liquid-solid interface (5).

In the present work, TED examinations were performed on (001) plan-view samples of InGaAs layers. The TED patterns showed the fundamental spots expected for the zinc-blende crystal structure, and in addition lines of diffuse intensity running parallel to the [110] and $[\bar{1}10]$ directions, which were located slightly away from the fundamental spots, as will be discussed in detail later. No satellite spots associated with the fundamental spots were observed for any of the layers, such as those reported by Norman and Booker (9) and Norman (15) and shown to be related to the fine scale modulated contrast.

<110> cross-section DF TEM images of the layer grown at 600°C with a growth rate of 2.0nm/s taken with the (220), $(\bar{2}\,\bar{2}\,0)$, $(2\,\bar{2}\,0)$ and (004) reflections are shown in Fig. 5.2. The {220} DF micrographs showed a strong fine scale modulated contrast with a periodicity of 8-20nm and which has a preferred orientation. For the (220) reflection, the fine scale modulated contrast was elongated along the [001] growth direction perpendicular to the **g**-vector. The contrast is visible throughout the whole epitaxial layer, from the region near the layer/substrate interface to the layer surface. The effect of reversing **g** on the fine scale modulated contrast was determined by using the $(\bar{2}\,\bar{2}\,0)$ and (220) reflections in the $(\bar{1}\,10)$ cross-section of the same layer (Fig. 5.2(a) and (b)). This results in no change of the appearance of the fine scale modulated contrast, but does lead to a changing of the modulated contrast from bright to dark and vice versa for TEM DF micrographs. The $(2\,\bar{2}\,0)$ TEM DF obtained from the (110) cross-section of the same layer shows a similar fine scale modulated contrast to the (220) DF micrograph obtained from the $(\bar{1}\,10)$ cross-section. However, the fine scale modulated contrast disappears when imaged using the (004) reflection, as shown in Fig. 5.2(d). A random and ill-defined back ground contrast is visible, which may be associated with a random fluctuation in the concentration of the mixed Group III elements in the layer (20). These results indicate that the directions of principal strain associated with the composition modulation lie in the growth plane along the [100] and [010] directions and not in the [001] growth direction, i.e. the morphology of the spinodal decomposition is two dimensional (13,15).

All of the layers listed in Table 5.1 were examined by TEM, mostly with both plan-view and cross-section specimens. The contrasts observed for all of these specimens showed the same general trends as those illustrated in the plan-view micrographs of Fig. 5.1 and the cross-section micrographs of Fig. 5.2. For the {220} reflections, all the micrographs showed in addition a fine scale mottled (speckle) contrast on a scale of ~4-5nm. This fine scale mottled contrast showed no preferred orientations such as <100> directions, which will be discussed in detail in section 5-2-4.

Effects of growth conditions such as substrate temperature and growth rate were investigated by the <110> cross-section DF TEM technique using the {220} reflections.

Figure 5.2

Cross-section TEM DF micrographs from $In_xGa_{1-x}As$ (x=0.53) MOCVD layer grown at 600°C using 2.0nm/s. (a) ($\bar{2}\,\bar{2}\,0$) and (b) (220) micrographs from same area of the layer. Modulated contrast is reversed (e.g. see area indicated by the arrow) as the sign of reflection is changed. (c) ($2\,\bar{2}\,0$) micrograph, showing a fine scale modulated contrast. (d) (004) micrograph, showing the absence of a fine scale modulated contrast.

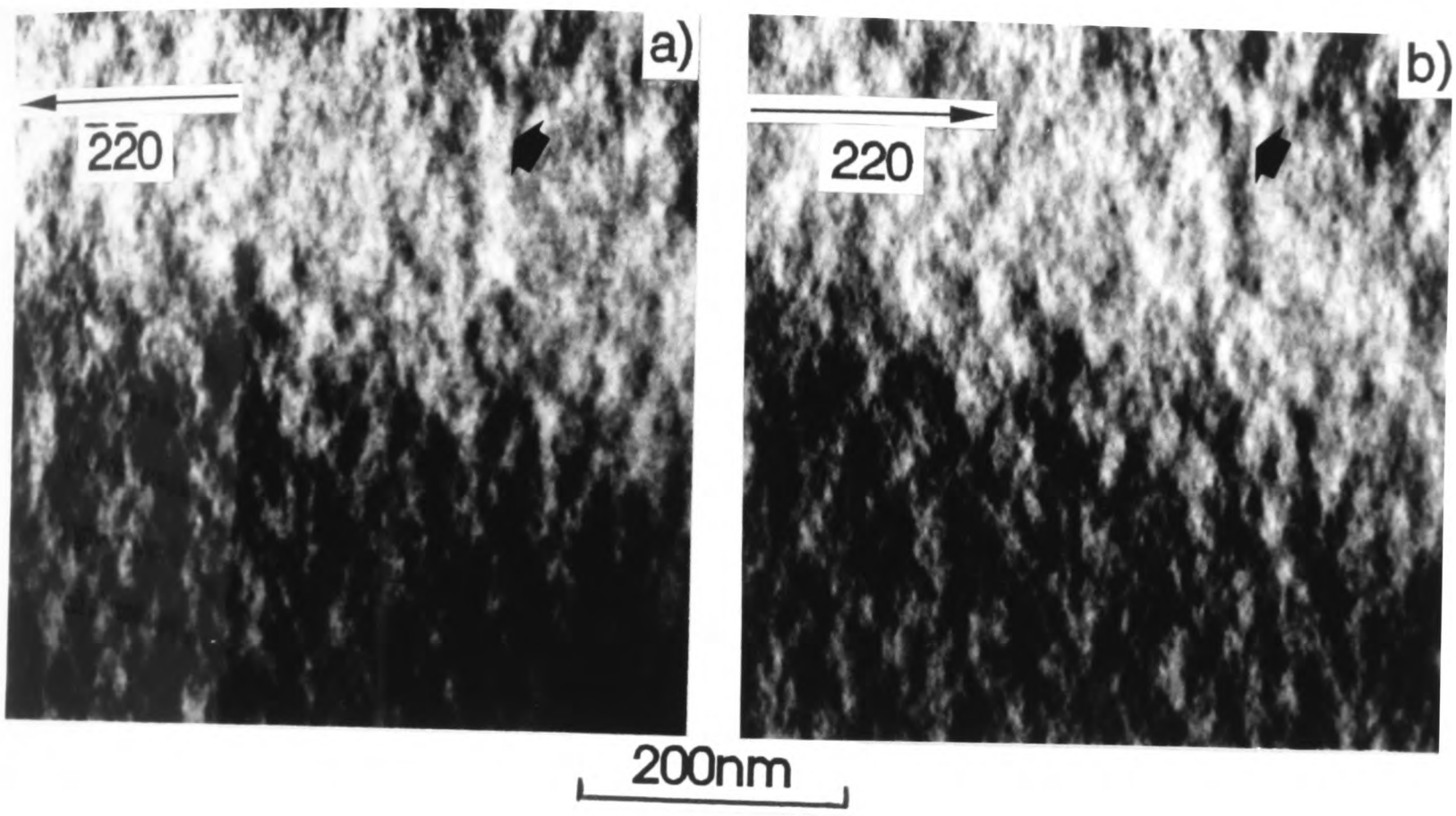

Fig. 5.2

Fig. 5.3(a), (b), (c) and (d) show micrographs of the layers grown at 550, 600, 650 and 700°C with a growth rate of 0.2nm/s, respectively. All the micrographs were taken at the exact Bragg condition. All the layers show a fine scale modulated contrast on a scale of ~8-20nm, which is elongated along the [001] growth direction. The wavelength (dark to dark) of the fine scale modulated structure along the $[\bar{1}10]$ direction was ~8-10nm in the layer grown at 550°C, ~10-15nm at 600°C, ~10-20nm at 650°C and ~10-20nm at 700°C, indicating a coarsening of the clustering as the temperature increased.

Effects of growth rate on the fine scale modulated contrast were investigated by examining the layers grown at 550 and 650°C with the fast growth rate of 2.0nm/s and the slow growth rate of 0.2nm/s. The results obtained from (220) TEM DF micrographs (not shown) indicate that the wavelength of the fine scale modulated contrast observed from the layer grown at 550°C with the fast growth rate is smaller than that of the layer grown at the same substrate temperature with the slow growth rate. No significant difference was detected in the layers grown at 650°C with fast and slow growth rates. These TEM results suggest that, for a growth temperature of 550°C, the slow growth rate enables deposited atoms to have more time to reach favourable sites, so resulting in a coarsening of the wavelength of the alloy clustering.

The fine scale modulated contrast was characterised by weak beam imaging techniques using **g**(220)-3**g** and **g**(220)-4**g** conditions on (001) plan-view specimens. Examination of five layers showed only a strong randomly distributed fine scale speckle contrast with no preferred orientation. The wavelength of the fine scale speckle contrast obtained using **g**(220)-3**g** (~4nm) (e.g. see Fig. 5.7(a)) was slightly larger than that using **g**(220)-4**g** (~3.5nm).

Annealing experiments were performed to investigate further the origin of the fine scale modulated contrast. The aim of these experiments was to explore the possibility of any development or degradation of the characteristic fine scale modulated contrast occurring in the InGaAs layers during thermal treatment. The layers grown at 550 and 717°C with a growth rate of 0.95nm/s were annealed at 550°C for 91 hours and 600°C for 744 hours, respectively. Orthogonal <110> cross-section TEM specimens were prepared of the layer

Figure 5.3

Cross-section ($\bar{2}20$) TEM DF micrographs from InGaAs MOCVD layers grown at (a) 550°C, (b) 600°C, (c) 650°C and (d) 700°C using 0.2nm/s. All the layers exhibit a fine scale modulated contrast. Note increase of the wavelength of the modulated contrast along the [110] direction as the growth temperature increases.

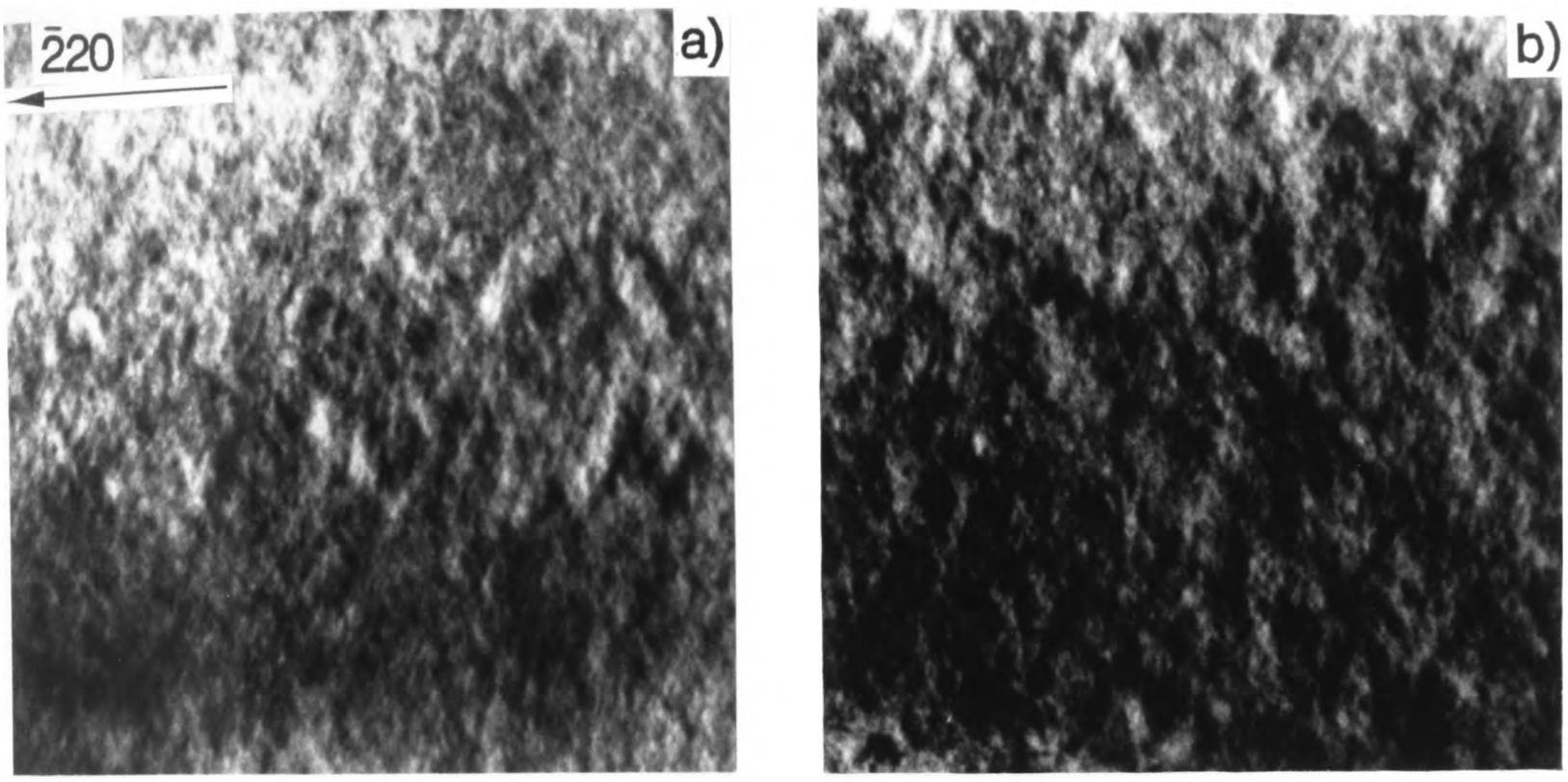

Fig. 5.3

grown at 550°C and annealed at 550°C. TEM (220) DF micrographs (not shown) revealed no significant difference between the as-grown and annealed layers. In both the specimens, a fine scale modulated contrast (~8-10nm) was visible and no change in the wavelength of the fine scale contrast was detected, which is consistent with the calculation of diffusion distances at the annealing temperature, i.e. the low bulk diffusion coefficient does not allow time for atoms to move to favourable sites.

{110} cross-section and (001) plan-view TEM specimens were also prepared of the layer grown at 717°C and annealed at 600°C. In Fig.5.4 are shown cross-section TEM (220) DF micrographs obtained from the middle regions of the as-grown and annealed specimens. The as-grown specimen showed a strong fine scale modulated contrast elongated along the [001] growth direction perpendicular to the **g**220 vector of wavelength ~10-20nm (Fig.5.4(a)). The annealed specimen showed an ill-defined mottled contrast with no preferred orientation (Fig.5.4(b)).

TED investigations were carried out on chemically thinned (001) plan-view specimens of both the as-grown and annealed InGaAs epitaxial layers. In Fig. 5.5(a) is shown the [001] TED pattern of the as-grown layer. Lines of diffuse intensity are visible parallel to the [110] and $[\bar{1}10]$ directions, which pass close to, but some distance away from, all the zinc-blende type main spots hk0 (such that h+k=4n, where n is an integer). No diffuse lines pass close to the central 000 spot (Fig. 5.5(c)). Satellite-like intensity appears to occur near the diffraction spots, i.e. the zinc-blende type spots <h00> are elongated along the <100> directions. The satellite-like spots are attributed to the intersection of [110]-oriented diffuse lines with $[\bar{1}10]$-oriented diffuse lines in reciprocal space. For the [001] pole TED pattern obtained from the annealed specimen, Fig. 5.5(b), the characteristic features were closely similar. The reciprocal distance between the maximum of intensity of the line $[\bar{1}10]_p$ and spots pp0 is nearly independent of the order p and is about ~3-5% of the modulus **g**220 of the 220 reciprocal vector. These results are in general similar to those reported by Glas et al. (21,24) for InGaAs and InGaAsP layers and Fig. 5.5(c) is taken from Glas et al.(24). Narayanan and Copley (25), on the other hand, examining GaAs, presented similar [110]-oriented diffuse intensity lines but in this case they passed through the main zinc-blende type

Figure 5.4

Cross-section {220} TEM DF micrographs from (a) the as-grown and (b) annealed samples of InGaAs MOCVD layer grown at 717°C using 0.95nm/s. The as-grown sample shows a fine scale modulated contrast, whereas the annealed sample shows an ill-defined mottled contrast.

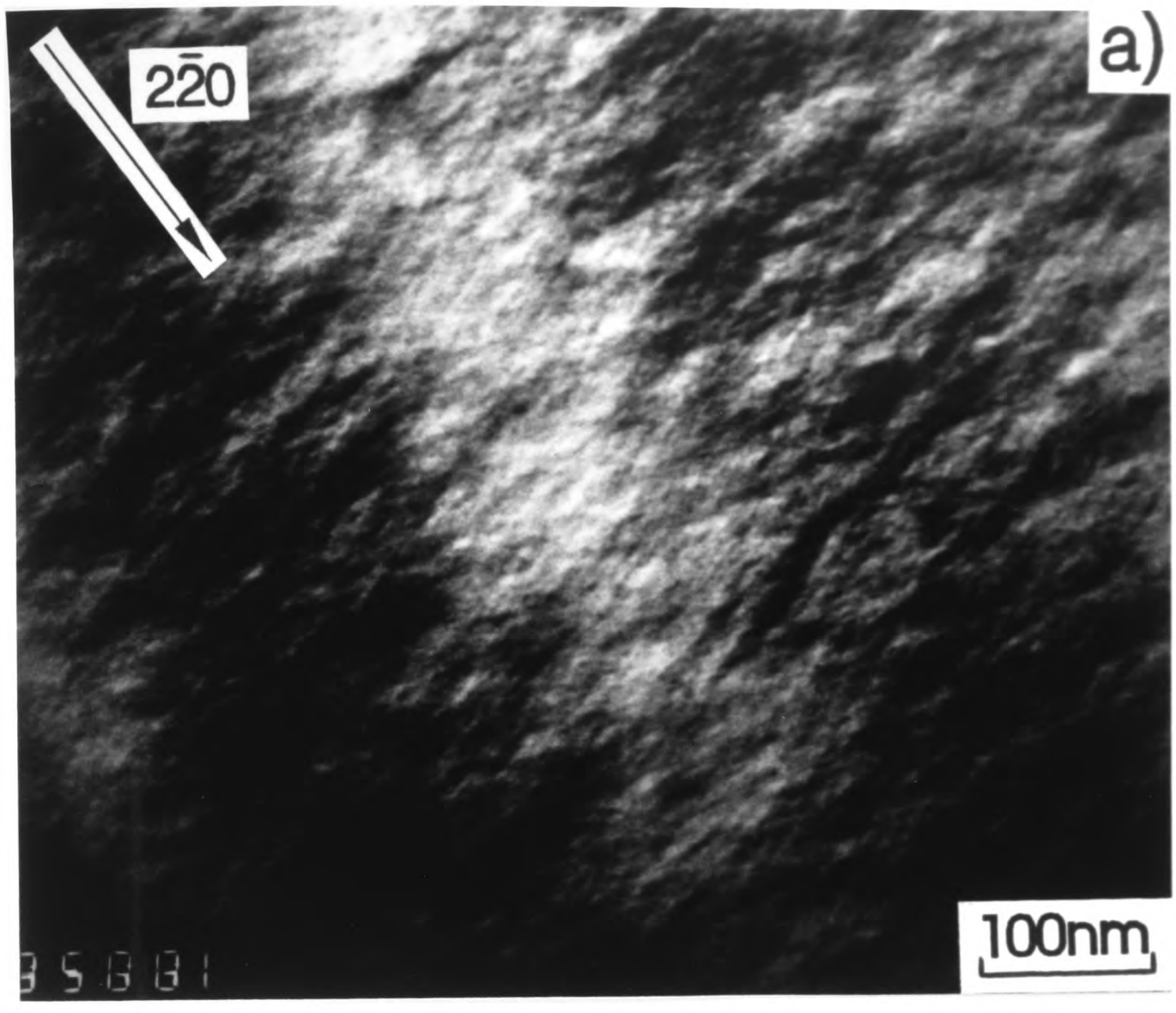

Fig. 5.4

Figure 5.5

Plan-view [001] TED patterns from (a) the as-grown and (b) annealed samples of the InGaAs MOCVD layer grown at 717°C using 0.95nm/s. <110> oriented diffuse intensity and elongation of <h00> spots are visible in both patterns.

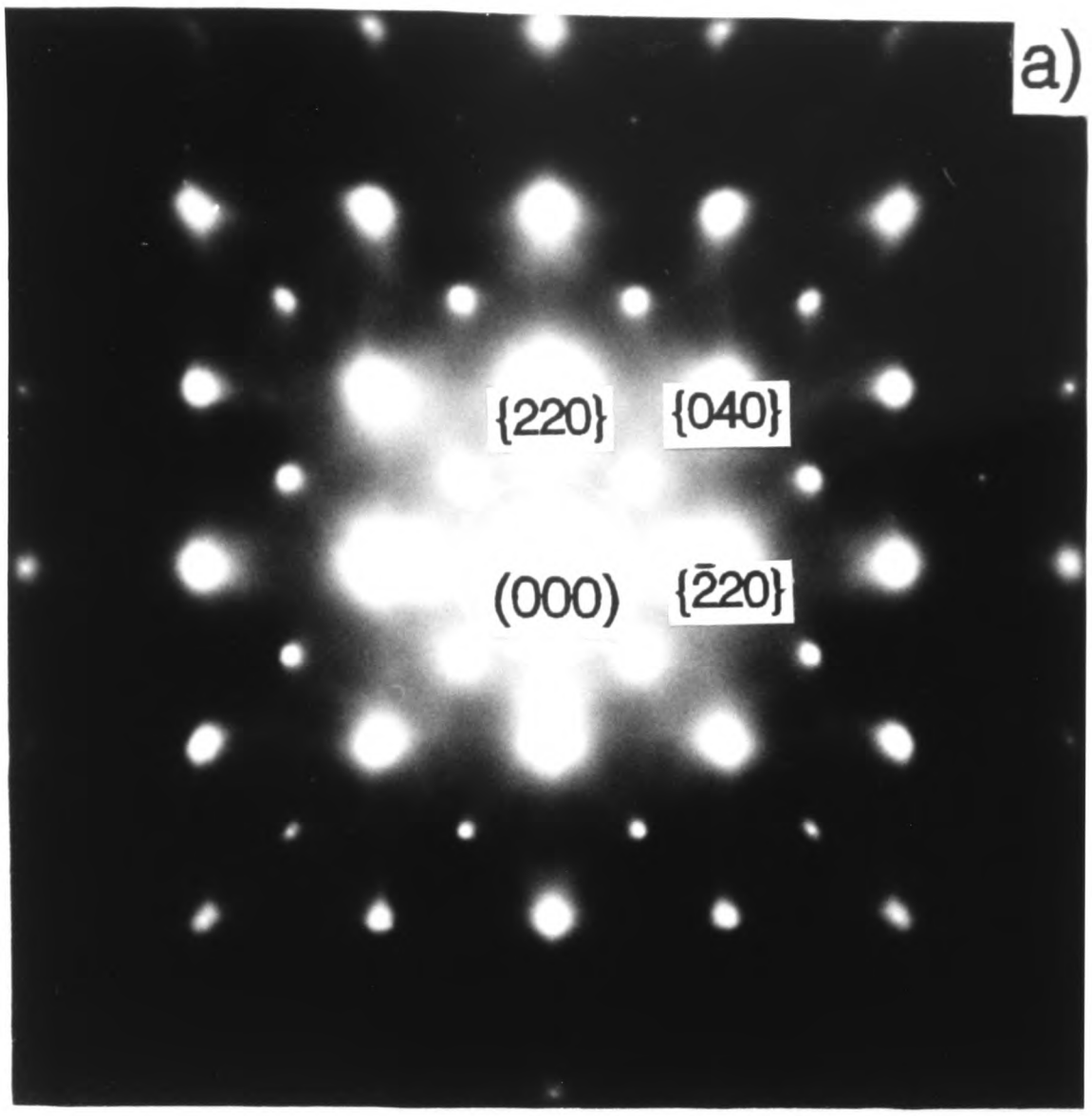

Fig. 5.5

Figure 5.5

(c) Schematic diagram (ref.20) of the most intense portions of the <110> lines of diffuse intensity present in the [001] TED patterns of the as-grown and annealed samples of the InGaAs MOCVD layer grown at 717°C using 0.95nm/s.

c)

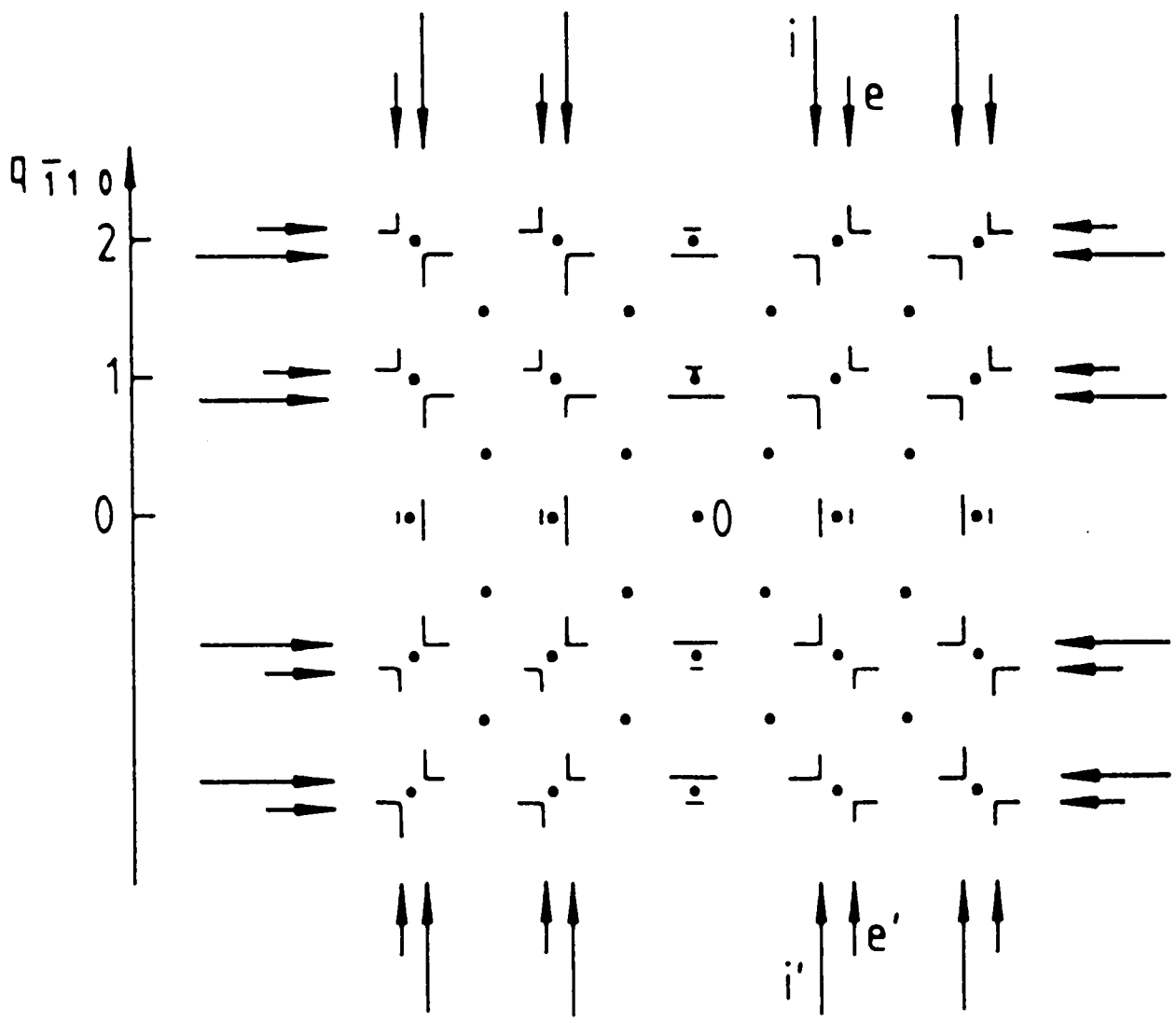

Fig. 5.5

spots and they attributed this phenomenon to thermal scattering of electrons due to phonons. However, in the present work, the diffuse intensity lines were located slightly away from the zinc-blende structure diffraction spots for the $In_xGa_{1-x}As$ layers indicating that this phenomenon is different from the results reported by Narayanan and Copley (25). Instead, Glas (20) and Glas et al. (21) suggested that the InGaAs lines could be related to static atomic displacements from the average lattice, which will be discussed in more detail in section 5-2-4 and 5-4-2.

Fig. 5.6 shows plan-view TEM (220) DF micrographs obtained from the as-grown and annealed specimens. The as-grown specimen, Fig. 5.6(a), showed a fine scale modulated contrast with a periodicity of ~10-20nm. The annealed specimen showed no evidence for a fine scale modulated contrast associated with alloy clustering, but revealed an ill-defined mottled contrast with no preferred orientation and a characteristic scale of less than ~5nm. This observation is consistent with the results obtained from cross-section TEM investigations.

In Fig. 5.7 are shown **g**(220)-3**g** weak beam images, which were taken from the same regions of Fig. 5.6. For the as-grown sample, Fig. 5.7(a), the micrograph shows quite different characteristic features, as compared to the **g**(220) DF image, Fig. 5.6(a). First, the fine scale modulated contrast which was attributed to a composition modulation due to alloy clustering disappeared. Secondly, a characteristic fine scale speckle contrast was visible on a scale of ~4nm with no preferred orientations but this fine scale speckle contrast appears to be randomly elongated. For the annealed sample, Fig. 5.7(b), a similar fine scale speckle contrast was visible on a scale of ~4nm but the morphology of the speckle contrast appears to be slightly different from that of the as-grown specimen.

In summary, plan-view and cross-section TEM and TED examinations were employed to characterise the fine structure of InGaAs layers grown at temperatures ranging from 500 to 717°C. The results obtained showed that there exists a fine scale modulated contrast (~8-20nm) elongated along the [100] and [010] directions, which is associated with alloy clustering possibly occurring as a result of spinodal decomposition. The wavelength of the fine scale modulated contrast increases with growth temperature. The results also

Figure 5.6

Plan-view (220) TEM DF micrographs from (a) the as-grown and (b) annealed samples of the InGaAs MOCVD layer grown at 717°C using 0.95nm/s. The as-grown sample exhibits a fine scale modulated contrast, whereas the annealed sample shows no evidence for a fine scale modulated contrast, but it does show a fine mottled contrast.

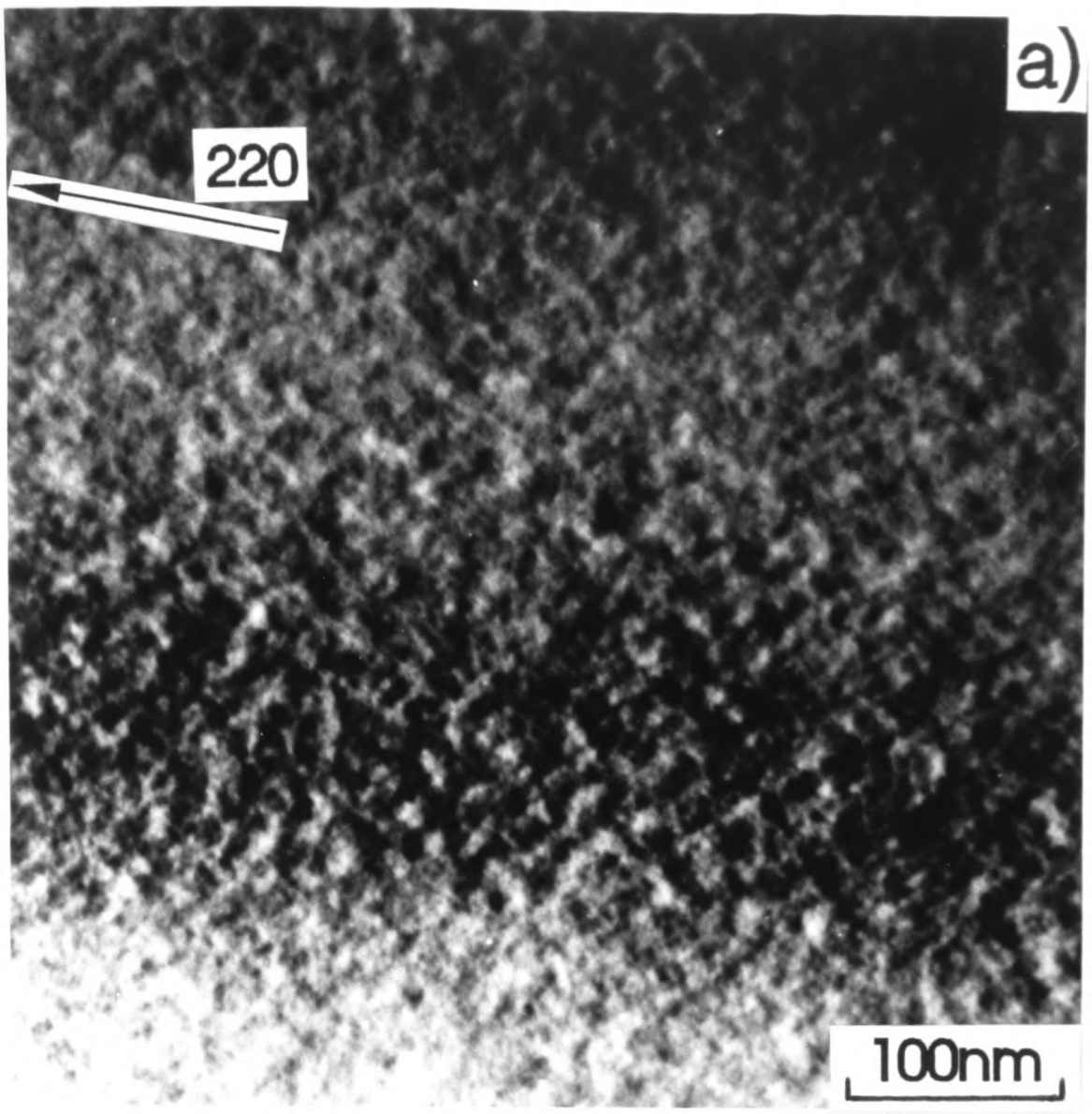

Fig. 5.6

Figure 5.7

Plan-view **g**(220)·3**g** TEM DF micrographs from (a) the as-grown and (b) annealed samples of the InGaAs MOCVD layer grown at 717°C using 0.95nm/s. Both samples exhibit a fine speckle (mottled) contrast (with a pseudo-period of ~4.5nm) having no preferred orientations.

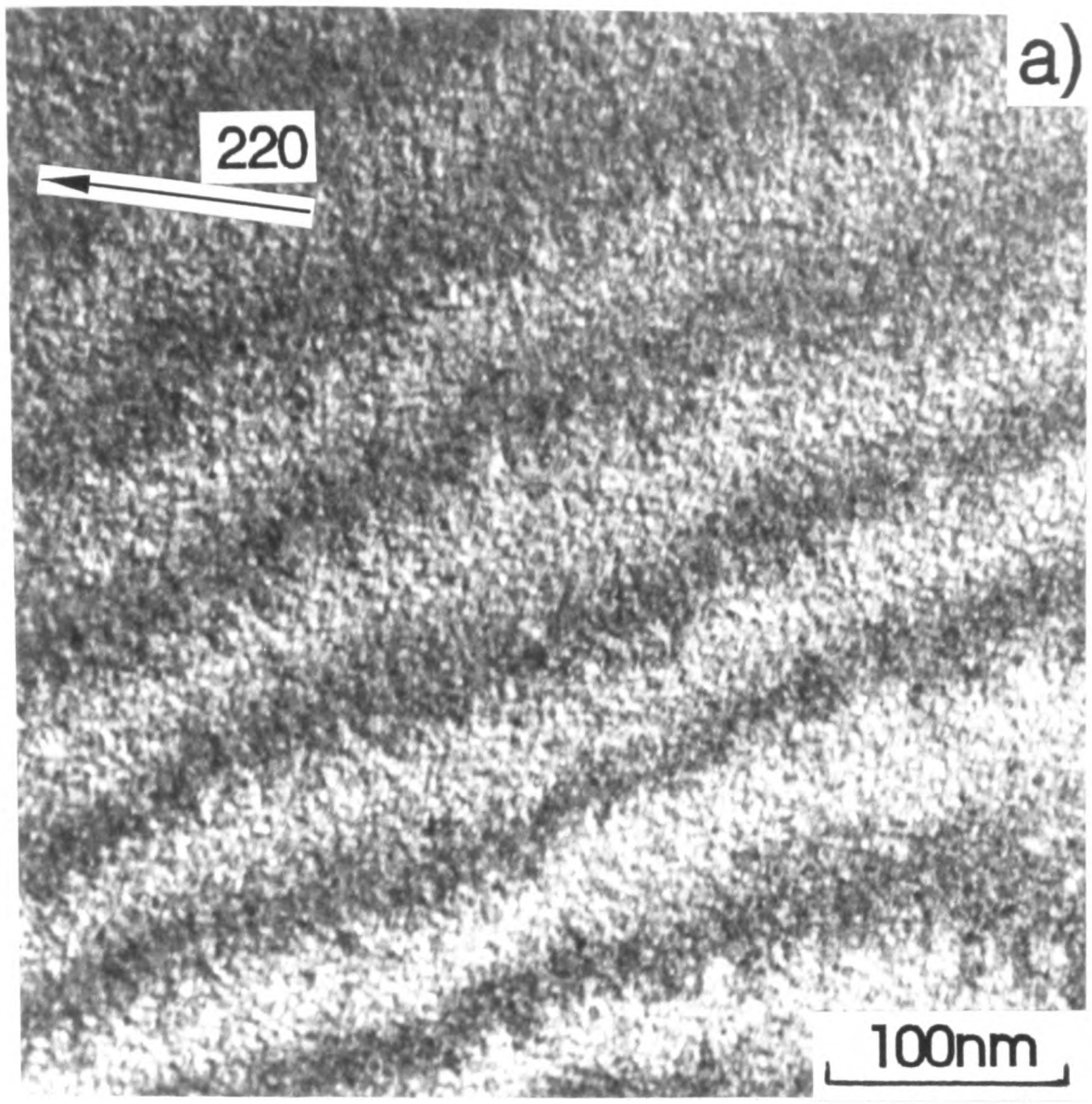

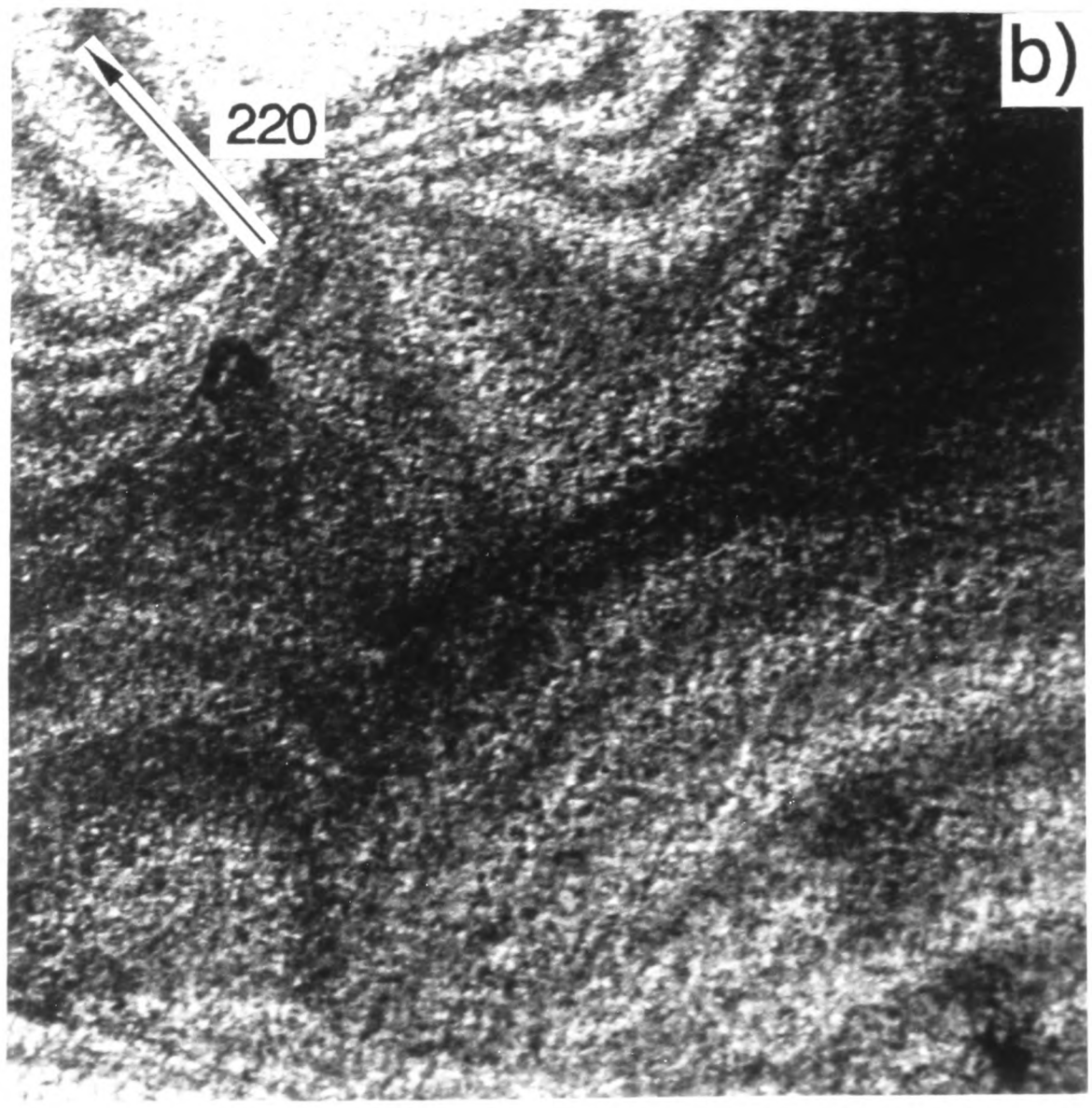

Fig. 5.7

showed that there exists a fine scale mottled contrast (~4-5nm) showing no preferred orientations such as <100> directions. Weak beam images show an ill-defined fine scale speckle contrast (~4nm).

5-2-3 TEM observation of composition variations

Cross-sectional TEM was used to characterise the structure of InGaAs layers. In this section, the (002) TEM DF technique, which is sensitive to chemical composition, was employed to investigate the spatial variation in composition.

For a ternary alloy such as $In_xGa_{1-x}As$, the structure factor (26),

$$F_{002} = 4[(f_{Ga} - f_{As}) + x_{In}(f_{In} - f_{Ga})] \qquad (5\text{-}1)$$

where x_{In} is the In concentration on the Group III element sublattice in the compound semiconductor and f_{Ga}, f_{In} and f_{As} are the atomic scattering factors of Ga, In and As, respectively. The intensity, **I**, of the (002) TEM DF image is proportional to F_{002}^2 (26), i.e. contrast of the (002) DF micrographs is dependent on the variation of the composition, **x**, in $In_xGa_{1-x}As$ alloy layers.

Fig. 5.8(a) shows a cross-section (002) DF micrograph of the layer grown at 550°C with 0.2 nm/s, which exhibits fine lines of contrast running parallel to the layer surface, i.e. perpendicular to the **g**002 vector. The thicknesses of the fine lines of contrast were irregular and ranged from ~3nm to ~5nm. This contrast corresponds to a variation of composition in the layer in the [001] growth direction. Fig. 5.8(b) shows a similar micrograph of InGaAs grown at 550°C with 2.0 nm/sec. Strong irregular bands of contrast are visible, running approximately perpendicular to the [001] growth direction, implying the existence of composition fluctuations. The epitaxial InGaAs layer grown at 650°C with 0.2 nm/s showed broad lines of contrast(Fig. 5.8(c)).

These lines and bands of contrast, which correspond to compositional variations, were attributed to instabilities in growth conditions such as substrate rotation, non-uniform flux, or

Figure 5.8

Cross-section (002) TEM DF micrographs from InGaAs MOCVD layers grown at (a) 550°C using 0.2nm/s, (b) 550°C using 2.0nm/s and (c) 650°C using 0.2nm/s. (a) shows bands of contrast parallel to the layer surface. In (b), irregular bands of eontrast are visible approximately parallel to the layer surface. (c) shows no periodic bands of contrast.

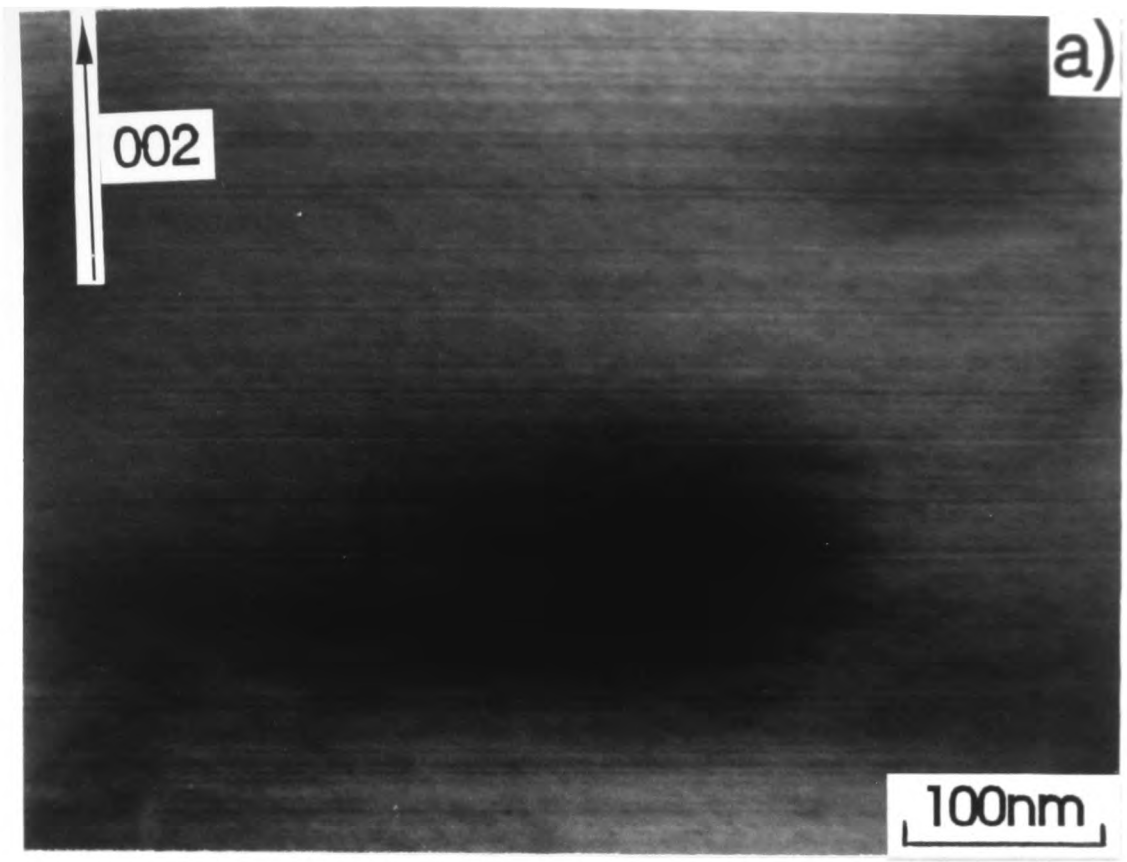

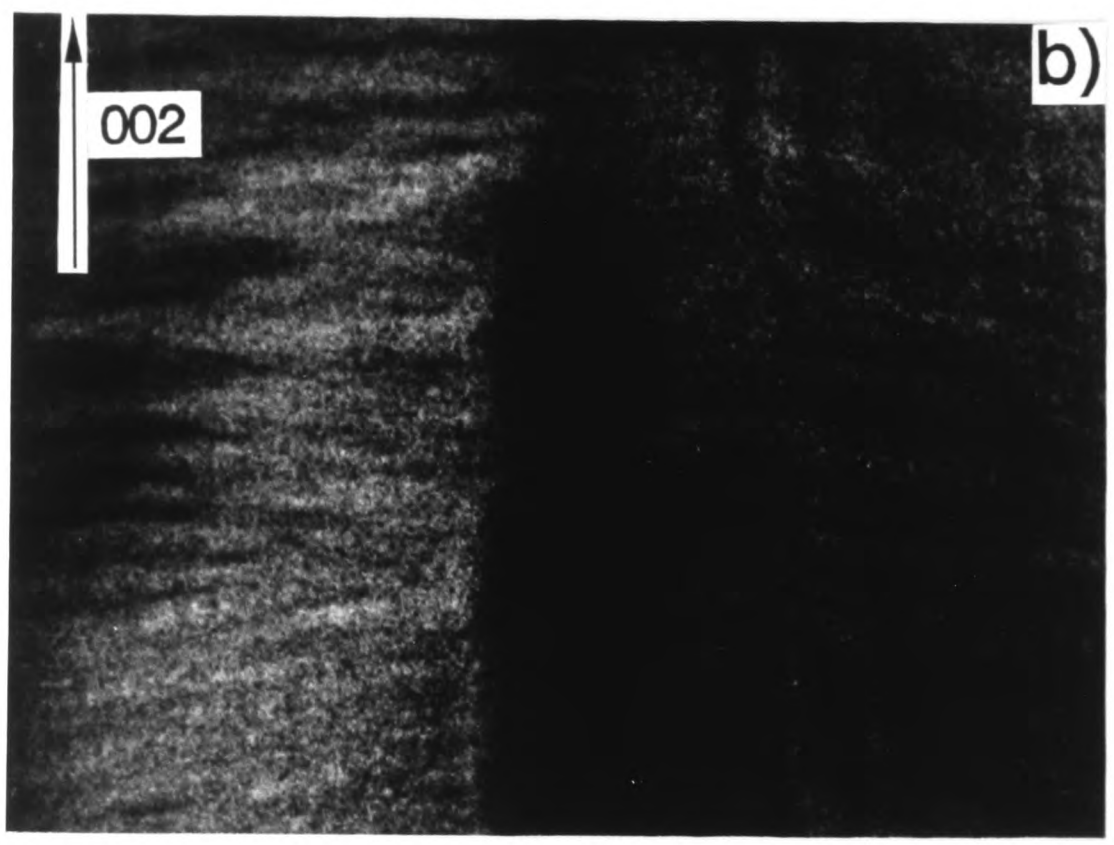

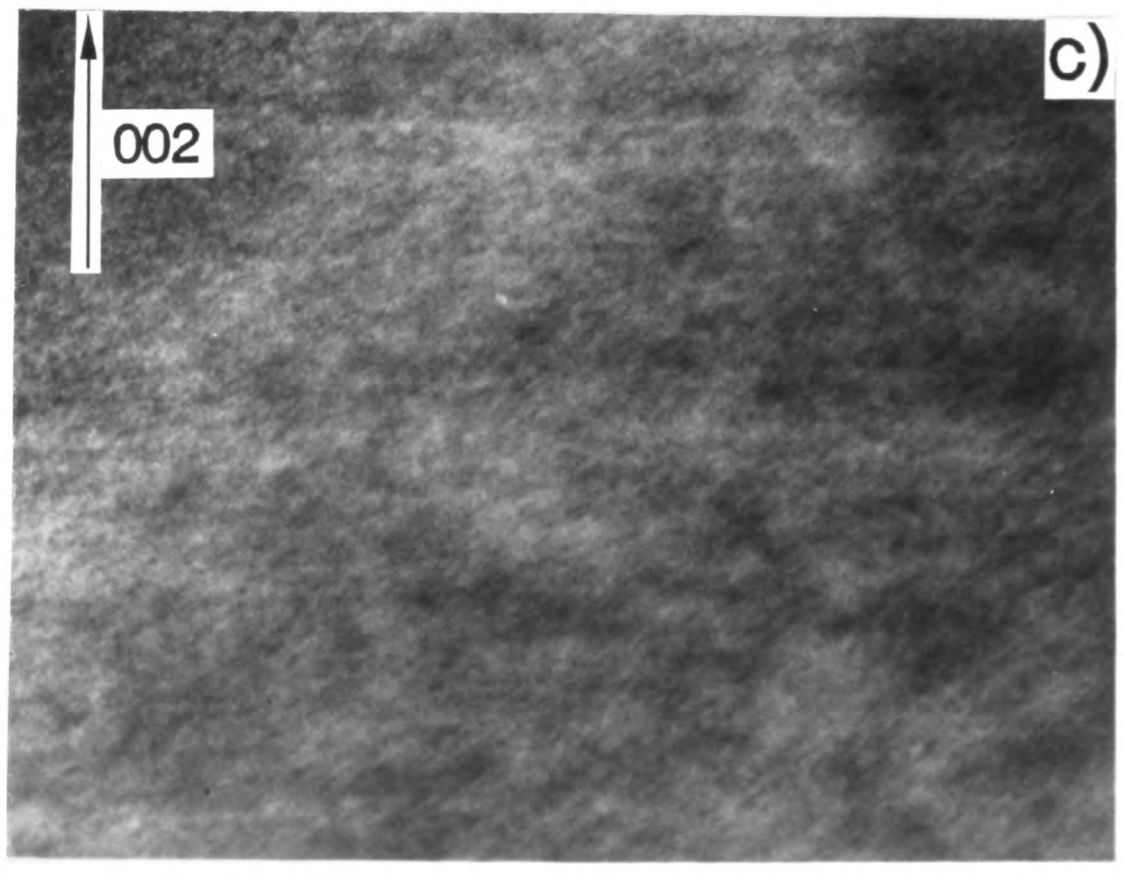

Fig. 5.8

fluctuations in pressure and temperature (15,26-29). Alvai et al.(27) reported composition oscillations in MBE III-V compound semiconductors and interpreted these oscillations as arising from small variations in the flux profile of the group III elements over the substrate and the substrate rotation. Similar composition variations in MOCVD epitaxial AlGaAs layers were reported by Kuesters et al.(28). They suggested that the compositional variations within the MOCVD epitaxial AlGaAs layers are associated with instabilities in the reactant flux. For similar MOCVD InGaAs layers grown at 600°C on (001) InP, bands of contrast resulting from composition fluctuation was also observed using the (002) TEM DF technique (29). This composition change was directly measured by high spatial resolution EDX microanalysis using a Vacuum Generators HB501 STEM and found to vary from x=0.4 to 0.5 in the $In_xGa_{1-x}As$ layer.

Composition modulations detected in the present specimens could be due to either a fluctuation in reactant concentrations and pressure over the InP substrate or instabilities of the source controllers used to regulate gas flows and temperatures, as suggested by Norman (15), who found composition modulation in the [001] growth direction in MOCVD InGaAs layers. The different composition modulations in InGaAs grown at 650°C with 0.2 nm/s, could be due to either fast surface and bulk diffusion or more stable conditions over the substrate. Large scale irregular contrast observed in InGaAs grown at 550°C with the fast growth rate of 2.0 nm/s, as compared to the slow growth rate sample, could be associated with a more unstable flux fluctuation and/or gas flow over the substrate, but not to thermodynamical properties such as spinodal decomposition.

5-2-4 Discussion

$In_xGa_{1-x}As$ layers grown over a wide range of temperatures with different growth rates have been evaluated using cross-section and plan-view TEM techniques. A fine scale modulated contrast occurred for all the layers. This observation is consistent with the works of other authors (5-15), who found the similar characteristic fine scale modulated contrast on a scale of ~5-20 nm for InGaAs and other ternary and quaternary III-V layers.

The **g**{220} and **g**{400} TEM investigations showed that a quasi-periodic fine scale modulated contrast results from the presence of quasi-periodic strain fields simultaneously present in the elastically soft [100] and [010] directions in the crystal (6,15). The presence of such strain fields could be associated with a short wavelength composition fluctuation arising from spinodal decomposition (12,15). Formation mechanisms for the fine scale modulated contrast were proposed by Norman and Booker (9) and Chu et al.(12). Norman and Booker (9) suggested that a fine scale modulated contrast could be evolved from phase separation occurring during cooling down from the growth temperature through bulk solid state diffusion. Chu et al.(12) examined spinodal decomposition in InGaAs and InGaAsP layers grown by hydride transport VPE using the TEM technique. They observed a quasi-periodic fine columnar contrast and proposed a surface diffusion spinodal decomposition mechanism during epitaxial layer growth, which is responsible for the occurrence of a fine scale columnar structure. Liddle et al.(30) used the pulsed laser atom probe (PLAP) to assess composition variations in MOCVD $In_xGa_{1-x}As$ layers. Composition differences were sometimes revealed, but it was not definitely established whether these corresponded to the fine scale modulated structure observed by TEM.

Recently, Glas (20) and Glas et al.(21), however, reported an observation of diffuse intensity in TED patterns obtained from ternary and quaternary III-V semiconductor alloys. They examined the information obtained by diffuse X-ray and electron scattering about both the statistical atomic configurations and the deviation from disorder. Their observation of diffuse <110>-oriented intensity located slightly away from the sphalerite main spots led them to distinguish this phenomena as being caused by static atomic displacements rather than by phonon scattering (25), which results in a similar <110>-oriented diffuse intensity passing exactly through the main spots. In order to interpret this behaviour, they used the valence force field (VFF) model (22,23) to calculate the atomic positions in random and ordered ternary III-V compound alloys. In their model, the equilibrium positions of atoms were determined by minimizing the deformation energy, which includes structural terms such as the equilibrium bond angle, bond-stretching and bond bending constants of atoms present at all the atomic sites and nearest neighbour sites. The diffuse scattering was then calculated

kinematically by the contribution to the structure factors of the chemical and position disorder. The results obtained from the calculations suggested that the characteristic diffuse intensity oriented along <110> directions in the TED patterns of InGaAs grown on (001) InP could be a result of static atomic displacements associated with a totally random distribution of the atomic species on the sites of the mixed Group III sublattice. It was also concluded that the fine scale modulated contrast observed in {220} and {400} DF micrographs is responsible for the <110>-oriented diffuse intensity and results from static atomic displacements from the average lattice.

On the contrary, Mahajan et al.(8) considered that the presence of a fine scale contrast is directly due to spinodal decomposition and that the elongation of {h00} spots along <100> directions in TED patterns obtained from InGaAsP layers tilted in the TEM results from the fine scale modulated contrast. It is possible that the elongated spots observed by Mahajan et al.(8) arise from the intersection of the <110>-oriented diffuse lines referred to above.

Norman and Booker (9) and Norman (15) investigated LPE InGaAsP and MBE InGaAs layers using TEM and TED techniques. They showed evidence of a fine scale modulated contrast (~5-20nm in scale) and strong <100> satellite spots associated with all of the main spots except for the central 000 spot. The spacing of the satellite spots in the TED patterns corresponded precisely with the wavelength of the fine scale modulated structure in the micrographs. It was concluded that the observed satellite spots most probably arise from a periodic variation of lattice parameter and/or composition along the <100> directions of the crystal possibly caused by spinodal decomposition of the layers. They also reported <110>-oriented diffuse intensity in the [001] TED patterns of the layers, which is similar to that observed in the present work.

In this work, as already described in section 5-2-2, a post-growth annealing experiment was introduced to evaluate the behaviour of the quasi-periodic fine scale contrast observed in InGaAs grown at 717°C. The **g**{220} TEM DF, weak beam **g**(220)-3**g** and selected area TED techniques were used and the results are shown in Fig. 5.4, 5.6 and 5.7. The **g**{220} TEM DF micrographs taken from cross-section and plan-view specimens of the as-grown and annealed materials showed a considerable difference in the nature of the

contrast and the wavelength. The as-grown specimen showed both the fine scale modulated contrast (10-20nm in scale) which is attributed to alloy clustering, and the fine scale mottled contrast (~4-5nm), whilst the annealed specimen exhibited no fine scale modulated contrast. Instead, an ill-defined fine scale mottled contrast (~4-5nm) was visible, which showed no preferred orientations. This indicates that bulk diffusion of In and Ga on the mixed Group III sublattice changes the atomic configurations during annealing, which results in different characteristic contrasts in the DF micrographs.

Solid state self diffusion coefficients have been measured for binary III-V semiconductor alloys such as InAs and GaAs using radio tracer techniques (31,32). The values for In and Ga atoms were in the range $4x10^{-17}$ - $5x10^{-18}$ cm^2/s for 600°C, at which the specimen was annealed for 744 hours. Although these values were measured for binary III-V alloys, we assume similar values for In and Ga atoms in the ternary $In_xGa_{1-x}As$ alloy.

Assuming that the self diffusion coefficient in the bulk is ~$5x10^{-18}$ cm^2/s, we can estimate the diffusion distance, x, using the general expression given by Cahn (33), i.e.

$$x^2 = 2 \mid D \mid t \qquad (5\text{-}2)$$

where x is the diffusion distance, D is the diffusion coefficient and **t** is the diffusion time. For an anneal time of 744 hours, this gives a diffusion distance of In and Ga in InGaAs of ~50nm, which is more than sufficient to account for the elimination of the as-grown composition modulation of wavelength 10-20nm. If the temperature of 600°C is above the critical temperature for spinodal decomposition in the bulk of the layer, the alloy will be randomized through a solid state bulk diffusion process. Therefore, the ill-defined fine scale mottled (speckle) contrast visible on a scale of ~4nm (Fig. 5.4(b) and 5.6(b)) could be a characteristic contrast associated with the random distribution of atoms in the mixed Group III sublattice and caused by static atomic displacements from the average lattice. Contrary to the present work, Glas (20) and Glas et al.(21) have attributed the fine scale modulated contrast to static atomic displacements.

The results obtained from weak beam and TED examinations showed similar characteristic features in both as-grown and annealed specimens, indicating a similar origin for these features. In order to identify the origin of the diffuse lines of diffracted intensity oriented along <110> directions, selected area TED and weak beam techniques were used. TED patterns were obtained from a ~1μm diameter selected area using the plan-view specimens of the as-grown and annealed InGaAs layers, which exhibited different characteristic contrasts to each other in TEM **g**(220) DF micrographs, as in Fig. 5.6. In Fig. 5.5 are shown [001] TED patterns of the as-grown and annealed specimens. No noticeable differences were detected. Weak beam images of the same regions of Fig. 5.6 taken using the **g**(220)-3**g** condition are shown in Fig. 5.7. The **g**(220)-3**g** weak beam images revealed a similar fine speckle contrast on a scale of ~4nm in the as-grown and annealed specimens, although they showed different morphologies of the contrast with no preferred orientations such as the <100> directions found in the **g**(220) DF micrograph of the as-grown sample.

The results obtained from the TEM DF and weak beam investigations suggest the following. First, there coexist the fine scale modulated contrast associated with alloy clustering and the ill-defined fine scale speckle (mottled) contrast probably related to the static atomic displacements. Second, the fine scale speckle contrast is responsible for the <110>-oriented diffuse lines in the [001] TED patterns. A possible model for the coexistence of the fine scale modulated contrast and the fine scale speckle contrast is as follows. For the as-grown specimen, a sinusoidal composition modulation of In-rich and Ga-rich regions along the [100] and [010] directions occurs, Fig. 5.9(a). For either In-rich or Ga-rich regions, there may also exist preferred statistical atomic distributions of the mixed Group III sublattice. For the InGaAs alloy, we consider three kinds of atomic configurations: i) one As with three In and one Ga; ii) one As with two In and two Ga; iii) one As with one In and three Ga. Therefore, for the In-rich regions, case i) is more probable than others, although there exist cases ii) and iii). The solid line and dotted line indicate a composition modulation and a statistical atomic distribution with associated atomic displacements within the composition modulation, respectively. For the annealed specimen, the composition

Figure 5.9

Suggested model for the existence of a fine scale modulated contrast and a fine speckle (mottled) contrast. (a) For the as-grown specimen, a sinusoidal composition modulation (the solid line) and a statistical atomic distribution (the dotted line) are present. (b) For the annealed specimen, the sinusoidal composition modulation is absent but a statistical atomic distribution is present.

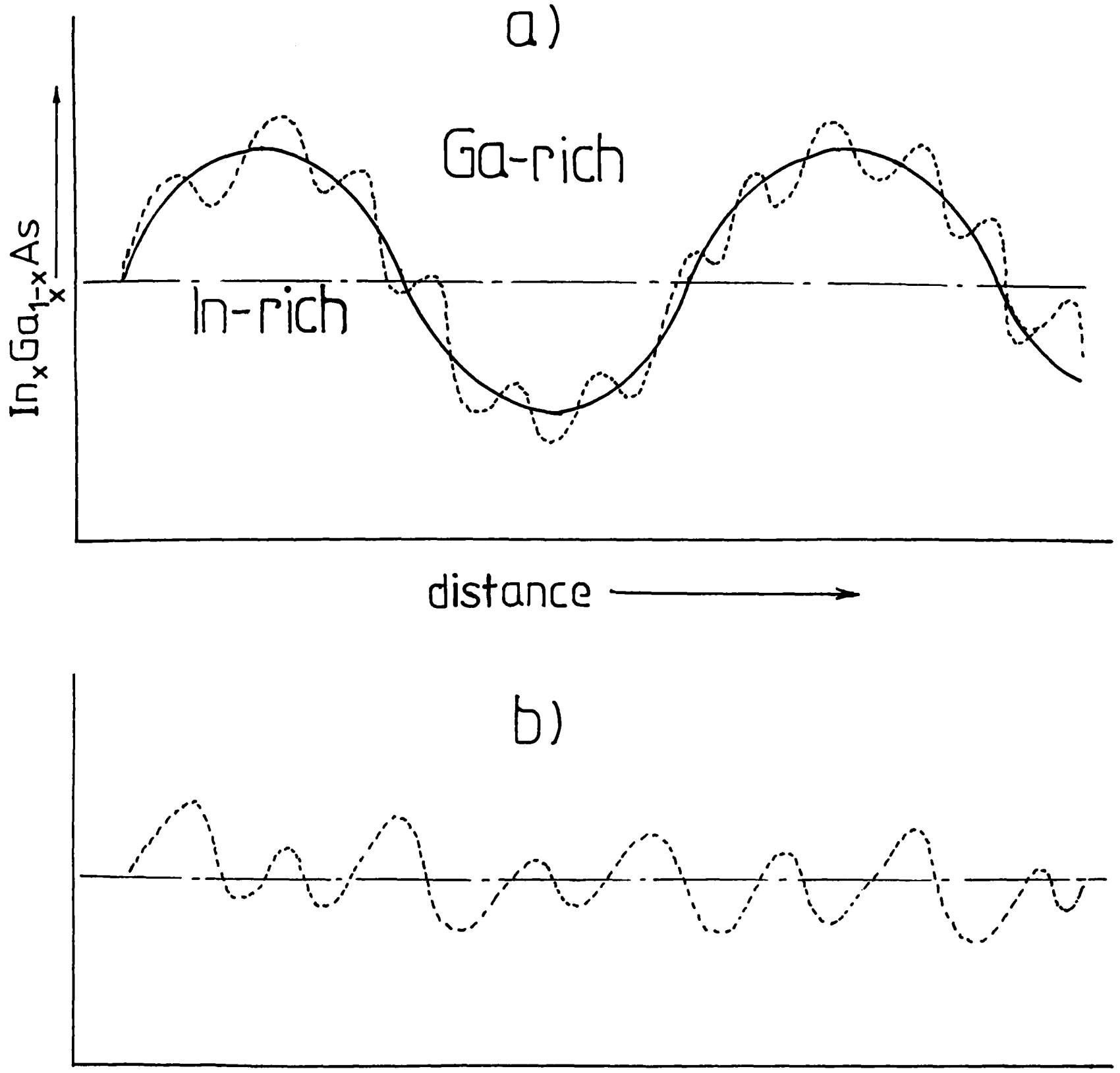

Fig. 5.9

modulation is absent and only the statistical random distributions of the three different cases i), ii) and iii) occurs, Fig. 5.9(b).

When the as-grown specimen was imaged by strong beam **g**{220} DF, the micrograph showed up both the fine scale modulated contrast on a scale of ~10-20nm and the fine scale speckle contrast on a scale of ~4nm. However, when the specimen was imaged by **g**(220)-3**g** weak beam condition, the micrograph showed up only the fine scale speckle contrast. This indicates the coexistence of alloy clustering and static atomic displacements. A possible reason for the different TEM contrasts is different contrast mechanisms. There are two possible sources for the TEM contrast: a) lattice parameter variations giving rise to diffraction contrast; b) local atomic configurations producing scattering factor contrast (34). When the as-grown specimen was imaged by the strong two beam **g**{220} condition, the micrograph could show up both the fine scale modulated contrast due to diffraction contrast and the fine scale speckle contrast due to scattering factor contrast. However, in order to obtain the weak beam image, the specimen is tilted far from the normal two beam condition. This indicates that the imaging condition is far off the Bragg condition. For a structure that has composition, and hence lattice parameter, modulations in the [001] and [010] directions, but not in the [001] direction, it can be argued that diffraction contrast effects when the specimen is tilted far off the Bragg position will be small. Therefore, the micrograph could show up only the scattering factor contrast which may be related to local atomic configurations. This is consistent with the observation of the fine scale speckle contrast in the as-grown and annealed specimens when imaged by the weak beam condition.

[001] TED investigations by Norman and Booker (9) and Norman (15) quantitatively showed a direct relationship between the fine scale modulated contrast and satellite spots. In this study, no such satellite spots were observed. Instead, both [001] TED patterns obtained from the as-grown and annealed specimens exhibited <110>-oriented diffuse intensity lines, although **g**(220) DF micrographs showed different contrast features. Furthermore, the weak beam images exhibited a similar fine scale speckle contrast. These results strongly indicate that the <110>-oriented diffuse lines are associated with the fine scale speckle contrast, i.e. due to statistical static atomic displacements.

A possible model is suggested to explain the coexistence of the alloy clustering and static atomic displacements. Using the mechanism introduced, we can suggest the growth behaviours of alloy clustering and statistical atomic arrangements. The fine scale modulated contrast occurs at the growing surface due to alloy clustering, resulting in a composition modulation. During the decomposition into In-rich and Ga-rich regions at the growing surface, the suggested three kinds of different atomic configurations may occur, depending on the composition, as described above. Since such composition modulation is not stable in the bulk of the layer, post-growth annealing will randomize the composition modulation. This randomization may introduce well-distributed three kinds of different atomic configurations, cases i), ii) and iii), which could be responsible for the different morphologies of the fine scale speckle contrast.

5-3 Alloy clustering in InP_ySb_{1-y} layers

5-3-1 Experimental

InP_ySb_{1-y} alloy layers have been calculated to have a very large enthalpy of mixing due to the large difference in lattice constant between the InP and InSb binary components (35). However, in spite of the presence of a miscibility gap, the InP_ySb_{1-y} layers studied in this work have been successfully grown using the MOCVD technique (36). The MOCVD growth experiments were performed in an atmospheric pressure, horizontal, infrared heated reactor (37). The reactants were trimethylindium (TMIn) and trimethylantimony (TMSb), kept in temperature controlled baths at 11 and 15°C, respectively and phosphine, 10% balanced in H_2. The ambient was Pd-diffused H_2 with flow adjusted to give a total flow rate of 2.0 l/min. The molar flow rates of the reactants were f_{TMIn} = 4.33 μmol/min, f_{TMSb} = 5.49-20.3 μmol/min and f_{PH_3} = 20.3-203 μmol/min. The growth temperature was varied between 460 and 500°C and the growth rates were either 0.56 or 0.83nm/s. All the layers were grown on either n^+ (001) InAs or undoped (001) InAs substrates. The layer composition was determined from the lattice constant ,a, assuming Vegard's law,

$$a = 5.869y + 6.479\,(1-y) \qquad (5\text{-}3)$$

The details of the alloy layers examined are given in Table 5.2.

5-3-2 TEM, TED and HREM analyses

(001) plan-view specimens were initially used to characterise the epitaxial InP_ySb_{1-y} layers. Two beam TEM DF micrographs obtained from the plan-view specimen of an $InP_{0.74}Sb_{0.26}$ layer grown at 500°C are shown in Fig. 5.10. The $(\bar{2}20)$ and $(\bar{2}\,\bar{2}0)$ DF micrographs (Fig. 5.10(a) and (b)) reveal two sets of a quasi-periodic fine scale modulated contrast, elongated along the elastically soft [100] and [010] directions. The wavelength of the fine scale modulated contrast was 15-20 nm. In the (400) DF micrographs, Fig. 5.10(c), a fine scale modulated contrast is seen, aligned along the [010] direction perpendicular to the **g**-vector. The wavelength of the quasi-periodic fine scale modulated contrast was 15-20nm in the [010] direction. Similarly, a quasi-periodic fine scale modulated contrast with a wavelength of 15-20 nm in the [100] direction is visible in the [040] DF micrograph, as shown in Fig. 5.10(d). Such fine scale modulated contrast for other III-V materials has been attributed to the existence of quasi-periodic strain fields present in the crystal along the <100> directions (5-15). Likewise, the fine scale modulated contrast present in InP_ySb_{1-y} alloy layers could also be attributed to a result of surface diffusion spinodal decomposition during epitaxial layer growth (15), as discussed in section 5-2-2. No significant difference in the fine scale contrast was observed for specimens grown in the range 460 to 500°C. In addition, in the $(\bar{2}\,\bar{2}0)$ TEM DF micrograph, Fig. 5.10(b), a fine needle-like contrast is visible perpendicular to the **g** vector. The $(\bar{2}20)$ DF image shows no evidence for the fine needle-like contrast. The (400) and (040) DF micrographs, Fig. 5.10(c) and (d), show the fine needle-like contrast aligned along the $[\bar{1}10]$ direction, which is 45° from the <100> directions. All the layers showed similar structures, when examined using (001) plan-view TEM specimens.

Further structural investigations were performed on {110} cross-sectional TEM specimens of an $InP_{0.59}Sb_{0.41}$ layer grown at 470°C. TEM results obtained from **g**{220}

Table 5.2 Epitaxial InP_ySb_{1-y} MOCVD layers.

Sample No.	InP_ySb_{1-y} (y)	Growth temp. (°C)	Growth rate (nm/s)	Substrate
SC-81	0.53	460	0.56	InAs*
SC-90	0.55	470	0.56	InAs+
SC-77	0.59	470	0.56	InAs*
SC-23	0.74	500	0.83	InAs+

* = undoped; + = n^+ doped.

Figure 5.10

Plan-view {220} and {400} TEM DF micrographs from InP_ySb_{1-y} MOCVD layer (y=0.74) grown at 500°C using 3.0μm/hr, showing a fine scale modulated contrast on a scale of 10-20nm, which is elongated parallel to the <100> directions.

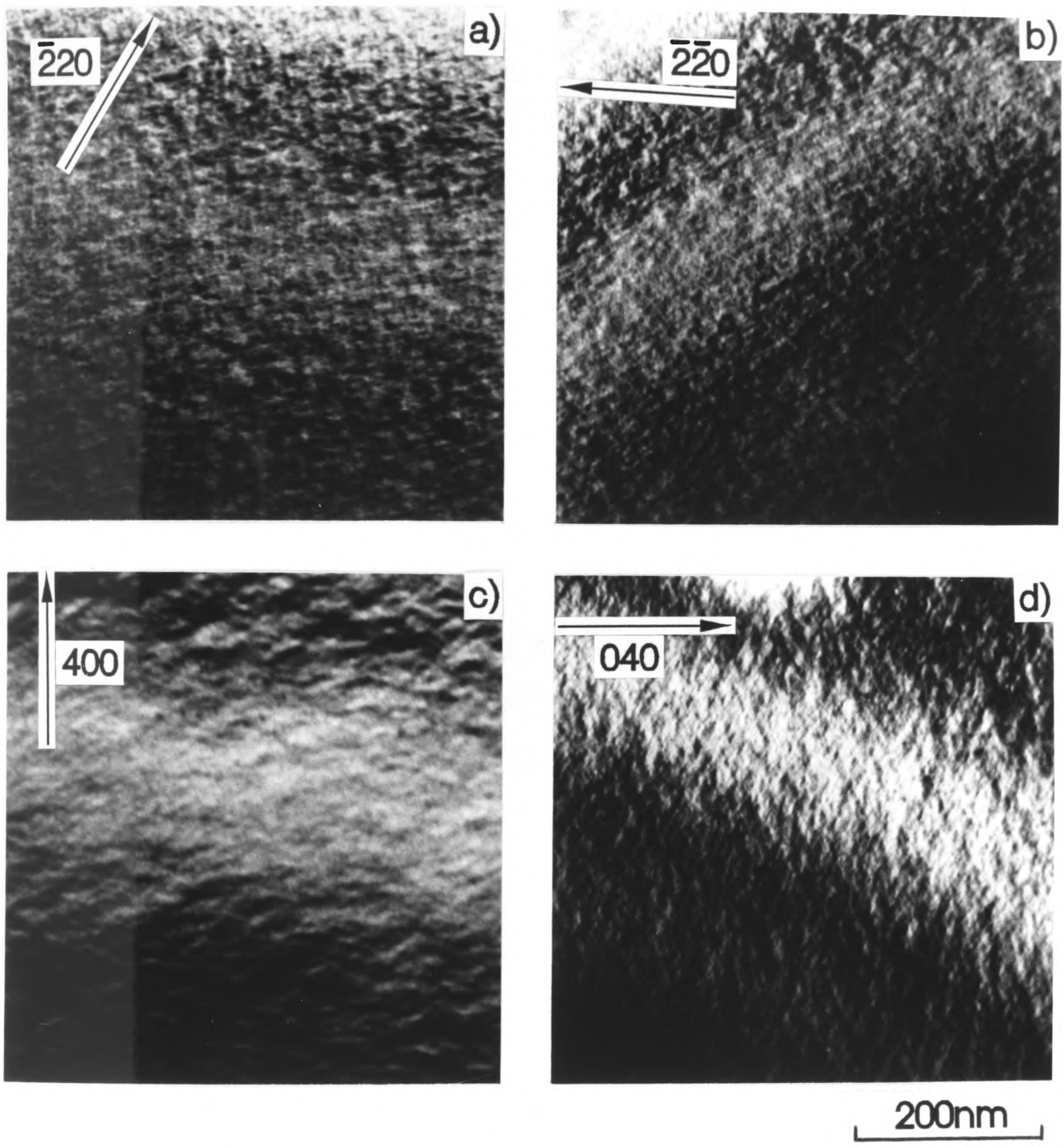

Fig. 5.10

diffraction contrast experiments are shown in Fig. 5.11. The main characteristic features found were as follows:

i) a quasi-periodic fine scale modulated contrast with wavelengths between 15 and 20 nm visible in both ($\bar{2}\,\bar{2}\,0$) and ($\bar{2}\,20$) DF micrographs;

ii) a quasi-periodic fine needle-like contrast with wavelengths between 1.5 and 2.0 nm visible solely in the TEM DF micrograph taken using the (220) reflection of the [$\bar{1}\,10$] pole TED pattern.

The fine scale needle-like contrast has a spacing measured to be ~1.5-2.0 nm in the [110] direction parallel to the (001) substrate surface. This is consistent with that (~1.7 nm) measured from TED patterns, which will be described later. The scale of fine needle-like contrast was estimated to be 10-30 nm in the [001] growth direction.

Similar TEM DF micrographs taken using the chemical composition sensitive (002) reflection are shown in Fig. 5.12. The (002) TEM DF image obtained from (110) cross-sectional specimen, Fig. 5.12(a), exhibited an uniform layer contrast. However, in the (002) DF micrograph taken from the ($\bar{1}\,10$) cross-section specimen, Fig. 5.12(b), a quasi-periodic fine needle-like contrast is visible, running perpendicular to the substrate and layer interface, i.e. parallel to the [001] growth direction. This was measured to have a spacing of ~1.5-2.0 nm in the [110] direction.

Two orthogonal <110> cross-section TED patterns were taken from the $InP_{0.59}Sb_{0.41}$ layer grown at 470°C and these are shown in Fig. 5.13. In Fig. 5.13(a) is shown the [110] TED pattern, which shows the fundamental zinc-blende spots and superlattice spots appearing at half way between the arrays of fundamental <111> spots, indicating the presence of CuPt-type ordering. The detailed investigations concerning atomic ordering will be described in chapter 6. In Fig. 5.13(b) is shown the [$\bar{1}\,10$] pole TED pattern which exhibits the fundamental spots expected for the zinc-blende crystal structure and other characteristic features. Diffuse streaks passing through the main spots are visible, which lie along the [110] direction and have a maximum in intensity at 1/8 and 7/8$\mathbf{g}_{220}$ positions. The length of streaks lying along the [110] direction through the main spots

Figure 5.11

Cross-section TEM results from InP_ySb_{1-y} MOCVD layer (y=0.59) grown at 470°C using 2.0μm/hr. (a) $(2\bar{2}0)$ and (b) (220) DF micrographs, showing a fine scale modulated contrast. (220) DF micrographs also shows a quasi-periodic fine needle-like contrast with wavelength of ~1.6nm-2.2nm, running along the [001] growth direction.

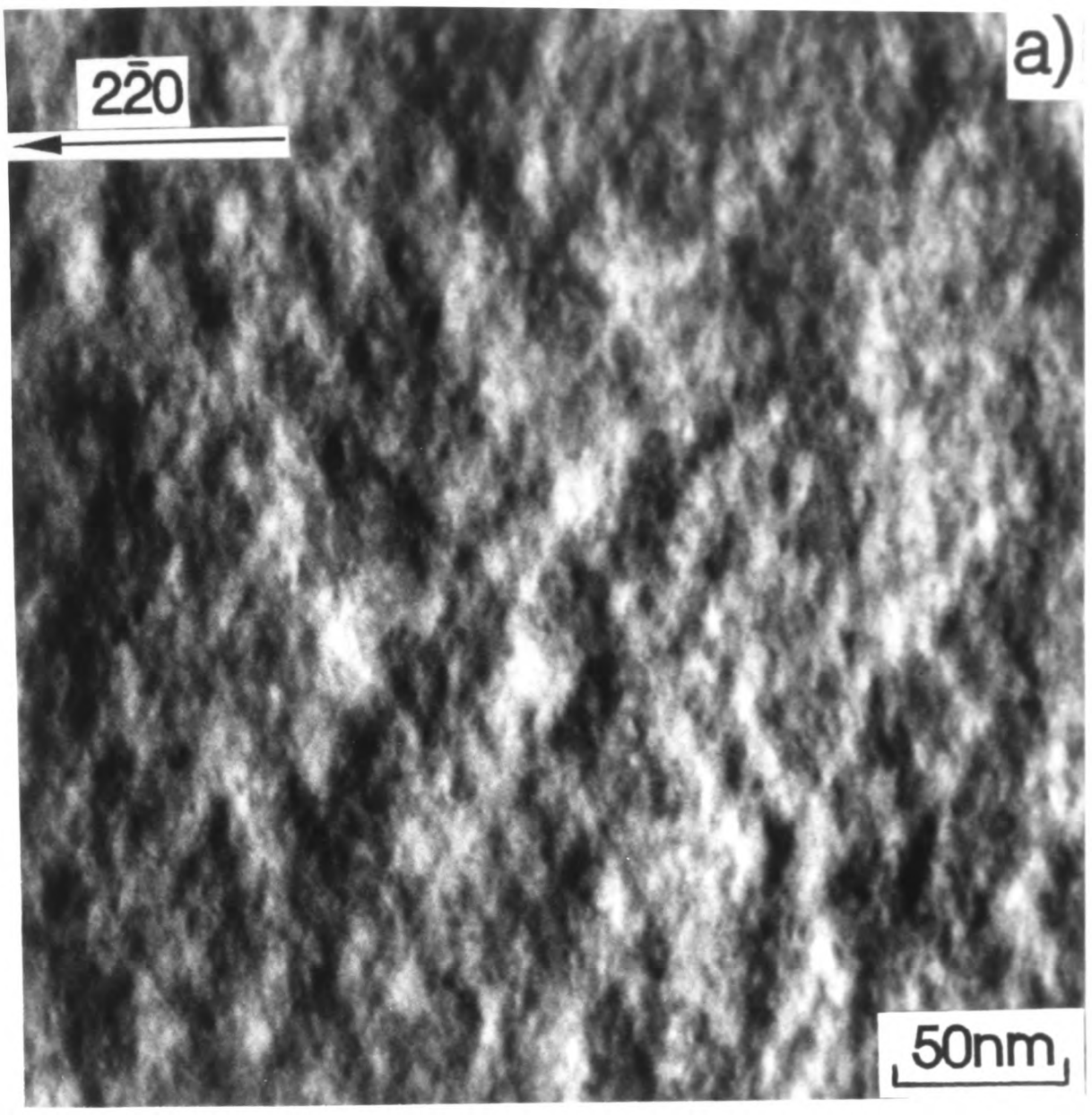

Fig. 5.11

Figure 5.12

TEM results from InP_ySb_{1-y} MOCVD layer (y=0.59) grown at 470°C using 2.0μm/hr. (a) [110] cross-section **g**(002) DF micrograph showing uniform contrast. (b) [$\bar{1}$10] cross-section **g**(002) DF micrograph showing a quasi-periodic fine needle-like contrast oriented perpendicular to the layer surface.

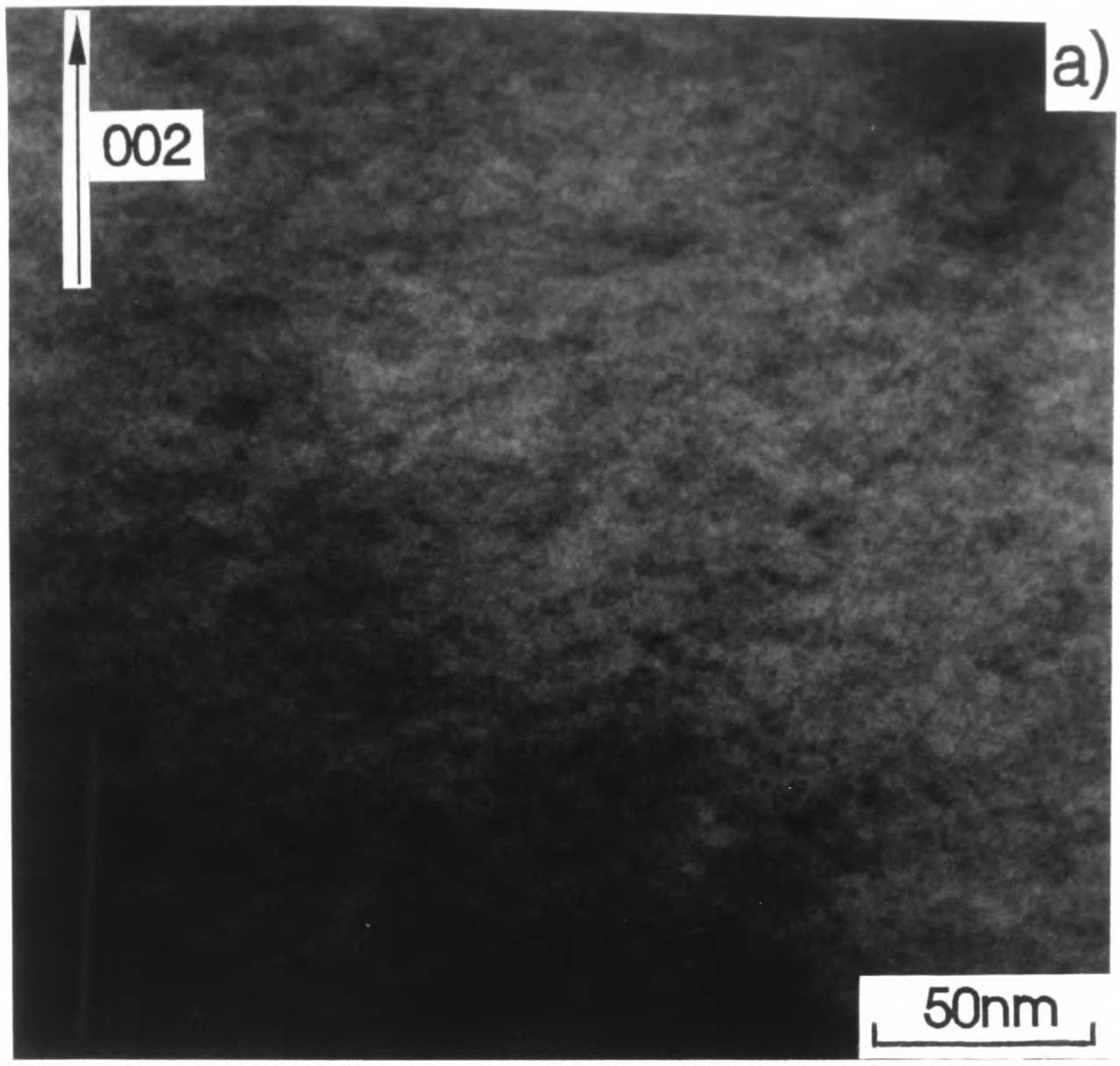

Fig. 5.12

Figure 5.13

TED patterns from InP_ySb_{1-y} MOCVD layer (y=0.59) grown at 470°C using 2.0μm/hr. (a) [110] pattern, showing the zinc-blende structure spots and 1/2{111} superlattice spots corresponding to CuPt-type ordering. (b) [$\bar{1}$10] pattern, showing the zinc-blende spots and [110]-oriented diffuse streaks associated with the main diffraction spots.

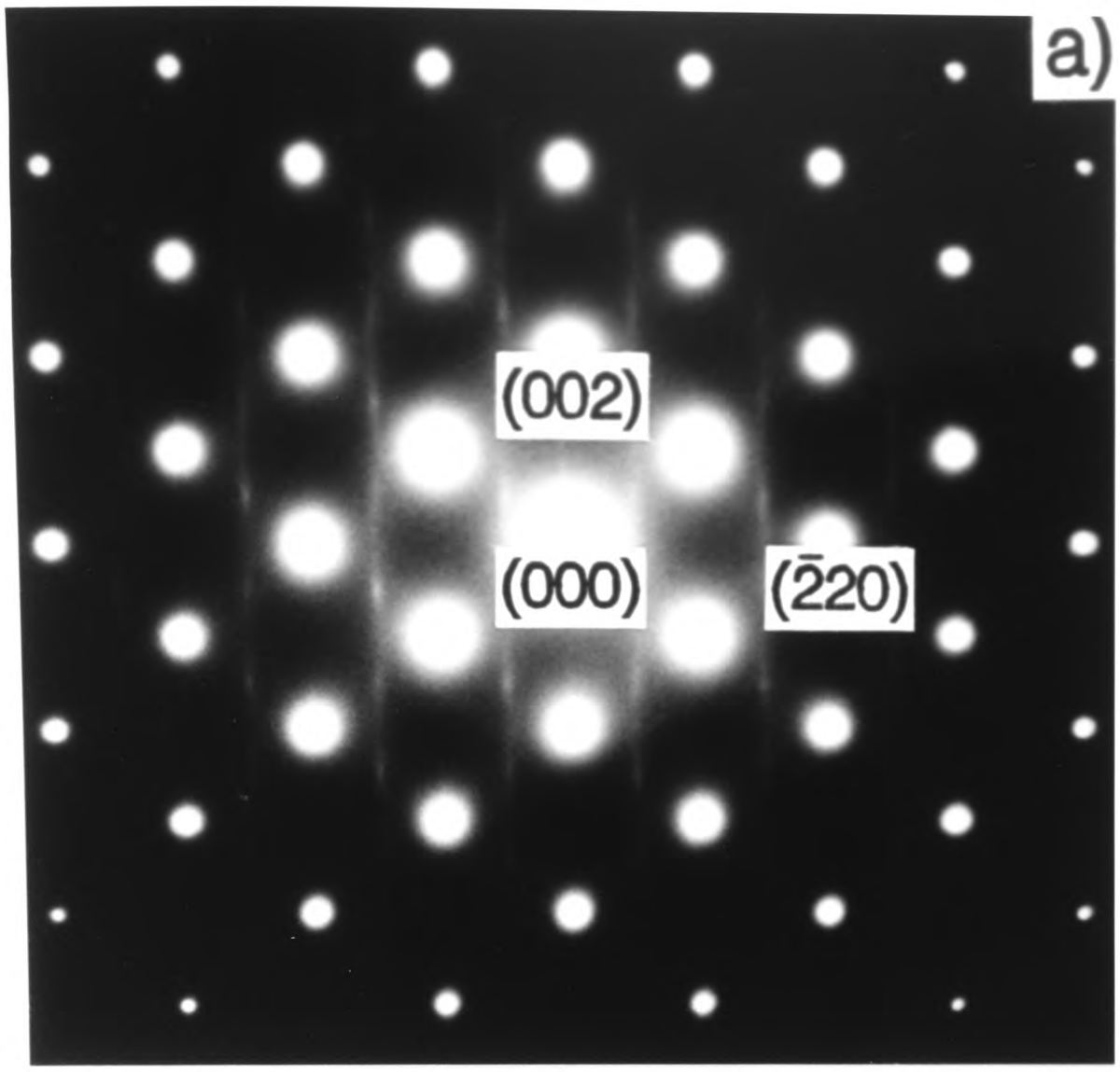

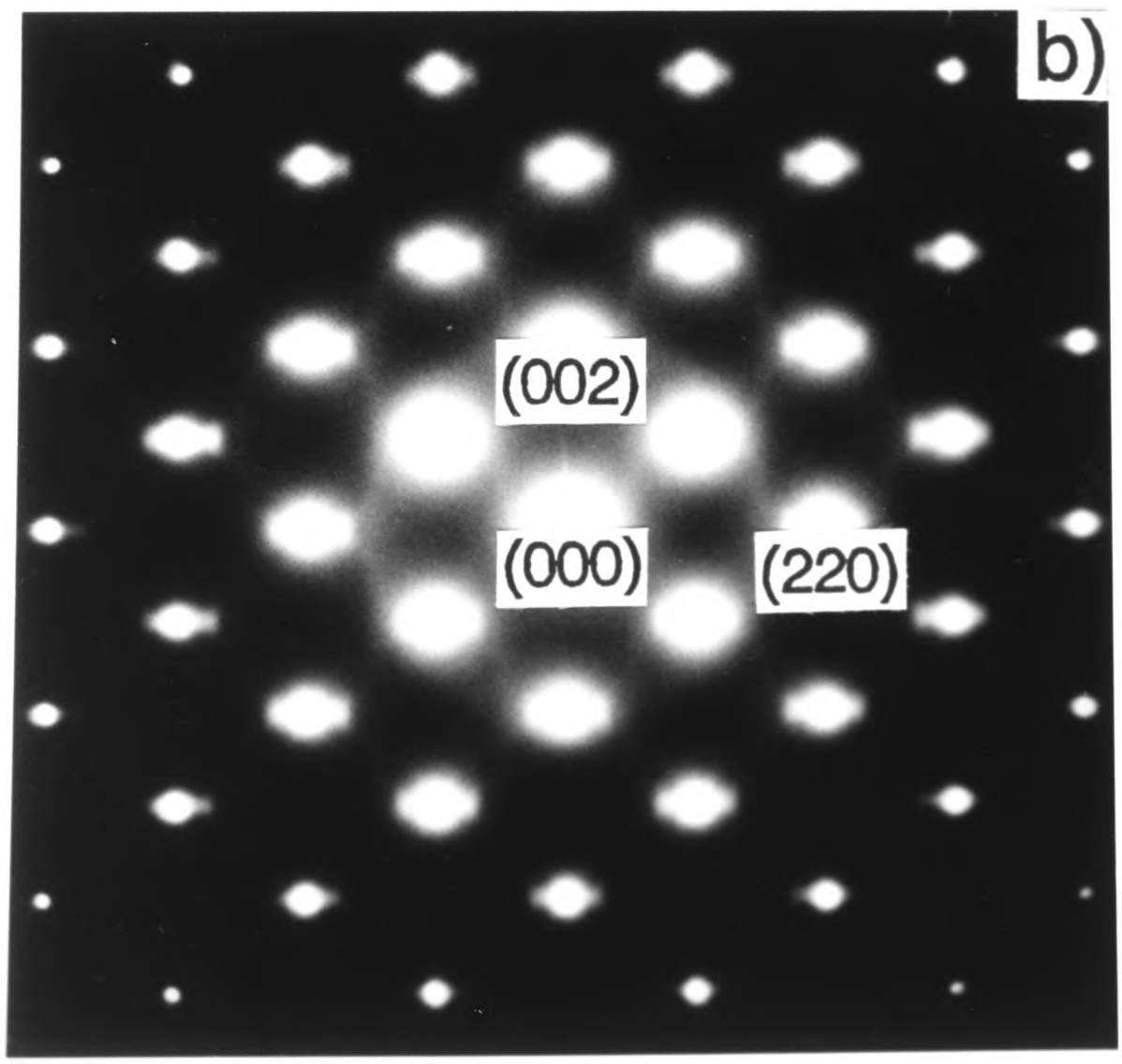

Fig. 5.13

remain unchanged with increasing order of the Bragg reflections. This suggests that the diffuse streak is associated with a shape effect (38). The TED results also showed evidence for the presence of diffuse streaks at the central 000 spots, which could arise by double diffraction. It is believed that the diffuse streaks through the main spots arise from thin disc shaped aggregation of atoms, which provides small centres of different scattering amplitudes (38). The diffuse streak length of 1/8g(220), taken as the distance between the maximum intensity and the main spots, corresponds to a periodic structure with a wavelength of ~1.8nm, which is in good agreement with the spacing of the fine needle-like TEM contrast imaged using the (220) and (002) reflections (Fig. 5.11 and 12).

The quasi-periodic fine needle-like contrast observed in the $InP_{0.59}Sb_{0.41}$ layer grown at 470°C (Fig. 5.11) has been imaged using HREM on a $(\bar{1}10)$ cross-sectional specimen, which shows diffuse streaks in the $[\bar{1}10]$ pole TED pattern, as in Fig. 5.13(b). The micrographs were taken using a JEOL 4000EX (extended Scherzer resolution of 0.165 nm at 56 nm defocus) operated at 400 kV. Fig. 5.14(a) is a HREM image taken from the same region as Fig. 5.11(b). A modulation in contrast with a wavelength of ~1.5-2.2 nm is present, consistent with that observed under two beam conditions using the (220) and (002) reflections but showing weaker contrast. The lattice is distorted between different regions and changes in contrast of the atom columns are visible along the [110] direction (indicated by arrows). This again suggests that aggregation of atoms with thin disc shapes may be responsible for both the existence of a quasi-periodic fine needle-like contrast and the diffuse streaks in $[\bar{1}10]$ TED patterns.

In order to generate images of the modulation due to only the diffuse streaks observed in the $[\bar{1}10]$ TED patterns, a computer-imaging technique was introduced. A HREM micrograph (Fig. 5.14(a)) was Fourier-transformed to form a diffractogram using a charge coupled device (CCD) camera and processed using the SEMPER programme (39). Each Bragg spot in the diffractogram (Fig. 5.14(c)) formed from the HREM image showed diffuse streaks in the [110] direction similar to those present in the selected area $[\bar{1}10]$ TED pattern (Fig. 5.14(b)). In order to remove the fine scale detail information from the lattice image and to reveal only the modulation associated with the streak, all parts of the diffractogram, except

Figure 5.14

(a) Cross-section [$\bar{1}$10] HREM micrograph of a fine needle-like contrast from InP_ySb_{1-y} MOCVD layer (y=0.59) grown at 470°C using 2.0μm/hr, showing modulated contrast with a wavelength of ~2.3nm. (b) [$\bar{1}$10] TED pattern obtained from the region in (a), showing diffuse streaks associated with the main spots. (c) Fourier transform of the HREM image in (a).

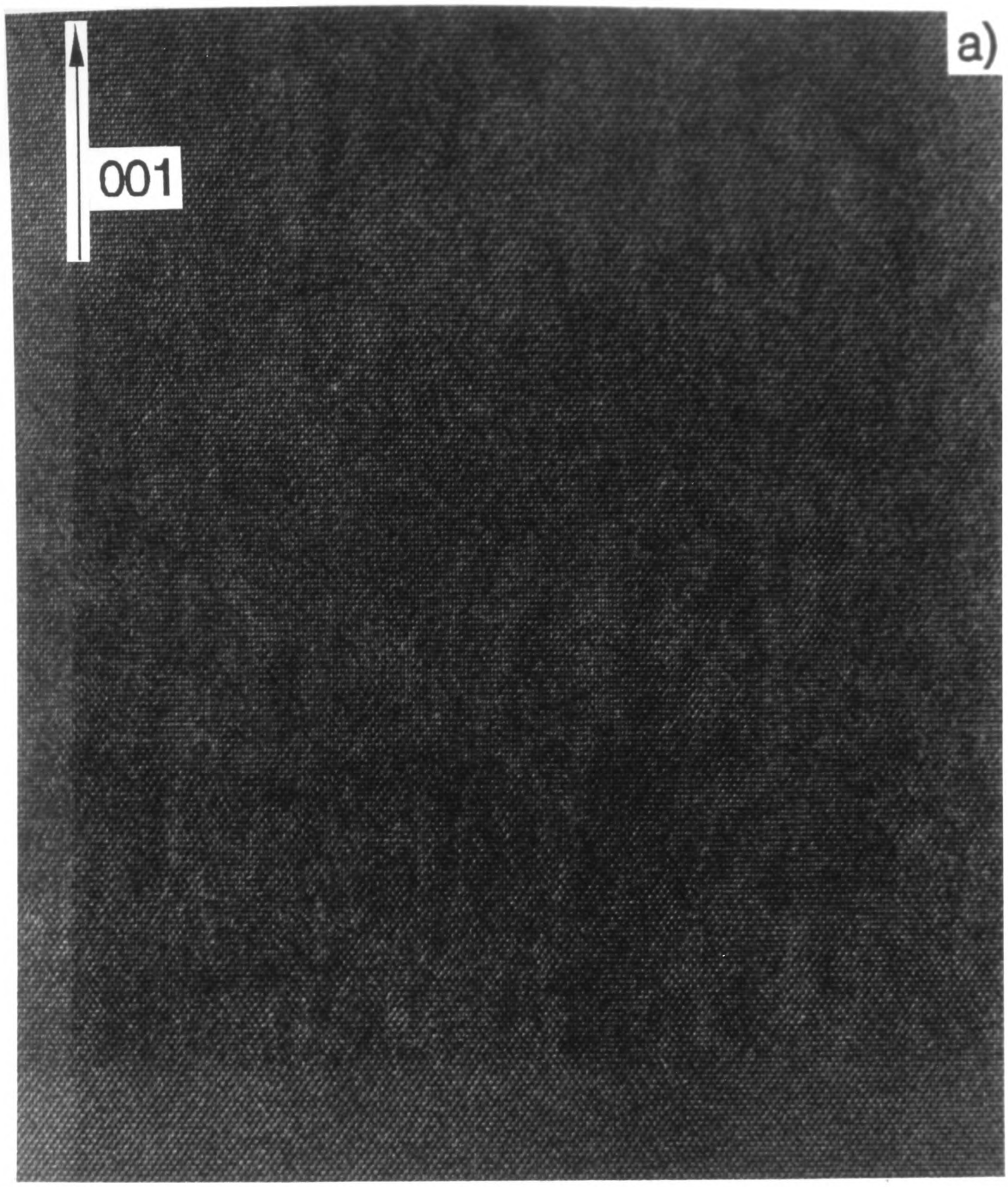

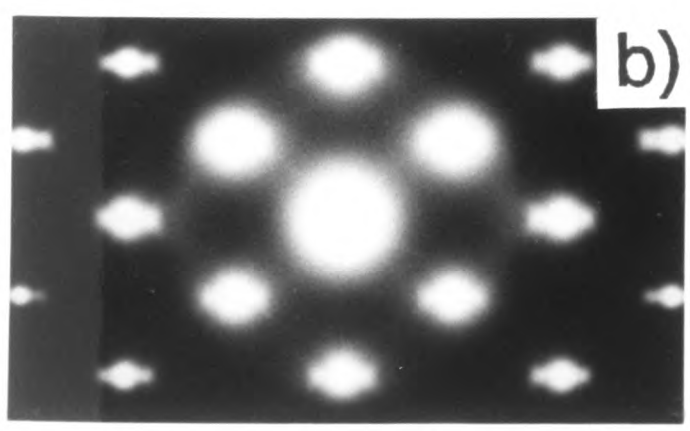

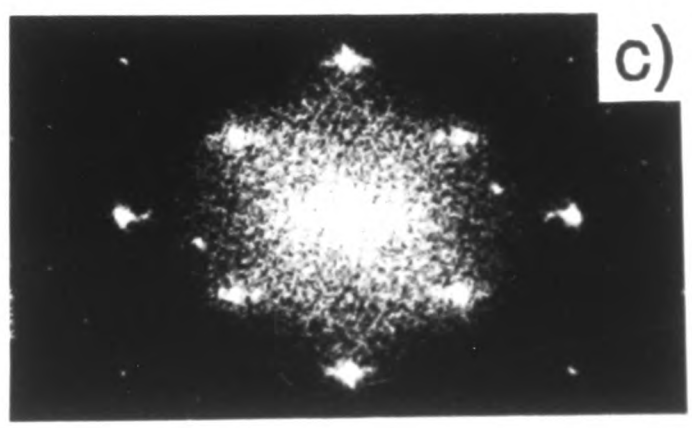

Fig. 5.14

one of the [110] streaks, were blocked out. A soft edge window was placed around the [110] streak near the (002) Bragg spot. This produced a wavy fine columnar-like contrast image elongated along the [001] growth direction, as shown in Fig. 5.15(b). In Fig. 5.15(a) is shown the enlarged HREM micrograph, which corresponds to part of Fig. 5.14(a). It is noteworthy that the fine columnar-like contrast obtained from the streak represents a quasi-periodic platelet of aggregation in the crystal of a wavelength of ~2 to 3nm.

In summary, plan-view and cross-section TEM and TED examinations were used to characterise the alloy clustering behaviour of InP_ySb_{1-y} alloy layers grown at 460 to 500°C. The results obtained from detailed TEM studies revealed that there exists a fine scale modulated contrast oriented in the <100> directions, and a quasi-periodic fine needle-like contrast oriented along the [001] growth direction. The $[\bar{1}10]$ TED pattern showed characteristic diffuse streaks along the [110] direction. TED results and computer HREM image processing have confirmed the direct relationship between the diffuse streak and the fine needle-like contrast visible in TEM micrographs.

5-3-3 Discussion

The TED and TEM results showed a quasi-periodic fine scale modulated contrast, which may result from the presence of a compositional modulation due to spinodal decomposition, and a quasi-periodic fine needle-like contrast elongated along the [001] growth direction. As discussed in section 5-2-3, a fine scale modulated contrast is related to the presence of quasi-periodic strain fields present in the crystal, which may be associated with composition modulations possibly due to spinodal decomposition (9-13,15). Unusual diffuse streaks were present passing through the fundamental spots along the [110] direction in the $[\bar{1}10]$ TED patterns and these were related to a quasi-periodic fine needle-like contrast visible in TEM micrographs. The origin of this characteristic streaking is not obvious.

Similar diffuse streaks were reported by Ihm et al.(40) in TED patterns from GaAsSb layers grown on (001) GaAs and InP substrates using MBE. The maximum intensity of their diffuse streaks appeared to be at the 1/8 and 7/8**g**(220) positions. The length of the diffuse

Figure 5.15

(a) Enlarged micrograph of HREM image in Fig. 5.14 (a). (b) A computer digitized image of the wavy contrast in the [001] growth direction formed using only the [110] diffuse streak.

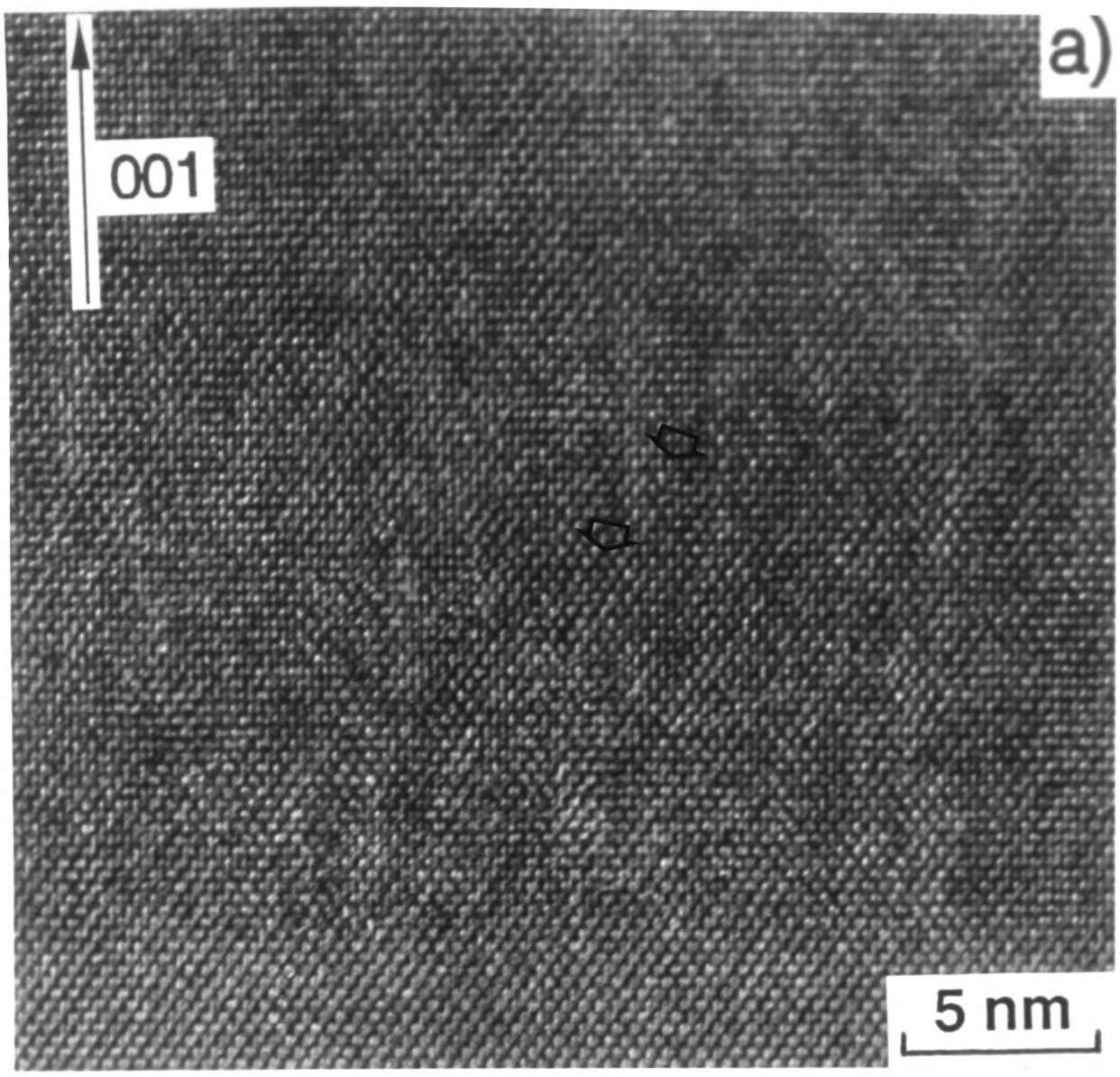
a)
001
5 nm

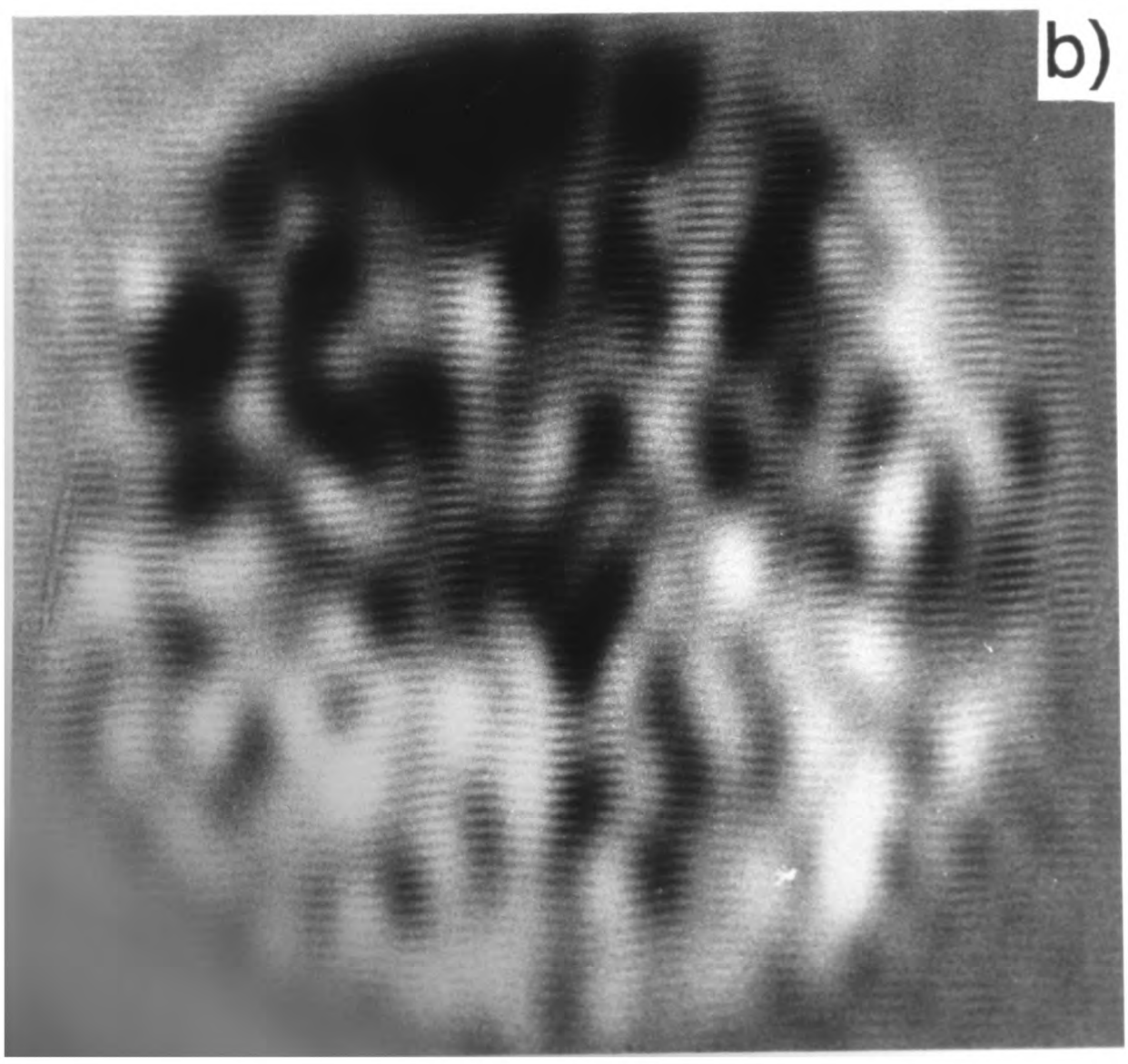
b)

streaks was reported to increase with increasing growth temperature from 480 to 580°C. It was suggested that such a diffuse streak elongated in the [110] direction may be due to the presence of a compositional fluctuation in that direction. The presence of such streaks along the [110] direction is similar to our results for InPSb, which show the presence of diffuse streaks in $[\bar{1}10]$ and [001] TED patterns of the layers.

Murgatroyd, Norman and Booker (41) investigated $GaAs_ySb_{1-y}$ (y=0.20, 0.5, 0.75) grown using MBE and reported similar diffuse streaks passing through the main spots along the [110] direction in [001] and $[\bar{1}10]$ TED patterns. The maximum in intensity of the diffuse streaks was $\pm 1/8\mathbf{g}220$. The diffuse streaks were strongest and best defined for y=0.75, present for y=0.5 and not observed for y=0.29. They concluded that a modulation is present in the [110] direction in the $GaAs_ySb_{1-y}$ layers, with a periodicity of $\sim 4d_{110}$.

Zhu et al.(41) reported diffuse streaks in TED patterns obtained from Y-Ba-Cu-O oxides. Two sets of streaks were observed along the [110] and $[\bar{1}10]$ directions. It was suggested that the diffuse streaks originate from quasi-periodic shear displacements in the crystal lattice due to the presence of off-stoichiometric oxygen. The main features found by Zhu et al., which are different from ours, are as follows:

i) increase of the streak length with increasing order of Bragg reflection.

ii) appearance of streaks in both [110] and $[\bar{1}10]$ directions.

iii) presence of modulated contrast parallel to the **g** vector used.

These differences indicate that a quasi-periodic fine needle-like TEM contrast and associated characteristic diffuse streaks in TED patterns are not related to shear displacements but due to thin disc-shaped aggregation of atoms (associated quasi-periodic lattice parameter variation).

In the present system, the diffuse streaks are present solely in the $[\bar{1}10]$ TED patterns. This suggests that the fine needle-like contrast and TED diffuse streaks found in InP_ySb_{1-y} layers grown using MOCVD may be associated with surface reconstruction during layer growth. From scanning tunnelling microscopy, an InP (001) - 2x4 surface reconstruction mode has been reported by Weiss et al.(43). We assume a similar surface reconstruction behaviour in InPSb. In a (001) 2x4 surface reconstruction, there is a missing P-dimer every 3 atoms along the [110] direction (44). As shown in Fig. 5.16(a), the long

Figure 5.16

(a) 'Missing-dimer' atomic model (ref.43,44) for the (2x4) reconstructed (001) surface of InP with P-P dimers in the [$\bar{1}$10] direction and [110] rows of P atoms within the surface cells. (b) [$\bar{1}$10] projection of arrangement of atoms, showing that the position of the missing dimer rows alternates along the [001] growth direction.

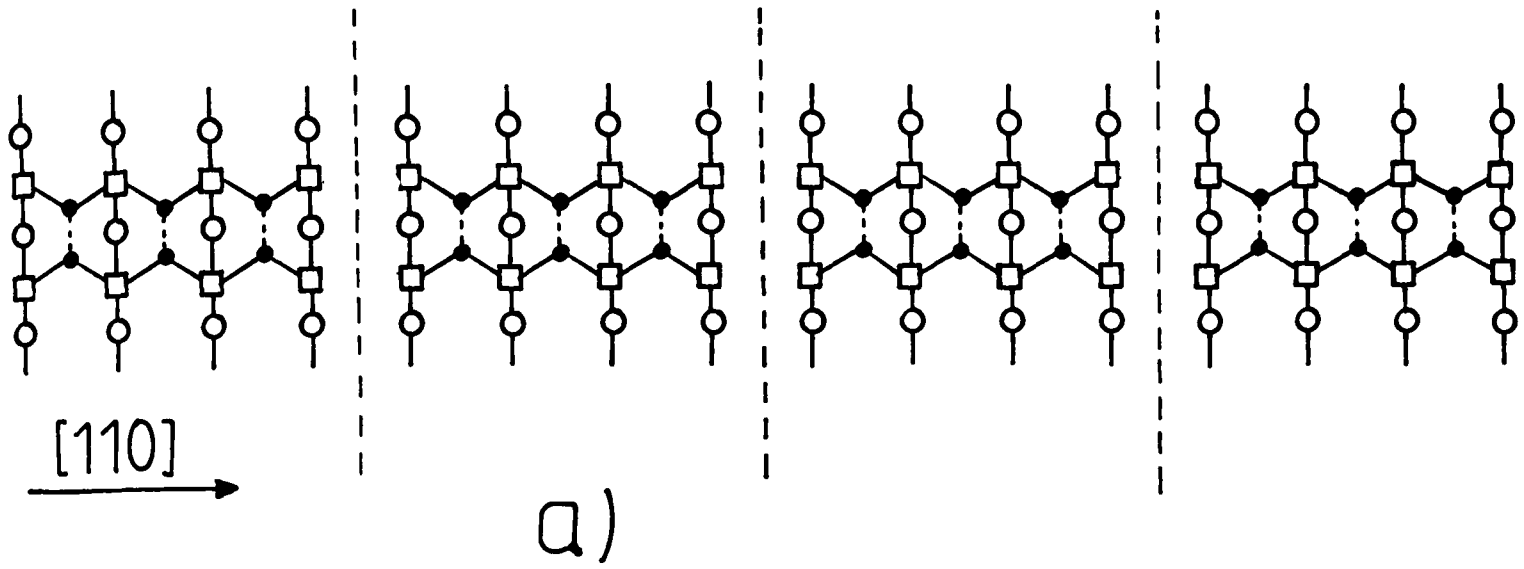

a)

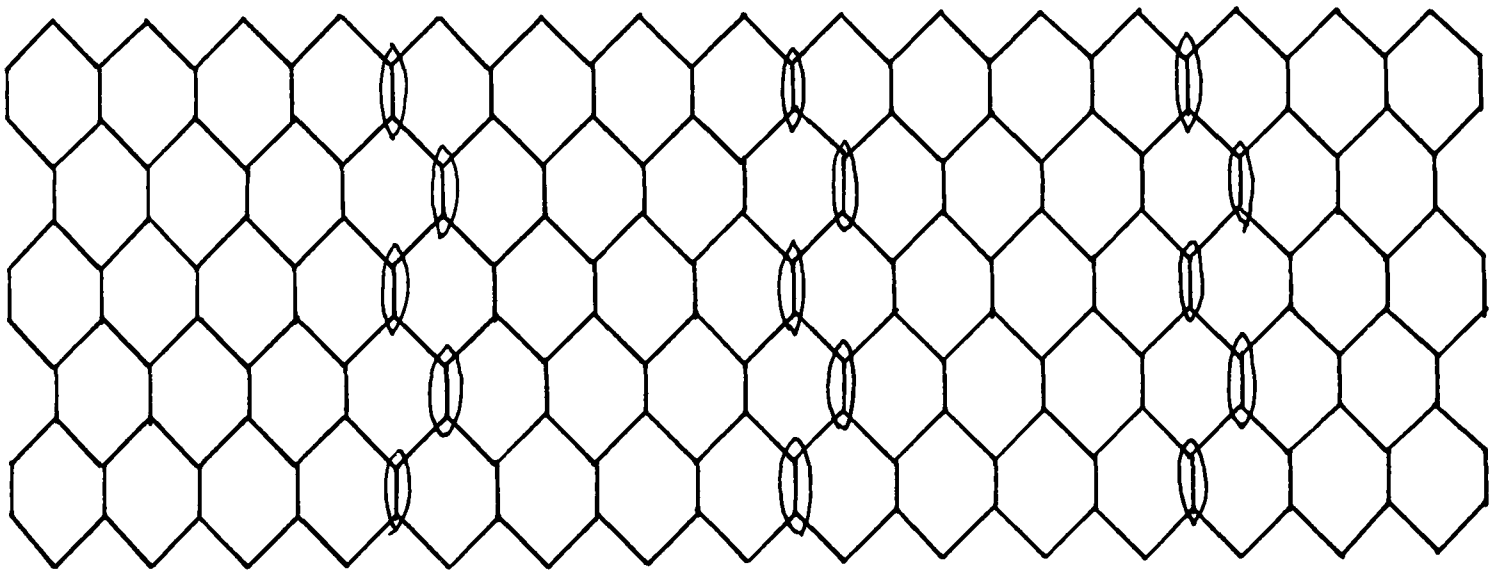

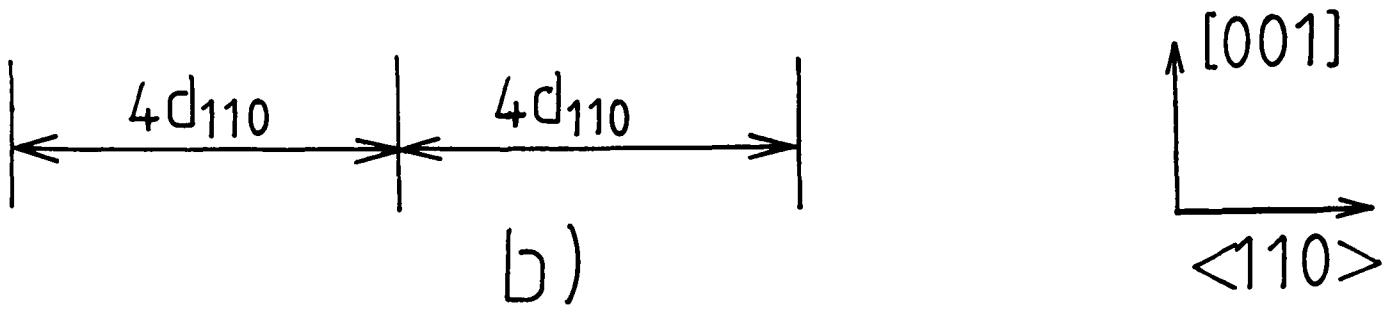

b)

Fig. 5.16

axis of the reconstructed surface, with a spacing of $8xd_{220}$, (i.e the distance between the missing dimers), is parallel to the [110] direction. It was shown from the TEM DF examinations that the wavelength of the fine needle-like contrast along the [110] direction is ~1.9 nm, which corresponds to approximately $8xd_{220}$. The fine needle-like contrast along the [001] growth direction was observed to be discontinuous and not straight, and the length of the contrast was found to vary from 6nm to 27nm. If this needle-like contrast feature is related to surface reconstruction, the position of the missing dimer rows would have to alternate along the [001] growth direction in order to produce the over 6 nm long morphology observed, as illustrated in Fig. 5.16(b). There are two possible mechanisms for the formation of the fine needle-like contrast. First, during dimerization, for adjacent cells that are out of phase, successive deposition of following monolayers may result in boundaries forming an array of APBs (in the CuPt-type ordering that also arises in the layers) along the [001] growth direction, which will be discussed in detail in chapter 6. Second, in the case of in-phase adjacent cells, as compared to the subsurface which is underneath dimers, the subsurface which is underneath the missing dimers experiences a different state of microscopic stress. This different stress may give rise to segregation of vacancies, Sb or P atoms, resulting in irregular sheets along the [001] growth direction. However, the exact mechanism for such a feature is still not obvious, since there is no direct way to obtain information concerning surface reconstruction behaviour during MOCVD growth, and so there is no available data about the surface reconstruction mode in InPSb alloy semiconductors. Nonetheless, we tentatively suggest that the characteristic needle-like feature in the MOCVD InP_ySb_{1-y} layers results from either boundaries or segregation of atoms related to surface reconstruction, leading to a quasi-periodic fine needle-like contrast visible only in the $[\bar{1}10]$ cross-section.

5-4 Alloy clustering in GaP_ySb_{1-y} layers

5-4-1 Experimental

The MOCVD growth was carried out in a horizontal, atmospheric pressure, infrared heated reactor (37). The reactants were trimethylgallium (TMGa) and trimethylantimony (TMSb), held in temperature controlled bubblers at -12 and 11°C, respectively, and phosphine consisting of a 10% mixture in Pd-diffused H_2. The molar flow rates were varied in the following ranges: f_{TMGa} = 1.92-2.88x10^{-5} mol/min, f_{TMSb} = 3.37-7.02x10^{-5} mol/min, and f_{PH_3} = 0.832-4.16x10^{-5} mol/min. The layer composition GaP_ySb_{1-y} was varied from y=0.51 to 0.77, the growth temperature between 500 and 600°C and the growth rate between 0.24 and 1.46nm/s. The layers were grown on (001) GaAs substrates. Details of layers examined are listed in Table 5.3.

5-4-2 TEM and TED analyses

TEM DF investigations using **g**<220> and **g**<400> reflections were carried out on (001) plan-view and <110> cross-sectional specimens to investigate the microstructure of GaP_ySb_{1-y} layers. The examinations showed a quasi-periodic fine scale modulated contrast similar to that previously observed in both the $In_xGa_{1-x}As$ and InP_ySb_{1-y} layers and attributed to alloy clustering due to spinodal decomposition occurring at the growing surface during layer growth. A quasi-periodic fine needle-like contrast occurred, which was also observed in the InP_ySb_{1-y} layers described above and attributed to segregation of atoms associated with rows of missing dimers present in the reconstructed surface during growth.

In order to investigate the diffracted intensity distribution in reciprocal space, detailed TED examinations were performed. The main characteristic features observed by plan-view and cross-section TED patterns were closely similar for all layers, although there were small differences depending on growth temperature, growth rate and layer composition. The intensity of diffuse streaks passing through the main spots depended on the growth

Table 5.3 Epitaxial GaP_ySb_{1-y} MOCVD layers

Sample No.	GaP_ySb_{1-y} (y)	Growth temp. (°C)	Growth rate (nm/s)	Substrate
3-38	0.58	500	0.24	GaAs
3-47	0.67	520	0.56	GaAs
3-37	0.59	530	0.76	GaAs
3-23	0.51	560	0.28	GaAs
3-24	0.75	560	0.56	GaAs
3-17	0.75	580	0.83	GaAs
3-44	0.77	600	1.46	GaAs

temperature and composition. Typical results obtained for a $GaP_{0.75}Sb_{0.25}$ layer grown at 560°C are as follows:

The [001] TED pattern was complicated, as shown in Fig. 5.17(a). The standard array of main spots associated with the zinc-blende type structure was present. The {200} spots were weak, which is consistent with the calculated difference of atomic scattering factors between GaP and GaSb. The other main features for the [001] pole TED pattern were:

i) lines of [110]-oriented diffuse intensity (A);

ii) diffuse streaks through the fundamental reflections, elongated along the [110] direction (B);

iii) satellite spots at 1/4 **g**220 positions (C);

iv) [010]-oriented diffuse intensity with spacing of 1/6**g**040 (D).

The lines of [110]-oriented diffuse intensity pass close to, but not through, the main spots, as described in section 5-2-4 for InGaAs. These [110]-oriented lines of diffuse intensity correspond to the intersection of the Ewald sphere with planes of diffuse intensity perpendicular to all <110> directions of the crystal. Their intensity varies with position and has a maximum intensity near to the main diffraction spots, as described earlier (Fig. 5.5).

The [112] TED pattern is illustrated in Fig. 5.17(b) and shows hexagonal shaped diffuse intensity aligned along the $[1\,\bar{1}\,1]$ direction (E). Maxima in intensity are located at the 1/4**g**220 and 1/4 **g**111 positions.

For the [110] TED pattern, Fig. 5.18(a), the higher order spots were elongated along the [001] and $[\bar{1}\,10]$ directions and hexagonal shaped diffuse intensity occurred along the [001] direction. For the $[\bar{1}\,10]$ TED pattern, Fig. 5.18(b), a diffuse streak through the fundamental spots was present, elongated along the [110] direction, whose length corresponds to the width of the fine needle-like structure visible in TEM micrographs observed from the $(\bar{1}\,10)$ cross-section specimen. High order spots were also elongated along the [001] direction and fine diffuse lines were present running through the main spots along the [111] and $[11\,\bar{1}]$ directions.

Figure 5.17

Plan-view TED patterns from GaP_ySb_{1-y} MOCVD layer (y=0.75) grown at 560°C using 2.0μm/hr. (a) [001] pattern, showing the following: i) the presence of [110]-oriented diffuse intensity (A); ii) a diffuse streak through the fundamental reflections which is elongated in the [110] direction (B); iii) satellite spots appearing at 1/4**g**220 positions (C); iv) [010]-oriented diffuse intensity with spacing of 1/6**g**040 (D). (b) [112] pattern, showing hexagonal shaped diffuse intensity with maxima at 1/4**g**220 and 1/4**g**111 positions (E).

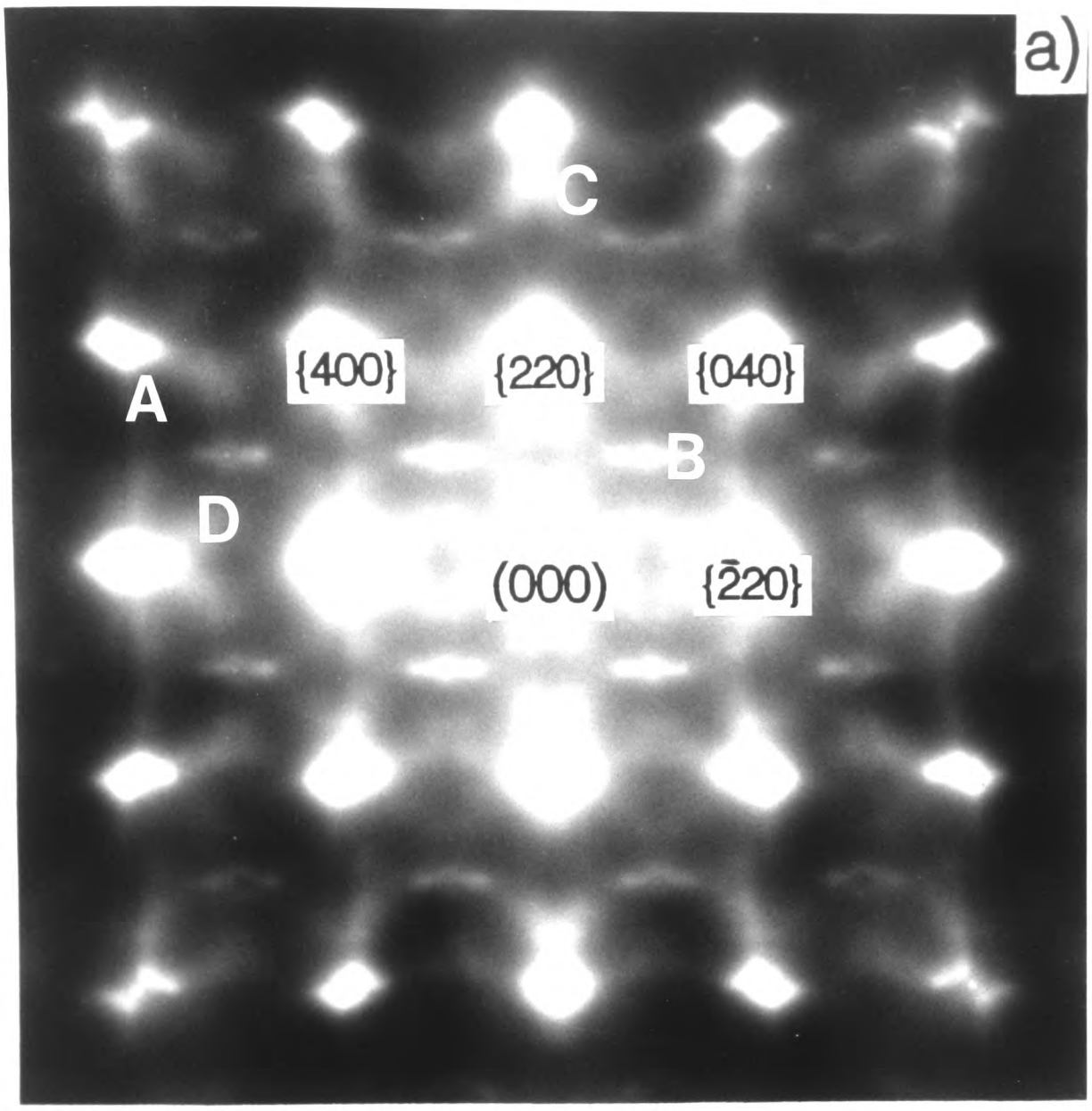
a)
C
{400}
{220}
{040}
A
B
D
(000)
{$\bar{2}$20}

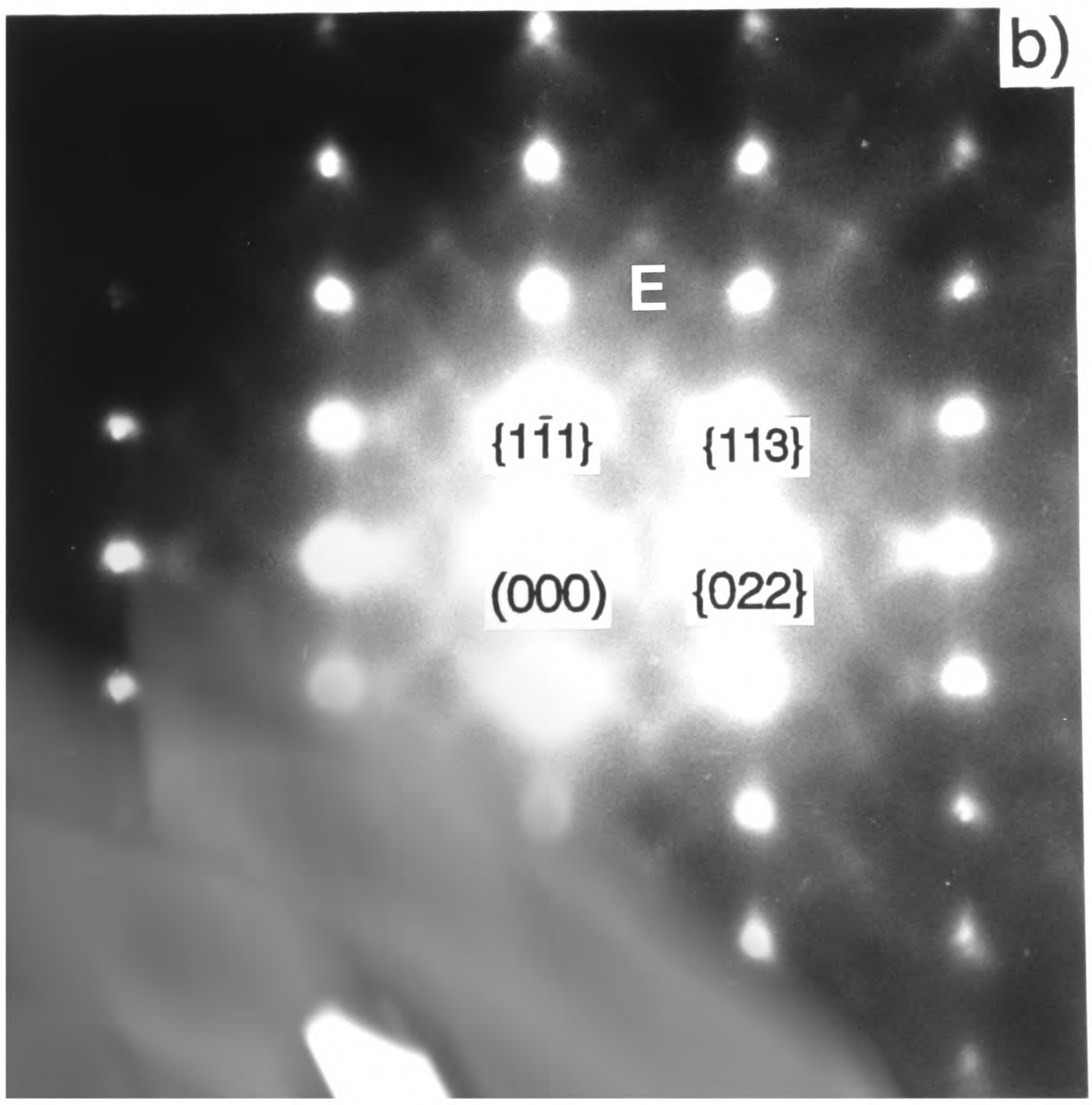
b)
E
{1$\bar{1}$1}
{113}
(000)
{022}

Figure 5.18

Cross-section TED patterns from GaP_ySb_{1-y} MOCVD layer (y=0.75) grown at 560°C using 2.0μm/hr. (a) [110] pattern, showing that the higher order spots are elongated along the <001> directions. Hexagonal shape diffuse intensity along the [001] growth direction is visible. (b) $[\bar{1}10]$ pattern, showing [110] diffuse streaks through the main spots corresponding to the pseudo-period of the fine needle-like contrast.

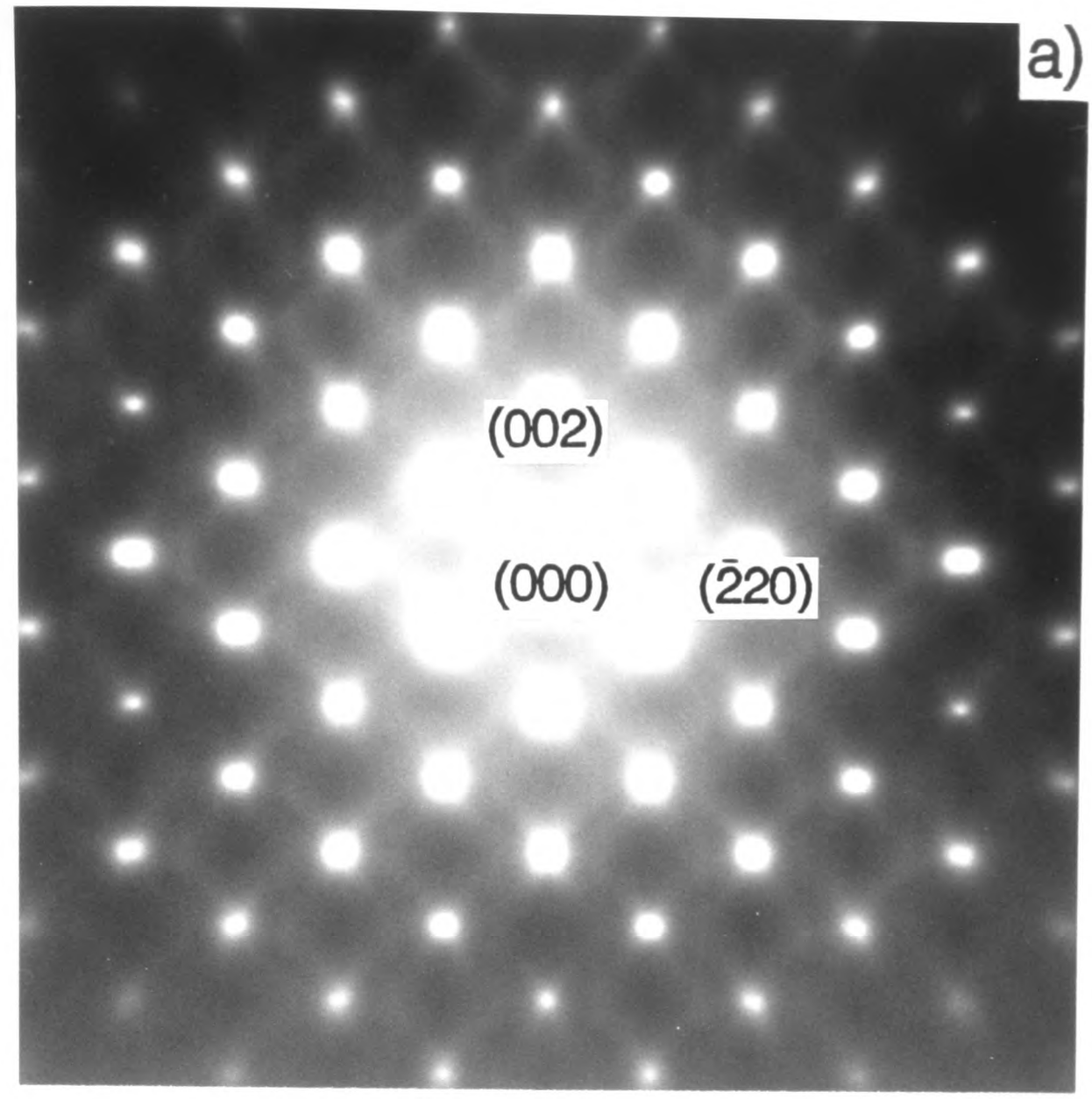

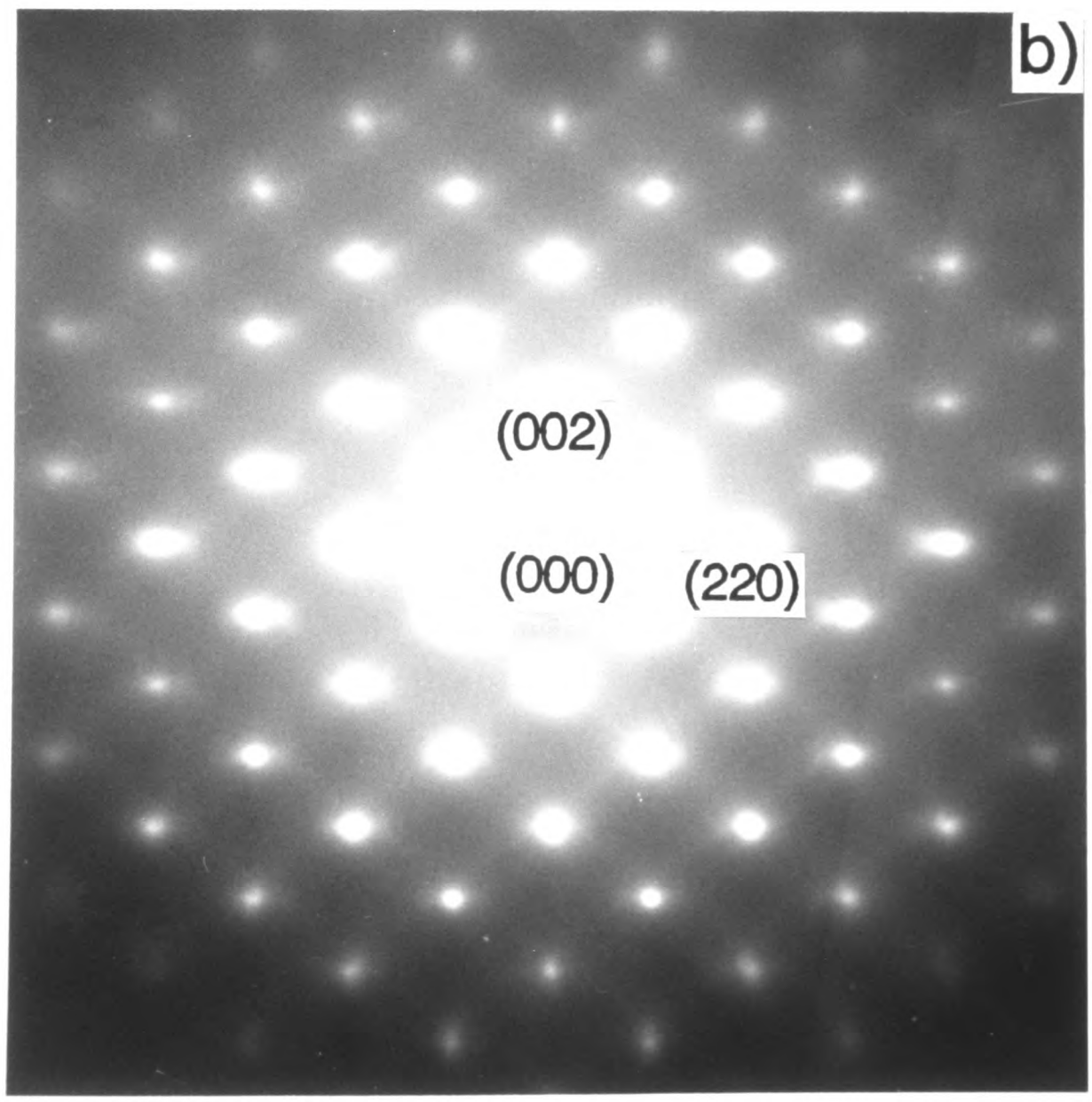

Fig. 5.18

The characteristic features in the TED patterns of the GaP_ySb_{1-y} layers are different from those reported by Glas et al.(21) for InGaAsP, who reported only the existence of {110}-oriented diffuse lines. As discussed by Glas et al.(21), one of the main features revealed by TED examinations is that the maxima in intensity of the [110] diffuse lines are located away from the main diffraction spots. This indicates that these characteristic features are not associated with phonon scattering, (i.e. similar [110]-oriented diffuse lines can occur as a result of phonon scattering), but in this case pass exactly through the main diffraction spots (25). In addition to the [110]-oriented diffuse lines, other complicated features were revealed by TED investigations. Diffuse streaks, elongated along the [110] direction, were present in the [001] and $[\bar{1}10]$ TED patterns, Fig. 5.17(a) and Fig. 5.18(b), respectively, which are thought to be similar to those in the InP_ySb_{1-y} layers. These may also arise from segregation, which may be due to stresses associated with surface reconstruction.

In order to interpret the origin of the diffuse lines, calculation of the structure of $GaP_{0.75}Sb_{0.25}$ using the Valence Force Field (VFF) model of Keating (22) and Martin (23), which was known to yield distributions of interatomic distances compatible with the extended X-ray absorption fine structure (EXAFS) results for disordered ternary alloys (42), was performed. Design of the model, in which the excess energy of a given distribution of atoms displaced from their virtual crystal (VC) sites in a ternary alloy was considered, and simulation of this model was performed by Dr. F. Glas, CNET, France, on a CONVEX 210 computer. Details of the crystal model and computer simulations have been reported elsewhere (20).

In Fig. 5.19 is shown the calculated distribution of diffuse intensity in a quadrant of a $[1\bar{1}2]$ reciprocal plane for the $GaP_{0.75}Sb_{0.25}$ layer. The grey scales have been adjusted so that the smoothly decreasing background arising from random disorder is almost entirely included in the first grey level. A part of the main features is reproduced. Hexagonal shaped diffuse intensity is present along the $[1\bar{1}1]$ direction. Fig. 5.20 displays the calculated distributions of diffuse intensity in a quadrant of a $[1\bar{1}0]$ reciprocal plane for the $GaP_{0.75}Sb_{0.25}$ layer. Elongation of high order spots observed in the $[1\bar{1}0]$ experimental diffraction pattern is reproduced: high order spots are elongated in the [001] and [110]

Figure 5.19

(a) Simulated diffraction pattern for the $(1\,\bar{1}\,2)$ reciprocal plane of GaP_ySb_{1-y} (y=0.75). Some of the features in the experimental TED pattern are exhibited.

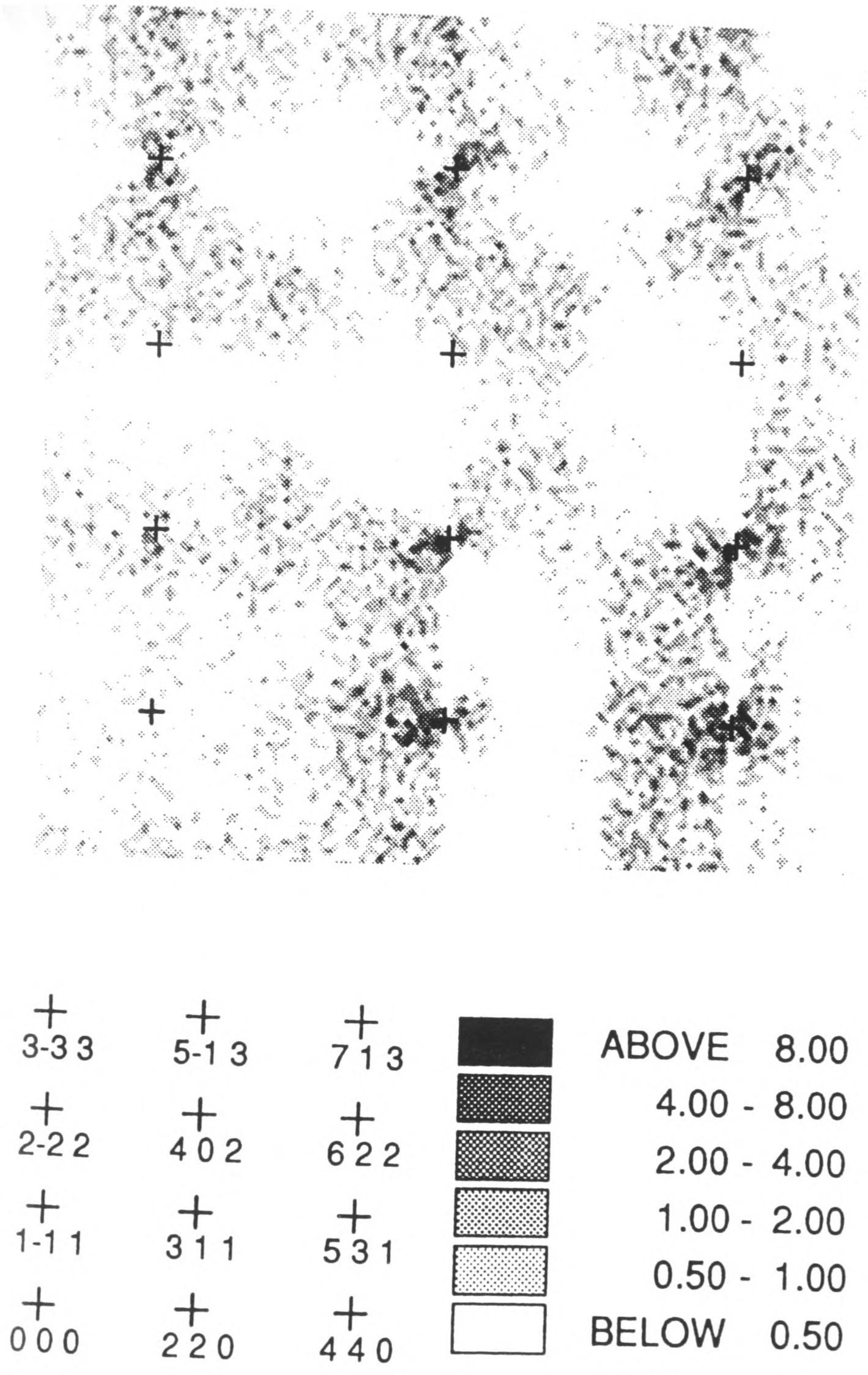
3-3 3
5-1 3
7 1 3
2-2 2
4 0 2
6 2 2
1-1 1
3 1 1
5 3 1
0 0 0
2 2 0
4 4 0
ABOVE 8.00
4.00 - 8.00
2.00 - 4.00
1.00 - 2.00
0.50 - 1.00
BELOW 0.50

Fig. 5.19

Figure 5.20

(a) Simulated diffraction pattern for the $(1\bar{1}0)$ reciprocal plane of GaP_ySb_{1-y} (y=0.75). Some of the features in the experimental TED pattern are exhibited.

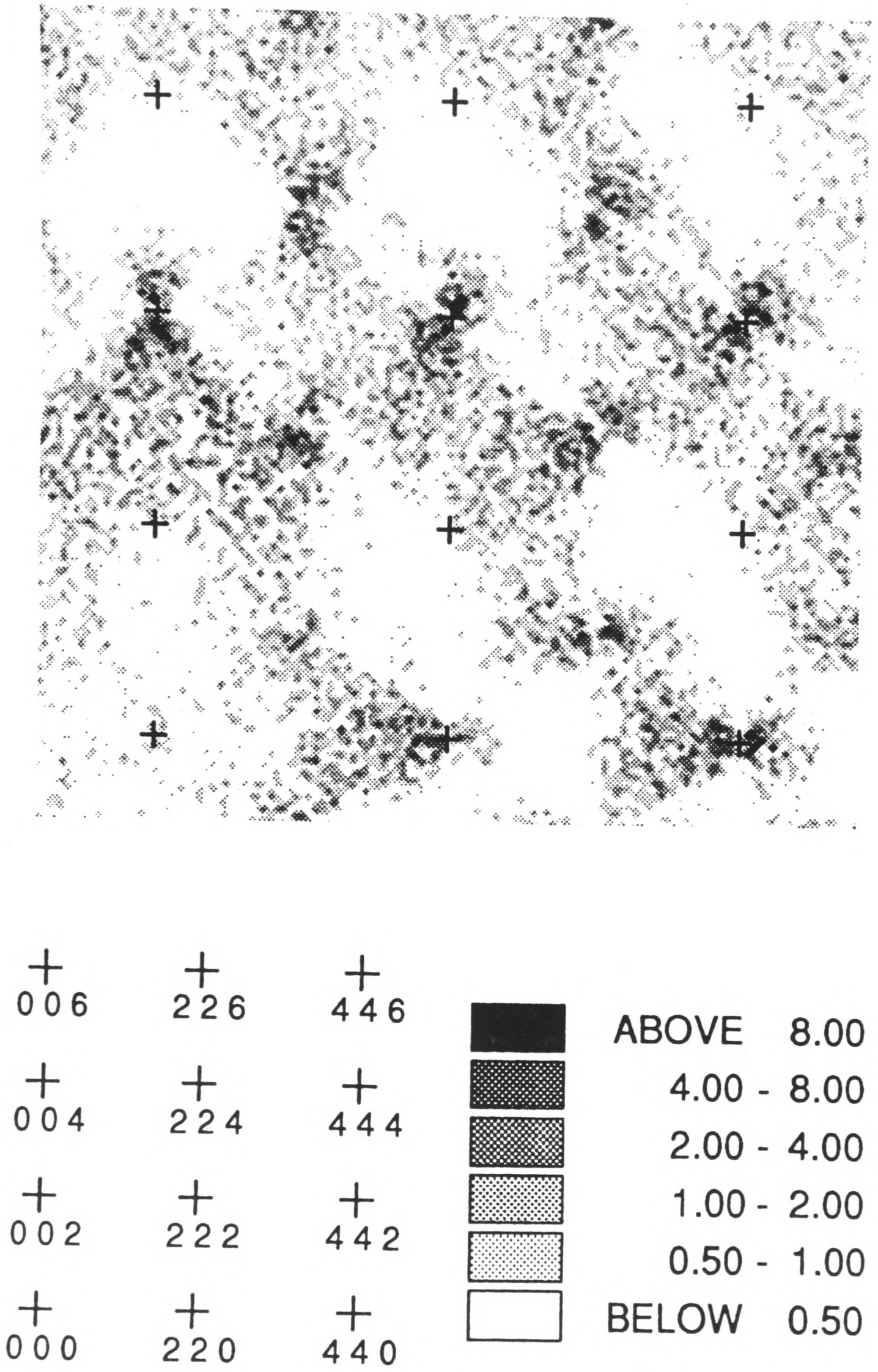
006
226
446
004
224
444
002
222
442
000
220
440
ABOVE 8.00
4.00 - 8.00
2.00 - 4.00
1.00 - 2.00
0.50 - 1.00
BELOW 0.50

Fig. 5.20

directions. However, the diffuse streaks passing through the fundamental spots, parallel to the [110] direction, are not reproduced, indicating that they are not associated with a statistically random distribution of atoms on the mixed Group V sublattice, but due to another source such as thin disc type segregation of atoms, as described for the InPSb layers. Better agreement between the experimental and calculated diffraction patterns would undoubtedly have occurred if in the simulations the effects of the fine needle-like contrast visible in the (220) and (002) TEM DF micrographs had been included.

The results obtained by TED examinations and simulations show that the observed distributions of diffuse intensity are partially consistent with random disorder. Consideration of random disorder leads to possible points which may be related to atomic configuration behaviour, i.e. deviation from mean virtual crystal sites even in a perfectly disordered alloy and atomic random distributions of atoms in the mixed sublattices. It is noteworthy that the observed [110]-oriented diffuse lines could arise by a static displacement of the sites of the mixed sublattices. Glas (20) demonstrated that in InGaAs the result of simulations of the displacements associated with chains of 2 or 3 In atoms in a GaAs matrix is consistent with those of the experimental observations. Likewise in GaPSb a number of short random chains of P or Sb atoms might be predicted. The random chains and atomic displacements induced by atoms along the <110> directions could result in the <110>-oriented diffuse lines.

In summary, in order to fully understand the characteristic features observed in the plan-view and cross-sectional TED patterns from GaPSb, more accurate models and simulations need to be performed. However, in spite of the lack of full information concerning the characteristic features, it is concluded that the diffuse lines elongated along the [110] direction arise from static displacements of the atoms on the mixed Group V sublattice, since the simulated patterns were induced solely by the contributions of random disorder.

REFERENCES-CHAPTER 5

1. B. de Cremoux, J. de Physique coll. C5, suppl. **No12**, (1982) C5-19.
2. K. Onabe, Jpn. J. Appl. Phys. **21** (1982) 964.
3. G.B. Stringfellow, J. Appl. Phys. **54** (1983) 404.
4. K. Ishida, T. Shumiya, T. Nomura, H. Ohtani and T. Nishizawa, J. Less-Common Matals, **142** (1988) 135.
5. P. Hénoc, A. Izrael, M. Quillec and H. Launois, Appl. Phys. Lett. **40** (1982) 963.
6. H. Launois, M. Quillec, F. Glas and M.J. Treacy, GaAs and Related Compounds, Alberquerque, Inst. Phys. Conf. Ser. **65** (1982) 537.
7. J.P. Gowers, Appl. Phys. **A31** (1983) 23.
8. S. Mahajan, B.V. Dutt, H. Temkin, R.J. Cava and W.A. Bonner, J. Cryst. Growth **68** (1984) 589.
9. A.G. Norman and G.R. Booker, J. Appl. Phys. **57** (1985) 4715.
10. A.G. Norman and G.R. Booker, Inst. Phys. Conf. Ser. **76** (1985) 257.
11. A.J. Bons, Y.S. Oei and F.W. Schapink, Inst. Phys. Conf. Ser. **60** (1989) 161.
12. S.N.G. Chu, S. Nakahara, K.E. Strege and W.D. Johston, J. Appl. Phys. **57** (1985) 4610
13. J.S. Roberts, G.B. Scott and J.P. Gowers, J. Appl. Phys. **52** (1981) 4018.
14. S.J. Bass, S.J. Barnett, G.T. Brown, N.G. Chew, A.G. Cullis, A.D. Pitt and Skolnick, J. Cryst. Growth **79** (1986) 378.
15. A.G. Norman, D.Phil. Thesis, Oxford University, 1987.
16. J.L. Benchimol, M. Quillec and S. Slempkes, J. Cryst. Growth **64** (1984) 96.
17. M. Quillec, J.L. Benchimol, S. Slempkes and H. Launois, Appl. Phys. Lett. **42** (1983) 886.
18. S. Mukai, J. Appl. Phys. **54** (1983) 2635.
19. P. Blood and A.D.C. Grassie, J. Appl. Phys. **56** (1984) 1866.
20. F. Glas, Inst. Phys. Conf. Ser. **100** (1989) 167.
21. F. Glas, C. Gors and P. Hénoc, Phil. Mag. **B62** (1990) 373.
22. P.N. Keating, Phys. Rev. **145** (1966) 637.

23. R.M. Martin, Phys. Rev **B1** (1970) 4005.

24. F. Glas, P. Hénoc and H. Launois, Inst. Phys. Conf. Ser. **76** (1985) 251.

25. C.H. Narayanan and S.M. Copley, Phys. Stat. Sol. **A23** (1974) 123.

26. P.M. Petroff, J. Vac. Sci. Technol. **14** (1977) 973.

27. K. Alavi, P.M. Petroff, W.R. Wagner and A.Y. Cho, J. Vac. Sci. Technol. **B1** (1983) 146.

28. K.-H. Kuesters, B.C. DeCooman, J.R. Shealy and C.B. Carter, J. Cryst. Growth **71** (1985) 514.

29. J.E. Bullock, C.J. Humphreys, A.G. Norman and J.M. Titchmarsh, Inst. Phys. Conf. Ser. **87** (1987) 643.

30. J.A. Liddle, R.A.D. Mackenzie, C.R.M. Grovenor and A. Cerezo, Inst. Phys. Conf. Ser. **100** (1989) 81.

31. V.M. Vorob'ev, V.A. Murov'ev and V.A. Pautelocv, Sov. Phys.-Sol. Stat. **23** (1981) 653.

32. F.H. Eisen and C.E. Birchonall, Acta Met. **5** (1957) 265.

33. J.W. Cahn, Acta Met. **10** (1962) 907.

34. V. Daniel and H. Lipson, Proc. R. Soc. London, Ser. A**181**, 368 (1943) and **182**, 378 (1944).

35. G.B. Stringfellow, J. Cryst. Growth **27** (1974) 21.

36. M.J. Jou, Y.T. Cherng and G.B. Stringfellow, Appl. Phys. Lett. **64** (1988) 1472.

37. C.P. Kuo, R.M. Cohen and G.B. Stringfellow, J. Crystal. Growth **64** (1983) 461.

38. P.B. Hirsch, A. Howie, R.B. Nicholson, D.W. Pashley and M.J. Whelan "Electron Microscopy of Thin Crystals" (Butterworths, London 1965) p320.

39. Y. Zhu, M. Suenaga and Y. Xu, Phil. Mag. Lett. **60** (1989) 51.

40. Y.-E. Ihm, N. Otsuka, J. Klem and H. Morkoc, Appl. Phys. Lett. **51** (1987) 2013.

41. I.J. Murgatroyd, A.G. Norman and G.R. Booker, J. Appl. Phys. **68** (1990) 1123.

42. Y. Zhu, M. Suenaga and A.R. Moodenbaugh, Phil. Mag. Lett. **62** (1990) 51.

43. M. Podgony, M.T. Czyzyk, A. Balzarotti, P. Letardi, A. Kisiel and M. Zimnal-Starnawska, Solid St. Commun., **55** (1985) 413.

44. W. Weiss, R. Hornstein, D. Schmeisser and W. Göpel, J. Vac. Sci. Technol. **B8** (1990) 715.

45. D.J. Chadi, J. Vac. Sci. Technol. **A5** (1987) 834.

CHAPTER 6

ATOMIC ORDERING IN $In_xGa_{1-x}As$, $InAs_ySb_{1-y}$ and InP_ySb_{1-y} COMPOUND SEMICONDUCTORS

6-1 Introduction

Since the first experimental observation of atomic ordering in GaAlAs epitaxial layers by Kuan et al.(1), long-range ordered structures have been reported in a number of III-V compound semiconductors grown by a variety of techniques such as LPE, MOCVD, VLE and MBE (e.g. see section 2-4-2).

Some III-V compound semiconductors such as $In_xGa_{1-x}P$ (x=0.5) exhibit a variation in band gap with changing growth conditions. Microstructural investigations performed on such layers showed that the presence of CuPt-type ordering correlated with a reduction of the band gap in comparison with disordered semiconductor alloys. It is generally believed that the formation of the CuPt-type ordered structure is a surface related phenomenon that occurs during layer growth. In order to interpret the formation of CuPt-type ordering in III-V compound semiconductors, several mechanisms, for example, the bond length model by Norman (2) and Suzuki et al.(3) and the concept of surface reconstruction by Murgatroyd et al.(4), have been proposed. In spite of these attempts, however, the exact formation mechanism for the atomic ordering still remains a matter of debate.

In this chapter, we present results obtained from detailed TED, TEM and HREM investigations of MOCVD $In_xGa_{1-x}As$, MOCVD and MBE $InAs_ySb_{1-y}$, and MOCVD InP_ySb_{1-y} layers. The TED results indicate that CuPt-type ordering occurs in many of the InGaAs, InAsSb and InPSb layers and that only two of the four possible {111} variants are present. The generation of the ordering occurs at the growing surface of the layers and there is a critical temperature below which the ordered structure is stable. The degree of ordering is strongly dependent on growth conditions and layer compositions. Ordered domain structures and antiphase domain boundaries occur in $In_xGa_{1-x}As$ (x=0.53). A possible model is proposed to describe the formation of the CuPt-type ordering in both the mixed Group III and V compound semiconductors.

6-2 Atomic ordering in MOCVD $In_xGa_{1-x}As$ layers

6-2-1 Experimental

$In_{0.53}Ga_{0.47}As$ layers were grown on (001) InP and GaAs substrates by atmospheric pressure MOCVD using sources of trimethylgallium (TMG), trimethylindium (TMI) and arsine and phosphine as sources. The horizontal MOCVD reactor used was described in ref. (5) and the growth conditions were given in section 5-2-1. Annealing was carried out to see if thermal bulk diffusion affects atomic ordering. In order to investigate the growth condition dependence of the ordering, a series of samples grown at different growth rates and growth temperatures was designed. Details of the samples examined are summarised in Table 5.1.

6-2-2 TED analysis of ordering behaviour

6-2-2-1 Effects of growth conditions on atomic ordering

In order to distinguish between the possible {111} ordered variants, the polarity of the [110] and [$\bar{1}$10] cross-section specimens was determined using the chemical etching and convergent beam electron diffraction techniques (6-8) described in chapter 3. These were used on the GaAs substrate of the epitaxial layer grown at 550°C with the slow growth rate of 0.2nm/s, which exhibited strong CuPt-type ordering on two of the {111} planes, and the result was assumed to apply to all the other InGaAs layers.

TED investigations were carried out on two orthogonal <110> cross-section specimens to examine the structure and degree of ordering in InGaAs layers, which were grown at temperatures ranging from 500°C to 700°C with the slow growth rate of 0.2 nm/s. The cross-section [$\bar{1}$10] TED patterns of all the layers showed only the fundamental zinc-blende structure spots. Conversely, some of the [110] TED patterns (Fig. 6.1) exhibited the fundamental zinc-blende structure spots, and strong superlattice spots half way between the

Figure 6.1

Cross-section [110] TED patterns from MOCVD $In_{0.53}Ga_{0.47}As$ layers grown at (a) 500°C, (b) and (c) 550°C, (d) 600°C, and (e) 650°C using 0.2nm/s. (b) and (c) are from layers grown on InP and GaAs respectively.

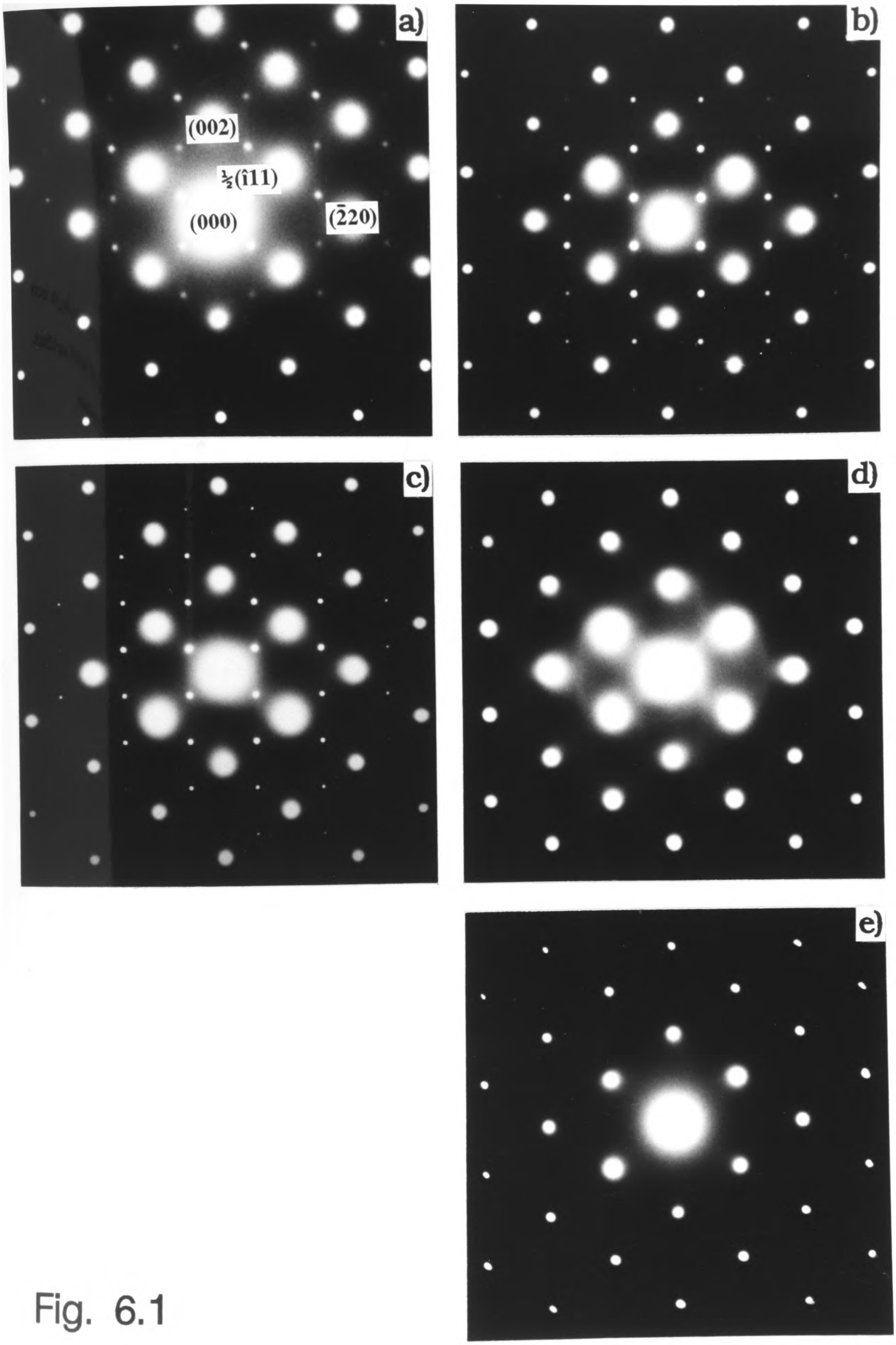

Fig. 6.1

rows of the fundamental spots parallel to the <111> directions; these superlattice spots are normally forbidden for the zinc-blende structure. This is consistent with the existence of an ordered structure in the layers along the <111> directions with a periodicity twice that of the zinc-blende structure. The mixed Group III atom sublattice of the InGaAs layer consists of alternating In-rich and Ga-rich {111} planes, as shown in Fig. 6.2. The 1/2{111} superlattice spots were connected by weak lines of diffuse diffracted intensity running along the [001] growth direction. However, the fundamental spots in these patterns were free of any diffuse intensity, indicating that the diffuse intensity is associated with imperfections in the ordered structure.

The features observed in the [110] TED patterns were strongly dependent on layer growth temperature (Table 6.1). The TED results for the slow growth rate of 0.2nm/s showed that the superlattice spots were of medium intensity for the layer grown at 500°C, reached a relative maximum intensity at 550°C, became weak in intensity at 600°C, and were absent at and above 650°C (Fig. 6.1).

For the medium growth rate of 0.95 nm/s, the ordering was again dependent on the growth temperature (Table 6.1). For [110] patterns (Fig. 6.3), the superlattice spots were absent for the layer grown at 500°C, exhibited weak intensity at 550°C, increased to medium intensity at 600°C and were again absent at 650°C and above. For the layer grown at 596°C, the [001] pattern (Fig. 6.4(a)) showed the fundamental zinc-blende structure spots together with weak satellite spots (marked 's') present at $\pm 1/4\mathbf{g}220$ positions in the $[\bar{1}10]$ direction. The $[\bar{1}10]$ pattern (Fig. 6.4(c)) showed no superlattice spots or diffuse intensity. The [110] pattern (Fig. 6.4(b)) showed strong superlattice spots at 1/2{111} positions which were elongated and slightly tilted towards <111> directions and were connected to each other by lines of diffuse diffracted intensity along the [001] growth direction. These lines imply the existence of rods of diffuse intensity in reciprocal space along the [001] direction. The intersection of these rods with the Ewald sphere gives satellite spots at $\pm 1/4\mathbf{g}220$ positions along the $[\bar{1}10]$ direction in the [001] pattern (Fig. 6.4(a)).

For the fast growth rate of 2.0 nm/s, the ordering was again dependent on the growth temperature (Table 6.1). The superlattice spots exhibited a maximum intensity for the layer

Figure 6.2

[110] projection of InGaAs atomic lattice perfectly ordered on $(1\,\bar{1}\,1)$ planes.

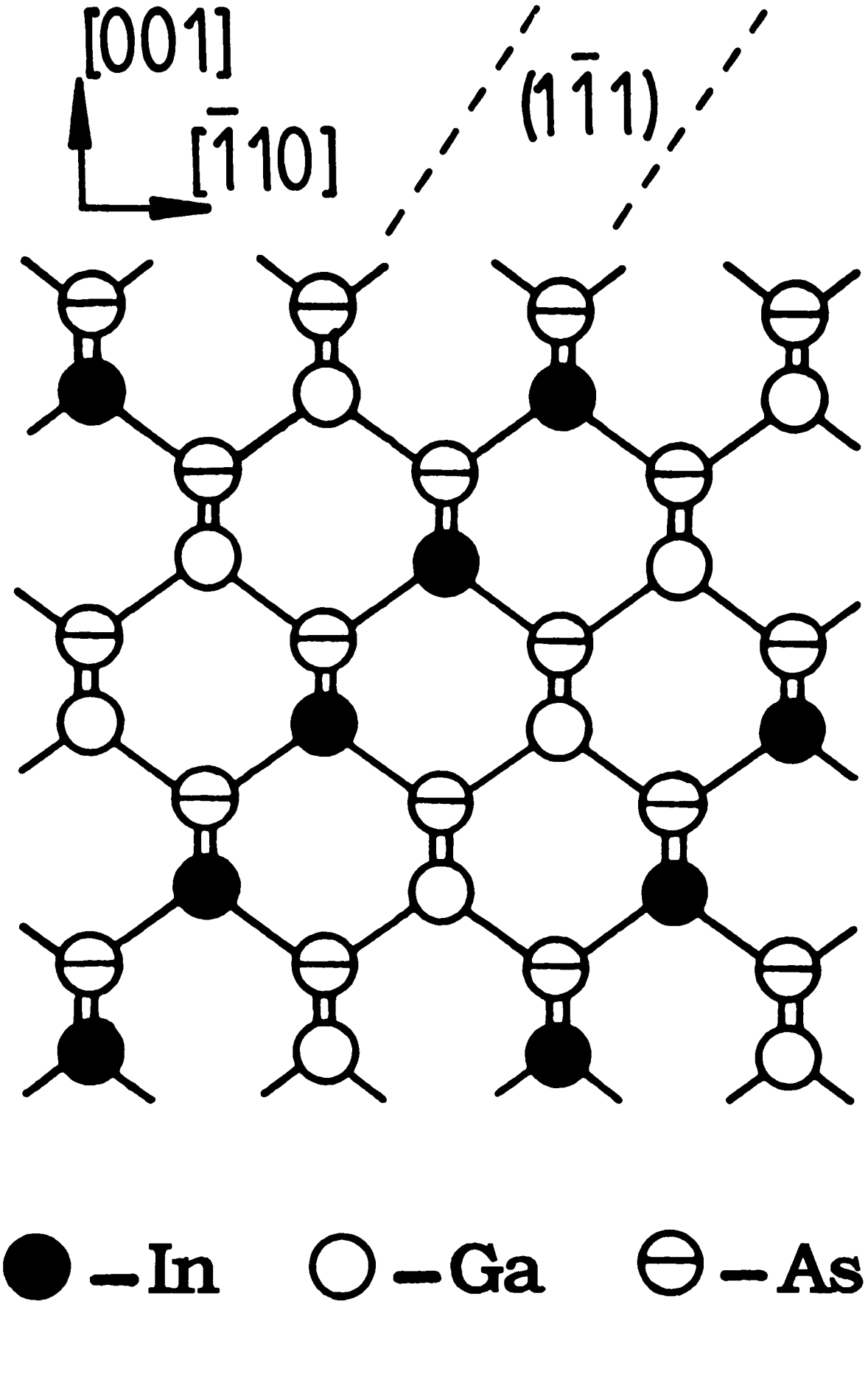

[110] projection

Fig. 6.2

Table 6.1 TED results of atomic ordering in MOCVD InGaAs layers.

Sample No.	Growth temp. (°C)	Growth rate (nm/sec)	Annealing treatment (°C/hours)	Intensity of extra spots
6460	500	0.20	-	medium
6316*	500	0.95	-	none
6462	550	0.20	-	v.strong
6462(a)	550	0.20	-	v.strong
6313*	550	0.95	-	weak
6313*	550	0.95	550/91	v.weak
6466	550	2.00	-	v.strong
5489	596	0.95	-	v.strong
6461	600	0.20	-	v.weak
6315*	600	0.95	-	meduim
6467	600	2.00	-	medium
6464	650	0.20	-	none
6312*	650	0.95	-	none
6468	650	2.00	-	none
6459	700	0.20	-	none
6317*	700	0.95	-	none
5488	717	0.95	-	none
5488	717	0.95	600/744	none

v. weak = very weak; v. strong = very strong. 6462(a): layer grown on GaAs.

* indicates layers ~200nm thick. The intensities of the extra spots in these specimens grown at 0.95nm/s can not be directly compared with the other intensities because the layers were thin (see page 85).

Figure 6.3

Cross-section [110] TED patterns from MOCVD InGaAs layers grown at (a) 500°C, (b) and (c) 550°C, (d) 600°C, (e) 650°C, and (f) 700°C using 0.95nm/s. (c) layer annealed at 550°C for 91 hr.

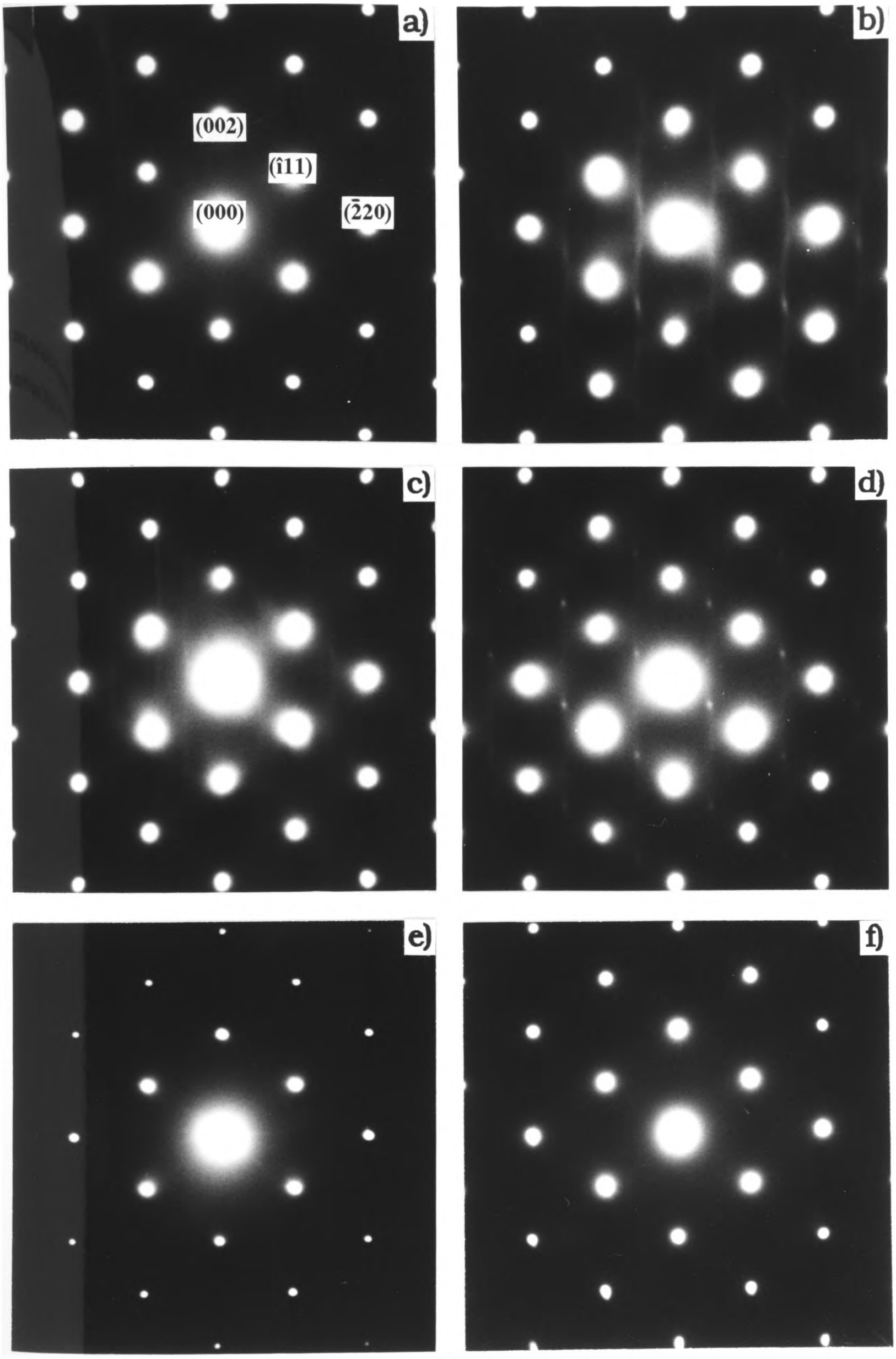

Fig. 6.3

Figure 6.4

TED patterns from MOCVD InGaAs layer grown at 596°C using 0.95nm/s. (a) Plan-view [001] TED pattern showing satellite spots at $\pm 1/4\mathbf{g}220$ positions. (b) Cross-section [110] TED pattern showing fundamental zinc-blende spots and superlattice spots. (c) Cross-section [$\bar{1}$ 10] TED pattern showing only fundamental zinc-blende spots.

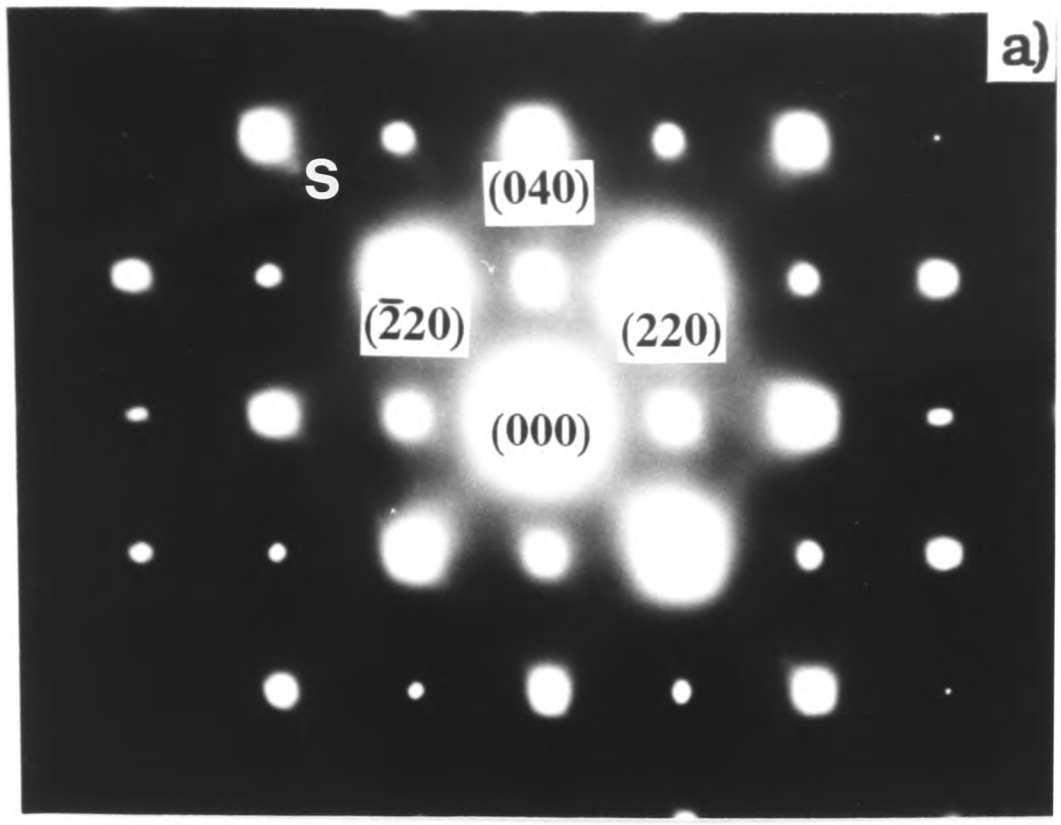

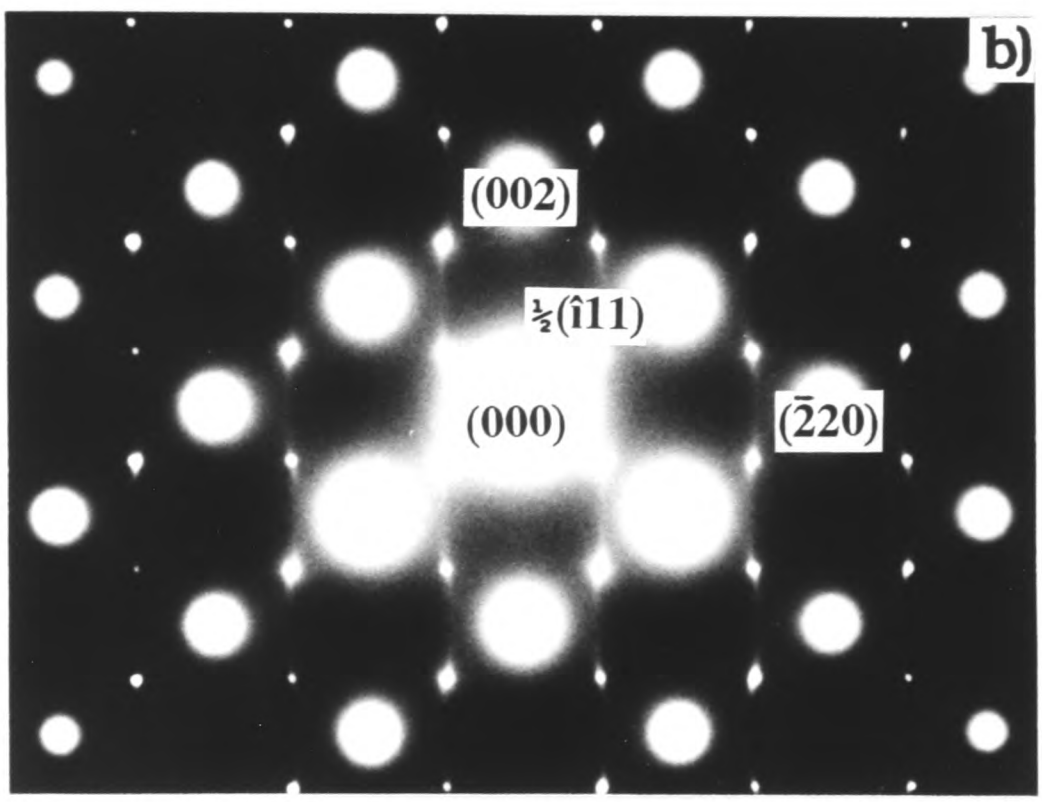

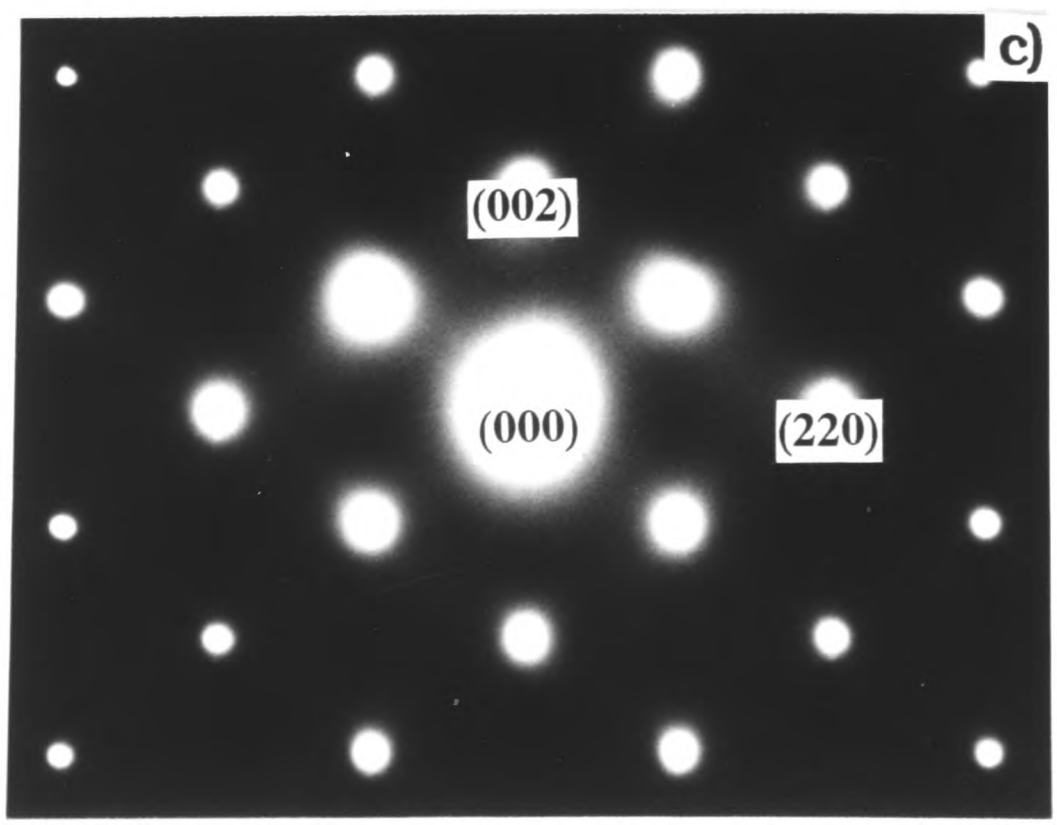

Fig. 6.4

grown at 550°C, decreased to medium intensity at 600°C and were absent at 650°C (Fig. 6.5). For the layer grown at 600°C, Fig. 6.5(b), an anisotropy of the degree of ordering between the two {111} variants was present, the $(1\,\bar{1}\,1)$ variant being dominant over the $(\bar{1}\,11)$ variant. This anisotropy is generally attributed to an off-cut of the substrate from the exact (001) orientation (7-10). Gomyo et al.(10) reported a similar anisotropy for superlattice spots in InGaP layers and attributed it to a substrate off-cut towards the $[\bar{1}\,10]$ direction.

The layers grown using the slow growth rate of 0.2nm/s and the fast growth rate of 2.0nm/s are compared to characterise the growth condition dependence of the ordering in the InGaAs layers. For most of the layers grown at the medium growth rate of 0.95nm/s (Table 6.1), the thickness was only ~200nm. For specimens with such thin layers examined by cross-section selected area TED corresponding to an area ~1μm across, most of the intensity of the fundamental zinc-blende structure spots arises from the substrate rather than the layer. Consequently, for these layers the relative intensity of the superlattice and fundamental spots in the TED patterns can not be directly compared with the analogous relative intensities obtained from specimens with thick layers. The patterns of Fig. 6.3 came from thin layers and so the superlattice spots are weaker, while the patterns of Fig. 6.4 came from thick layers and so the superlattice spots are stronger.

For a growth temperature of 550°C, variation of the growth rate from 0.2 to 2.0 nm/s did not have a significant effect on the intensity of the superlattice spots, e.g. see Fig. 6.1(b) and Fig. 6.5(a). For a growth temperature of 600°C, however, a significant reduction in the intensity of the superlattice spots was found to occur, as the growth rate decreased from 2.0 to 0.2nm/s, e.g. see Fig. 6.1(d) and Fig. 6.5(b). The shapes of the superlattice spots in the layers grown at 500°C and 550°C with the slow growth rate of 0.2nm/s were spherical, e.g. see Fig. 6.1(a), (b) and (c). However, those of the superlattice spots in the layers grown at 550°C using the fast growth rate of 2.0nm/s were elongated in a direction tilted a few degrees (~20°) from the [001] growth direction with the superlattice spots from the two different variants being tilted in opposite directions, Fig.6.5(a). This suggests the presence

Figure 6.5

Cross-section [110] TED patterns from MOCVD InGaAs layer grown at (a) 550°C, (b) 600°C and (c) 650°C using 2.0nm/s. Intensity of superlattice spots decreases with increasing growth temperature.

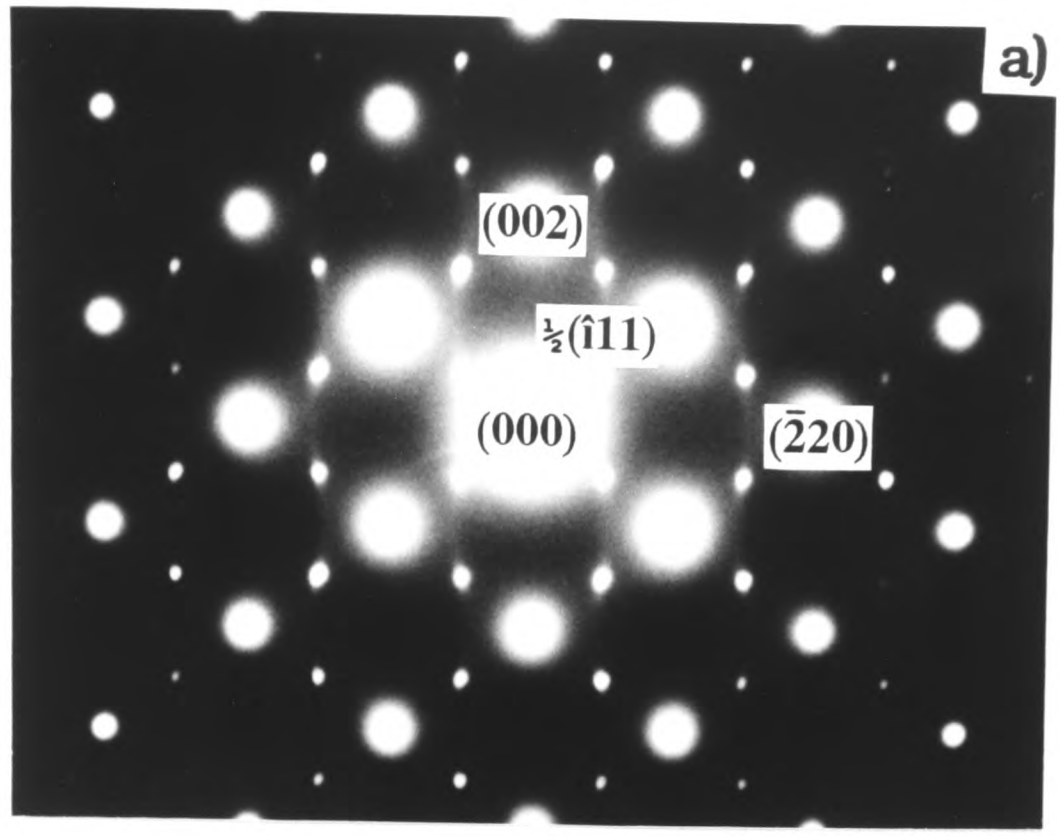

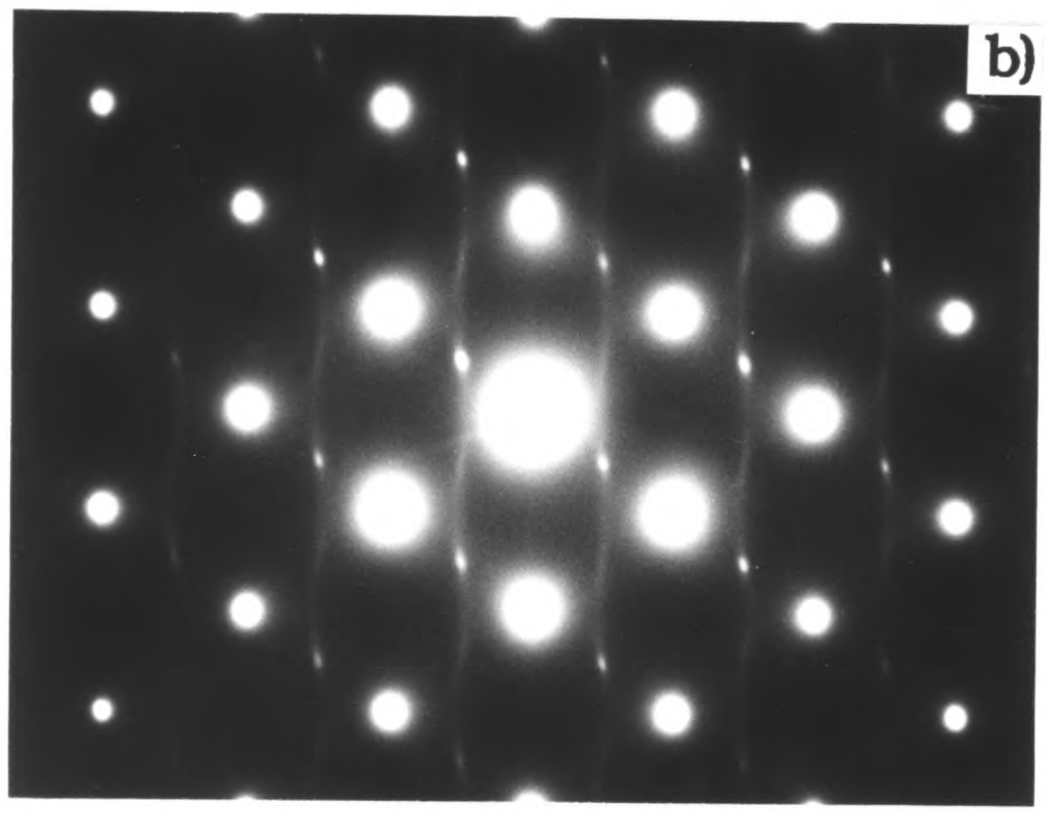

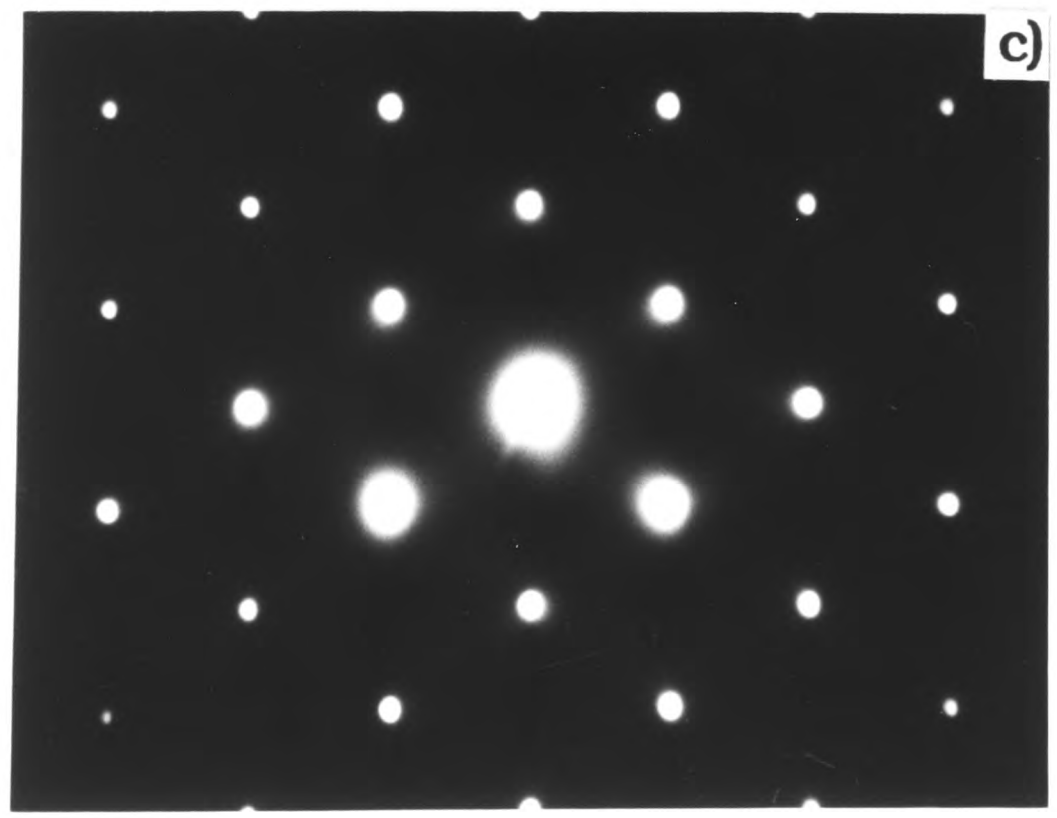

Fig. 6.5

of planar imperfections, i.e. APBs in the ordered structure lying tilted a few degrees (~20°) from the (001) plane.

6-2-2-2 Effects of lattice misfit strains and post-growth annealing on atomic ordering

Shahid et al. (9) have reported evidence for CuPt-type ordering in the multilayered regions of $In_xGa_{1-x}As_yP_{1-y}$ layers grown by vapour levitation epitaxy (VLE), but not in thick (1-3μm) InGaAs layers. Based on this observation, they argued that the presence of interface strain facilitates the formation of an ordered structure.

In order to investigate whether the lattice misfit strain affects the CuPt-type ordering, an $In_{0.53}Ga_{0.47}As$ layer (6462(a)) was grown onto a (001) GaAs substrate at 550°C with the slow growth rate of 0.2nm/s, which are the same growth conditions as the layer grown lattice matched onto a (001) InP substrate shown in Fig.6.1(b).

Lattice misfit (f) can be calculated from (11):

$$f = 2\frac{a_2 - a_1}{a_2 + a_1} \qquad (6\text{-}1)$$

where a_2 and a_1 are the lattice parameters of materials 1 and 2, respectively. Calculations from equation (6.1) and measurements of lattice spacings from selected area TED patterns showed that there is no lattice misfit between the $In_{0.53}Ga_{0.47}As$ layer and the InP substrate, but a misfit of 3.57% between the $In_{0.53}Ga_{0.47}As$ layer and the GaAs substrate. In Fig.6.1(c) is shown the [110] TED pattern obtained from the $In_{0.53}Ga_{0.47}As$/GaAs layer. No difference was observed in the TED patterns obtained from the layers grown on InP and GaAs, indicating that lattice misfit strain has a negligible effect on the intensity and shape of the superlattice spots.

The occurrence of the CuPt-type ordering on only two of the four possible {111} variants implies that an important role is played by the growing surface, influencing the generation of the ordered structure during growth. In order to investigate whether the ordered structure could arise or be disordered by a bulk thermally activated process, i.e. to

investigate the possibility of the evolution of the ordering in the bulk of the layer, post-growth annealing experiments were carried out. Since there is no asymmetry of the <111> directions in the bulk material, if the ordering observed in the epitaxial layers was due to a bulk diffusion process, the CuPt-type ordered structure would be expected to occur on all four sets of {111} planes, if it arose during annealing treatments.

Two samples were examined, i.e. InGaAs layers grown at 550°C and 717°C, both with a growth rate of 0.95 nm/s. The layer grown at 550°C showed CuPt-type ordering, whereas the layer grown at 717°C did not. A piece of the layer grown at 550°C was annealed at the growth temperature of 550°C for 91 hours and a piece of the sample grown at 717°C was annealed at 600°C for 744 hours. The annealing treatments were performed in a sealed quartz ampoule, with crushed GaAs and InP, evacuated to $< 10^{-6}$ Torr.

(001) plan-view and two orthogonal {110} cross-section specimens of these two annealed epitaxial layers were investigated by selected area TED. The results obtained from the layer grown at 550°C showed ordering still on two sets of {111} planes, Fig.6.3(c), with the superlattice spots having slightly weaker intensity than those of the as-grown layer, (Fig. 6.3(b)), implying that the pre-existing ordered structure was not bulk diffusion induced, and that it was unstable in the bulk because it was to a small extent destroyed by a thermally activated process. Furthermore, TED examination of the layer grown at 717°C both before and after annealing at 600°C revealed no superlattice spots associated with CuPt-type ordering or any other ordered structures, indicating that the CuPt-type ordering observed in the InGaAs layers is not a bulk diffusion-induced phase. Therefore, the post-growth annealing experiments strongly suggest that the ordering present in the $In_{0.53}Ga_{0.47}As$ layers is formed solely at the surface of the layers during growth, and is a surface-stabilized growth-induced structure.

6-2-3 TEM and HREM analyses of ordered structure

The results obtained from the TED examinations showed that the $In_{0.53}Ga_{0.47}As$ layers contain CuPt-type ordering on {111} planes, consisting of ordered regions formed of

repeating monolayers of Group III atoms along only two of the four possible <111> directions, i.e. ....InAs/GaAs/InAs/GaAs.... Plan-view and cross-sectional TEM DF and HREM techniques were employed to investigate the microstructure of the ordered regions in the layers. In order to avoid the strong background intensity in the image due to the transmitted beam, the 1/2{331} and 1/2{113} superlattice spots were used to form TEM DF images. Strongly excited 1/2{331} and 1/2{113} two beam conditions were obtained by tilting the sample to **g**{331} and **g**{113} respectively (12). Imaging with a 1/2($\bar{1}1\bar{3}$) superlattice spot reveals the ($\bar{1}11$) ordered domains as bright, while imaging with a 1/2($1\bar{1}\bar{3}$) superlattice spot reveals the ($1\bar{1}1$) ordered domains as bright. Similarly, imaging with a 1/2 ($\bar{3}3\bar{1}$) superlattice spot reveals the ($\bar{1}11$) ordered domains as bright, while imaging with a 1/2($\bar{3}31$) superlattice spot reveals the ($1\bar{1}1$) ordered domains as bright. Those regions that remain dark for both images are unordered material. The layers grown at 500°C and 550°C with a growth rate of 0.2 nm/s, and 550°C with a growth rate 2.0 nm/s, were examined because these showed the higher degrees of ordering.

The TEM DF results showed that the morphology of the ordered regions is strongly dependent on the growth conditions used. Fig. 6.6(a) and (b) show 1/2{113} TEM DF micrographs taken from the same area of a [110] cross-section specimen of the layers grown at 550°C with 0.2nm/s and reveal the regions ordered on ($\bar{1}11$) and ($1\bar{1}1$) planes, respectively, as bright. Columnar-like regions of the two ordered variants are present which originate at the interface between the InGaAs layer and the InP and propagate through the full layer thickness of ~4μm. They range from ~0.2 to ~0.75μm in width. Dark contrast features are visible in the ordered regions, which have no definite orientation and range from 10nm to 60nm in width. 1/2{331} DF micrographs showed similar dark wavy contrast. It is concluded from the results of HREM examinations, described later, that these latter features are antiphase domain boundaries (APBs). Not all of the layer is ordered and fairly sharp boundaries exist between both regions of the two ordered variants and the ordered and disordered regions. These boundaries run roughly parallel to the [001] growth direction.

Fig. 6.6(c) and (d) show 1/2{331} DF micrographs taken from the same area of a [110] cross-section specimen of the layer grown at 550°C with 2.0nm/s and columnar-like

Figure 6.6

Cross-section [110] TEM DF micrographs from MOCVD InGaAs layers grown at 550°C using (a) and (b) 0.2nm/s, and (c) and (d) 2.0nm/s. (a) and (b) 1/2{113} DF micrographs from same area. (c) and (d) 1/2{331} DF micrographs from same area. For both layers, region A is $(\bar{1}11)$ ordered domain, region B is $(1\bar{1}1)$ ordered domain, region C is unordered, and D is anti-phase boundary.

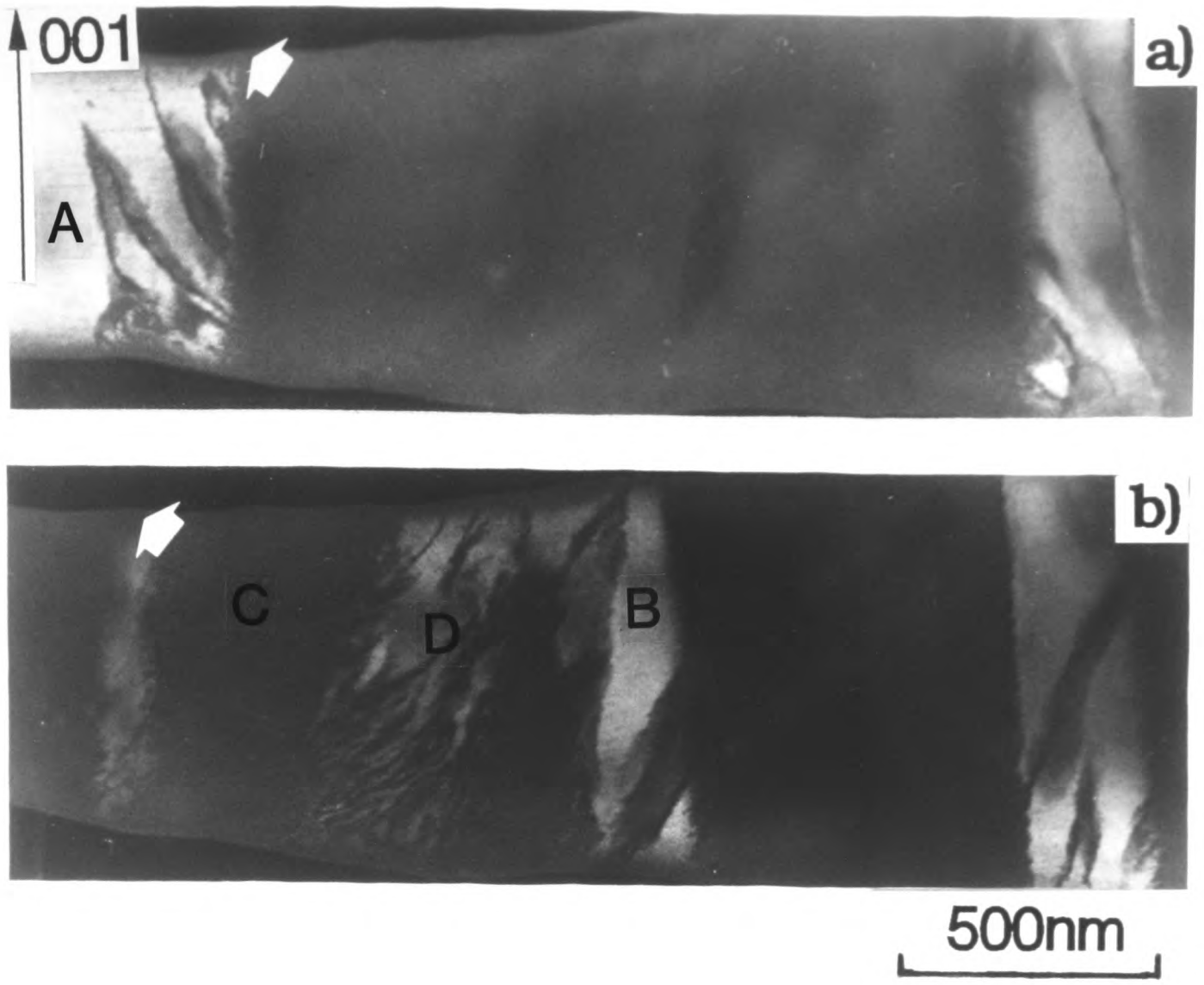

Fig. 6.6

regions of the two ordered variants ~0.1 to ~0.6μm in width are present. A high density of dark ribbon-like contrast features considered to be APBs are visible in the ordered regions. In some areas the APBs are tilted with respect to the (001) plane by ~20°, the sense of the tilt being opposite for the two variants. These tilted arrays of APBs are considered to be responsible for the tilting of the superlattice spots in the [110] TED pattern of this sample (Fig. 6.5(a)).

In Fig. 6.7 are shown 1/2{331} DF micrographs taken from the same area of a [110] cross-section specimen of the layer (6462(a)) grown on (001) GaAs at 550°C with 0.2nm/s. Columnar-like regions of the two ordered variants ~0.1 to ~0.6μm in width are present. Dark contrast features are visible in the ordered regions with no definite orientation, in agreement with the [110] TED pattern taken from the same area (Fig.6.1(c)), which shows circular superlattice spots.

Fig. 6.8 shows 1/2{331} DF micrographs taken from a [110] cross-section specimen of the layers grown on InP at 550°C with 0.2nm/s and 2.0nm/s, and grown on GaAs at 550°C with 0.2nm/s. The ordered regions are strongly dependent on the growth conditions used. Although the TED patterns exhibited no significant difference in the intensity and shape of the superlattice spots for the layers grown with 0.2nm/s on InP and GaAs substrates, e.g. see Fig. 6.1(b) and (c), the layer grown on GaAs showed a higher density of APBs (Fig. 6.8(b)). Furthermore, not the whole layer grown on InP at 550°C with 0.2nm/s was ordered (Fig. 6.8(a)), whilst almost the whole layer grown on InP at 550°C with 2.0nm/s was ordered and contained a higher density of APBs (Fig. 6.8(c)). In both the layers the ordered regions originate at the layer/substrate interface. In the layer grown on GaAs, the density of APBs decreased on going from the interface to the surface, which might be related to strain relaxation.

A (001) plan-view specimen of the layer grown at 550°C with 0.2nm/s was tilted 18° from the [001] pole along the two orthogonal {400} Kikuchi bands to reach the <103> poles. Dark field micrographs of the same area of the layer were taken using strongly excited 1/2{331} superlattice spots, using a small objective aperture to eliminate interference from the other reflections. For these plan-view specimens, the samples were thinned from

Figure 6.7

Cross-section [110] TEM 1/2{331} DF micrographs from same area of MOCVD InGaAs layer grown on GaAs at 550°C using 0.2nm/s. Region A is $(\bar{1}11)$ ordered domain, region B is $(1\bar{1}1)$ ordered domain, and C is anti-phase boundary.

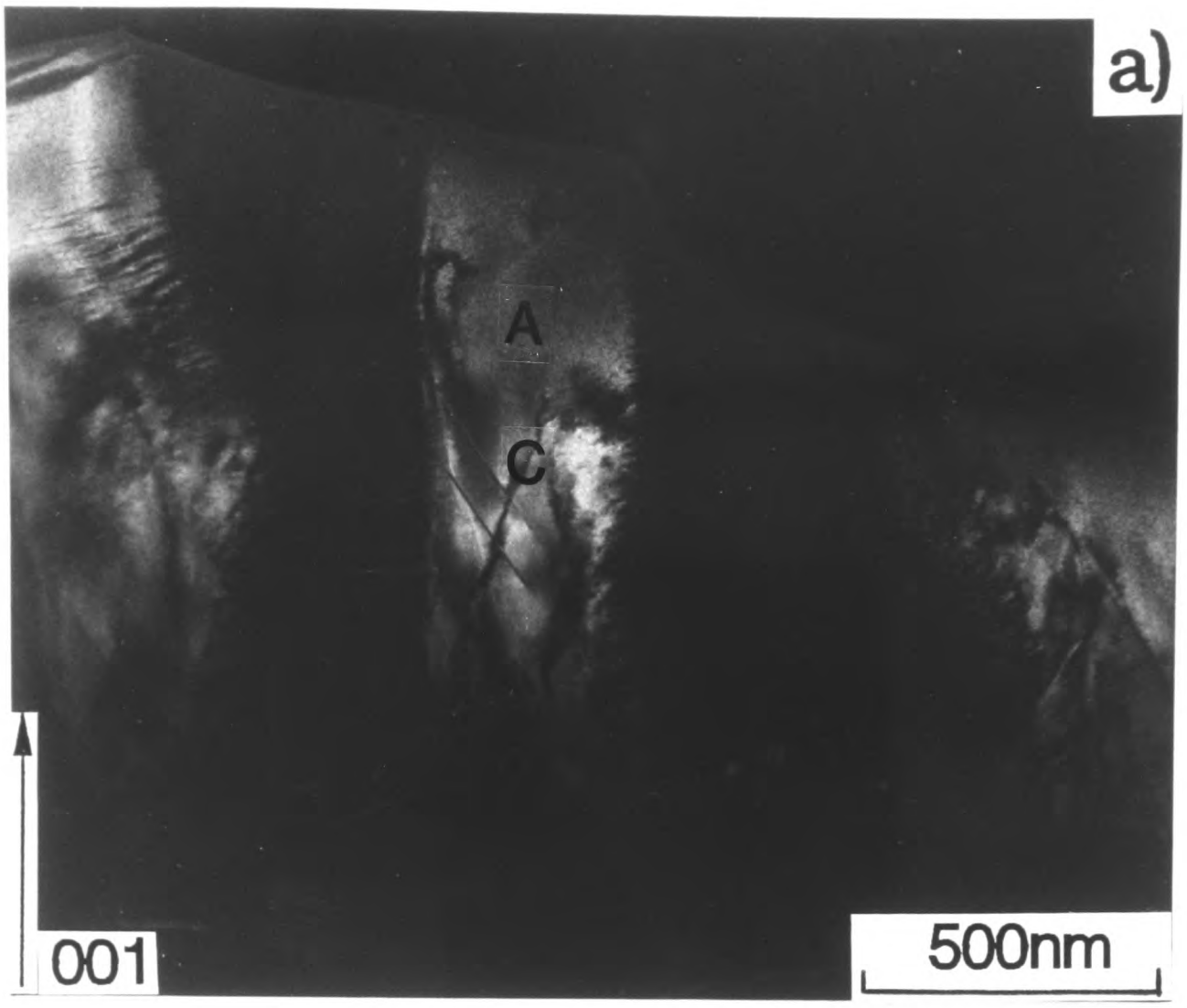

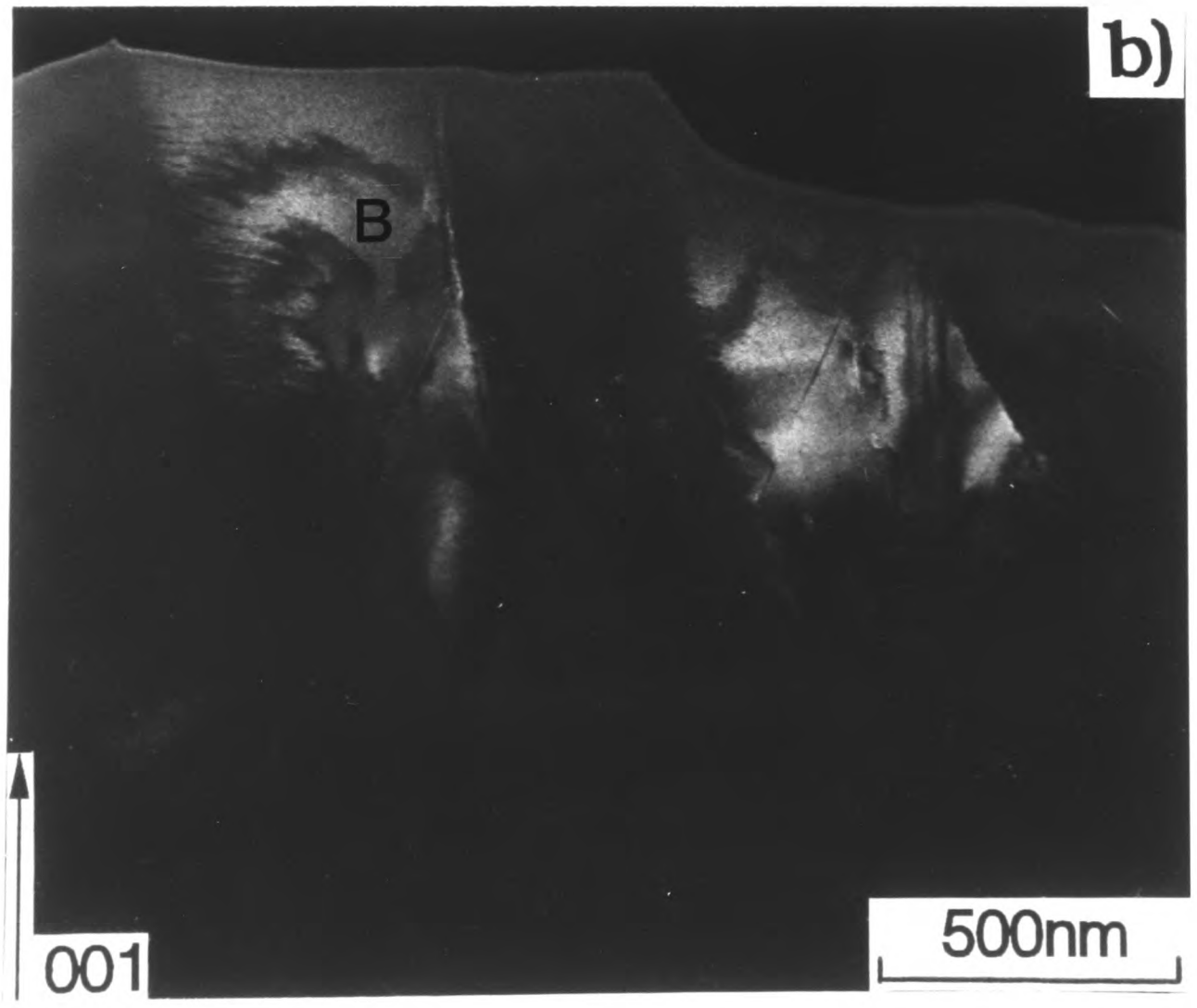

Fig. 6.7

Figure 6.8

Cross-section [110] TEM 1/2{331} DF micrographs from MOCVD InGaAs layers grown at 550°C (a) on InP using 0.2nm/s, (b) on GaAs using 0.2nm/s, and (c) on InP using 2.0nm/s. Arrows show anti-phase boundaries.

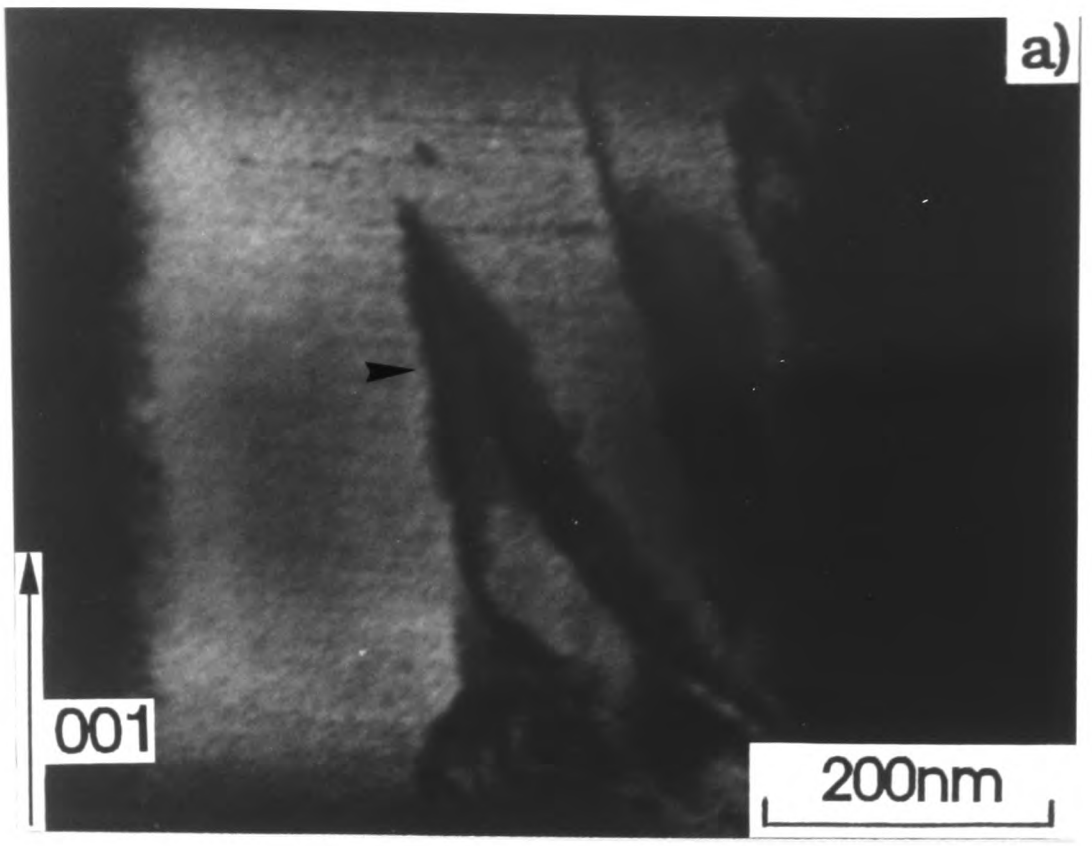

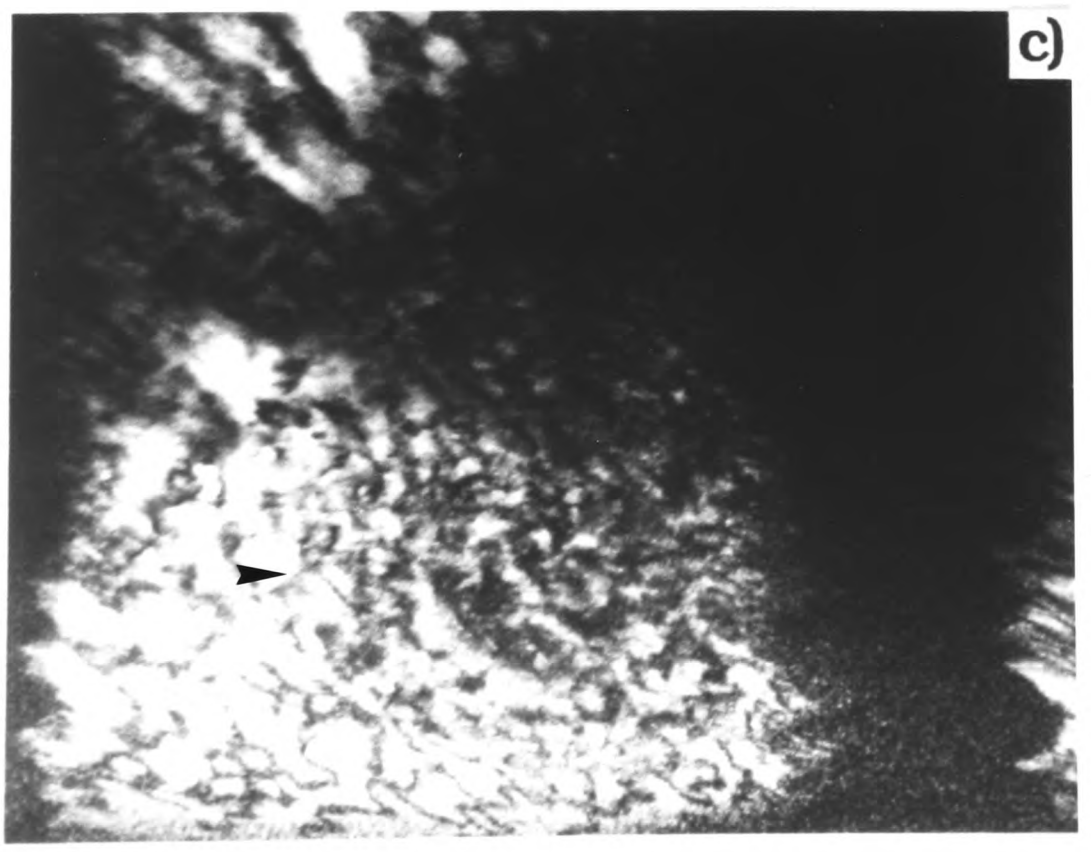

Fig. 6.8

the back-side and the foil thicknesses were 100 to 200nm. The two micrographs, Fig. 6.9(a) and (b), show the regions ordered on $(\bar{1}11)$ and $(1\bar{1}1)$ planes, respectively, as bright. Not all of the layer was ordered, which is consistent with the cross-section micrographs of Fig. 6.6(a) and (b). The results suggest that the ordered regions of the two variants nucleated separately. The ordered regions have 'eye-brow' shapes 0.2 - 0.55μm across oriented in opposite senses for the two variants, with unordered material in between. The planar boundaries between the two ordered variants are roughly parallel to <331> directions. Dark ribbon-like contrast with random configurations is visible in the ordered regions.

Fig. 6.10(a) and (b) show similar 1/2{331} plan-view DF micrographs taken from the same area of the layer grown at 550°C with 2.0nm/s. The micrographs again show the regions ordered on $(\bar{1}11)$ and $(1\bar{1}1)$ planes. Almost the whole layer was ordered and again the ordered regions of the two variants nucleated separately. The ordered regions have triangular shapes ~0.2 to 0.7μm across oriented in opposite senses for the two variants. The regions of the two variants have sharp boundaries which show some preferred alignment. The boundaries between the two variants in these micrographs, which were taken close to the [103] and [013] poles, lie along <311>, <131> and <331> directions. The boundaries lying along the <331> directions, which are less sharp, could be lying on the orthogonal (110) and $(\bar{1}10)$ planes as suggested from the [110] cross-section TEM micrographs. The sharper boundaries along the <311> directions probably correspond to boundaries on {311} planes. Dark ribbon-like contrast is visible in the ordered regions with preferred orientations and this may correspond to APBs. Linear contrast features (marked 'L') running through approximately the middle of the domains, and boundaries apparently between separate regions of the same variant, are also visible in the micrographs running along one of the <331> directions which could correspond to features lying on one of the {110} planes.

In Fig. 6.11(a) is shown a 1/2{331} DF micrograph of a (001) plan-view specimen of the layer grown at 500°C with 0.2nm/s. The ordered regions are similar to those of the layer grown at 550°C with 2.0nm/s and range in size from ~0.05 to ~0.6μm across. However, unlike the 550°C grown layer, not all of the layer was ordered. Fig. 6.11(b) shows a similar 1/2{331} DF micrograph of a (001) plan-view specimen of the layer grown

Figure 6.9

Plan-view [001] TEM 1/2{331} DF micrographs from same region of MOCVD InGaAs layer grown at 550°C using 0.2nm/s showing as bright areas the regions ordered on (a) ($\bar{1}$ 11) and (b) (1 $\bar{1}$ 1) planes. The whole layer is not ordered.

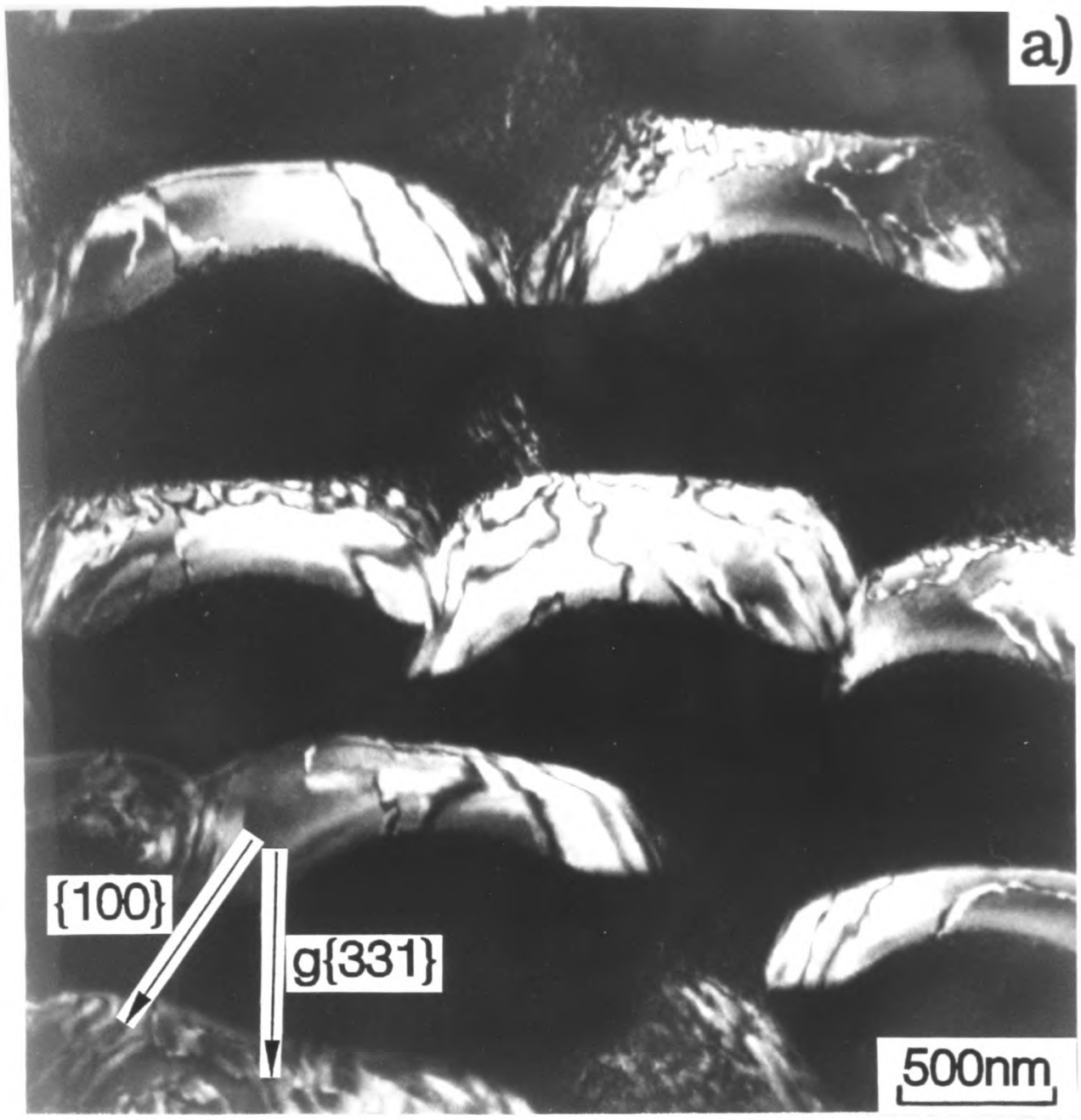

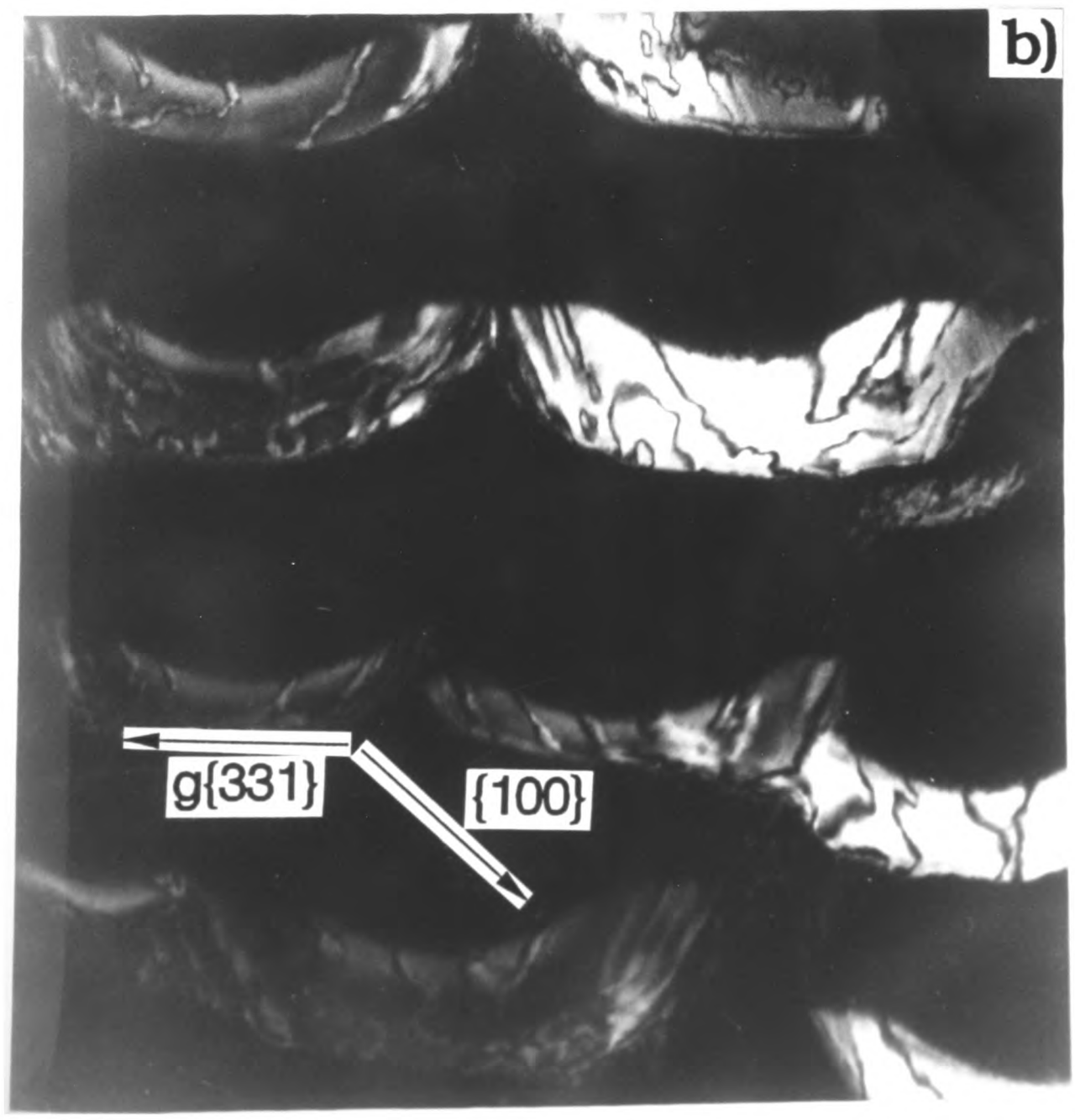

Fig. 6.9

Figure 6.10

Plan-view [001] TEM 1/2{331} DF micrographs from same region of MOCVD layer grown at 550°C using 2.0nm/s showing regions ordered on (a) $(\bar{1}\,11)$ and (b) $(1\,\bar{1}\,1)$ planes. The whole layer is ordered.

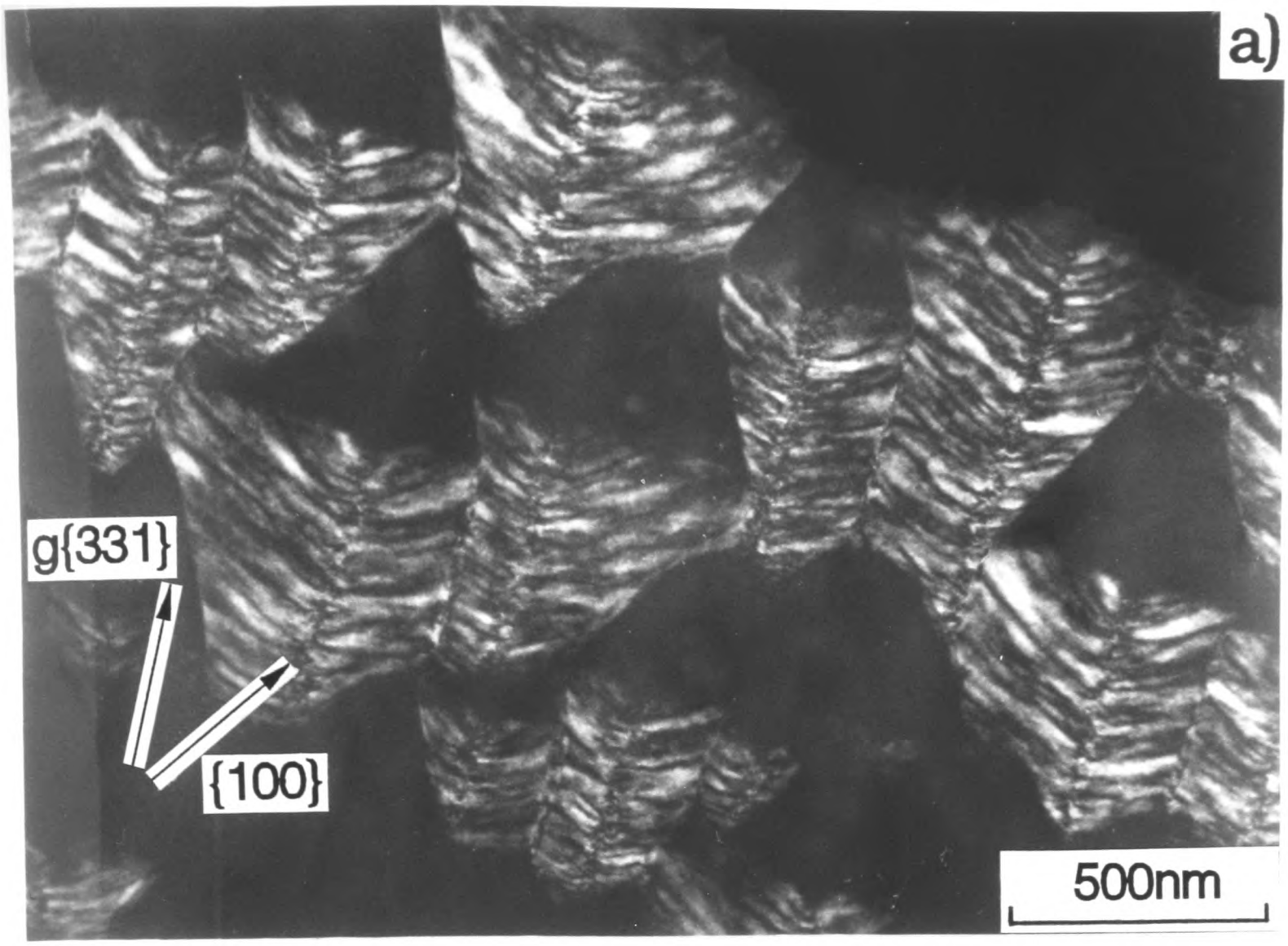

Fig. 6.10

Figure 6.11

Plan-view [001] TEM 1/2{331} DF micrographs from MOCVD InGaAs layers showing regions ordered on ($\bar{1}$11) planes. (a) layer grown on InP at 500°C using 0.2nm/s. (b) layer grown on GaAs at 550°C using 2.0nm/s. For the latter layer, morphology of ordered regions is different from that of corresponding layer grown on InP (Fig. 6.9).

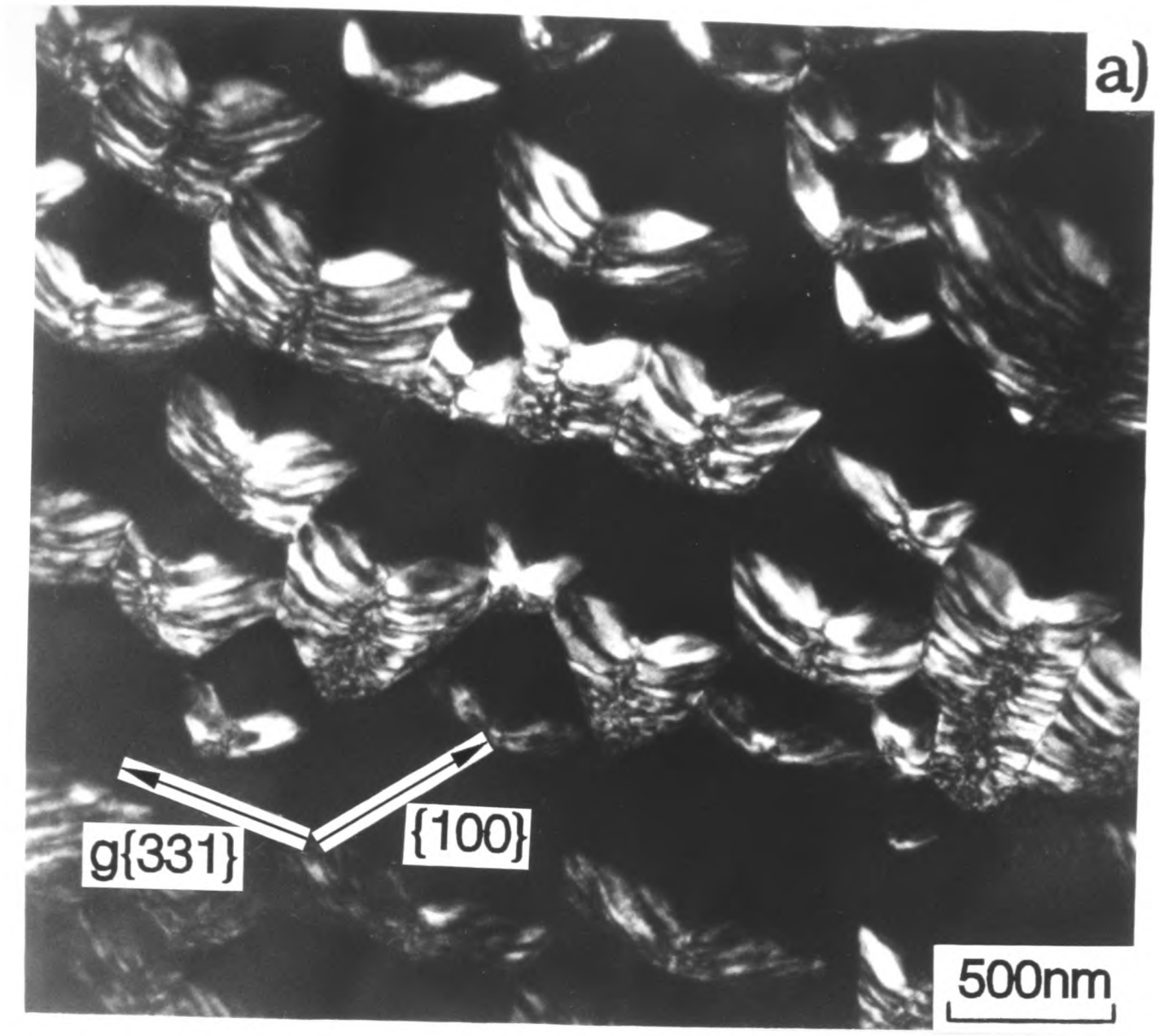

Fig. 6.11

on a GaAs substrate at 550°C with 0.2nm/s. The characteristic features are different from those of the other layers described above. This observation indicates that either the lattice misfit strain has some effects on the ordered structure during growth, or the morphology of the ordered regions could be related to the morphology of the original substrate surface, e.g. surface steps. Nonetheless, not all of the layer was ordered. The ordered regions are elongated along a <110> direction and range from ~0.2 to ~1.2μm in width.

The HREM technique was employed to produce more information concerning the ordered structure and imperfections in the ordered regions. High resolution lattice images of [110] cross-section specimens of the layers grown at 550°C and 596°C with growth rates of 2.0nm/s and 0.95nm/s respectively were taken at 400 kV on a JEOL 4000EX microscope using two different sizes of objective apertures. Initially a DF micrograph was obtained by using a small objective aperture, which selected just the $(\bar{1}\,1\,\bar{1})$ main spot and a $1/2(\bar{3}\,3\,\bar{3})$ superlattice spot of the [110] TED pattern. Such a micrograph of the cross-section specimen of the layer grown at 550°C with 2.0nm/s is shown in Fig. 6.12(a). It was expected that ordered regions should show fringe contrast with a spacing of 0.678nm, which is double the {111} plane spacing of the $In_xGa_{1-x}As$ (x=0.53) layer. The micrograph shows $(\bar{1}\,1\,\bar{1})$ fringes of this double spacing, and also shows the presence of planar defects causing these fringes to be shifted by half a period, which is characteristic of APBs (8). Some of these APBs are narrow, e.g. A, and lie parallel to the electron beam, whereas others are broad, e.g. B, and are inclined to the electron beam. It is concluded that the dark ribbon-like contrast features observed in the [110] cross-section 1/2{331} DF micrographs of Fig. 6.6(c) and (d) described earlier are APBs. The presence of these APBs in the ordered regions is considered to be responsible for the elongation and tilting of superlattice spots observed for the fast growth rate sample and may also be the origin of the [001] wavy lines of diffuse diffracted intensity running through the superlattice spots in the [110] TED patterns.

In order to confirm this hypothesis, the optical diffractogram technique was used for comparison with the selected area TED results. Optical diffraction patterns are obtained using a standard optical diffractometer (13) with a He-Ne laser illumination source. An electron micrograph negative of the optimum lattice image was directly mounted in the ray

Figure 6.12

(a) Cross-section [110] DF HREM image, obtained using $(\bar{1}\,1\,\bar{1})$ and $1/2(\bar{3}\,3\,\bar{3})$ spots, of MOCVD InGaAs layer grown at 550°C using 2.0nm/s. $(1\,\bar{1}\,1)$ superlattice fringes 0.678nm apart are present. A indicates narrow APBs lying parallel to electron beam and B indicates broad APBs inclined to electron beam. (b) [110] TED pattern from region including (a) showing 1/2{111} superlattice spots. (c) Optical diffraction pattern from HREM image of (a). In both (a) and (b) superlattice spots are elongated and tilted away from [001] growth direction.

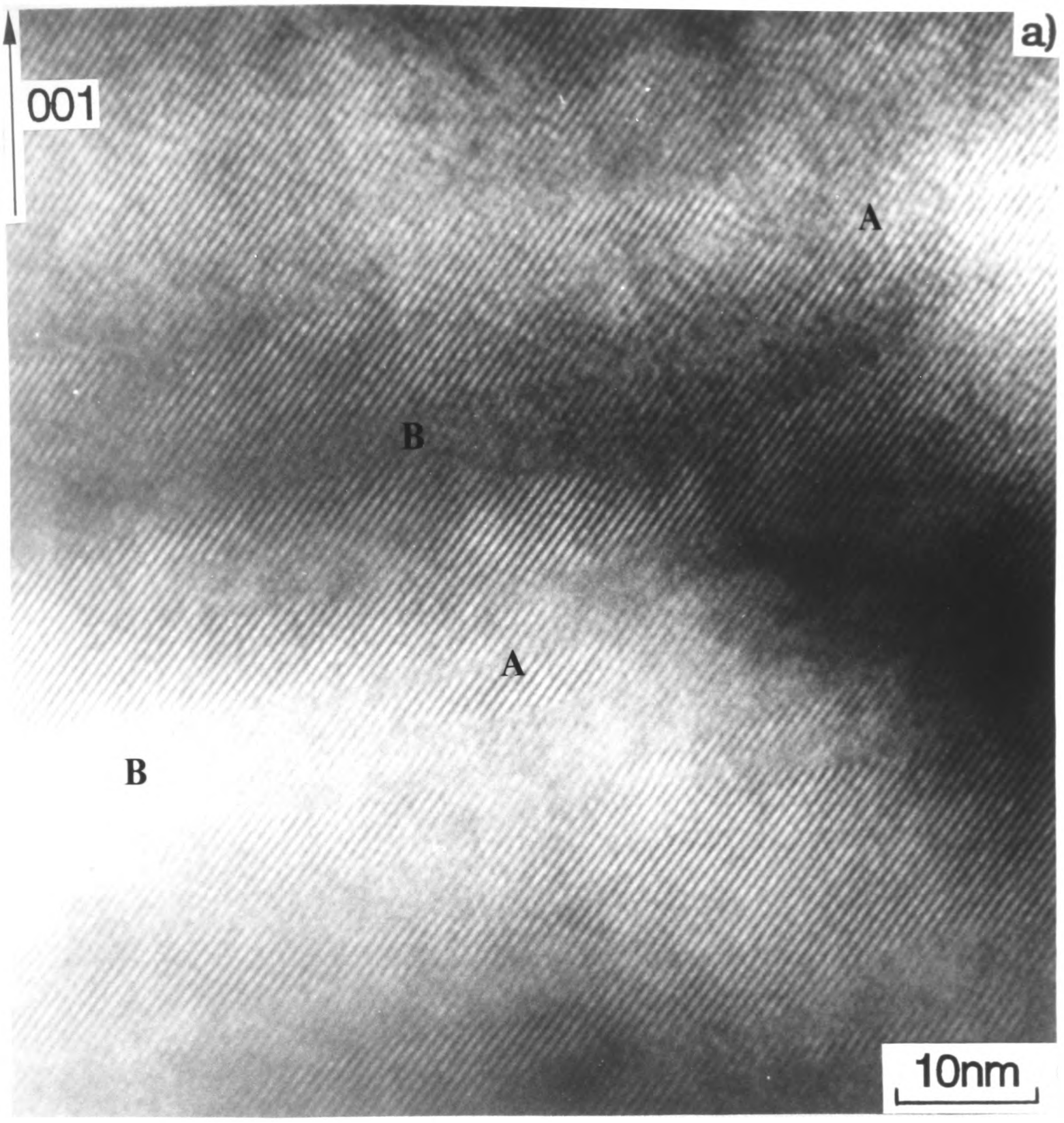

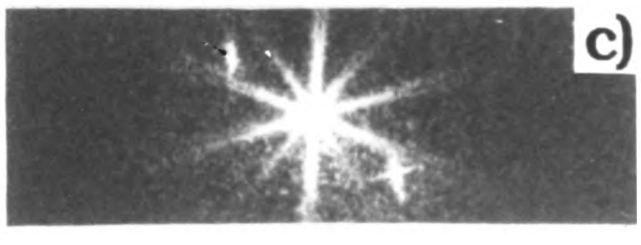

Fig. 6.12

path at normal incidence. Polaroid type 52 film was used to record the information. A circular aperture with diameter of 15 mm was employed to select the region of a HREM image negative from which the diffraction pattern was recorded. Optical diffraction patterns were obtained from a HREM micrograph including planar defects such as APBs, as shown in Fig. 6.12(a). Fig. 6.12(c) and (b) compare the optical diffraction pattern with the corresponding selected area [110] TED pattern from the same region of the specimen. Two main features of the electron diffraction pattern are clearly visible in the optical pattern, i.e. i) the presence of the 1/2{111} superlattice spots; ii) elongation of the superlattice spots and tilting ~15° from the [001] growth direction. It is noteworthy that the optical diffractogram taken from a planar defect-free region showed only spherical superlattice spots. Therefore, it can be concluded from these observations that the elongation and tilting of the superlattice spots in the diffraction patterns is directly associated with the existence of planar defects such as APBs tilted from (001) planes.

HREM lattice images of a [110] cross-section specimen of the layer grown at 596°C with 0.95nm/s were also taken at 400 kV on a JEOL 4000EX microscope using the second largest objective aperture (~0.88Å^{-1}) including the all the spots out to {331}, Fig. 6.13. The image shows ordering with a periodicity double that of the {111} 'close-packed' planes of InGaAs over a fairly large area with no APBs. The thinnest areas of the specimen exhibited no doubling in periodicity, which is in good agreement with the work of Norman et al.(14). They investigated ordered lattice image contrast of AlInAs layers using a multislice image simulation technique (15) performed by a 256 x 256 point fast Fourier transform programme and reported that for thin crystals, < 75 Å, very weak contrast effects are visible. The optical diffractogram technique was also used to confirm the present HREM work and revealed only the ($\bar{1}$ 11) variant of the ordered structure. This is consistent with the HREM results, which show a doubling in periodicity along the [$\bar{1}$ 11] direction, but not the [1 $\bar{1}$ 1] direction.

Figure 6.13

Cross-section [110] HREM image from MOCVD InGaAs layer grown at 596°C using 0.95nm/s, showing a lattice periodicity which is double that of the {111} planes of InGaAs. Inset is optical diffraction pattern taken from HREM image. The one variant of 1/2{111} superlattice spots in the optical diffraction pattern is consistent with the HREM image.

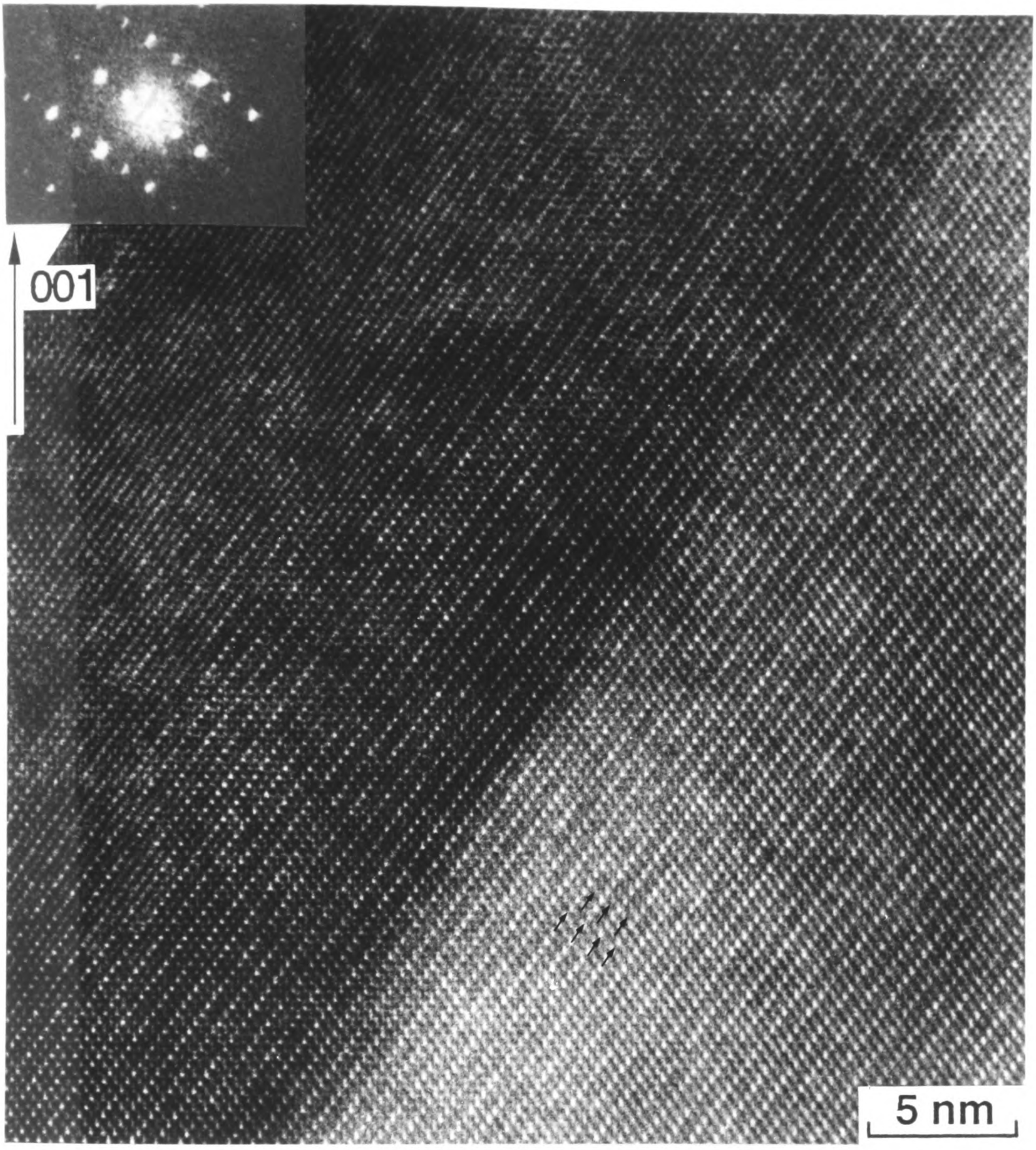

Fig. 6.13

6-2-4 Effects of experimental techniques on ordering

We now consider the possible effects of the experimental assessment techniques themselves on the observation of CuPt-type ordering. In order to study any modification of the ordered structure due to the ion milling process, we thinned cross-section specimens under two different conditions. First, a cross-section TEM specimen of a MOCVD $In_{0.53}Ga_{0.47}As$ layer grown at 600°C was prepared by mechanical polishing the specimen down to ~40μm thick and then subsequently thinning using Ar^+ ion milling at liquid nitrogen temperature. Secondly, another piece of the same sample was thinned by mechanical polishing and Ar^+ ion milling at room temperature. TED examinations showed that the specimen thinned at room temperature exhibited a lower degree of ordering than the specimen thinned at liquid nitrogen temperature, indicating that the ordering present in the bulk specimen was decreased by the Ar^+ ion milling at room temperature. This suggests that some of the TEM ordering results published in the literature by other workers may be incorrect because such ion milling is mostly performed at room temperature. Therefore, in the present work, all the specimens reported on were thinned at liquid nitrogen temperature.

We also consider the effect of electron beam damage. A cross-section specimen of an MBE $InAs_{0.4}Sb_{0.6}$ layer grown at 370°C was thinned using Ar^+ ion milling at liquid nitrogen temperature and examined at 400 kV in the JEOL 4000EX microscope. The specimen was exposed for 20 hours using a beam current of ~126μA. TED results subsequently obtained using a Philips CM 12 operated at 120 kV and a beam current of ~10μA showed that the exposed specimen exhibited a lower degree of ordering than the unexposed specimen. Therefore, in the present work, none of the specimens reported on were exposed to high beam currents for long times. These observations are very important for the investigation of atomic ordering in III-V compound semiconductor layers. Therefore, one must take a great deal of care not to induce artifacts by specimen preparation and TEM examination in order to obtain representative data concerning ordering behaviour.

6-2-5 Discussion

The results obtained from the TED examinations described in section 6-2-2 showed that CuPt-type ordering occurs in MOCVD InGaAs epitaxial layers grown using a variety of growth conditions. Only the $(\bar{1}11)$ and $(1\bar{1}1)$ ordered variants were present. The superlattice spots associated with the ordered structure in [110] cross-section patterns were often elongated and tilted ~20° from the [001] growth direction and connected by lines of diffuse diffracted intensity running approximately along the [001] growth direction, indicating that the ordered structure is not perfect. TEM showed the presence of regions ordered on either $(\bar{1}11)$ or $(1\bar{1}1)$ planes only, and planar imperfections such as APBs within these regions. The ordering was strongly dependent on the growth conditions (Table 6.1). The cross-section TED results are summarised as follows:

A) Effects of growth temperature on the ordering;

i) The intensity of the superlattice spots decreases with increasing growth temperature above 550°C for both growth rates of 0.2 and 2.0nm/s;

ii) The intensity of the superlattice spots decreases with decreasing growth temperature below 550°C for the layer grown using the slow growth rate of 0.2nm/s;

iii) (data not available for below 550°C and 2.0nm/s);

B) Effects of growth rate on the ordering

i) At 550°C, the intensity of the superlattice spots does not change significantly with growth rate;

ii) At 600°C, the intensity of the superlattice spots increases with increasing growth rate;

iii) At high growth rates, the superlattice spots became elongated in a direction tilted 10-20° from the [001] growth direction, the spots corresponding to the two {111} variants being tilted in opposite directions.

The existence of ordered structures in III-V compound semiconductors was predicted by Srivastava, Martins and Zunger (16), who investigated the stability of ordering in semiconductor alloys using a first-principles local-density total energy minimisation method. They showed that ordered intermediate phases could be the thermodynamically stable low temperature form and that the driving force for the formation of the ordered structures is strain-reduction. In the $In_xGa_{1-x}P$ system, the CuAu-I type and chalcopyrite type ordered structures, both consisting entirely of tetrahedra of Group III atoms around a Group V atom, each with two In atoms and two Ga atoms, are calculated to have lower energies than other ordered structures such as the CuPt-type with ordering along <111> directions (17). Thus, the CuPt-type ordered structure results in less reduction in strain energy in the bulk alloys, and so is less stable than the chalcopyrite and CuAu-I type ordered structures in the bulk. Bernard et al. (18) also calculated that the CuPt-type ordered structure is always unstable with respect to the disordered phase. These calculations are consistent with the results obtained from the present post-growth annealing experiments, which were performed to investigate if existing ordering developed and if ordering nucleated in the bulk of the layer. The results showed that the ordering is neither induced nor stable in the bulk layers. In spite of its instability, the CuPt-type ordering is commonly observed, not only in the present InGaAs system, but also in a wide variety of III-V compound semiconductor layers grown using the non-equilibrium growth techniques of MOCVD and MBE. These theoretical and experimental results strongly indicate that the CuPt-type ordering is a growth-induced phase and occurs solely at the growing surface.

Approaches by Norman (2), Suzuki et al.(3), Murgatroyd et al.(4) and Bellon (8) have attempted to explain the occurrence of the CuPt-type ordering in III-V compound semiconductors based upon the stand-point of atomic configurations on the growing layer surface. As described above, since the ordering is unstable in the bulk and is a growth-induced structure, the atomic arrangement for the ordering on the growing surface could be controlled by the surface atomic mobility, as will be discussed later. This is consistent with the work of Kuan et al.(1), who reported the first experimental evidence for ordering in MOCVD and MBE $Al_xGa_{1-x}As$ layers grown on (110) and (001)-oriented substrates, which

exhibited CuAu-I type ordering. They found that layers grown on (110) substrates are more highly ordered than layers grown on (001) substrates and attributed this to the higher atomic mobility on the (110) surface. Growth of the ordered structure may proceed by a process of two-dimensional nucleation and layer-by-layer growth (2). Thus, successive growth of ordered monolayers may lead to the formation of macro-ordered regions in the layers. However, since the degree of ordering is strongly dependent on growth conditions, we consider the ordering behaviour in relation to the growth kinetics. In order to explain the ordering behaviour observed for the InGaAs layers grown at 500°C to 700°C with 0.2 and 2.0nm/s, the two competing processes of surface-stabilised ordering and bulk equilibrium disordering are considered (8,19).

For the growth of InGaAs, when In and Ga atoms are incident on the growth surface, they will initially be randomly distributed. In order to lower the surface chemical potential energy, the In and Ga atoms diffuse into the most energetically stable sites, which may result in a surface ordered structure (as discussed in detail in section 6-5). The degree and relative volume fraction of ordering will depend on both the lifetime of the In and Ga atoms before incorporation into the crystal lattice by the overgrowth of the next monolayer and the relaxation time taken for the In and Ga atoms to move to the energetically stable ordered states. For a growth temperature of 500°C, the In and Ga atoms have a longer relaxation time than those of the layer grown at 550°C, although they have the same lifetime if the growth rate is the same. Therefore, in this case, the relaxation time for the In and Ga atoms would be a rate controlling factor for the degree of ordering; the degree and volume fraction of ordering is determined by a kinetic limit for the surface ordering due to the reduction in mobility of the In and Ga atoms in the growing surface at the lower temperature.

We distinguish three growth temperature zones, which show different ordering behaviours, namely, 500°C, 550°C and 600°C. First, for the slow growth rate of 0.2nm/s, the degree of ordering decreased with decreasing growth temperature from 550°C to 500°C. This indicates that for this growth rate, the lifetimes for 500°C and 550°C are the same, but the 550°C grown layer has a shorter relaxation time than the 500°C grown layer. Therefore, higher ordering could be achieved in the 550°C layer. This experimental result is

consistent with the models proposed by Norman (2), Suzuki et al.(3), Murgatroyd et al.(14) and Bellon et al.(8), which depend on the assumption that the CuPt-type ordering is controlled by a surface diffusion process. Kuan et al.(1) also reported a similar behaviour in AlGaAs, suggesting that a higher mobility of Group III atoms such as Al and Ga on the growing surface may lead to the higher degree of ordering.

Secondly, for a growth temperature of 550°C, the degree of ordering was not dependent on growth rate, i.e. the layers grown at 0.2 and 2.0nm/s both showed a relatively high degree of ordering. However, APBs occurred with a higher density in the 2.0nm/s layer, indicating that the ordered structure is more imperfect in this layer. Because the degree of ordering was a maximum at 550°C for both growth rates, this indicates that at 550°C, the relaxation times of the In and Ga atoms are shorter than their lifetimes at both growth rates, so that a high degree of ordering may be achieved. However, the shorter lifetimes for the In and Ga atoms in the 2.0nm/s layer could lead to the higher density of APBs observed in this layer.

Thirdly, at a growth temperature of 600°C, the degree of ordering was less than for the 550°C layers, and the degree of ordering decreased with decreasing growth rate from 2.0nm/s to 0.2nm/s. For this growth temperature, consideration of the lifetime and relaxation time suggests two possible cases concerning the degree of ordering: a) for both growth rates, high ordering should occur because the 600°C layer has a shorter relaxation time than the 550°C layer; b) the 0.2nm/s layer should have higher degree of ordering than the 2.0nm/s layer because, with the same relaxation time, the 0.2nm/s layer has a longer lifetime. Experimental observations showed that neither of these cases occurred. These results suggest that for this temperature, a process involving disordering should be considered. Therefore, in this case, two competing processes may control the behaviour of the CuPt-type ordering, e.g. the surface-stabilized ordering and the bulk diffusion-induced equilibrium disordering within the layer. As calculated by Bernard et al.(18), the CuPt-type ordered structure is unstable with respect to the disordered phase in the bulk of the layer. Therefore, the buried In and Ga atoms occupying the ordered sites would tend to disorder in the bulk of the layer during further growth by bulk diffusion in order to lower the free

energy state in the bulk. The bulk disordering may depend on the diffusion time for disordering within a transition region close to the growing surface. At a growth temperature of 600°C, since the surface diffusion of the In and Ga atoms is fast, the surface-stabilized ordered structure could be readily achieved even at the fast growth rate of 2.0nm/s. Therefore, the degree of observed ordering could be determined by a second process, i.e the disordering of the ordered structure frozen in the bulk.

Fourthly, at layer growth rates of 0.2 and 2.0nm/s, the degree of ordering decreased with increasing growth temperatures from 550°C to 600°C and then was absent when grown at and above 650°C. In this case, the ordering behaviour may be associated with the increased rate of the bulk diffusion-induced disordering because of a reduction in the thermodynamic equilibrium degree of the surface-induced ordering.

Kim et al.(20) have investigated the layer depth dependence of interdiffusion in AlGaAs/GaAs superlattice structures and found that the activation energy of Ga and Al interdiffusion is smaller near to the epitaxial layer surface than far from the surface and the diffusion is faster, supposedly because of a higher concentration of point defects close to the layer surface. Similar interdiffusion behaviour may also be expected in the InGaAs system. Thus, the bulk diffusion-induced disordering could occur mainly in a transition region just underneath the growing surface of the layers aided by an excess vacancy population, leading to the reduction in the degree of ordering observed in the slow growth rate layer in comparison to the higher growth rate layer.

Kurtz et al.(19) investigated the effects of growth conditions on the degree of the CuPt-type ordering in $Ga_xIn_{1-x}P$ (x=0.5) layers. In their work, the degree of ordering was indirectly deduced from the band gap measured using photocurrent spectroscopy (21). They reported that the band gap of InGaP layers varies as a function of growth conditions. Curves of growth rate against growth temperature for different band gaps showed three regions with different ordering behaviours: i) the degree of ordering decreased with increasing growth rate; ii) the degree of ordering decreased with decreasing growth rate; iii) the degree of ordering decreased with increasing growth temperature, regardless of growth rate. In order to interpret such ordering behaviours, they considered competing processes

associated with the residence time of the Group III atoms on the surface, the surface relaxation time to reach the ordered surface state and the transition time for disordering. For the first region, the lower degree of ordering was attributed to the shorter residence time for the Group III atoms. For the second region, the lower degree of ordering was attributed to the longer transition time due to the longer residence time. For the third region, the lower degree of ordering was attributed to a deterioration in the surface.

The growth-induced ordering behaviour in the present InGaAs layers is similar to the results of Kurtz et al.(19) for InGaP layers. However, although the general features of the explanation suggested by Kurtz et al.(19) are similar to our explanation given above, some aspects of our explanation are different. In the present work, the ordering behaviour was considered to be controlled by atomic mobility both on the surface and in the transition region, and the thermodynamic equilibrium degree of the surface-induced ordering with respect to disordering. The present work showed the ordering behaviour directly. Kurtz et al.(19) derived indirectly the degree of ordering using the measurements of band gap under the assumption that the band gap depends solely on the degree of ordering. But in the layers grown over a wide range of conditions, the band gap may be affected by growth-induced composition modulations, alloy clustering (which results in a fine scale modulated contrast and a coarse scale tweed-like contrast), defects and ordered structure (which includes planar defects such as APBs and boundaries between two ordered variants). Another point is related to their measurement accuracy; variations of band gap between the different growth temperature layers is often on the limit of detection. Therefore, the ordering behaviour deduced may not be correct. Nonetheless, the overall behaviour is reasonably described and comparable to the present work.

6-2-6 Conclusion

TED results showed that the CuPt-type ordering occurs in many of the $In_{0.53}Ga_{0.47}As$ layers grown on (001) substrates using a wide variety of conditions. Only two of the four possible {111} variants, i.e. $(\bar{1}11)$ and $(1\bar{1}1)$, were observed. Columnar-

like ordered regions of the two variants were observed and the ordered regions nucleated separately. The ordered regions originate at the substrate/layer interface and extend throughout the full layer thickness of ~4μm. Between the ordered regions, there were sometimes unordered regions. APBs were present in the ordered regions and these are considered to be responsible for the elongation and tilting of the superlattice spots. The observation of only two of the four possible variants and post-growth annealing results strongly indicate that the ordering occurs solely at the growing surface and is unstable in the bulk of the layer. In order to interpret the growth dependence of the ordering, a model based on two competing processes of surface-induced ordering and bulk diffusion-induced disordering was proposed. The surface-induced ordering was considered to be controlled by the two factors of lifetime and relaxation time of the mixed Group III atoms both on the surface and in a transition region beneath the growing surface, whilst the bulk disordering was considered to be controlled by the two factors of the thermodynamic equilibrium degree of the surface-induced ordering and the diffusion time within the transition region.

6-3 Atomic ordering in MBE and MOCVD $InAs_ySb_{1-y}$ layers

6-3-1 MBE $InAs_ySb_{1-y}$ layers

6-3-1-1 Experimental

The $InAs_ySb_{1-y}$ layers examined in the present work were grown on (001) GaAs, InAs or InSb substrates by the MBE method over a wide range of temperatures and across the full composition range. All the layers were grown at a growth rate of ~0.17nm/s. Details of the layers examined are listed in Table 4.1. In order to investigate the thermal stability of the atomic ordering present in $InAs_ySb_{1-y}$, a layer grown at 430°C was then annealed for 3 hours at 370°C in the growth kit and other layers grown at 370°C and 430°C were sealed in quartz ampoules, evacuated to less than 10^{-6} Torr, and annealed at 296°C for

48 hours and at 350°C for 95 hours, respectively. The effects of elastic strain and Si-doping on the atomic ordering were also investigated.

6-3-1-2 TED and TEM analyses of $InAs_ySb_{1-y}$ layers

TED examinations were made of two orthogonal <110> cross-section specimens of the layers. The [110] and [$\bar{1}$10] cross-section specimens were distinguished, as described in chapter 3. The [110] cross-section TED patterns obtained from the $InAs_ySb_{1-y}$ (y=0.2 to 0.8) layers grown at 370°C are shown in Fig. 6.14. The TED pattern taken from the $InAs_{0.4}Sb_{0.6}$ layer exhibited the fundamental zinc-blende spots but also strong 1/2{111} superlattice spots, indicating the presence of CuPt-type ordering on the ($\bar{1}$11) and (1$\bar{1}$1) planes. The superlattice spots were elongated towards the [001] growth direction and slightly tilted from this direction. The superlattice spots were joined together by [001] lines of very weak diffuse diffracted intensity, which corresponds to rods of diffuse intensity in reciprocal space aligned along the [001] growth direction. The intersection of these [001] rods of diffuse intensity with the Ewald sphere results in the weak satellite spots present around the fundamental zinc-blende spots detected in [001] plan-view TED patterns. The existence of weak diffuse diffracted intensity could be attributed to either a breakdown of the ordered structure in the [001] direction or sharp planar defects in the ordered domains (12), as discussed in section 6-2-2. The elongation of the superlattice spots can be interpreted as a consequence of either the morphology of the ordered domains or a strained superlattice structure in the layer.

As described in section 4-3-2, composition sensitive **g**(002) TEM DF investigations showed that some of the InAsSb layers consisted of two phase materials due to phase separation and some of them consisted of single phase material (e.g. see Table 4.3). Phase separation occurs in the InAsSb layers when grown within a miscibility gap, $T_g \leq 400°C$, and the layers contain alternating platelets of different alloy compositions, e.g. approximately $InAs_{0.3}Sb_{0.7}$ and $InAs_{0.7}Sb_{0.3}$, which have tetragonally distorted crystal lattices, as discussed in section 4-3-3 (Table 4.3). Therefore, each tetragonally distorted

Figure 6.14

Cross-section [110] TED patterns from MBE $InAs_ySb_{1-y}$ layers with (a) y=0.2, (b) 0.4, (c) 0.6 and (d) 0.8 grown at 370°C showing 1/2{111} superlattice spots. Intensity of superlattice spots is maximum at y=~0.5.

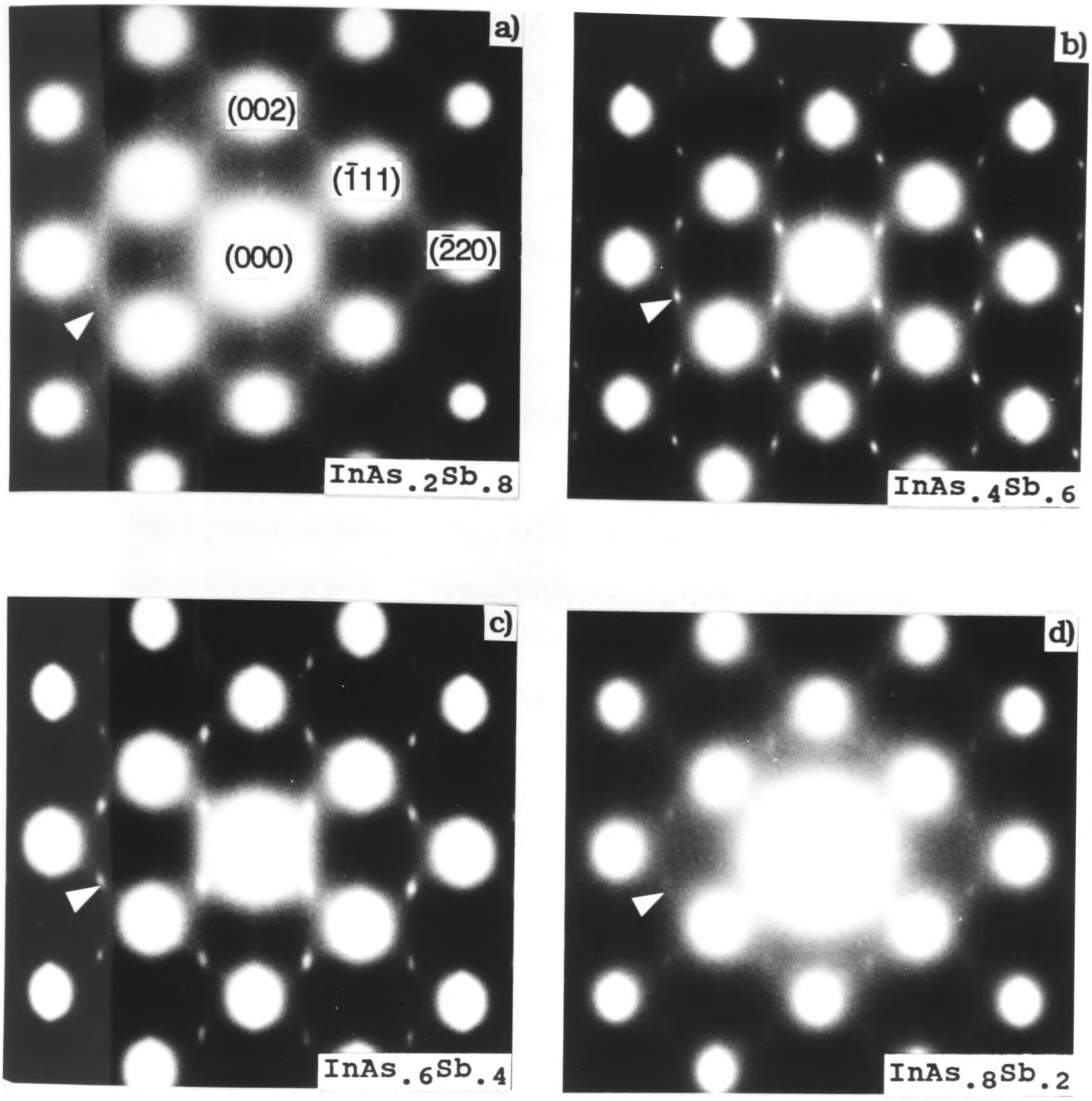

Fig. 6.14

platelet has a different size unit cell. This size difference could be the reason for the elongation of the superlattice spots because each selected area TED pattern comes from several platelets. The evidence for the CuPt-type ordering in both types of platelet was obtained using TED examinations and confirmed by taking two beam DF TEM micrographs using one of the superlattice spots, as discussed later in this section. In order to observe the superlattice spots arising from each plate-like phase, the specimen was tilted out along the (220) Kikuchi band from the [110] pole to have strongly excited (004) main spots. The tilted TED pattern of the $InAs_{0.4}Sb_{0.6}$ layer grown at 370°C clearly showed the superlattice spots associated with each of the $InAs_{0.34}Sb_{0.66}$ and the $InAs_{0.71}Sb_{0.29}$ phases, respectively.

The intensity of the superlattice spots was closely the same on going from area to area within individual layers. There was a consistent trend on going from layer to layer. For the $InAs_{0.2}Sb_{0.8}$, $InAs_{0.4}Sb_{0.6}$, $InAs_{0.6}Sb_{0.4}$ and $InAs_{0.8}Sb_{0.2}$ layers grown at 370°C, the superlattice spot intensities were weak, strong, strong and weak, respectively (Table 6.2). Hence, as the value of y increased, the ordering progressively increased, was a maximum at y=0.5, and then decreased. The observed change in ordering could be due to a change in either the volume fraction of the ordered material, or the degree of ordering. The occurrence of a maximum ordering at y=0.5 for these MBE $InAs_ySb_{1-y}$ layers is consistent with the finding of Jen et al.[22] for analogous MOCVD layers. The $[\bar{1}10]$ cross-section TED patterns obtained from all the layers showed no such superlattice spots indicating no similar atomic ordering on the (111) and $(\bar{1}\,\bar{1}\,1)$ planes, i.e. InAsSb layers grown on (001) substrates show CuPt-type ordering on only two of the four possible {111} planes, namely, the $(\bar{1}11)$ and $(1\bar{1}1)$ planes.

The effects of growth temperature on the ordering behaviour in the layers grown at temperatures ranging from 295°C to 470°C were investigated by TED. Fig. 6.15 (a), (b) and (c) illustrate the [110] TED patterns taken from the MBE $InAs_ySb_{1-y}$ layers ($y \cong 0.5$) grown at 320, 370 and 430°C, respectively. The 320°C pattern exhibited weak ordering, the 370°C and 400°C patterns exhibited strong ordering and the 430°C pattern exhibited weak ordering. No evidence of the ordering was observed for the 295°C and 470°C layers.

Table 6.2 TED results of atomic ordering in MBE InAsSb layers.

Sample number	y	T_g (°C)	Buffer layer	T_a (°C)	Intensities of extra spots	Doping
IC 247	0.5	295	GaAs		v. weak	no
IC 249	0.5	320	InSb		weak	no
IC 262	0.5	340	InAs		medium	no
IC 121	0.2	370	InAs		weak	no
IC 118	0.4	370	InAs		strong	no
IC 264	0.5	370	InAs		strong	no
IC 285	0.5	370	InAs		medium	Si*
IC 124	0.6	370	InAs		strong	no
IC 119	0.8	370	InAs	296/48hr	weak	no
IC 265	0.5	400	InAs		strong	no
IC 209	0.56	430	InAs		medium	no
IC 209	0.56	430	InAs	350/95hr	medium	no
IC 213	0.56	430	GaAs		medium	no
IC 219	0.56	430	GaAs		weak	Si
IC 284	0.5	430	GaAs		weak	Si*
IC 288	0.5	430	GaAs	370/3hr	weak	no
		370	GaAs	370/2hr	medium	no
IC 248	0.5	470	GaAs		none	no

y = nominal composition in $InAs_ySb_{1-y}$; T_g = growth temperature (°C). T_a = annealing temperature (°C). v.weak = very weak ordering. Si* indicates doping concentration of $5x10^{18}/cm^3$.

Figure 6.15

Cross-section [110] TED patterns from MBE $InAs_ySb_{1-y}$ layers (y=~0.5) grown at (a) 320°C, (b) 370°C and (c) 430°C. Intensity of superlattice spots is maximum at 370°C.

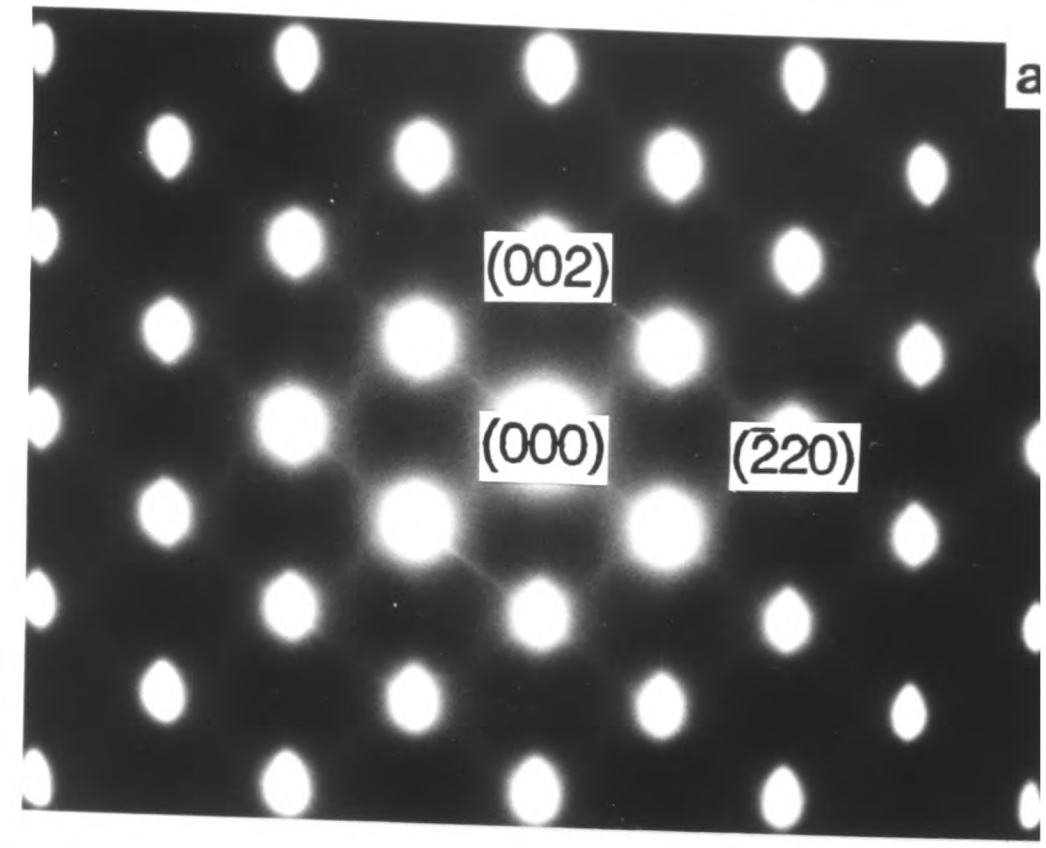

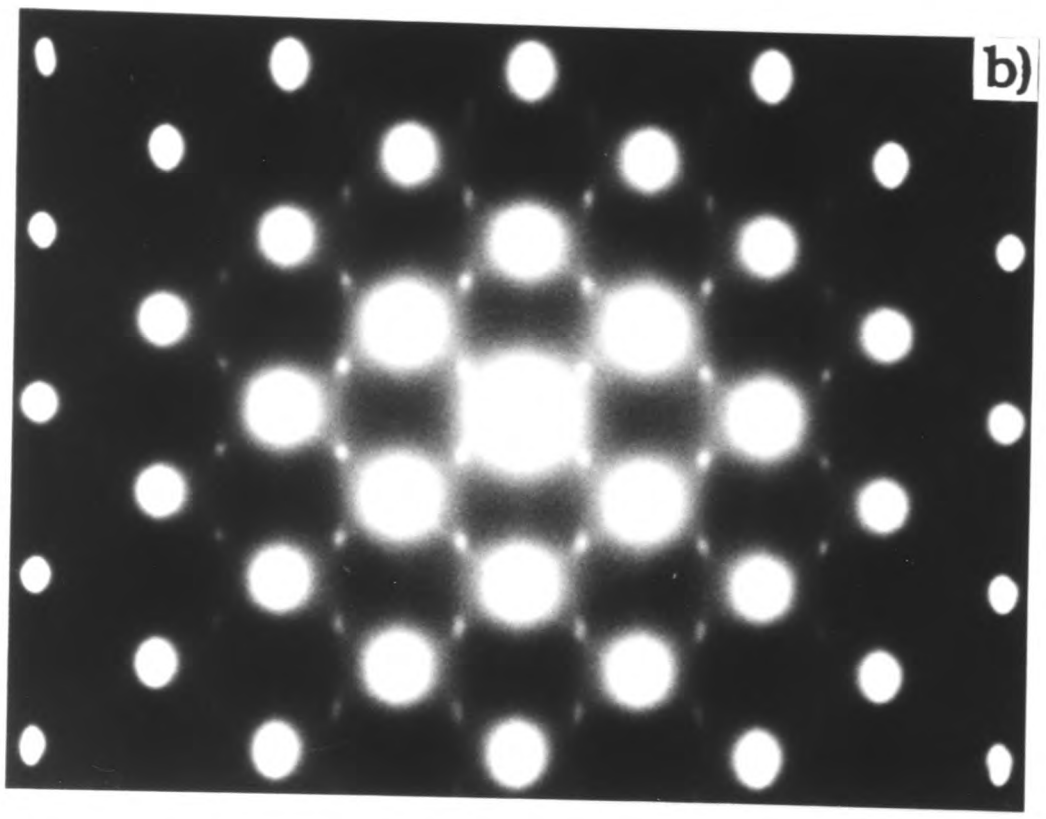

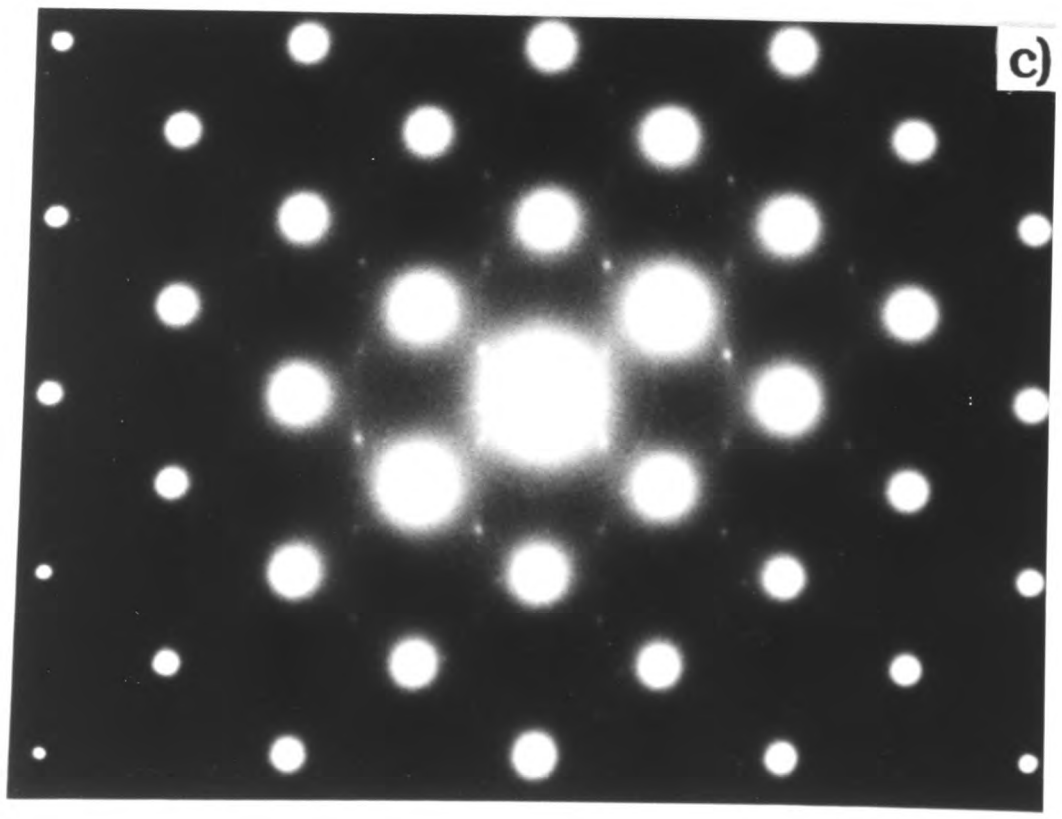

Fig. 6.15

[$\bar{1}$10] TED patterns revealed no evidence for either CuPt-type ordering or change in the patterns with increasing growth temperature.

In order to investigate the thermal stability of the ordering, the specimens that exhibited ordering were annealed and re-examined. These specimens were: a) $InAs_{0.8}Sb_{0.2}$ grown at 370°C and annealed at 296°C for 48 hr; b) $InAs_{0.56}Sb_{0.44}$ grown at 430°C and annealed at 350°C for 95hr; c) $InAs_{0.5}Sb_{0.5}$ grown at 430°C and annealed at 370°C for 3hr. The intensities of the superlattice spots of all of these annealed specimens were weaker than those of the as-grown specimens, indicating that the CuPt-type ordered structure present in these mixed Group V compound semiconductors is unstable in the bulk layer. The CuPt-type ordering is also unstable enough to be destroyed by exposure to an electron beam. Thus, when a thin TEM specimen of the $InAs_{0.4}Sb_{0.6}$ layer of Fig. 6.14(b) was exposed for 20 hours in the electron beam of 400kV and beam current of ~126μA (Fig. 6.16(a)), the intensity of the superlattice spots of the electron beam damaged layer became much weaker.

TED examinations have also been performed to investigate the effects of lattice mismatch and doping on the CuPt-type atomic ordering in $InAs_{0.56}Sb_{0.44}$ layers grown at 430°C. In Fig. 6.16(b) and (c) are shown the [110] TED patterns taken from undoped $InAs_{0.56}Sb_{0.44}$ layers grown on (001) InAs and GaAs, respectively and which exhibited a similar intensity of the superlattice spots due to atomic ordering. There are 3.63% and 9.45% lattice mismatches between $InAs_{0.56}Sb_{0.44}$ and InAs, and between $InAs_{0.56}Sb_{0.44}$ and GaAs, respectively. This suggests that elastic strain associated with lattice mismatch has a minor effect on the intensity of the superlattice spots associated with the ordering, which is consistent with the results described above for InGaAs layers. However, the higher mismatch may result in a higher density of planar defects such as APBs in the ordered regions, as described in section 6-2-3.

The intensity of the superlattice spots in a [110] TED pattern obtained from the $InAs_ySb_{1-y}$ ($y \cong 0.5$) layer doped with $5x10^{18}cm^{-3}$ Si atoms and grown at 430°C (Fig. 6.16(d)) is weaker than that of the undoped layer (Fig. 6.15(c)). As has been reported previously (23-26), Si-doping slows the development of the CuPt-type atomic ordering in

Figure 6.16

Cross-section [110] TED patterns from MBE $InAs_ySb_{1-y}$ layers. (a) Pattern from $InAs_ySb_{1-y}$ layer (y=0.4) grown at 370°C and then exposed to 400kV electron beam for 20 hr. Superlattice spots are weak compared with corresponding unexposed layer of Fig. 6.14(b). (b) and (c) Patterns from $InAs_ySb_{1-y}$ layer (y=0.56) grown at 430°C on InAs and GaAs respectively. No significant differences are visible. (d) Pattern from Si-doped $InAs_ySb_{1-y}$ layer (y=0.56) grown at 430°C. Superlattice spots are weak compared with corresponding undoped layer of Fig. 6.15(c).

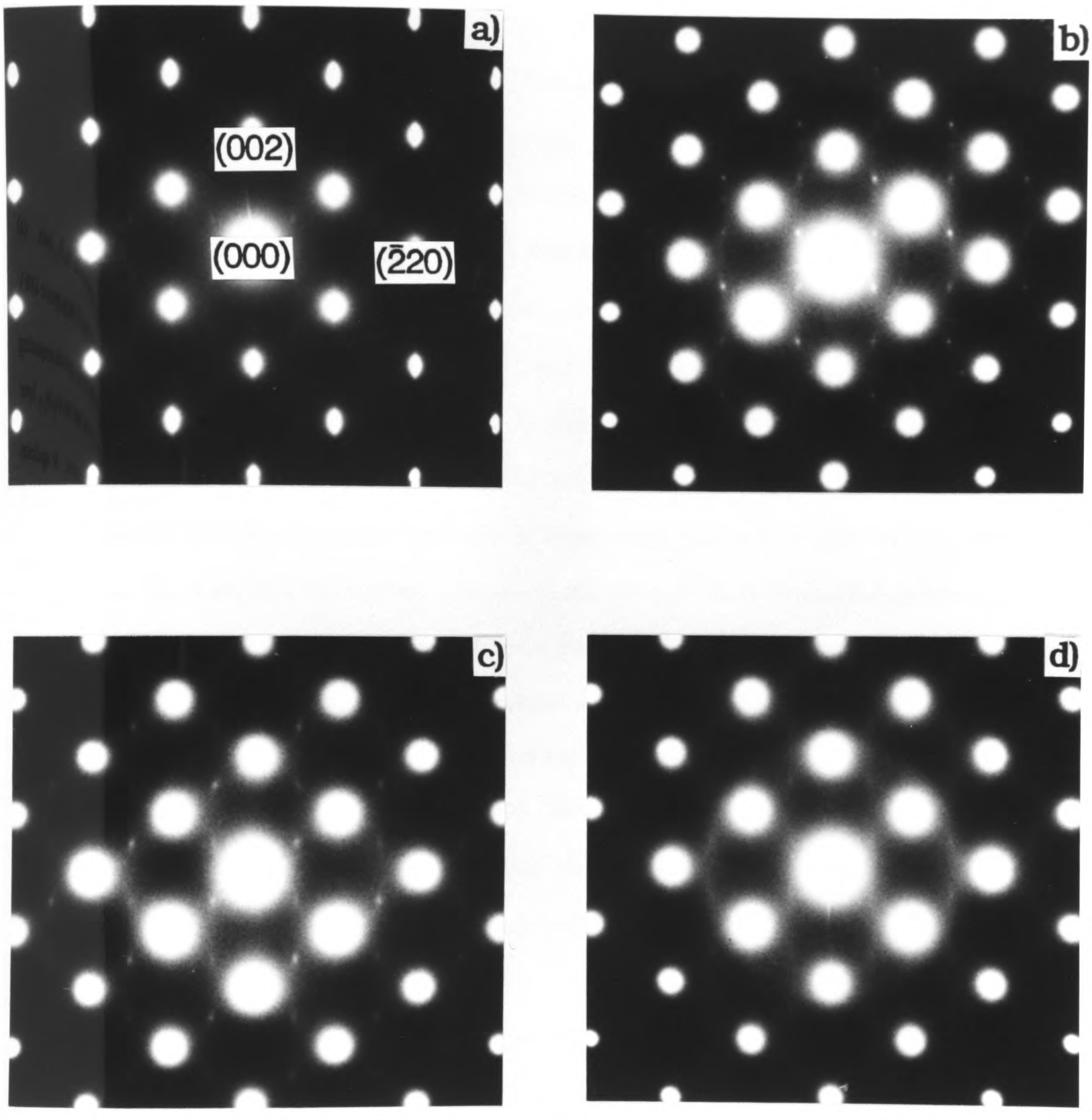

Fig. 6.16

InGaP layers, i.e. Si atoms may either act as a scattering barrier to diffusion of both As and Sb atoms (26) or lead to enhanced interdiffusion rates under the growing surface in a transition region leading to disordering of the CuPt-type ordering in the bulk as observed for intentionally grown superlattice structures (27).

In Fig. 6.17 is shown a TEM DF micrograph obtained using a strongly excited $1/2(\bar{3}\,3\,\bar{1})$ superlattice spot from a [110] cross-section specimen of an $InAs_{0.4}Sb_{0.6}$ layer grown at 370°C. Well distributed small white regions ~3 to ~20nm across indicate the CuPt-type ordered phase on the $(\bar{1}\,11)$ plane. This phase is better developed in As-rich regions (indicated by 'A') rather than Sb-rich regions (indicated by 'S'). A TEM DF micrograph obtained for the other variant using an $1/2(\bar{3}\,31)$ superlattice spot exhibited similar ordered microdomains. For both of these micrographs, the dark regions correspond to either the other ordered variant, much less ordered material or unordered material.

Similar DF TEM investigations were performed on [110] cross-section specimens of the InAsSb layers consisting of single phase material (e.g. IC 121 and IC 209). Results showed small plate-like ordered domains ~15 to ~70nm across.

Another important feature of the MBE $InAs_ySb_{1-y}$ layers is diffuse diffracted intensity visible in the $[\bar{1}\,10]$ TED patterns. Fig. 6.18 shows an $InAs_{0.5}Sb_{0.5}$ layer grown at 370°C and weak lines of diffuse diffracted intensity are seen running parallel to the [001] growth direction. These [001] lines occur at $\sim{}^{1}/_{6}g220$ positions indicating a modulation in the [110] direction of the layers with a periodicity of $\sim 3d_{110}$. They imply that there are many monolayer abrupt changes of the [110] modulations in the [001] growth direction (4). Murgatroyd et al.(4) examined (001) MBE $GaAs_ySb_{1-y}$ layers and reported a similar modulation along the [110] direction with a periodicity of $4d_{110}$.

Reflection high energy electron diffraction (RHEED) studies of (001) MBE $GaAs_ySb_{1-y}$ layers showed a (2x4) reconstructed surface, which consists of a series of identical cells, each comprising a block of 2x3 'A' atoms (e.g. see Fig.6.26). Each of the three pairs of atoms corresponds to a reconstructed dimer along the $[\bar{1}\,10]$ direction, giving a $2d_{\bar{1}\,10}$ repeat distance. Individual cells are separated from one another in the [110] direction by a single row of vacancies in the $[\bar{1}\,10]$ direction, giving a $4d_{110}$ repeat distance.

Figure 6.17

Cross-section [110] TEM 1/2($\bar{3}\,3\,\bar{1}$) DF micrograph from MBE $InAs_ySb_{1-y}$ layer (y=0.4) grown at 370°C. Small white regions are ordered phase corresponding to the ($\bar{1}\,11$) variant.

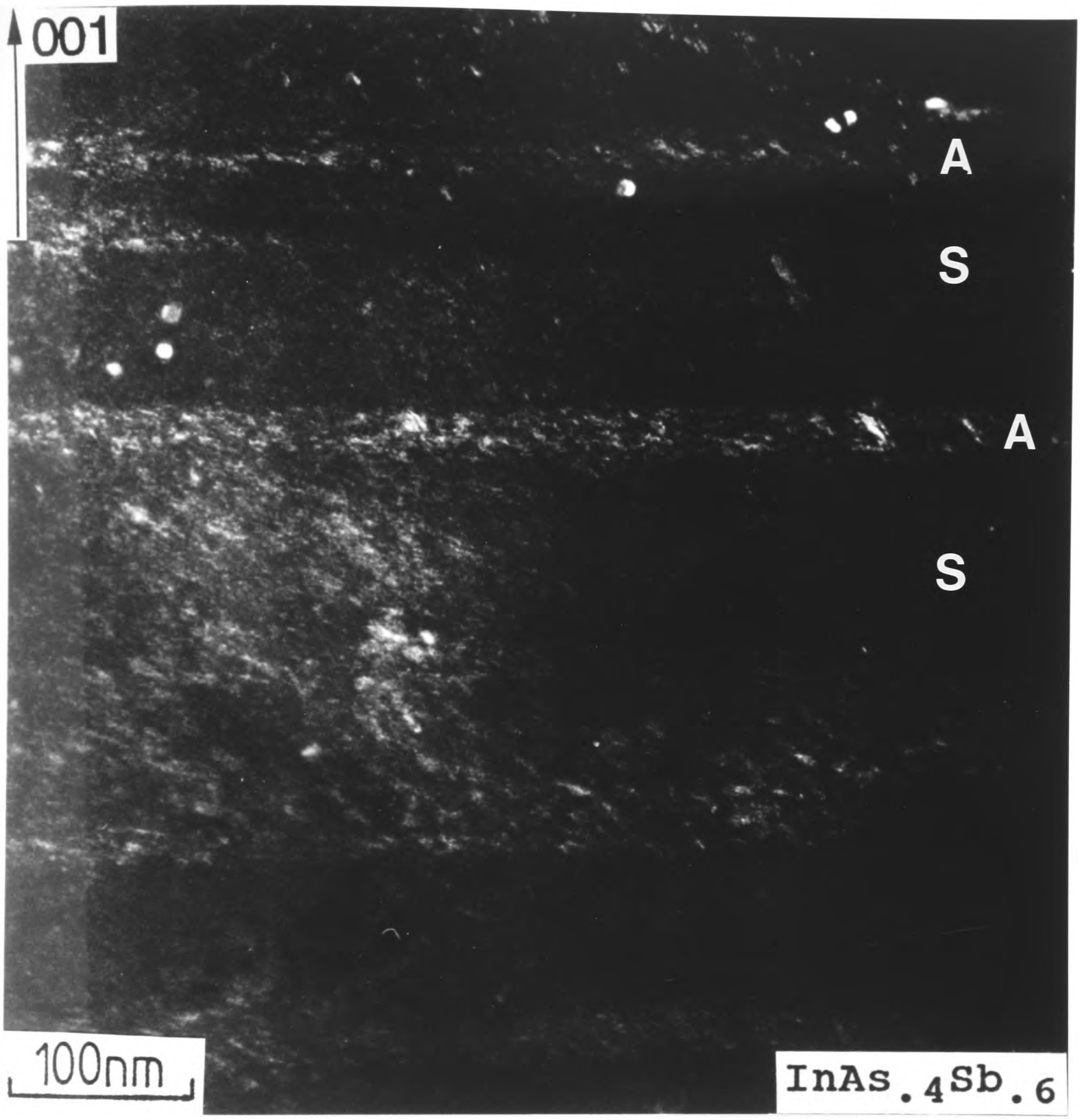

Fig. 6.17

Figure 6.18

Cross-section [$\bar{1}$10] TED pattern from MBE $InAs_ySb_{1-y}$ layer (y=0.5) grown at 430°C, showing lines of diffuse intensity along [001] at 1/6**g**220 positions. This indicates a modulation with a periodicity of ~$3d_{110}$ in the [110] direction.

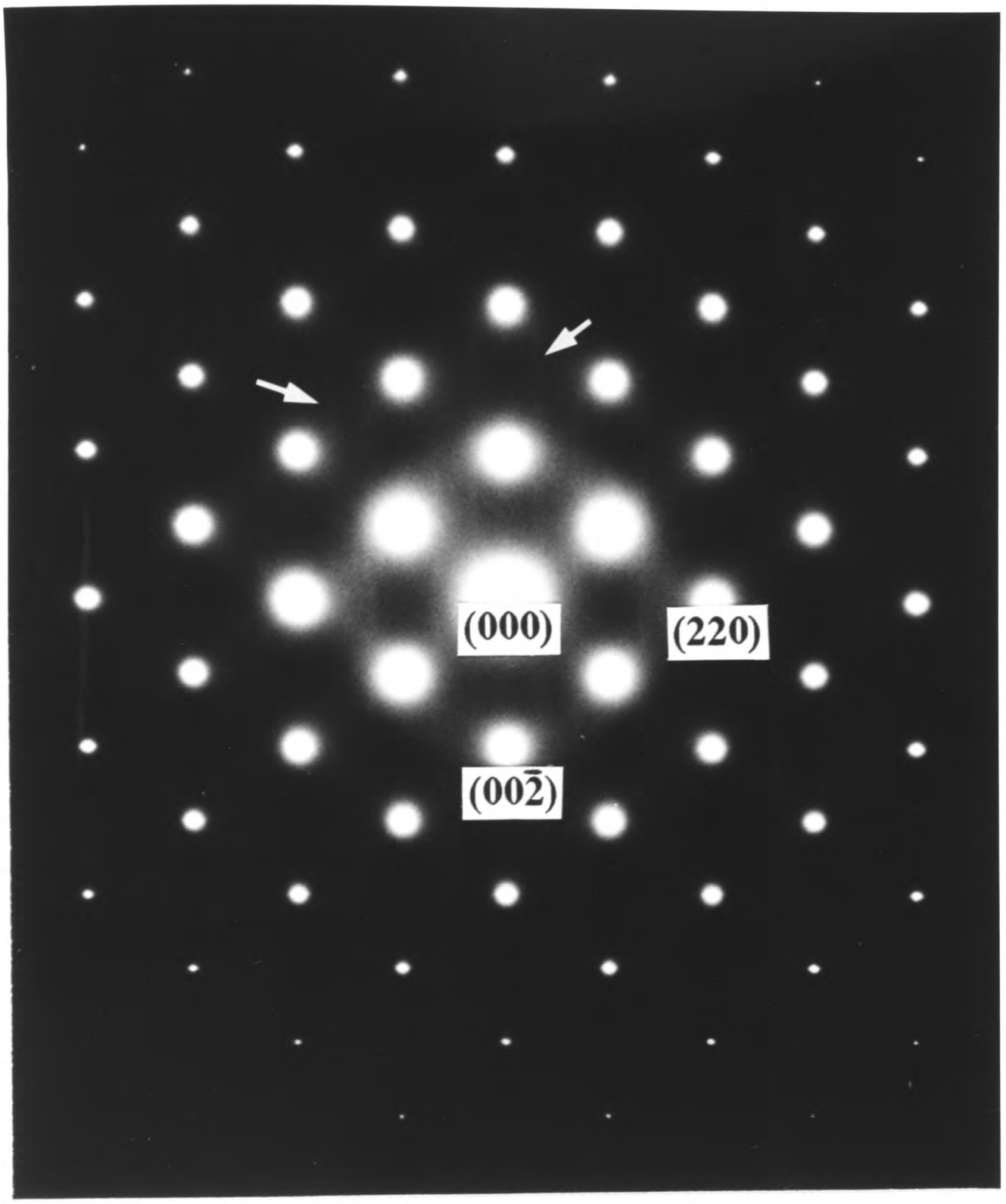

Fig. 6.18

For $GaAs_ySb_{1-y}$ layers, Murgatroyd et al.(4) used the model of the (001) GaAs surface to explain their experimental results and replaced the As-As dimers by As-Sb dimers. Furthermore, they assumed that the As-Sb atoms in all of the dimers are oriented in the same sense. As a result, each cell contains a row of three As atoms in the [110] direction and an adjacent similar row of the three Sb atoms. On the basis of this model, the behaviours were considered. When the deposition of As and Sb atoms occurs, the rows of vacancies along the $[1\bar{1}0]$ direction between the cells become filled with As and Sb atoms. For adjacent cells that are out of phase, Fig. 6.26(b), the joining up creates an APB. When subsequent monolayers go down, atomic ordering occurs on the $(\bar{1}11)$ planes and a small area of APB builds up on the (110) plane. Thus, it was concluded that these boundaries represent a modulation of the atomic structure in the [110] direction with a repeat distance of $4d_{110}$.

The surface reconstruction of the growing $InAs_ySb_{1-y}$ layers was determined from in-situ RHEED studies. For the $InAs_{0.5}Sb_{0.5}$ layers grown at 430°C, a weak/medium strength RHEED pattern corresponding to a (2x3) reconstruction was observed (28). Based on a missing row dimer model, which would be applicable to an As-stabilized (001) GaAs surface, we assume the (2x3) reconstructed surface consists of a series of identical cells, each comprising a block of 2x2 'A' atoms. Each of the two pairs of atoms corresponds to a reconstructed dimer along the $[\bar{1}10]$ direction, giving a $2d_{\bar{1}10}$ repeat distance. Individual cells are separated from one another in the [110] direction by a single row of vacancies in the $[\bar{1}10]$ direction, giving a $3d_{110}$ repeat distance. Like GaAsSb layers, the InAsSb diffuse diffracted intensity in the $[\bar{1}10]$ TED patterns running along the [001] growth direction could be associated with a modulation of the atomic structure in the [110] direction with a repeat distance of $3d_{110}$.

6-3-2 MOCVD $InAs_ySb_{1-y}$ layers

6-3-2-1 Experimental

The $InAs_ySb_{1-y}$ layers examined in this section were grown by MOCVD at Utah University in the U.S.A. in a horizontal atmospheric pressure, infrared heated reactor using trimethylindium (TMIn), trimethylantimony (TMSb), and arsine as reactants. The growth temperatures were 400°C and 450°C, and the growth rate was varied between ~0.12 and ~0.22nm/s. The layer thicknesses were 0.4 to 0.6μm. Either (001) undoped InAs or InSb substrates were used. The layer compositions of the InAsSb samples were determined from X-ray diffraction with the assumption of Vegard's law. The thicknesses of the layers were measured from TEM cross-section micrographs. Details of the layers examined are listed in Table 6.3.

6-3-2-2 TED, TEM and HREM analyses

Cross-section TED examinations have been carried out to investigate ordering in the MOCVD InAsSb layers. The TED results of the $InAs_{0.47}Sb_{0.53}$ layer grown at 450°C showed that the $[\bar{1}10]$ pattern, Fig. 6.19(b), exhibits fundamental zinc-blende spots and 1/3{111} spots associated with twins. The [110] pattern, Fig. 6.19(a), exhibits the two sets of $1/2(\bar{1}11)$ and $1/2(1\bar{1}1)$ superlattice spots which are circular and indicate the existence of the CuPt-type ordered structure. Fig. 6.20 shows a schematic of the atomic configuration of fully ordered $InAs_{0.5}Sb_{0.5}$ in the [110] projection. It exhibits alternating InAs and InSb layers on the $(1\bar{1}1)$ planes with a doubling in periodicity along the $[1\bar{1}1]$ direction, which gives rise to the $1/2(1\bar{1}1)$ superlattice spots in the [110] TED patterns. These spots have equal intensity in most specimens, indicating that the degree of ordering is closely the same for the two different variants.

The superlattice spots were present for $InAs_ySb_{1-y}$ layers with y varying from 0.09 to 0.53 (Table 6.3). However, the $InAs_ySb_{1-y}$ (y=0.94) layer did not exhibit such

Table 6.3 TED results of atomic ordering in MOCVD $InAs_ySb_{1-y}$ layers

$InAs_ySb_{1-y}$ (y)	Growth temp. (°C)	Growth rate (nm/sec)	Substrate	Intensities of extra spots
0.94	400	0.12	InAs	none
0.53	450	0.15	InSb	medium
0.47	450	0.17	InSb	medium
0.39	450	0.22	InSb	strong
0.09	400	0.20	InSb	v.weak

v.weak=very weak.

Figure 6.19

TED patterns of MOCVD $InAs_ySb_{1-y}$ layer (y=0.47) grown at 450°C. (a) Cross-section [110] TED pattern shows 1/2{111} superlattice spots. (b) Cross-section [$\bar{1}$10] pattern shows twin spots but no superlattice spots.

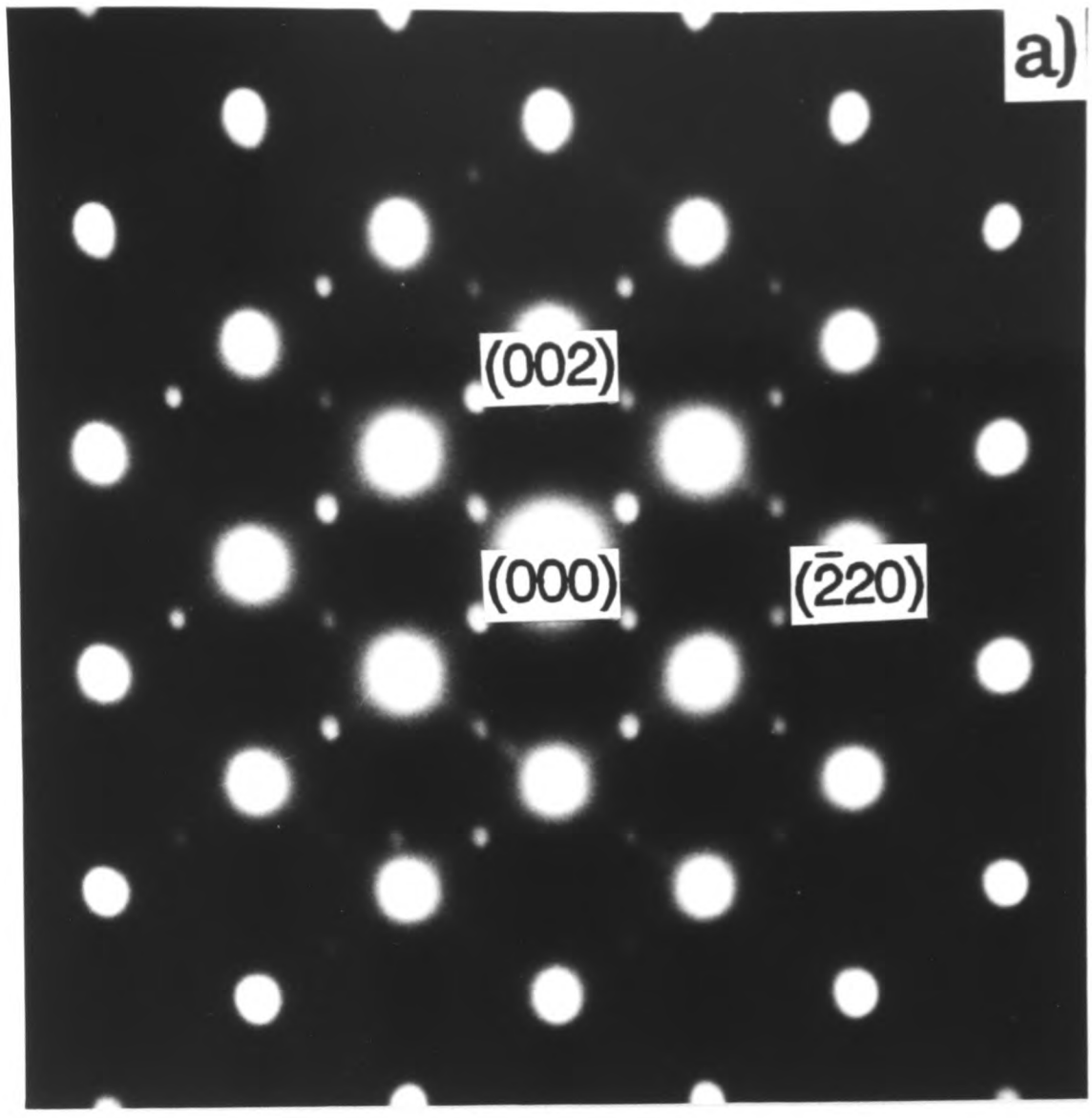

Fig. 6.19

Figure 6.20

[110] projection of InAsSb atomic lattice perfectly ordered on $(1\,\bar{1}\,1)$ planes.

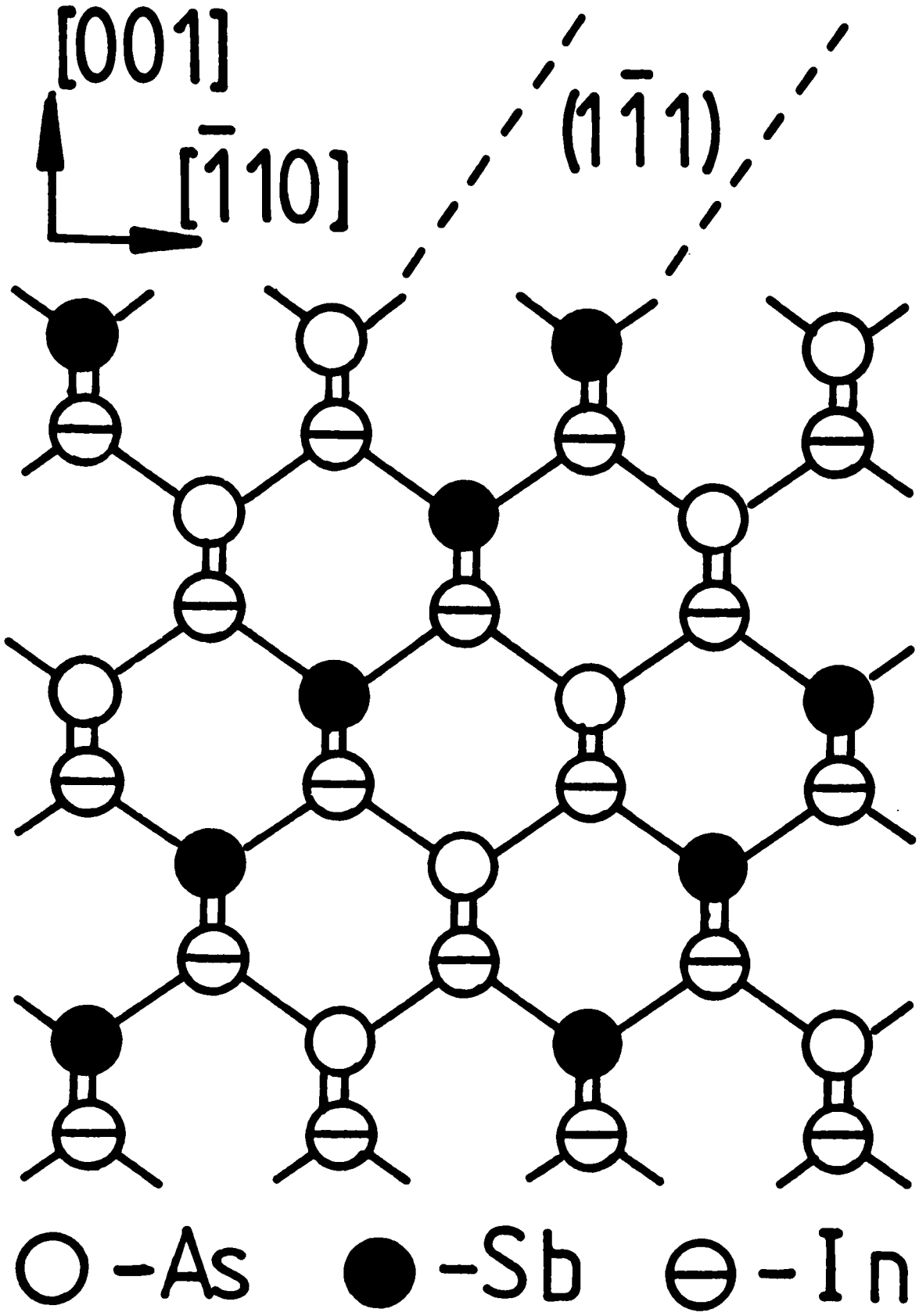

[110] projection

Fig. 6.20

superlattice spots. This observation may be interpreted in two possible ways. First, the growth rate of ~0.12nm/s for the $InAs_{0.94}Sb_{0.06}$ is low. We have already discussed the role of the two competing processes of surface-induced ordering and bulk diffusion-induced disordering in forming the CuPt-type ordered structure in the InGaAs layers. As this ordering is predicted to be unstable in the bulk, the ordered structure could subsequently disorder in the bulk layer (a transition region) during further epitaxial growth by a bulk diffusion process. At the low growth rate of ~0.12nm/s, although the surface-induced ordering in the bulk of the layer may occur, the degree of ordering achieved in the bulk layer may decrease due to an increased rate of disordering by bulk diffusion in the transition region close to the growing surface.

Secondly, the absence of the ordering in the $InAs_{0.94}Sb_{0.06}$ layer may be attributed to a small volume fraction of the ordered phase in the layer. When an AB_yC_{1-y} ternary alloy fully orders with the CuPt-type structure, the ordered material has an equal number of B and C atoms. Therefore, for the $InAs_{0.94}Sb_{0.06}$ layer, the ideal highest volume percent of the ordering is only 12% (6% of As and 6% of Sb atoms). However, in practice a smaller volume fraction of the ordered structure would be expected to occur. Therefore, the small volume fraction of the ordered phase formed in the layer may lead to the non-detection of the superlattice spots by TED. The relative intensities of the TED superlattice spots for all the layers are summarised in Table 6.3. The superlattice spots of the $InAs_{0.91}Sb_{0.09}$ layer exhibit very weak intensity. For this layer grown using a growth rate of ~0.20nm/s, the highest possible volume of the ordering is 18%.

In Fig. 6.21(a) and (b) are shown 1/2{331} TEM DF micrographs of the same area of a (001) plan-view specimen of the $InAs_{0.39}Sb_{0.61}$ layer grown at 450°C with a growth rate of ~0.22nm/s. The micrographs were obtained using two different 1/2{331} superlattice spots after tilting the specimen ~18° about the orthogonal <100> tilt axes to two different <103> poles. The two micrographs show the areas ordered on $(\bar{1}11)$ and $(1\bar{1}1)$ planes, which appear bright. Almost the whole layer is ordered. The two variants of the ordering occupy separate and well-defined regions, which is similar to the ordering behaviour observed above for the mixed Group III semiconductor InGaAs. The ordered regions range

Figure 6.21

Plan-view [001] TEM 1/2{331} DF micrographs of same area of MOCVD $InAs_ySb_{1-y}$ layer (y=0.39) grown at 450°C using ~0.22nm/s, showing ordered regions containing a high density of APBs. (a) ($\bar{1}$11) variant, (b) (1$\bar{1}$1) variant.

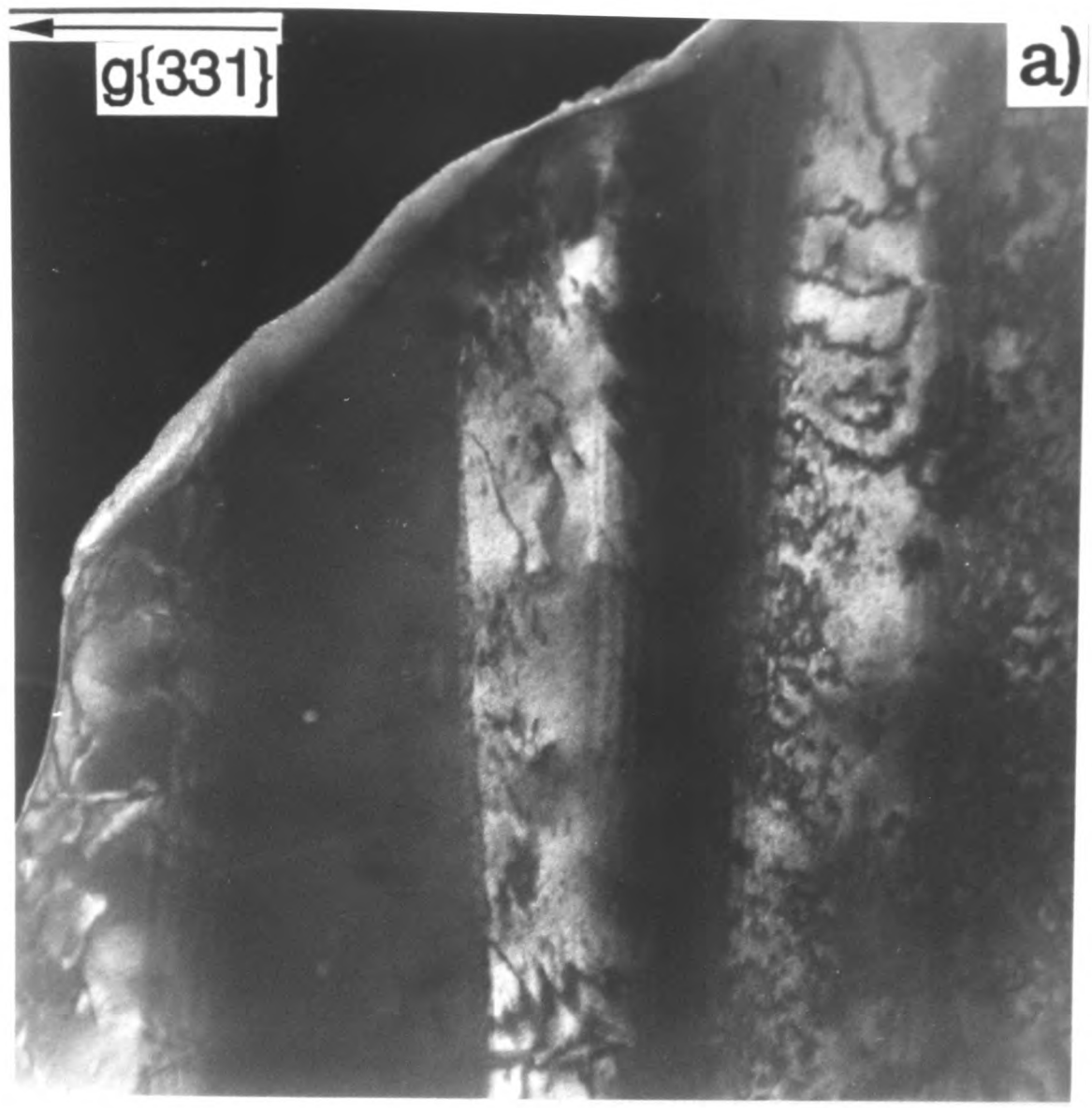

Fig. 6.21

in size from ~0.2 to ~0.5μm across. A high density of dark ribbon-like contrast features with no specific configuration are present, and these are considered to be APBs, as described in section 6-2-3. Boundaries between the regions ordered on $(\bar{1}11)$ and $(1\bar{1}1)$ planes lie along <331> directions. A $1/2(\bar{3}3\bar{1})$ TEM DF micrograph was obtained from a [110] cross-section of the $InAs_{0.39}Sb_{0.61}$ layer grown at 450°C. The micrograph (not shown) exhibited columnar-like regions ordered on $(\bar{1}11)$ and $(1\bar{1}1)$ planes, which contained a high density of APBs. The two variants of the ordering occupied separate regions, which is consistent with the plan-view results.

These ordered regions present in the $InAs_{0.39}Sb_{0.61}$ layer were imaged using HREM. The [110] cross-section image, Fig. 6.22, was taken at 200kV on an Akashi 002B microscope using the second largest objective aperture, which includes all the spots out to {331}. A lattice periodicity which is twice that of the {111} planes of InAsSb is clearly visible in both the $(1\bar{1}1)$ and $(\bar{1}11)$ directions, which corresponds to the presence of the superlattice spots of the two different variants in the [110] TED patterns. This doubling occurs by the growth of alternating As-rich and Sb-rich monolayers on {111} planes. The ordered regions associated with the $(\bar{1}11)$ and $(1\bar{1}1)$ two variants are divided by a twin (marked 'T'). Planar defects such as APBs are often observed in the HREM image, i.e. the region indicated by A in Fig. 6.22, where the (111) fringes are shifted by half a superlattice structure period.

6-3-3 Discussion

The maximum intensities of the superlattice spots, (i.e. the maximum degree of ordering), present in the MBE and MOCVD $InAs_ySb_{1-y}$ layers were observed at different temperatures. For the MOCVD layers, the degree of ordering was a maximum at 450°C, whereas for the MBE layers, the maximum was obtained at 370 to 400°C. This difference could be due to different layer growth mechanisms for these two growth techniques. For MOCVD and MBE $InAs_ySb_{1-y}$ layers, the degree of ordering was a maximum at $y \cong 0.5$. The composition of the CuPt-type fully ordered phase is A_2BC: in the ternary alloy of

Figure 6.22

Cross-section [110] HREM image obtained from MOCVD $InAs_ySb_{1-y}$ layer (y=0.39) grown at 450°C, showing a lattice periodicity which is double that of the {111} planes of InAsSb. T indicates twinned material. At regions A the {111} fringes are shifted on crossing an APB.

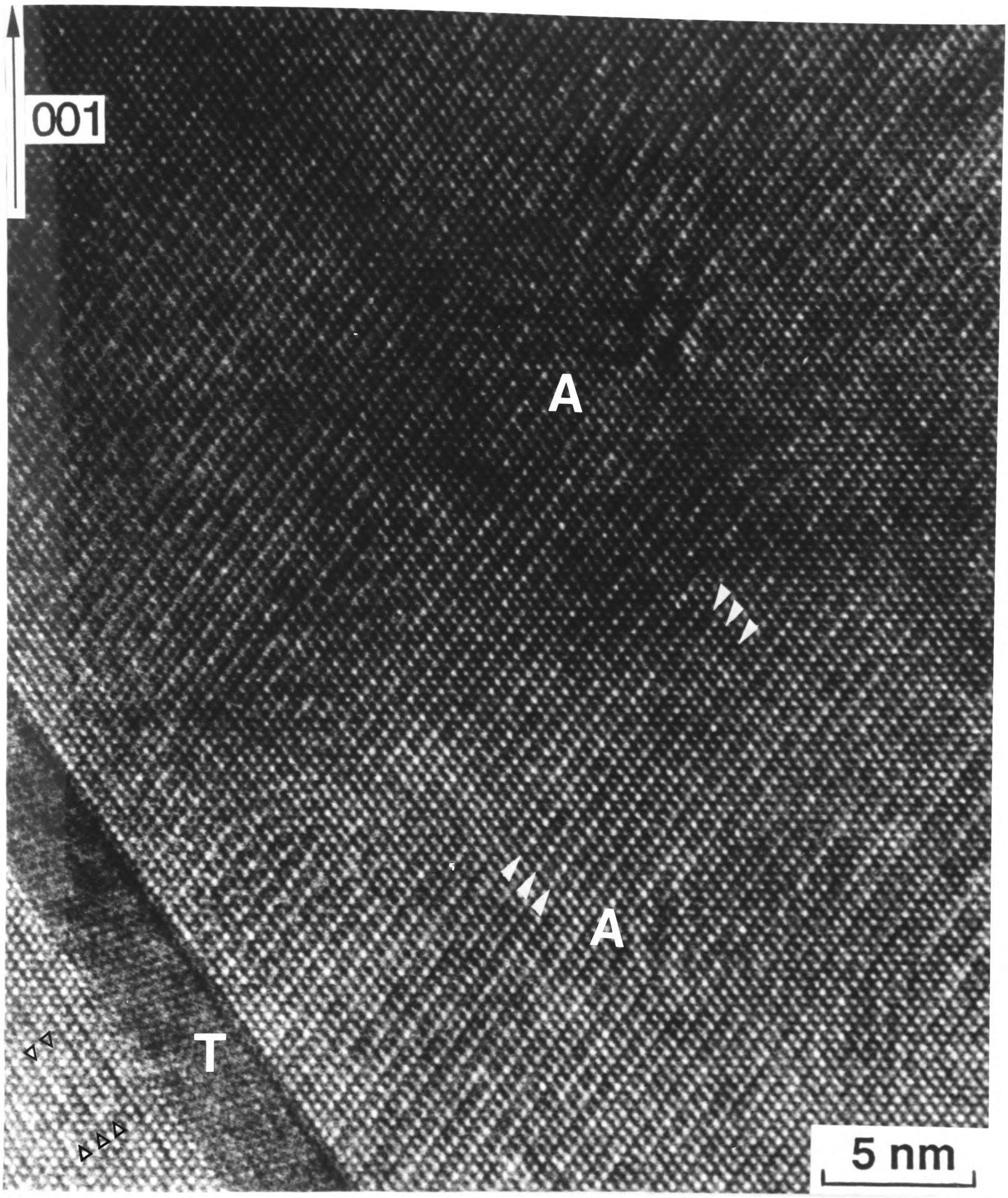

Fig. 6.22

AB_yC_{1-y}, this structure consists of equal number of B and C atoms. The maximum degree of ordering occurring at y=0.5 agrees well with this aspect. For the $InAs_ySb_{1-y}$ system, the CuPt-type ordered structure consists of equal number of As and Sb atoms. Therefore, the highest possible volume percent of ordering for a specimen with y=0.5 is 100% (50% of As and 50% of Sb). In general, the intensity of the superlattice spots of the MOCVD layers was stronger than that of the MBE layers. It could be related to partial suppression of the ordering due to phase separation occurring in the MBE layers. As described in chapter 4, phase separation occurs in the InAsSb MBE layers when grown at and below 400°C. Therefore, during epitaxial growth, the surface-induced ordering may be hindered by the phase separation process, leading to a reduced degree of the ordering. This suggestion was confirmed by the TEM DF technique performed on the MBE and MOCVD layers. As shown in Fig. 6.17 and Fig. 6.21, the regions ordered on one of the four possible {111} variants exhibits different characteristic morphology in the two layers. The MBE layer shows the ordered regions consisting of small microdomains (~3 to ~70nm across), whereas the MOCVD layer exhibits well-defined uniform ordered regions (~0.2 to ~0.5μm across) with a high density of planar defects such as APBs.

The CuPt-type ordered phase was calculated to be unstable with respect to the disordered alloy by Bernard et al.(18). Nonetheless, in the present work, such ordering occurred in the MBE and MOCVD InAsSb layers grown over a wide range of temperatures and compositions. The stability of the ordering in the bulk of the layers was studied by post-growth annealing and doping experiments. In the present work, Si-doping reduced the degree of ordering, which is consistent with the observations of several authors, who investigated effects of Mg, Zn and Se-doping on the CuPt-type ordering observed in the $In_xGa_{1-x}P$ layers (23-26). In the Zn-doped layers grown at temperature between 650°C and 700°C, no ordering occurs when the effective carrier concentration is $0.8x10^{18}$ to 10^{19} cm^{-3} (23-25). For the Se-doped layers grown at 670°C, the ordering decreases when the carrier concentration increases from $7x10^{18}$ to $1x10^{19}cm^{-3}$ (26). For the Mn-doped layers grown at 680°C, no ordering occurs when the carrier concentration is $1x10^{18}cm^{-3}$ (23). It was reported that the absence of the ordering in Zn, Mg, and Se-doped layers could be

associated with the randomization of the cation sublattice due to dopant atom diffusion during deposition (23). Unfortunately, there is no suitable information concerning the diffusion constant of Si in InAsSb layers. Nevertheless, it can be concluded either that the Si atoms in the present InAsSb layers randomise the ordered structure in a similar manner to Zn, Mg and Se atoms or that the Si atoms enhance bulk diffusion leading to disordering beneath the growing surface (27).

6-4 Atomic ordering in MOCVD InP_ySb_{1-y} layers

6-4-1 Experimental

Theoretical calculations have shown the existence of a very large positive enthalpy of mixing due to the large difference in lattice constant between InP and InSb binary components in InP_ySb_{1-y} semiconducting alloys (29,30). However, the InP_ySb_{1-y} layers studied in this section have been successfully grown by the MOCVD technique (31) in an atmospheric pressure, horizontal, infrared heated reactor (32). Details of growth conditions used are listed in Table 5.2. (001) plan-view and {110} cross-section specimens were prepared to investigate the CuPt-type ordering in the layers.

6-4-2 TED analyses

[110] and $[\bar{1}10]$ TED patterns were obtained from InPSb layers grown at temperatures ranging from 460°C to 500°C. The results showed CuPt-type ordering on two sets of the four possible {111} planes in all the layers. <112> pole TED patterns obtained from the InP_ySb_{1-y} (y=0.53 to 0.59) layers grown at 450°C and 470°C using a growth rate of ~0.55nm/s exhibited evidence for a similar intensity of the superlattice spots, indicating a similar degree of ordering. However, there was a lower degree of ordering in the InP_ySb_{1-y} (y=0.74) layer grown at 500°C using ~0.83nm/s. This reduction is attributed to a smaller volume fraction of ordered material and/or a smaller degree of ordering. Unlike

other systems such as InGaAs and InAsSb, diffuse streaks associated with the fundamental zinc-blende spots along the [110] direction were observed in the [$\bar{1}$10] diffraction patterns of all the InPSb layers, which could be due to segregated atoms associated with periodic arrays of missing dimers related to surface reconstruction during layer growth, as discussed in chapter 5 for InPSb and GaPSb layers.

6-5 Discussion: a formation mechanism for atomic ordering in III-V compound semiconductors

TEM and TED examinations have shown that CuPt-type ordering occurs in both mixed Group III and V ternary semiconductor layers grown under a wide range of temperatures, growth rates and compositions. Orthogonal <110> cross-section and (001) plan-view TED, TEM and HREM techniques have been successfully employed to investigate the ordering behaviours in detail. Only two of the four possible {111} ordered variants were observed, the development of which is likely to be related to the (001) surface structure. If the ordering were formed by a bulk diffusion process, all of the four possible variants would be expected to be present, since the (111), ($\bar{1}$11), (1$\bar{1}$1) and (11$\bar{1}$) variants are equivalent in a bulk layer. Post-growth annealing and doping experiments also indicate that the ordering observed is not stable in the bulk layer.

Bernard et al.(18) have calculated bulk formation enthalpies of ordered and disordered phases using first-principles total-energy methods and showed that the ordered intermediate structure is unstable in the bulk equilibrium since for large $\Delta a/a$, the positive volume deformation energies exceed the negative structural relaxation energies, whereas, for small $\Delta a/a$, the positive excess electro-static energies lead to instability. Therefore, the CuPt-type ordering observed in the mixed Group III and mixed Group V semiconductor layers is most likely induced at the growing surface during epitaxial layer deposition. Development of the ordering may proceed by a two-dimensional nucleation and layer-by-layer growth process (2) during non-equilibrium growth. The three dimensional macro-

ordered regions, i.e. domains, occurring in the layers could be formed as a consequence of the "freezing-in" of successive surface-induced ordered monolayers.

In order to explain the occurrence of the CuPt-type ordering, several mechanisms involving surface characteristic properties have been proposed. Norman (2) and Suzuki et al.(3) have suggested a mechanism based on the bond-length model to explain the ordering observed in MOCVD $Al_xIn_{1-x}As$ and $In_xGa_{1-x}P$ layers. Their arguments involve the participation of two kinds of mechanisms, e.g. ordering within each (001) plane and ordering for successive (001) ordered planes. The first mechanism was attributed to, in the case of InGaP, the anisotropic site occupation affinity for the Group III atoms, Ga and In, due to both a bond length difference between Ga-P and In-P, and a dangling bond direction asymmetry on the P-stabilized (001) surface (2,3). The second mechanism was ascribed to the presence of {111}B microfacets (3), where {111}B variants indicate $(\bar{1}11)$ and $(1\bar{1}1)$ planes. The bond-length model seems to describe well the ordering in the mixed Group III AlInAs and InGaP layers. There are two drawbacks in this model. First, the presence of {111}B microfacets is questionable. Secondly, the driving force for the lateral shift of the ordered (001) plane on the growing surface with respect to the underlying monolayers is not clear. This model also can not explain the existence of the $(\bar{1}11)$ and $(1\bar{1}1)$ ordering in the mixed Group V InAsSb and GaAsSb (4) layers. If we apply this bond-length model to InAsSb, the In-Sb and In-As bonds are of unequal length (the former being longer). In this case the As and Sb atoms would alternate along the [110] direction and the rows of As and Sb atoms would occur along the $[\bar{1}10]$ direction. Consequently, ordering would be expected to occur on the (111) and $(11\bar{1})$ planes, but not on the $(\bar{1}11)$ and $(1\bar{1}1)$ planes, contrary to experimental evidence obtained from the present work. This suggests that the occurrence of the ordering is associated not only with strain-reduction due to the accommodation of the differences of both the bond-length and dangling-bond angles, but also with the surface properties, e.g. surface reconstruction.

Recently, Suzuki and Gomyo (33) re-examined the previously proposed bond-length model in order to rationalize the presence of {111}B microfacets and suggested a new step-terrace-reconstruction formation mechanism. This is based on a reconstruction of the steps

and terraces at the Group V atom stabilized vicinal (001) surface, on which parity of the number of the [110] Group III atom rows for each terrace is even. This new model can explain their experimental results, but can not explain the formation of the {111}B ordering in the mixed Group V semiconductor layers.

Bellon et al.(8) have proposed a simple model to explain the formation of the 'so-called' substrate-driven {111} ordering observed in $Ga_xIn_{1-x}P$ layers. They assumed that the following rules apply during the layer growth:

i) growth is controlled by the deposition of the Group III species to the surface, their migration and incorporation to steps;

ii) once a Group III terrace has grown, it is immediately covered by Group V atoms;

iii) the lowest internal energy configurations for a Group V centred tetrahedron at the surface correspond to a tetrahedron with either a base of three Ga atoms and a summit of one In atom or a base of three In atoms and a summit of one Ga atom.

Using these rules, they explained the absence of {111}A variants, i.e. $(11\bar{1})$ and $(\bar{1}\bar{1}\bar{1})$ planes, the anisotropic effect of the surface misorientation toward $[1\bar{1}0]$ and the absence of ordering in the layers grown on {111}B substrates, but this model can not explain the formation of the {111}B ordering in the mixed Group V layers.

Murgatroyd, Norman and Booker (4) have proposed a mechanism based on surface reconstruction to interpret the occurrence of the CuPt-type ordering observed in MBE $GaAs_ySb_{1-y}$ layers. Their TED and TEM examinations revealed only the $(\bar{1}11)$ and $(1\bar{1}1)$ of the four possible variants, and a structure modulation along the [110] direction with a periodicity of $4d_{110}$. Reflection high energy electron diffraction (RHEED) results revealed evidence for a (2x4) surface reconstruction present during layer growth with a repeat distance of $4d_{110}$ along the [110] direction. It was postulated that the As-Sb atoms in all of the surface dimers are oriented in the same sense, giving a reconstruction in which each cell contains a row of three As atoms in the [110] direction and an adjacent similar row of three Sb atoms (Fig. 6.23). When subsequent monolayers are deposited, similar 2x3 cells are formed. The two rows of three As atoms and three Sb atoms in the [110] direction in a cell

Figure 6.23

'Missing-dimer' atomic model (ref.4) for the (2x4) reconstructed (001) surface of $GaAs_{0.5}Sb_{0.5}$ with As-Sb dimers in the $[\bar{1}10]$ direction and [110] rows of As atoms and of Sb atoms within the surface cells. (a) in-phase cells. (b) out-of-phase cells.

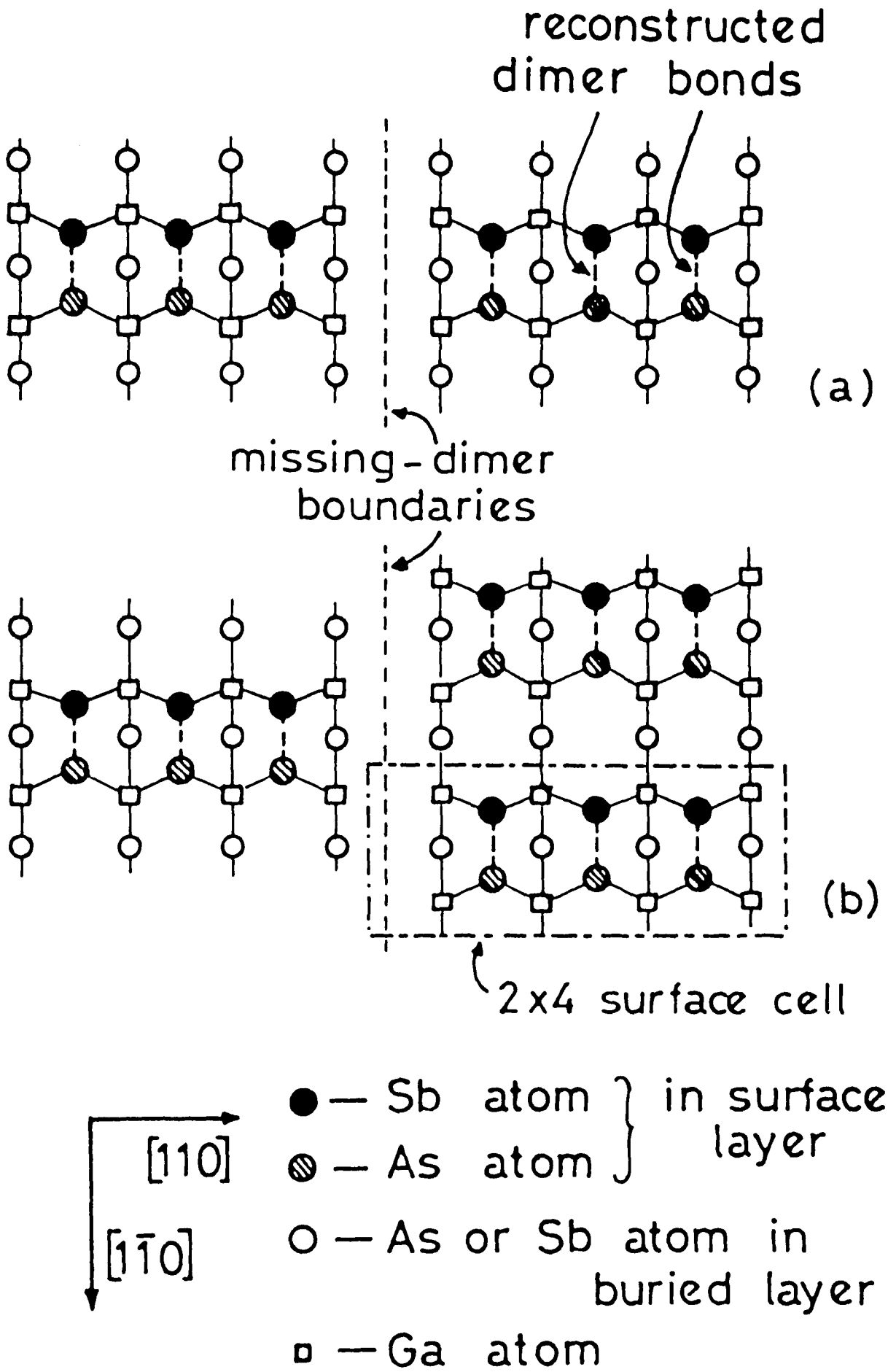
reconstructed
dimer bonds
(a)
missing-dimer
boundaries
(b)
2x4 surface cell
[110]
[1$\bar{1}$0]
● — Sb atom
⊘ — As atom
in surface layer
○ — As or Sb atom in buried layer
▫ — Ga atom

Fig. 6.23

in the surface are overgrown by a similar two rows of three As and three Sb atoms in the next monolayer, resulting in a small area of atomic ordering on the Group V sublattice on a {111} plane. It was suggested that $(\bar{1}11)$ and $(1\bar{1}1)$ variants of the ordering would be determined by the preferential occupation of the surface sites by As or Sb atoms. This model can explain the {111}B ordering in the mixed Group V ternary layers, but the driving force for the preferential occupation is not clear.

Recently, LeGoues et al.(34) have proposed a growth mechanism based on the influence of atomic scale stress present at the reconstructed (001) Si surface during growth to explain the occurrence of the CuPt-type ordering observed in SiGe alloy layers. In their experimental work, the four possible and equivalent variants in SiGe were observed, corresponding to ordering on (111), $(\bar{1}11)$, $(1\bar{1}1)$ and $(11\bar{1})$ planes. Evidence was also obtained by LEED examinations for the change from a 2x1 to 1x1 reconstruction. In order to test the effects of the surface structure on the occurrence of the {111} ordering, they grew SiGe layers on a Si (001) substrate. The first 500nm of the layer was grown directly on the substrate, so that a (2x1) reconstruction was achieved. TED patterns showed ordering in this first grown layer. Then the growth was continued on the surface after it had been saturated with Sb, and this resulted in a (1x1) reconstruction. TED examination of this latter grown layer showed no ordering. This observation establishes that the ordering is entirely due to surface factors. It was suggested that the formation of a dimer structure results in compressive or tensile stresses underneath the surface, which gives rise to lateral site-segregation (Fig. 6.24(a)). Atomic sites under compressive stress prefer Si (which has a smaller atomic radius), while sites under tensile stress prefer Ge (which has a larger radius). Fig. 6.24(b) shows a double layer which has grown on top of the initial surface. There is an alternating double layer of Si and Ge atoms, so that the four variants of the ordering can be achieved with SiSi-GeGe-SiSi-type structures along the <111> directions.

Theoretical calculations performed by Bernard at al.(35) showed that the CuPt-type ordering is more stable than chalcopyrite ordering due to a stabilising surface reconstruction (dimerization). Froyen and Zunger (36) also showed by first-principles total-energy calculations that the equilibrium thermodynamics of a reconstructed cation-terminated

Figure 6.24

(a) [110] atomic projection (ref.34) of the (001) 2x1 surface of SiGe. Large solid circles indicate sites under compressive stress, favouring Si occupancy. Large open circles indicate sites under tensile stress, favouring Ge. Small circles indicate sites with little preference for Si or Ge. (b) Proposed growth process (ref.34): the third and deeper layers in (a) are assumed immobile, when two monolayers are added.

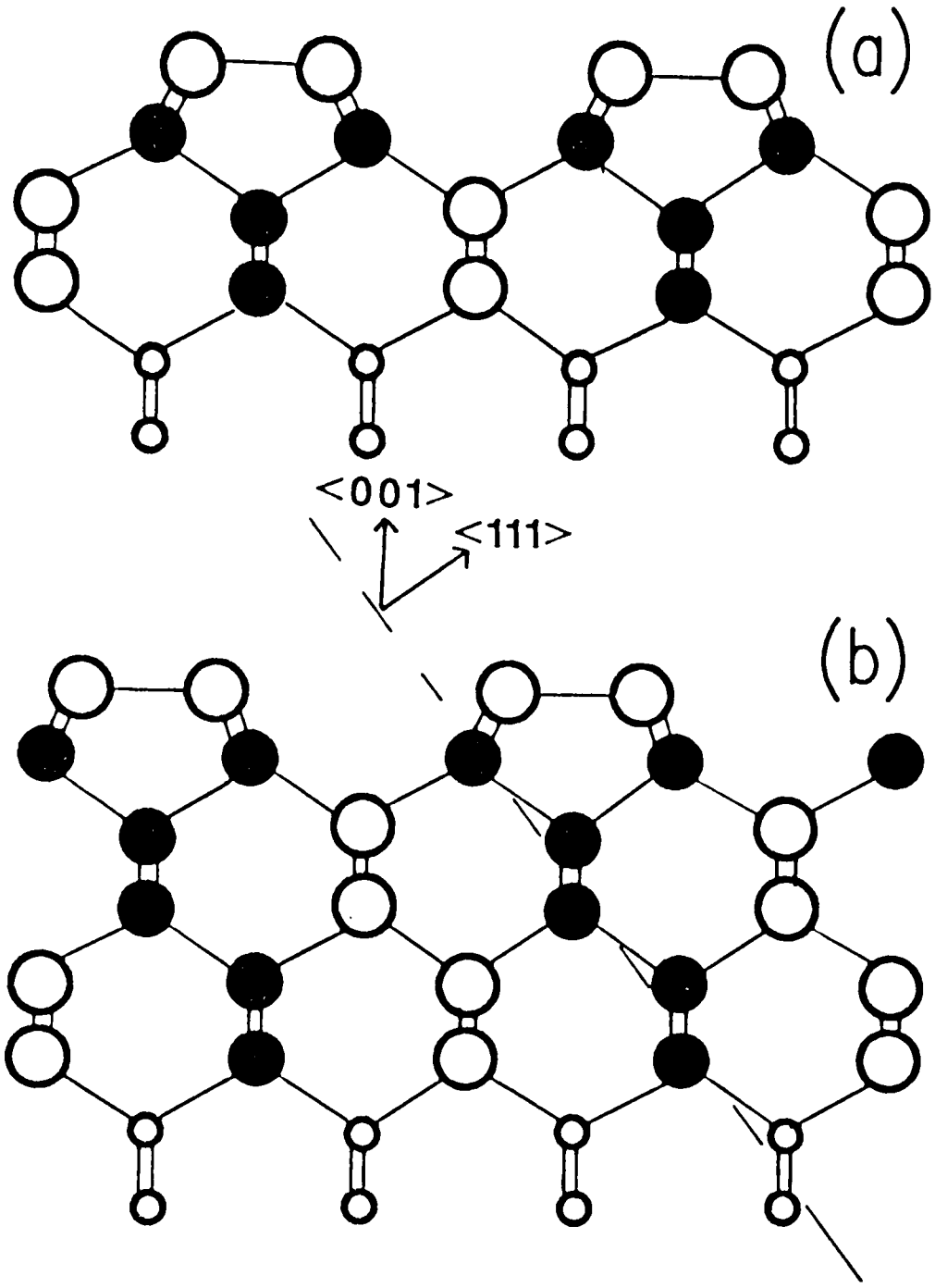

Fig. 6.24

surface can drive the CuPt-type ordered structure in $GaInP_2$. They concluded that this surface-induced ordering can develop into macroscopic domains if the atomic movement is limited to the top surface layer only or to within the top four layers.

We consider that surface reconstruction plays an important role in the generation of the two sets of the CuPt-type ordering observed in both the mixed Group III InGaAs layers and the mixed Group V InAsSb layers investigated in this study. Unfortunately, no direct results concerning the surface reconstruction of MOCVD InGaAs in the present work are available, since in-situ surface analysis such as RHEED was not possible during the MOCVD layer growth.

In the present work, the surface reconstruction of the InAsSb layers was, however, examined using RHEED during MBE growth. RHEED patterns of $InAs_ySb_{1-y}$ (y=0.5) grown at temperatures ranging from 340°C to 430°C were recorded during growth, and revealed the presence of a (2x3) reconstructed surface. This indicates a periodicity of $3d_{110}$ (~13.3Å) in the [110] direction of the crystal, which is consistent with the periodicity of a modulation deduced from the $[\bar{1}10]$ TED patterns of the layers, i.e. $\pm n/6[220]$ streaks (Fig. 6.18).

Surface strain influences the structure of a layer surface. Appelbaum and Hamann (37) calculated subsurface strains in the Si (001) dimer-reconstructed surface using Keating's model (38) and reported that the stress induced by surface layer reconstruction can produce sizable elastic distortion of deeper layers, i.e. in order to form a dimer, two atoms initially separated by 3.84Å move together to form a bond having a 2.3-2.4Å bond length. The backbonds of the two surface atoms are therefore heavily bent and large strains are observed extending down to the fifth layer of the specimen.

Kelires and Tersoff (39) investigated surface and bulk equilibrium in SiGe alloys by a direct simulation. They found striking results for the (2x1) dimer reconstruction of the (100) surface of a SiGe alloy, i.e. alternating atoms in both the third and fourth layers of the specimen are under compressive or tensile stresses. These atomic scale stresses can result in specific atomic arrangements, so that atomic sites under a compressive stress would rather be

occupied by smaller atoms, whilst sites under tensile stress prefer larger radius atoms (Fig. 6.24(a)).

As described before, MBE $InAs_{0.5}Sb_{0.5}$ in our work exhibits the (2x3) reconstruction. In Fig. 6.25 is illustrated a [110] cross-section of a 2x reconstructed (001) $InAs_{0.5}Sb_{0.5}$ surface. When monolayers are deposited, surface dimers are formed. As shown in Fig. 6.25, dimers on the surface consist of either As-As, As-Sb or Sb-Sb bonds, leading to pronounced bending of the backbonds of the subsurface layer, and so (001) InAsSb dimer-reconstructed surface gives rise to modulating compressive and tensile stresses below the top two atom layers at the surface (34). Appelbaum and Hamann reported that this strain occurred down to even the fifth layer for Si. These microscale stresses give rise to preferential occupation by one of the two Group V atomic species, depending on their senses. Sites under compressive stress prefer to be occupied by the smaller pairs of atoms such as In-As, whereas sites under tensile stress favour the larger pairs of atoms such as In-Sb. As shown in Fig. 6.25, a double layer of the subsurface would tend to consist of alternating pairs of In-As and In-Sb atoms along the $[1\,\bar{1}\,0]$ direction in the crystal. A similar argument can also be applied to mixed Group III InGaAs layers, which exhibit the same {111}B ordering.

Dobson et al. (40), using the RHEED technique, have analysed a clean MBE GaAs (001) surface grown at 520°C and reported a (2x4) reconstruction (with the RHEED beam parallel to the [110] direction, a 2x reconstruction was observed). This indicates that the surface has a structural periodicity of $2d_{1\,\bar{1}\,0}$ in the $[1\,\bar{1}\,0]$ direction of the crystal. Similarly, the 4x reconstruction was observed with the electron beam parallel to $[\bar{1}\,10]$ direction, which indicates a repeat distance of $4d_{110}$ in the [110] direction on the surface. The theoretical work of Chadi (41) and the experimental scanning tunnelling microscopy (STM) results of Pashley et al.(42) both confirmed that the As-rich (001) GaAs surface may be (2x4) reconstructed, with the structure illustrated in Fig. 6.26.

Although there is no available information concerning the MOCVD layer surface reconstruction, we may assume that the (2x4) or the (2x1) surface reconstructions also occur in the MOCVD InGaAs layers. However, $(\bar{1}\,10)$ cross-section TED results of the InGaAs

Figure 6.25

[110] atomic projection of the (2x) reconstructed (001) InAsSb surface, showing proposed growth process of ordered structure.

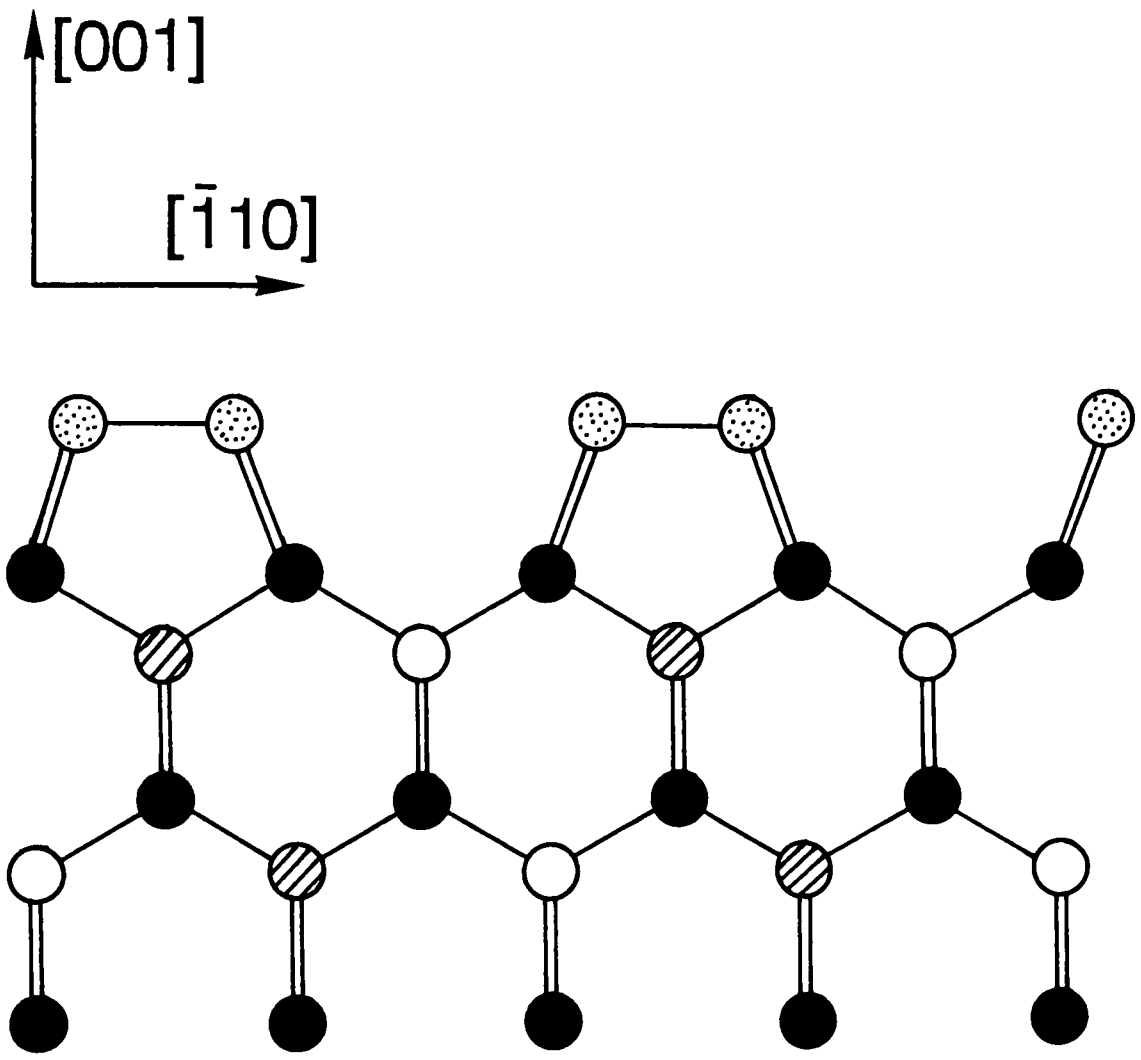

As or Sb atoms

In atoms

As atoms

Sb atoms

Fig. 6.25

Figure 6.26

'Missing-dimer' atomic model (ref.41,42) for the (2x4) reconstructed, Group V stabilized, (001) GaAs surface. (a) in-phase cells. (b) out-of-phase cells.

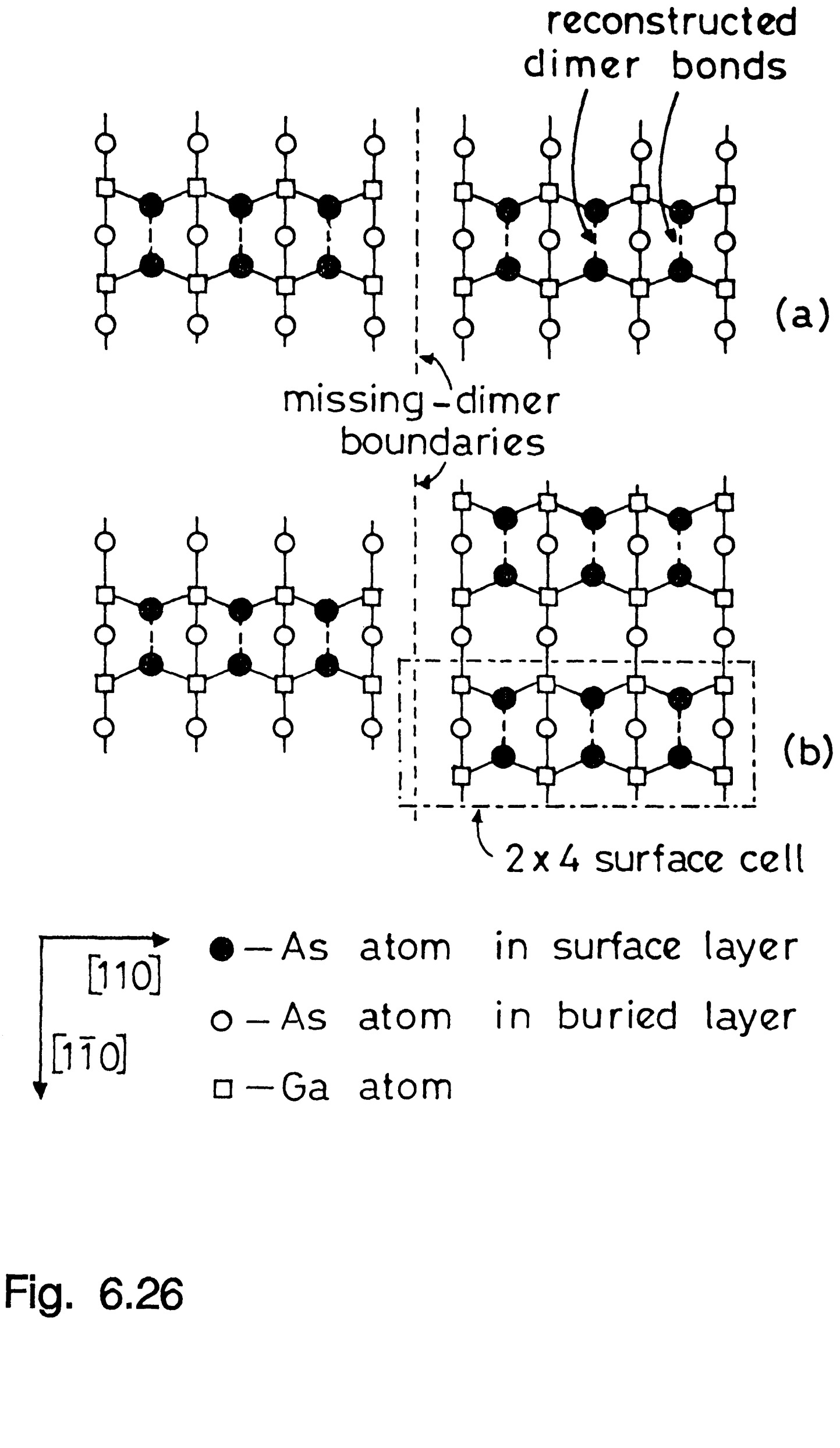
reconstructed
dimer bonds
(a)
missing-dimer
boundaries
(b)
2x4 surface cell
[110]
[1$\bar{1}$0]
● — As atom in surface layer
○ — As atom in buried layer
□ — Ga atom

Fig. 6.26

layers demonstrated the absence of a modulation in the [110] direction, suggesting that the (2x1) surface reconstruction may occur. Therefore, we now consider the (2x1) surface reconstruction in the InGaAs layer. As was the case in the mixed Group V layer, the (2x1) surface reconstruction gives rise to subsurface stresses, in turn leading to site-specific atomic segregation in the alloy. Thus, atomic sites under compressive stress prefer to be occupied by pairs of smaller atoms such as Ga-As, whilst sites under tensile stress favour pairs of the larger atoms such as In-As. As shown in Fig. 6.27, a double layer in the subsurface consists of alternating pairs of In-As and Ga-As running along the [$\bar{1}$10] direction.

The proceeding arguments of course assume that the bulk diffusion coefficients at the growth temperatures are sufficiently low that the surface strain induced {111}B ordering due to surface reconstruction can propagate into the macroscopic layer thickness without disordering by a bulk diffusion process.

In the present work it is now proposed that the CuPt-type ordered structure observed in the mixed group III and V ternary semiconductor InGaAs and InAsSb layers is due to a mechanism based on micro-scale stresses underneath the growing surface, present as a result of surface reconstruction (34,37,39). As discussed in section 6-2-4, randomization of the ordered phase could occur through a bulk diffusion process when the thermodynamic equilibrium degree of the surface-induced ordering decreases. As the CuPt-type ordered structure is known to be thermodynamically unstable in the bulk layer, the macro-ordered regions observed in the bulk layer are produced as a consequence of surface ordering overgrowth and "freezing-in" processes. Under conditions of the availability of a sufficiently high amount of thermal energy for bulk diffusion to overcome the free energy reduction due to the ordering, the bulk-diffusion-induced disordering occurs to lower the total free energy state in the bulk layer (18).

6-7 Role of surface steps in atomic ordering

It is known that growth on misoriented substrates gives rise to anisotropic occurrence of the two {111} ordered variants (7,8,43,44). This anisotropic intensity of the two sets of

Figure 6.27

[110] atomic projection of the (2x) reconstructed (001) InGaAs surface, showing proposed growth process of ordered structure.

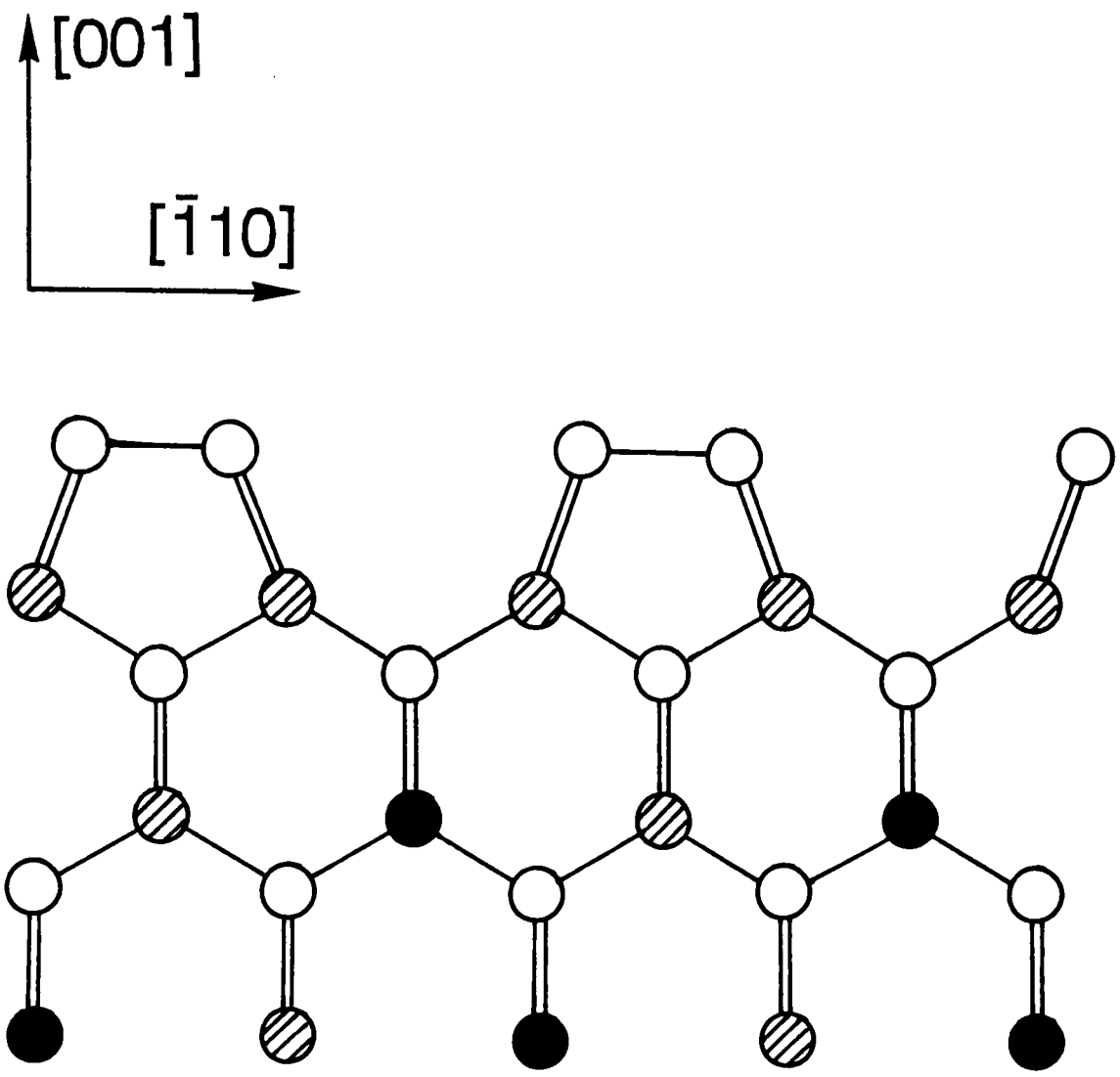

● In atoms

▨ Ga atoms

○ As atoms

Fig. 6.27

superlattice spots indicates that one of the two ordered variants is more developed than the other. Augarde et al.(7) investigated effects of substrate orientation on the evolution of certain CuPt-type ordered variants in $In_xGa_{1-x}P$ layers. They showed that when the layer is grown on (001) GaAs 6° off towards the $[1\,\bar{1}\,0]$ direction, the formation of only the $(1\,\bar{1}\,1)$ ordered variant occurs. However, when the layer was grown on (001) GaAs 6° off towards the [110] direction, the formation of the $(1\,\bar{1}\,1)$ and $(\bar{1}\,11)$ ordered variants occurred. In order to explain the occurrence of one variant in their layer, they proposed that the lowest internal energy configurations for a Group V centred tetrahedron at the surface correspond to a tetrahedron with either a base of three Ga atoms and a summit of one In atom or a base of three In atoms and a summit of one Ga atom. As shown in Fig. 6.28, if the base of the tetrahedron at the step consists of atoms of the same type A, i.e. either Ga or In, the Group III adatom that will bind to the site is determined and will be of type B, i.e. either In or Ga, respectively. Therefore, if rows R1 and R2 are rows of A atoms, row R3 will be of B atoms according to this assumption. Thus, when surface ordering occurs, only one variant can exist.

In order to understand the role of surface steps in ordering, we consider the growth of InGaAs layers on vicinal (001) GaAs substrates. Fig. 6.29(a) shows the (110) projection of GaAs misoriented from [001] towards the $[\bar{1}\,10]$ direction by a few degrees. The resulting surface ABCD has steps of height a/2. If a 2x surface reconstruction occurred, As atoms on the surface (along rows AB and CD) would move to form dimers as indicated by the arrows, since leaving a dangling bond at a surface step is energetically unstable. The occurrence of dimerization would result in compression and tension regions underneath the surface AB and CD. In the presence of In, Ga and As atoms, atomic rearrangements occur and the situation after the growth of a monolayer of $InGaAs_2$ is shown in Fig. 6.29(b). As discussed above, atomic sites under compression prefer to be occupied by Ga atoms, whilst atomic sites under tension favour to be occupied by In atoms. The new surface is EFBG, and the step is laterally displaced towards the left by $a/2\sqrt{2}$. When another monolayer of $InGaAs_2$ is grown, atomic rearrangements again occur as shown in Fig. 6.29(c). Since the step is displaced by $a/2\sqrt{2}$ with respect to the underlying layer, compression and tension regions are

Figure 6.28

Schematic (ref.7) of diatomic steps for an (001) Group III-V substrate with mean surface tilted towards the $[1\,\bar{1}\,0]$ direction. R3 corresponds to Group III atoms which are going to be incorporated during subsequent layer growth at the steps. Large circles indicate Group III atoms and small circles indicate Group V atoms.

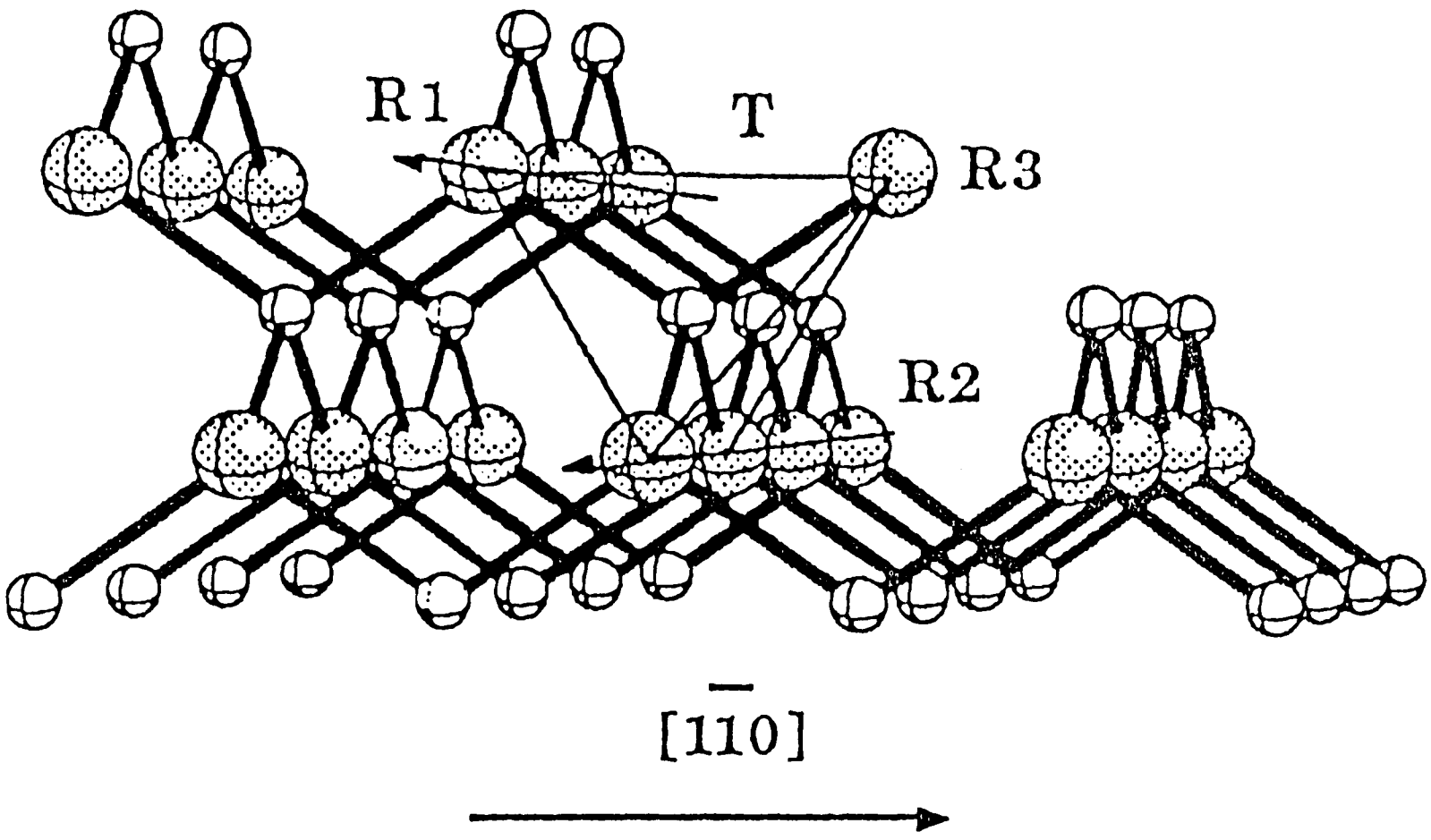

Fig. 6.28

Figure 6.29

Schematic diagrams of (a) a vicinal (001) GaAs surface; a (2x4) reconstruction occurs at B and As atoms move to form dimers during reconstruction; (b) after growth of one monolayer of $InGaAs_2$, reconstruction-induced rearrangement of atoms occurs; (c) after the growth of two monolayers of $InGaAs_2$, evolution of CuPt-type ordering on the $(\bar{1}\,11)$ planes occurs.

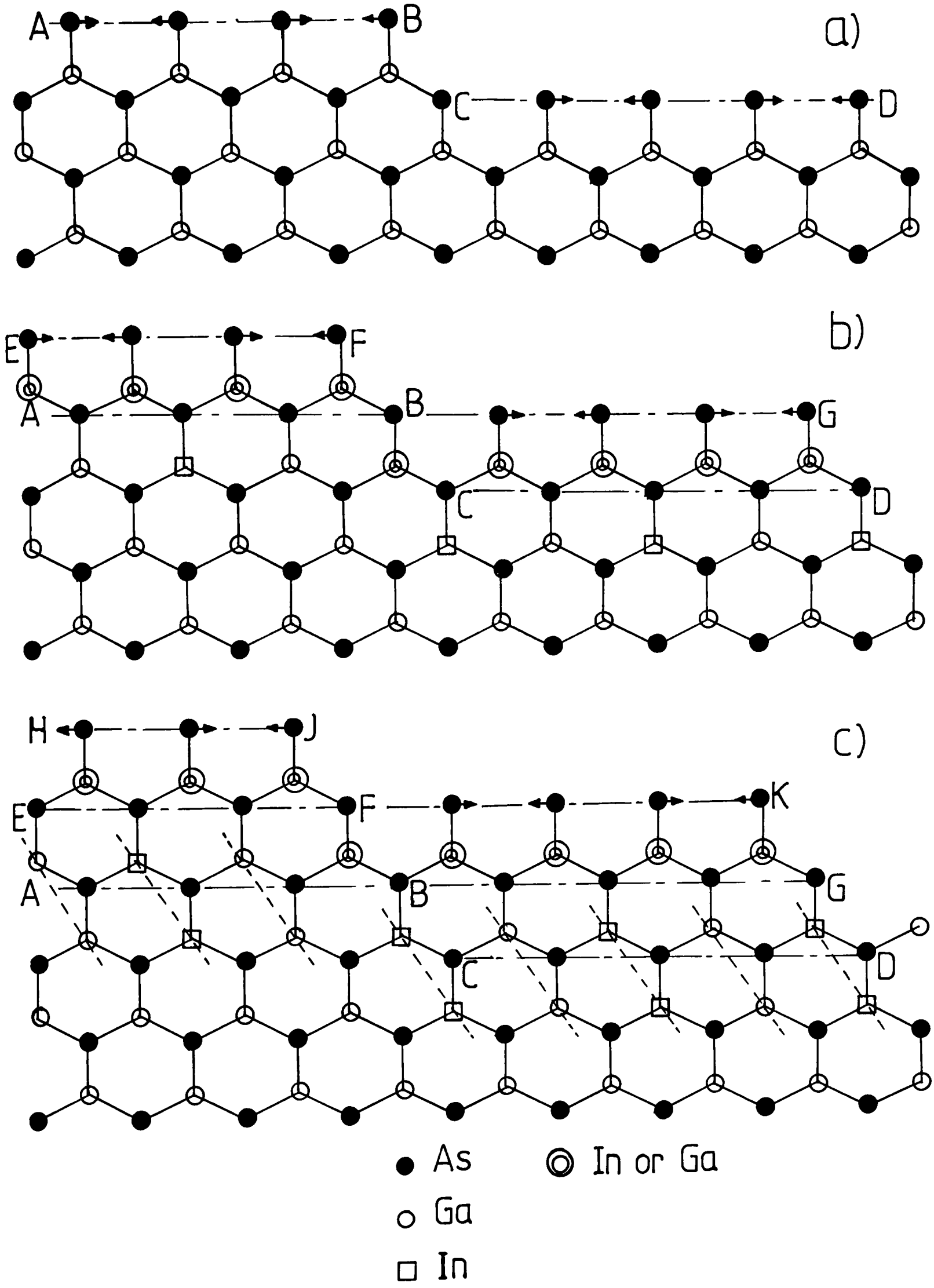

Fig. 6.29

also displaced by the same distance along the [1 $\bar{1}$ 0] direction. This displacement of the step (i.e. compression and tension regions) gives rise to segregation of same Group III atoms on the ($\bar{1}$ 11) planes. The new position of the surface is HJFK and CuPt-type ordering is visible on the ($\bar{1}$ 11) planes, indicated by the dotted lines in Fig. 6.29(c). Furthermore, if the (001) substrate is tilted towards the [1 $\bar{1}$ 0] direction by a few degrees, then ordering will occur on the (1 $\bar{1}$ 1) planes in a similar manner.

This suggested model shows how one variant can predominantly evolve over the other, indicating that surface steps can determine the formation of a certain ordered variant. For the InGaAs layers examined in this work, plan-view TEM DF micrographs (Fig. 6.9, 6.10 and 6.11) showed a characteristic morphology of the two ordered variants present, which nucleated separately and oriented in opposite senses. This complicated morphology of the ordered regions could be associated with the surface roughness of the substrates. An uneven surface results in areas which are inclined towards both the [$\bar{1}$ 10] and [1 $\bar{1}$ 0] directions. Areas tilted towards the [$\bar{1}$ 10] direction would give rise to the ($\bar{1}$ 11) variant, whilst areas tilted towards the [1 $\bar{1}$ 0] direction would result in the (1 $\bar{1}$ 1) variant. This suggests that the surface roughness of the substrate could be directly revealed by the morphologies of the ordered regions. Therefore, it can be concluded that the complicated morphology of ordered regions observed in the InGaAs (Fig. 6.9, 6.10 and 6.11) could be related to the surface roughness of the substrates used for growth.

The regions of the two variants have boundaries lying along <311> and <331> directions. These characteristic directions may be related to anisotropic properties of substrate surfaces induced by etching or polishing. It may be possible that etching (or polishing) results in different surface step structures, depending on materials. It is noteworthy that the morphology of the ordered regions of the InGaAs layers grown on InP substrates were similar to each other but different from the InGaAs layer grown on a GaAs substrate (e.g. see (Fig. 6.9, 6.10 and 6.11)).

The morphology of the ordered regions was dependent on growth conditions. First, the layer grown at 550°C with a slow growth rate showed a large amount of unordered material between the two variant ordered regions. Secondly, the layer grown at 550°C with

a fast growth rate showed a small amount of unordered material. Thirdly, the layer grown at 500°C with a slow growth rate did not show unordered material. This may be due to surface structure and kinetics in bulk diffusion-induced disordering. For the first layer, mixed Group III atoms on the growing surface and in the transition region beneath have enough time for ordering, and they have also enough time for disordering in the transition region. For the second layer, mixed Group III atoms on the growing surface and in the transition region still have sufficient time for ordering since the temperature is high, but they have insufficient time for disordering in the transition region because the ordered monolayers were shortly frozen in by the deposition of the next monolayers. For the third layer, mixed Group III atoms on the growing surface and in the transition region have sufficient time for ordering since the growth rate is low, but they have insufficient time for disordering in the transition region because the temperature and hence diffusion is low. This aspect is consistent with the TEM results described above. The bulk diffusion-induced disordering process may be controlled by kinetic limits.

In Fig. 6.30 is shown a schematic drawing of the two variant ordered regions (a) and a surface structure having 'hillocks' (b). The surface of the substrate could contain a number of such 'hillocks' inclined towards both the $[\bar{1}10]$ and $[1\bar{1}0]$ directions, as indicated by A and B, respectively. $[\bar{1}10]$ tilted areas (A regions) would give the $(\bar{1}11)$ variant, whilst $[1\bar{1}0]$ tilted areas (B regions) would give the $(1\bar{1}1)$ variant. The C regions parallel to the exact (001) plane would possibly result in both variants. With a slow growth rate, A, B and C regions start to order. Unlike the A and B regions, the C regions would randomly produce two variants, giving rise to small ordered regions. With further growth, the pre-existing ordered material tends to be disordered to lower the total bulk free energy state. This disordering process may first start to occur at the regions containing the two variants, since these regions are energetically more unstable. This disordering process could depend on the thermal energy state, i.e. as described above, and it could be kinetically controlled. Therefore, more unordered material is expected in the first layer than the other two layers (described above). This could explain the reason why there is no unordered material in the third layer. Therefore, it could be concluded that the dark regions may be

Figure 6.30

(a) Schematic of a (001) plan-view diagram of Group III-V layer showing the two variant ordered regions and unordered material in between. A indicates region ordered on $(1\,\bar{1}\,1)$ planes; B indicates region ordered on $(\bar{1}\,11)$ planes; C indicates unordered region. (b) Surface morphology of (001) substrate, including four 'hillocks'. Each 'hillock' consists of areas inclined towards $[1\,\bar{1}\,0]$ direction (A regions) and $[\bar{1}\,10]$ direction (B regions). C region is smooth surface parallel to the exact (001) plane. (c) Cross-section of the surface in (b) including two 'hillocks'.

a)

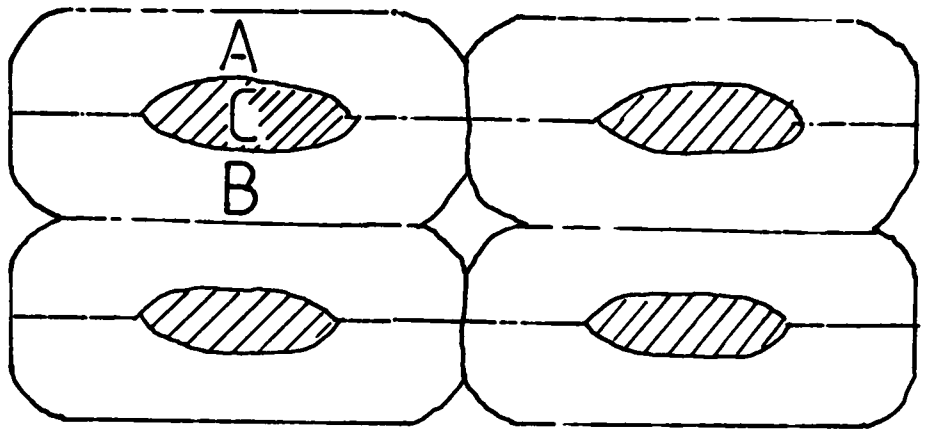

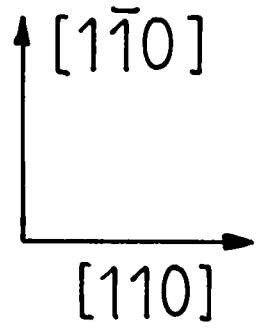

b)

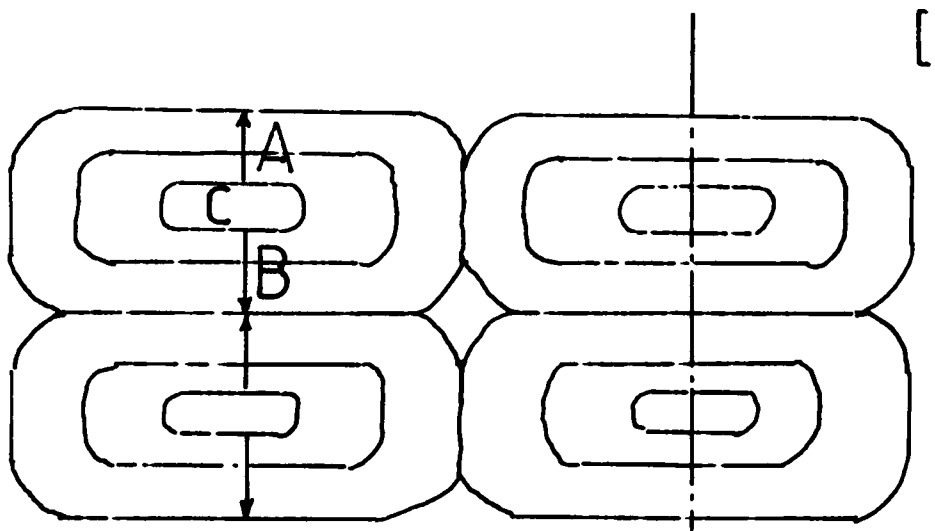

c)

Fig. 6.30

either fully disordered or contain small less ordered regions which may not be detected by TEM.

REFERENCES-CHAPTER 6

1. T.S. Kuan, W.I. Wang and E.L. Wilkie, Appl. Phys. Lett. **51** (1987) 51.
2. A.G. Norman, D.Phil. Thesis, Oxford University, 1987.
3. T. Suzuki, A. Gomyo and S. Iijima, J. Cryst. Growth **93** (1988) 396.
4. I.J. Murgatroyd, A.G. Norman and G.R. Booker, J. Appl. Phys. **68** (1990) 1123.
5. S.J. Bass and M.L. Young, J. Cryst. Growth **68** (1984) 129.
6. J. Taftϕ and J.H.L Spence, J. Appl. Cryst. **15** (1982) 60.
7. E. Augarde, M. Mpaskoutas, P. Bellon, J.P. Chevalier and G.P. Martin, Inst. Phys. Conf. Ser. **100** (1989) 155.
8. P. Bellon, J.P. Chevalier, E. Augarde, J.P. André and J.P. Martin, J. Appl. Phys. **66** (1989) 2388.
9. M.A. Shahid, S Mahajan, D.E. Laughlin and H.M. Cox, Phys. Rev. Lett. **58** (1987) 2567.
10. A. Gomyo, T. Suzuki and S. Iijima, Phys. Rev. Lett. **60** (1988) 2645.
11. M. Hockly, D. Phil. Thesis, Oxford University, 1983.
12. I. T. Murgatroyd, D.Phil. Thesis, Oxford University, 1987.
13. S.G. Lipson and H. Lipson, Optical Physics, Cambridge University Press, London (1967).
14. A.G. Norman, R.E. Mallard, I.J. Murgatroyd, G.R. Booker, A.H. Moore and M.D. Scott, Inst. Phys. Conf. Ser. **87** (1987) 77.
15. P. Goodman and A.F. Moodie, Acta Cryst. **A30** (1974) 280.
16. G.P. Srivastava, J.L. Martins and A Zunger, Phys. Rev. **B31** (1985) 2561.
17. A. Zunger and D.M. Wood, J. Cryst. Growth **98** (1989) 1.
18. J.E. Bernard, L.G. Ferreira, S.-H. Wei and A. Zunger, Phys. Rev. **B38** (1988) 6338.
19. S. Kurtz, J. Olson and A Kibbler, Appl. Phys. Lett. **57** (1990) 1922.
20. Y. Kim, A. Ourmazd, R. Malik and J. Rentschler, MRS Symp. Proc. **159** (1990) 351.
21. S. Kurtz and J. Olson, Proc. of the 19th IEEE Photovoltaic Specialists Conf. (IEEE, New York, 1987) p823.
22. H.R. Jen, K.Y. Ma and G.B. Stringfellow, Appl. Phys. Lett. **54** (1989) 1954.

23. T. Suzuki, A. Gomyo, I. Hino, K. Kobayashi, S. Kanata and S. Iijima, Jpn. J. Appl. Phys. **27** (1988) L1549.

24. E. Morita, M. Ikeda, O. Kumagai and K. Kaneko, Appl. Phys. Lett. **53** (1988) 2164.

25. A. Gomyo, T. Suzuki, K. Kobayashi, S. Kanata and I Hino, Appl. Phys. Lett. **50** (1987) 673.

26. J. Goral, S. Kurtz, J. Olson and A. Kibbler, J. Electr. Mater. **19** (1990) 95.

27. W.D. Laidig, N. Holonyak, M.D. Camras, K. Hess, J.J. Coleman, P.D. Dapkus and J. Bardeen, Appl. Phys. Lett. **38** 776 (1981).

28. I.T. Ferguson, A.G. Norman and R.A. Stradling, unpublished work.

29. G.B. Stringfellow, J. Cryst. Growth **27** (1974) 21.

30. M.J. Jou, Y.T. Cherng, H.R. Jen and G.B. Stringfellow, J. Cryst. Growth **93** (1988) 62.

31. M.J. Jou, Y.T. Cherng and G.B. Stringfellow, Appl. Phys. Lett. **64** (1988) 1472.

32. C.P. Kuo, R.M. Cohen and G.B. Stringfellow, J. Cryst. Growth, **64** (1983) 461.

33. T. Suzuki and A. Gomyo, J. Cryst. Growth **111**(1991) 353.

34. F.K. LeGoues, V.P. Kesan, S.S. Iyer, J. Tersoff and R. Tromp, Phys. Rev. Lett. **64** (1990) 2038.

35. J.E. Bernard, R.G. Dandrea, L.G. Ferreira, S. Froyen, S-H. Wei and A. Zunger, Appl. Phys. Lett. **56** (1990) 731.

36. S. Froyen and A. Zunger, Phys. Rev. Lett. **66** (1991) 2132.

37. J.A. Appelbaum and D.R. Hamann, Surf. Sci. **74** (1978) 21.

38. P.N. Keating, Phys. Rev. **145** (1966) 637.

39. P.L. Kelires and J. Tersoff, Phys. Rev. Lett. **63** (1989) 1164.

40. P.J. Dobson, B.A. Joyce, J.H. Neave and J. Zhang, J. Cryst. Growth, **81** (1987) 1.

41. D.J. Chadi, J. Vac. Sci. Technol. **A5** (1987) 834.

42. M.D. Pashley, K.W. Haberen, W. Friday, J.M. Woodall and P.B. Kirchner, Phys. Rev. Lett. **60** (1988) 2176.

43. M. Kondow, H. Kakibayashi and S. Minagawa, J. Cryst. Growth, **88** (1988) 291.

44. S. McKernan, B.C. DeCooman, C.B. Carter, D.P. Bour and J.R. Shealy, J. Mater. Res. **3** (1988) 406.

CHAPTER 7

TEM AND HREM STUDIES OF STRAINED LAYERS OF MBE $InAs_ySb_{1-y}$ SEMICONDUCTORS

7-1 Introduction

The $InAs_ySb_{1-y}$ strained layer superlattice (SLS) is of great importance because of its strong potential application as a long wavelength detector in the 8-12μm range (1,2). Osbourn (1) has shown that tensile strains in an $InAs_{y1}Sb_{1-y1}/InAs_{y2}Sb_{1-y2}$ SLS decrease the band gap below that of bulk $InAs_ySb_{1-y}$, indicating that $InAs_ySb_{1-y}$ SLSs are a direct alternative to $Cd_xHg_{1-x}Te$ semiconducting materials, the growth and processing of which have proved to be quite difficult. Non-equilibrium growth techniques such as MBE and MOCVD have been successfully employed to grow InAsSb SLSs (3-7).

In order that $InAs_ySb_{1-y}$ has a strain induced decrease of the band gap, the $InAs_ySb_{1-y}$ well regions should be under tensile stress (1). When lattice-mismatched layers exceeding a certain critical thickness are grown, the layers will be elastically relaxed by the introduction of crystallographic defects such as misfit dislocations, stacking faults and microtwins (8-12), thereby altering the electronic structure of the materials.

In the present work (chapter 4), MBE $InAs_{y1}Sb_{1-y1}/InAs_{y2}Sb_{1-y2}$ SLSs have been naturally grown by phase separation due to a miscibility gap under certain growth conditions. In addition MBE $InAs_{y1}Sb_{1-y1}/InAs_{y2}Sb_{1-y2}$ SLSs have been intentionally grown at a higher temperature at which a miscibility gap does not exist.

In this chapter, TEM and HREM are employed to analyse the structural properties of these layers, both naturally and intentionally grown, and to investigate the misfit strain relaxation mechanisms. The naturally occurring SLSs (n-SLSs) were grown at temperatures of 340 and 370°C, and the intentionally produced SLSs (i-SLSs) at 430°C. The TEM results presented in chapter 4 indicated that all the n-SLSs, except the n-SLS grown at 340°C, showed mainly 'short' stacking faults and 'short' microtwins. However, the n-SLS grown at 340°C showed mainly 'long' microtwins, and this was also the case for the i-SLS. We mainly examined three n-SLSs (IC118, IC124 and IC 237) and one i-SLS (IC 257) to study these defects in more detail. The atomic structure of the distorted crystal lattice, as well as the defect configurations, were determined using HREM. A possible mechanism for the relaxation of strain in SLSs is proposed.

7-2 Brief review on strain relaxation

7-2-1 Misfit dislocations in strained layer structures

When a single epitaxial layer is deposited on a single crystal substrate with a different lattice parameter, lattice mismatch strain between the two materials will be accommodated by either elastic distortion, plastic distortion (e.g. by introducing misfit dislocations) or by a combination of the two processes.

Let us consider a misfitting epitaxial layer, with the zinc-blende type structure, grown on a (100) substrate. Two of the four {111} slip planes intersect the (100) plane along the [011] direction and the other two along the $[0\,\bar{1}\,1]$ direction. For zinc-blende materials having the {111}<011> slip system, dislocations may form an orthogonal cross-grid having line vectors of [011] and $[0\,\bar{1}\,1]$ in the interfacial plane. Misfit dislocations lying along [011] or $[0\,\bar{1}\,1]$ with inclined Burgers vectors are of the so-called 60° type, named after the angle between the dislocation line and Burgers vector. Their Burgers vectors are along the $[\,\bar{1}\,01]$, [101], [110] or $[1\,\bar{1}\,0]$ directions, which are inclined to the (100) plane at an angle of 45°. They have a misfit-relieving edge component in the interfacial plane. The most effective dislocation configuration for misfit relief would be a cross-grid of pure edge dislocations, known as Lomer dislocations, having line vectors of <110> and Burgers vectors of a/2<110> lying in the (001) interface plane. Lomer dislocations can be formed by the combination of two glissile 60° dislocations.

In the case of strained layers when the epitaxial layer thickness exceeds the critical thickness, the misfit dislocation density per unit length (13), **n**, is given by:

$$\mathbf{n} = (a_2 - a_1)/a_1 a_2 \cong \Delta a/a \cdot 1/a \qquad (7\text{-}1)$$

where $\mathbf{a}_1$ and $\mathbf{a}_2$ are the relaxed lattice spacings of crystal planes **1** and **2**, respectively.

i.e. $$n = f/a \qquad (7\text{-}2)$$

where $f = \Delta a/a$ is the misfit, $\Delta a = a_2 - a_1$, and $a = (a_1 + a_2)/2$. Equation (7-1) is applicable only if i) all the misfit strain is relieved by misfit dislocations, and ii) the dislocations are of the ideal type for relief of mismatch, i.e. pure edge dislocations with Burgers vectors lying in the interfacial plane.

In a real case, the total mismatch strain, f, is relieved both plastically and elastically, with $f = p + e$, where p and e indicate plastic and elastic misfit strains, respectively. In general, misfit dislocations can have various Burgers vectors, but only the edge component in the interfacial plane, $\mathbf{b}_{eff}$, will be effective in relieving mismatch. Therefore, the more general form of Equation (7-2) is:

$$n = p/\mathbf{b}_{eff} \qquad (7\text{-}3)$$

The average spacing, S, between misfit dislocations is given by the inverse of Equation (7-3):

$$S = \mathbf{b}_{eff}/p \qquad (7\text{-}4)$$

It has generally been found that in heteroepitaxial layers, misfit dislocations are mostly of the 60° type when the misfit is small, i.e. <2%, (13,14), are of mixed 60° and 90° types for intermediate degrees of misfit (15) and are predominantly of the Lomer type for large degrees of misfit (16). Lomer dislocations are more efficient than 60° dislocations at relieving strain due to their larger misfit relieving edge component. The 60° and Lomer dislocations may be distinguished in cross-sectional HREM if they are viewed end-on and have Burgers vector $\mathbf{b}=a/2\langle 110\rangle$(17). The image of an 'end-on' 60° dislocation in the {110} plane has one terminating {111} fringe, whilst the image of a Lomer dislocation has two {111} terminating fringes, equivalent to two 60° dislocations, and has a Burgers vector equal to an a/2{110} spacing in the direction of the interfacial plane.

7-2-2 Models for relaxing lattice strains in strained layers

In a material with the zinc-blende type structure, a perfect dislocation has a Burgers vector **b**=a/2<110>. Of the three main types of dislocations, i.e. edge, screw or 60°, the edge type has the highest core energy (18-20). The screw type can not relax tetragonal lattice distortion. In systems with a small lattice mismatch such as GaP/(001) Si (21), TEM investigations have shown that the majority of the misfit dislocations are of the 60° type. In systems with a large lattice mismatch such as GaAs/(001) Si, Lomer dislocations are observed more frequently (22), possibly due to the combination of two 60° dislocations, as described in section 7-2-1.

The 60° dislocations with Burgers vector, **b**, inclined at 45° to the (001) interface, can glide through the layer to the interface, where they form misfit segments. Mechanisms for the formation of misfit segments by glide are illustrated in Fig 7.1. First, the grown-in threading dislocation (A in Fig 7.1) bends over into the plane of the misfitting interface, where it relieves misfit, and can glide out to the edge of the crystal. If the density of the threading dislocations is too low to relax the total lattice strain by the first mechanism, new dislocations can be generated by a second mechanism to continue relieving the misfit. This latter mechanism can be achieved by the nucleation of a dislocation at the surface and its subsequent glide down to the interface to give a half-loop (B in Fig. 7.1).

A dislocation can lower its energy by splitting into two dislocations, each with a smaller **b**, according to Frank's rule (18), since the energy of a dislocation is proportional to the square of its Burgers vector, i.e. $E \propto \mathbf{b}^2$. In the zinc-blende structure, therefore, dislocations having the smallest perfect Burgers vector **b**=1/2<110> may dissociate into two partial dislocations. For example, the perfect $1/2(\bar{1}01)$ dislocation (BB) can dissociate into two Shockley partials (BC and CB) having Burgers vectors of $1/6[\bar{1}\,\bar{1}\,2]$ and $1/6[\bar{2}\,11]$, as shown in Fig 7.2 (18).

In zinc-blende materials, the sign of the misfit stress determines the order in which the partials can nucleate as a result of the atomic configuration and stacking sequence of the {111} planes (23). For a 60° dislocation lying along a <110> direction parallel to the layer

Figure 7.1

Schematic drawing (ref.35) showing progressive stages (1 to 3) in generating misfit dislocations in a {001} semiconductor heterostructure. A-threading dislocation bends along interface. B-dislocation loop generated at surface glides down to interface.

Figure 7.2

Slip on a {111} plane of a zinc-blende type crystal for a glide dislocation. A perfect 1/2<110> dislocation (BB) can split into two Shockley partial 1/6<112> dislocations (BC and CB).

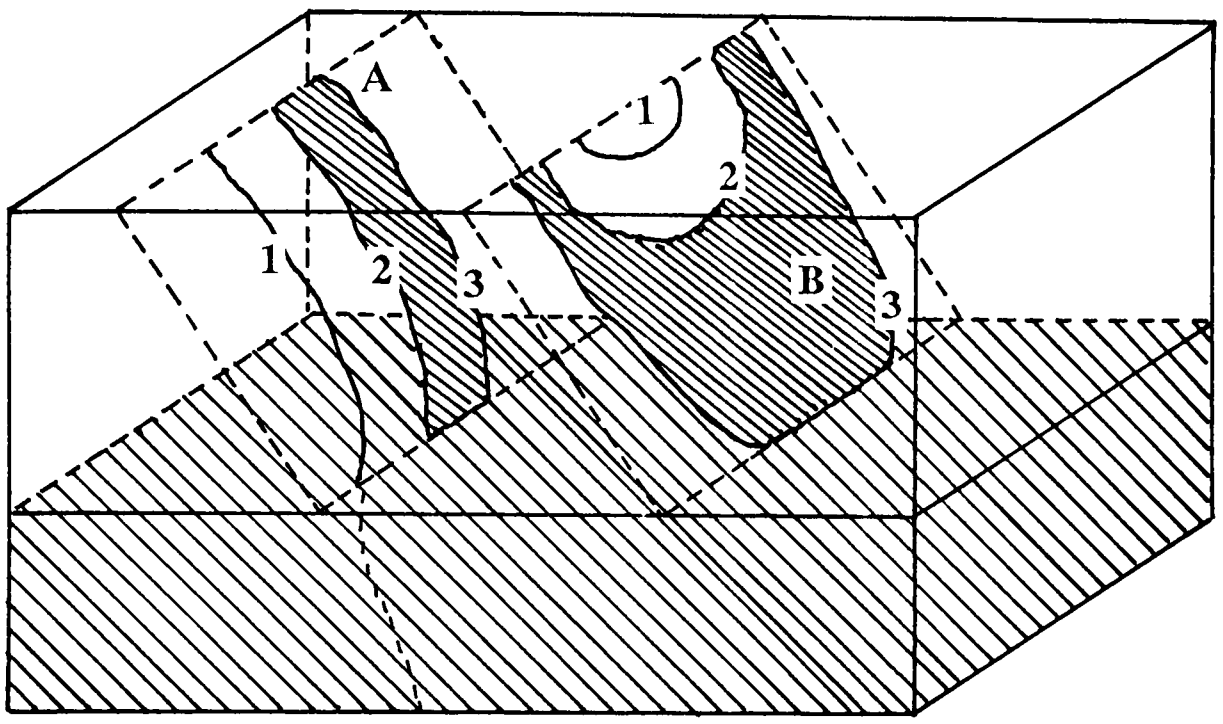

Fig. 7.1

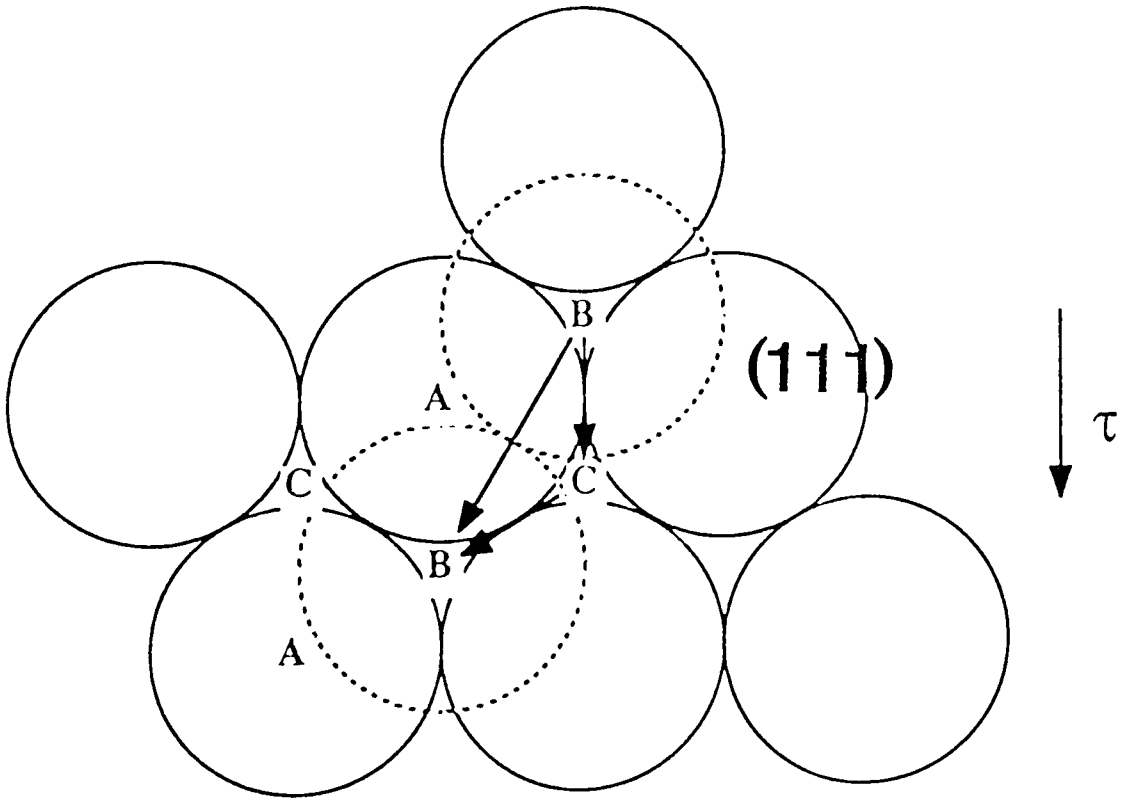

Fig. 7.2

interface, in the case of the layer being under tensile stress, the 90° Shockley partial nucleates first, after which the 30° Shockley partial can follow. If the stress field is compressive, the order is reversed. In both cases, the resolved shear stress on the {111} slip plane, τ, is in same direction as the Burgers vector of the 90° Shockley partial. τ makes an angle of 60° with the 30° Shockley partial (Fig. 7.2). Therefore, the force exerted by the stress field on the 90° Shockley partial is twice as large as that on the 30° Shockley partial. These geometric effects give rise to differences in the mechanisms of nucleation of partial dislocations for tensile or compressive stress (23).

7-3 Experimental

The samples investigated in this chapter were grown by MBE. For the three n-SLSs, the substrates were (001) Cr-doped, semi-insulating GaAs. A GaAs buffer layer ~0.5μm thick was grown at 550°C, followed by an InAs buffer layer ~80nm thick. $InAs_ySb_{1-y}$ layers ~4μm thick and with nominal compositions y=0.4, 0.5 or 0.6 were then grown at either 340 or 370°C and a growth rate of ~0.17nm/s. For comparison, an i-SLS was grown on an (001) InSb substrate with a graded buffer layer 0.75μm thick, whose composition varied from InSb to $InAs_{0.7}Sb_{0.3}$. The i-SLS was then grown with nominal compositions y1=0.3 and y2=0.7 and individual layer thickness 25.5nm at 430°C and ~0.17nm/s. A summary of the material systems studied is given in Table 7.1. TEM examinations were made of [110] and $[\bar{1}10]$ cross-section specimens. A Philips CM 20 and a JEOL 200CX operated at an accelerating voltage of 200kV, and a JEOL 4000EX operated at an accelerating voltage of 400kV, were used to characterise the specimens.

7-4 TEM and HREM analyses of defects in strained layers of $InAs_ySb_{1-y}$

Cross-section TEM examinations using the (002) reflection, which is sensitive to composition variations, demonstrated that phase separation occurs in $InAs_ySb_{1-y}$ under certain growth conditions (chapter 4). Phase separation gives rise to two phase materials,

Table 7.1 Defects in SLSs of $InAs_ySb_{1-y}$ grown by MBE.

Sample	Substrate	T_g (°C)	y	Type of SLS	$InAs_{y1}Sb_{1-y1}/InAs_{y2}Sb_{1-y2}$ (y1 , y2)	T (nm)	Defects
IC 237	GaAs	340	0.5	n-SLS	y1 = 0.33, y2 = 0.69	28.6	l-MT
IC 118	GaAs	370	0.4	n-SLS	y1 = 0.33, y2 = 0.74	20-200	s-SF, s-MT
IC 124	GaAs	370	0.6	n-SLS	y1 = 0.31, y2 = 0.74	20-200	s-SF, s-MT
IC 257*	InSb	430	0.3 0.7	i-SLS	y1 = 0.40 y2 = 0.74	25.5	l-MT (1 variant)

T_g = growth temperature. y = nominal composition in $InAs_ySb_{1-y}$. n-SLS and i-SLS = naturally and intentionally grown strained layer superlattices, respectively. T = average individual platelets/layer thickness in SLSs. s-SF = 'short' stacking fault, s-MT = 'short' microtwin, l-MT = 'long' microtwin. * indicates substrate off-cut~1.5°.

where the two phases have compositions $InAs_{y1}Sb_{1-y1}$ and $InAs_{y2}Sb_{1-y2}$, which were determined from selected area TED patterns. Fig 7.3 shows a [110] cross-section (002) DF micrograph of the n-SLS of nominal composition $InAs_{0.6}Sb_{0.4}$ (IC124). The image exhibits a non-uniform phase-separated structure with alternating platelets of $InAs_{0.31}Sb_{0.69}$ and $InAs_{0.74}Sb_{0.26}$ (Fig. 7.3). The inset is the corresponding selected area [110] TED pattern showing splitting of the higher order spots, which indicates that the lattices are tetragonally distorted. The plate-like structures are not exactly parallel to the layer surface and small deviations from the $[\bar{1}10]$ direction are evident. Platelet thicknesses vary from 20 to 200 nm. The majority of the defects are 'short' stacking faults and 'short' microtwins, i.e. these defects terminate at the interfaces between the platelets and extend over typically 1, 2 or 3 platelets.

Fig. 7.4(a) is a similar (002) DF micrograph of the n-SLS of nominal composition $InAs_{0.5}Sb_{0.5}$ (IC237). The majority of the defects are 'long' microtwins which extend through the complete grown layer. Two twin variants, (111) and $(11\bar{1})$, occurred in approximately equal concentrations. A similar micrograph of the i-SLS (IC257) is shown in Fig.7.4(b). 'Long' microtwins were the major crystallographic defects, with one variant dominating over the other. This anisotropy of formation of microtwins could be related to the off-cut of the GaAs substrate (25), which was ~1.5° off (001) about the <110> direction.

In general, when samples are viewed along the [110] direction, twins parallel to the (111) and $(11\bar{1})$ planes can be imaged. The angle between the (001) plane and {111} planes is 54° in cubic materials. The substrate off-cut produces an angle between the interface and the (001) plane, and this results in a staircase configuration on the substrate surface arising out of an array of atomic steps all of which have the same orientation (25). The measured angles between the (111) and $(11\bar{1})$ twin lamellae and the interface are both ~54° in the n-SLS (IC237), indicating that there is no significant off-cut. The corresponding angle between the (111) twin lamellae and the interface in the i-SLS (IC 257) was measured to be 56.5°, indicating an off-cut of ~1.5°, which is consistent with the anisotropy of formation of microtwins in this layer.

Figure 7.3

[110] cross-section TEM (002) DF micrograph of n-SLS of nominal composition $InAs_{0.6}Sb_{0.4}$ grown at 370°C (IC124), showing non-uniform plate-like structures arising from phase separation. Inset is corresponding [110] TED pattern from several platelets.

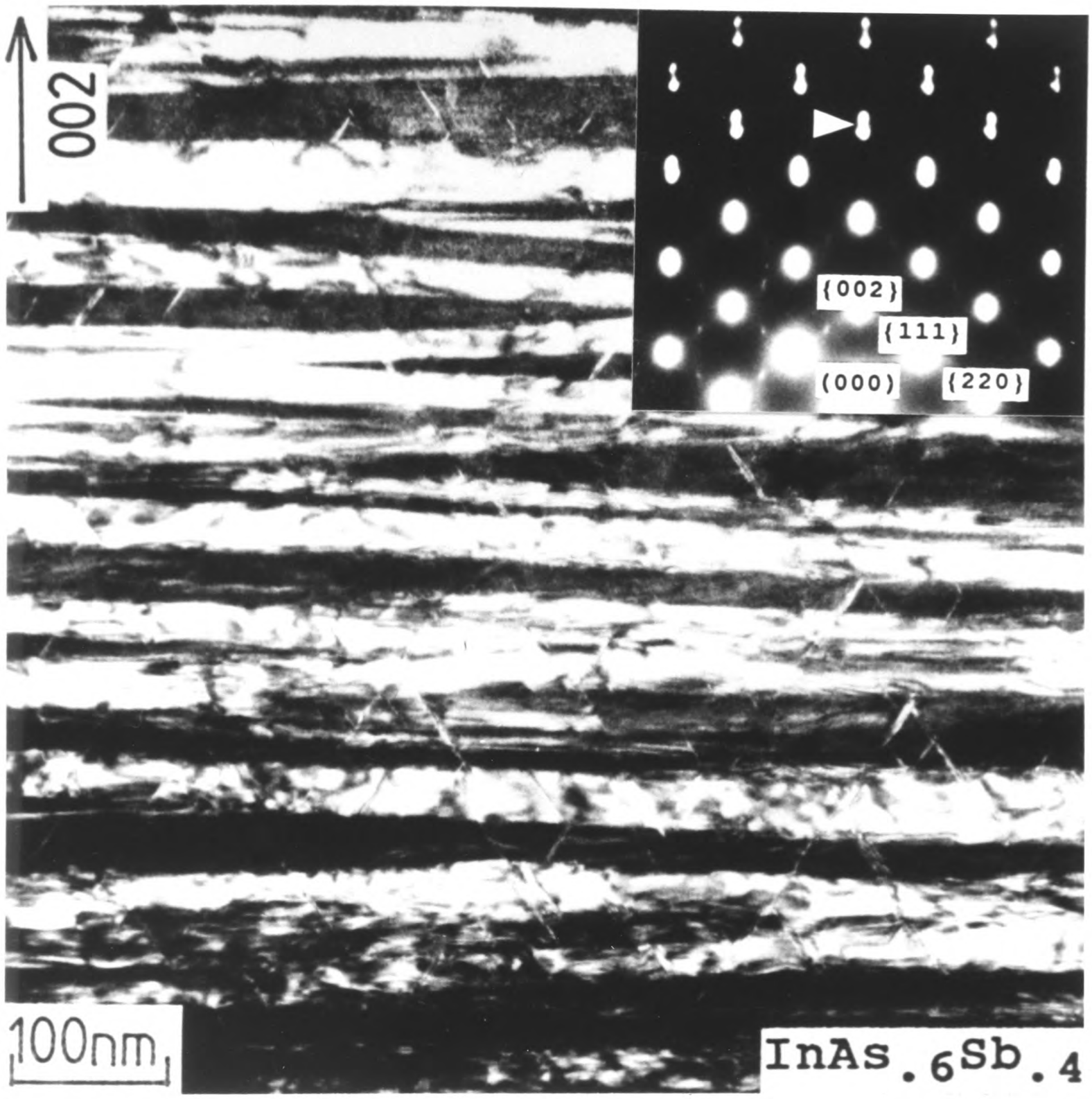

Fig. 7.3

Figure 7.4

(a) [$\bar{1}$10] cross-section TEM (002) DF micrograph of n-SLS of nominal composition $InAs_{0.5}Sb_{0.5}$ grown at 340°C (IC237). Note platelets and two twin variants. (b) [$\bar{1}$10] cross-section TEM (002) DF micrograph of i-SLS of InAsSb grown at 430°C (IC257). Note individual layers and one twin variant.

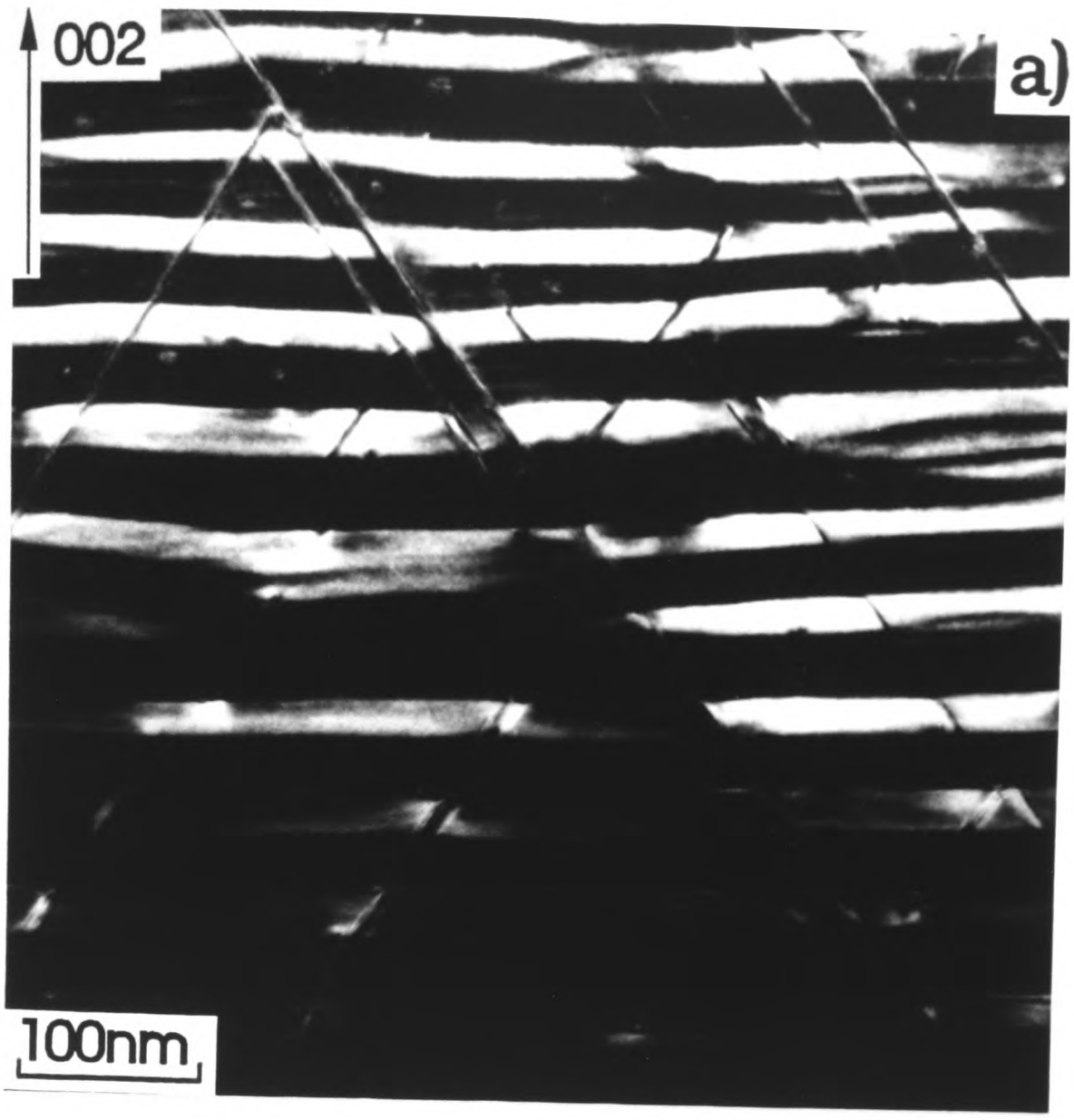

Fig. 7.4

Fig. 7.5 shows a [$\bar{1}$10] cross-section HREM lattice image of a part of a n-SLS (IC118) corresponding to the InAs buffer layer and the first InAsSb platelet of the subsequent layer of nominal composition $InAs_{0.4}Sb_{0.6}$. There are dislocations at the interface which from the extra planes in the images can be identified as Lomer dislocations. The mean spacing of these dislocations determined from a number of such images was ~66Å. (002) DF images showed that the first platelet was dark, i.e. was Sb-rich, and from the earlier TED patterns this indicated that the composition was $InAs_{0.33}Sb_{0.67}$.

The calculated lattice mismatch ($f = 2(a_1-a_2)/(a_1+a_2)$) (13) for $InAs_{0.33}Sb_{0.67}$ and InAs is ~4.1%. For this mismatch to be completely relieved by Lomer dislocations, the mean dislocation spacing calculated from equation (7-4) would be 52.6Å. The larger experimental value for the mean dislocation spacing indicates that not all of the strain in the first Sb-rich platelet was relieved by interface dislocations. A simple calculation indicates that ~80% was relieved.

Characteristic features of defect structures in IC 118 and 124 are different from those of IC 237 and IC 257. In IC 118 (Fig. 4.9(b)) and IC 124 (Fig. 7.3), the main defects are 'short' stacking faults and 'short' microtwins. It is suggested that most of these nucleate at the growing surface and glide down to the interface with the platelet below. However, in IC237 and IC 257 (Fig. 7.4(a,b)), the main defects are 'long' microtwins. It is suggested that these nucleate at the final layer surface, and glide down to either the InAs buffer layer or the interface between the InAs buffer layer and GaAs buffer layer. A few stacking faults are also present. The occurrence of different characteristic defects in these SLSs indicates that the lattice strain relaxation mechanisms in IC 237 and 257 may be different from those in IC 118 and IC 124.

Further detailed investigations have been carried out using high resolution electron microscopy (HREM) to investigate the defect structures in IC 124. A [$\bar{1}$10] cross-section HREM lattice image of an 'end-on' view of a pair of stacking faults (marked 'S'), nucleating at the interface between $InAs_{0.31}Sb_{0.69}$ and $InAs_{0.74}Sb_{0.26}$, is shown in Fig. 7.6. In order to identify the character of the observed defects, a Burgers circuit was made around the individual stacking faults in Fig. 7.6. The vectors required to close such circuits were found

Figure 7.5

[$\bar{1}$10] cross-section HREM lattice image of n-SLS of nominal composition $InAs_{0.4}Sb_{0.6}$ (IC118). Micrograph shows interface between InAs buffer layer and first $InAs_{0.33}Sb_{0.67}$ layer with 'edge-on' misfit dislocations of Lomer type indicated by arrows.

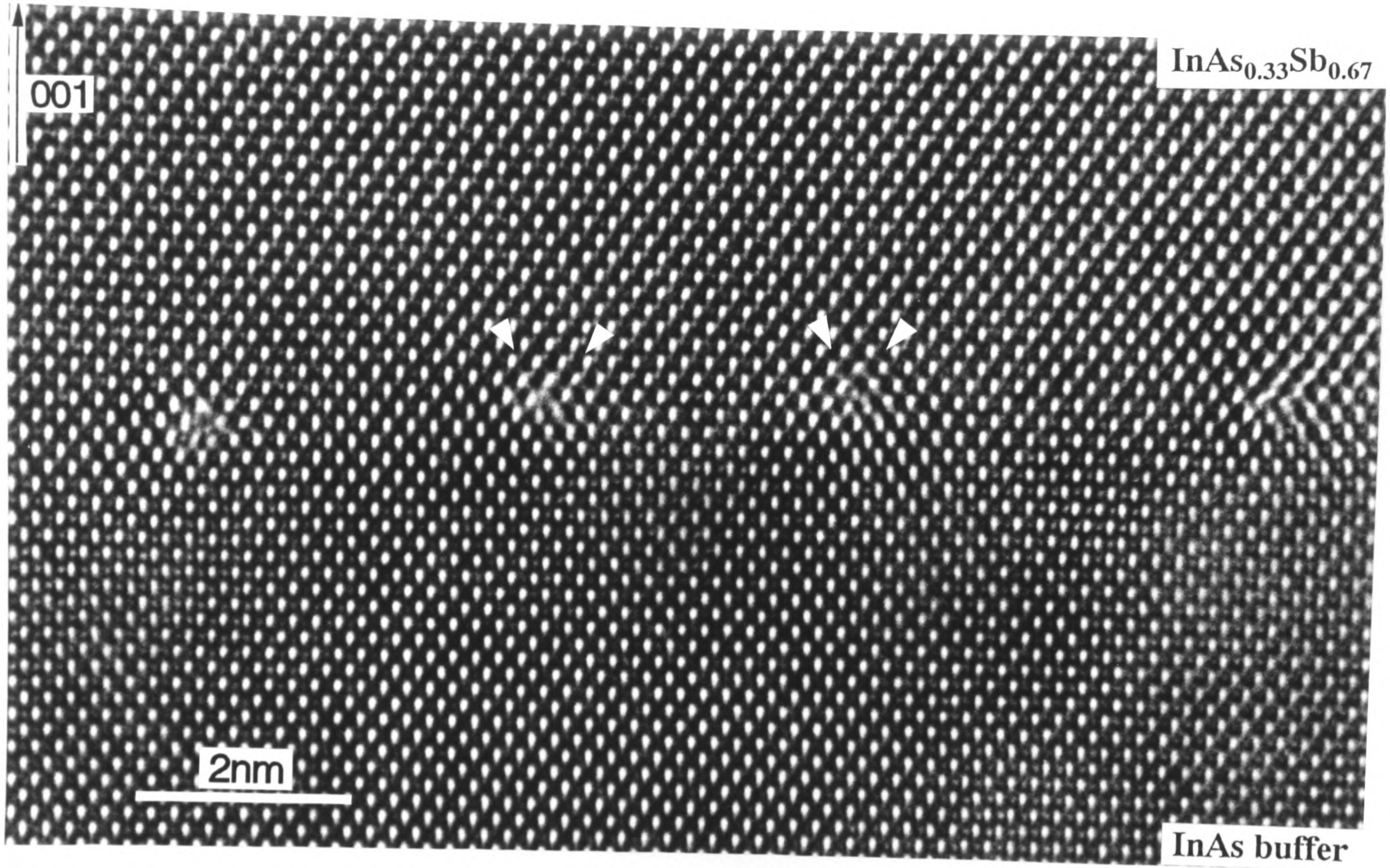

Fig. 7.5

Figure 7.6

[$\bar{1}$10] cross-section HREM lattice image of n-SLS of nominal composition $InAs_{0.6}Sb_{0.4}$ grown at 370°C (IC124), showing stacking faults indicated by 'S'.

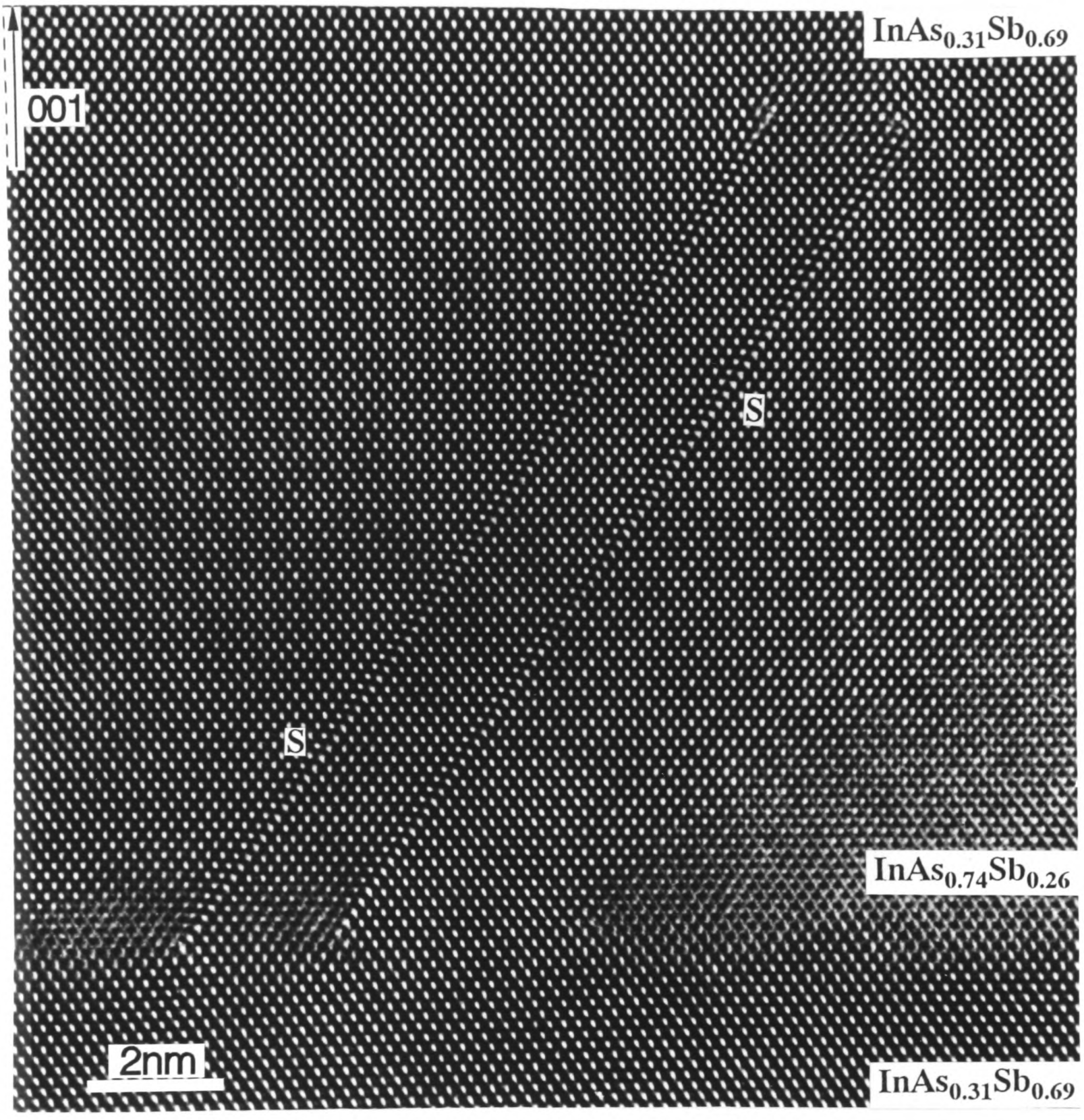

Fig. 7.6

to be 'zero'. This result indicates that each stacking fault is bounded by two partial dislocations with Burgers vectors of the same magnitude but opposite sign. A Burgers circuit around the individual partial dislocations showed them to be of 90° type with Burgers vector $1/6[1\,\bar{1}\,2]$. The stacking faults are intrinsic and are bounded by a 90° partial dislocation dipole. The suggested atomic model of the defect is illustrated in Fig 7.7. This was obtained by tracing the atom positions from the HREM lattice image. The atomic arrangements at the two ends of the stacking fault agreed well with those reported by Myung (26) for 90° partial dislocations in the diamond structure. Dashed lines indicate where atomic steps at the interfaces are considered to have occurred.

Fig.7.8 is a $[\bar{1}\,10]$ cross-section HREM lattice image of the n-SLS of nominal composition $InAs_{0.6}Sb_{0.4}$ grown at 370°C (IC124). The image shows a defect which starts as a stacking fault, and then increases in width to first three planes and then to four planes at points B, A, respectively. An undissociated 60° dislocation occurs in region B where the twin lamellae widen.

In Fig. 7.9 is shown a $[\bar{1}\,10]$ cross-section HREM lattice image of the n-SLS of nominal composition $InAs_{0.6}Sb_{0.4}$ grown at 370°C (IC124), showing the end of a twin, T, originating at the interface between $InAs_{0.31}Sb_{0.69}$ and $InAs_{0.74}Sb_{0.26}$. The suggested atomic model is illustrated in Fig. 7.10 based on the HREM lattice image. The presence of such microtwins may lead to some strain relaxation occurring between the two tetragonally distorted phases. The formation of this microtwin is likely to be associated with surface steps and partial dislocations, as shown in the atomic model.

As the platelets of the two phases are tetragonally distorted, it is expected that an angular deviation in the direction of {111} fringes transversing the plate-like interfaces should occur. This deviation was observed in IC 118, IC 124, IC 237 and IC 257 (e.g. see Fig.7.9). This degree of tetragonal distortion in the layers will be discussed in more detail in the following section.

In Fig. 7.11 is shown a $[\bar{1}\,10]$ cross-section HREM lattice image of the end of a twin in the compositional graded $InAs_ySb_{1-y}$ (y=0 to 0.3) buffer layer of the InAsSb i-SLS (IC257). The micrograph shows the widening of the twin bounded by the stacking faults, as

Figure 7.7

Suggested atomic model of intrinsic stacking fault shown in Fig. 7.6.

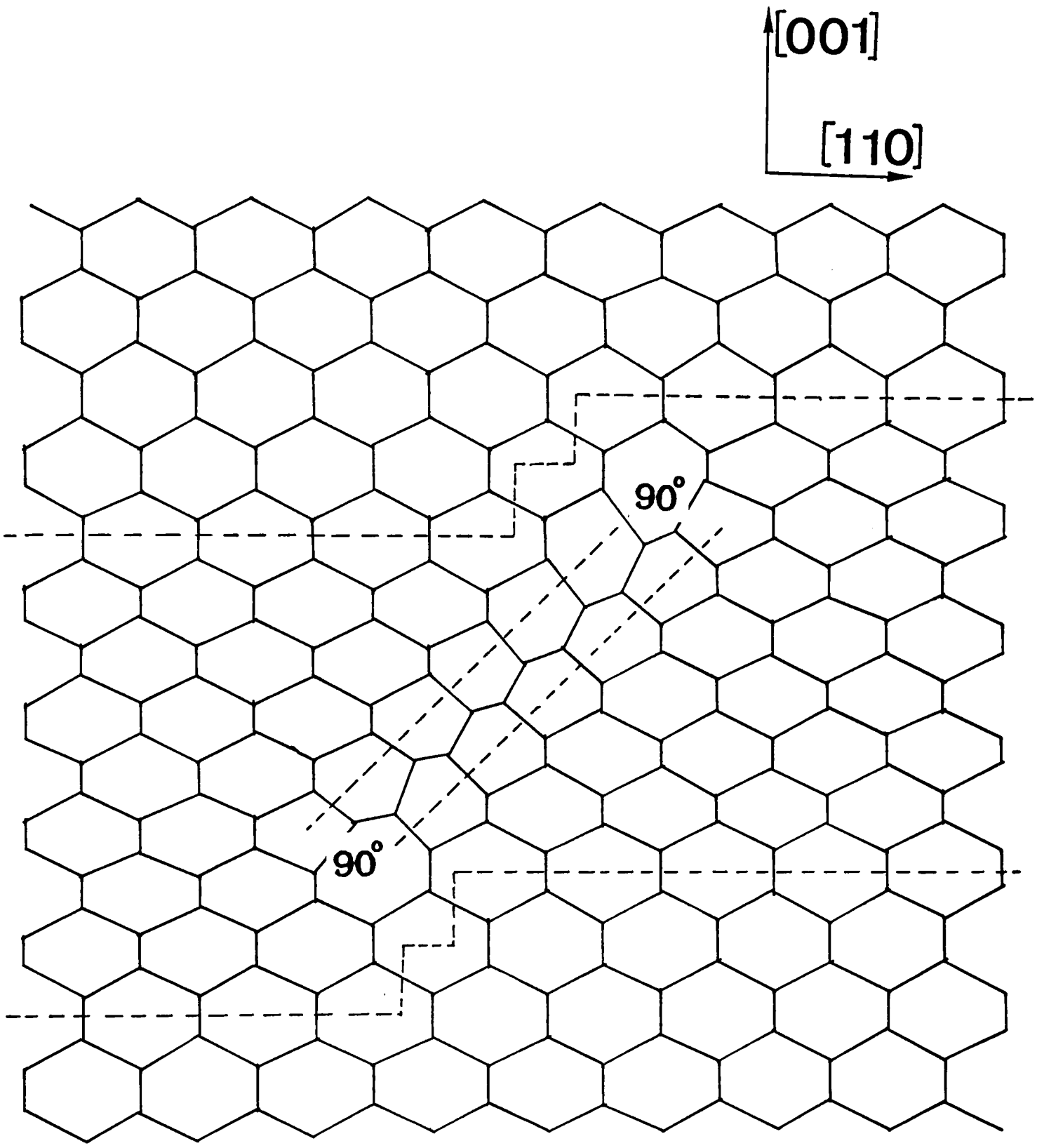

Fig. 7.7

Figure 7.8

[$\bar{1}$ 10] cross-section HREM lattice image of n-SLS of nominal composition $InAs_{0.6}Sb_{0.4}$ grown at 370°C (IC124), showing increase in width of twin lamella from three to four planes. An undissociated 60° dislocation occurs at B where twin lamella widens.

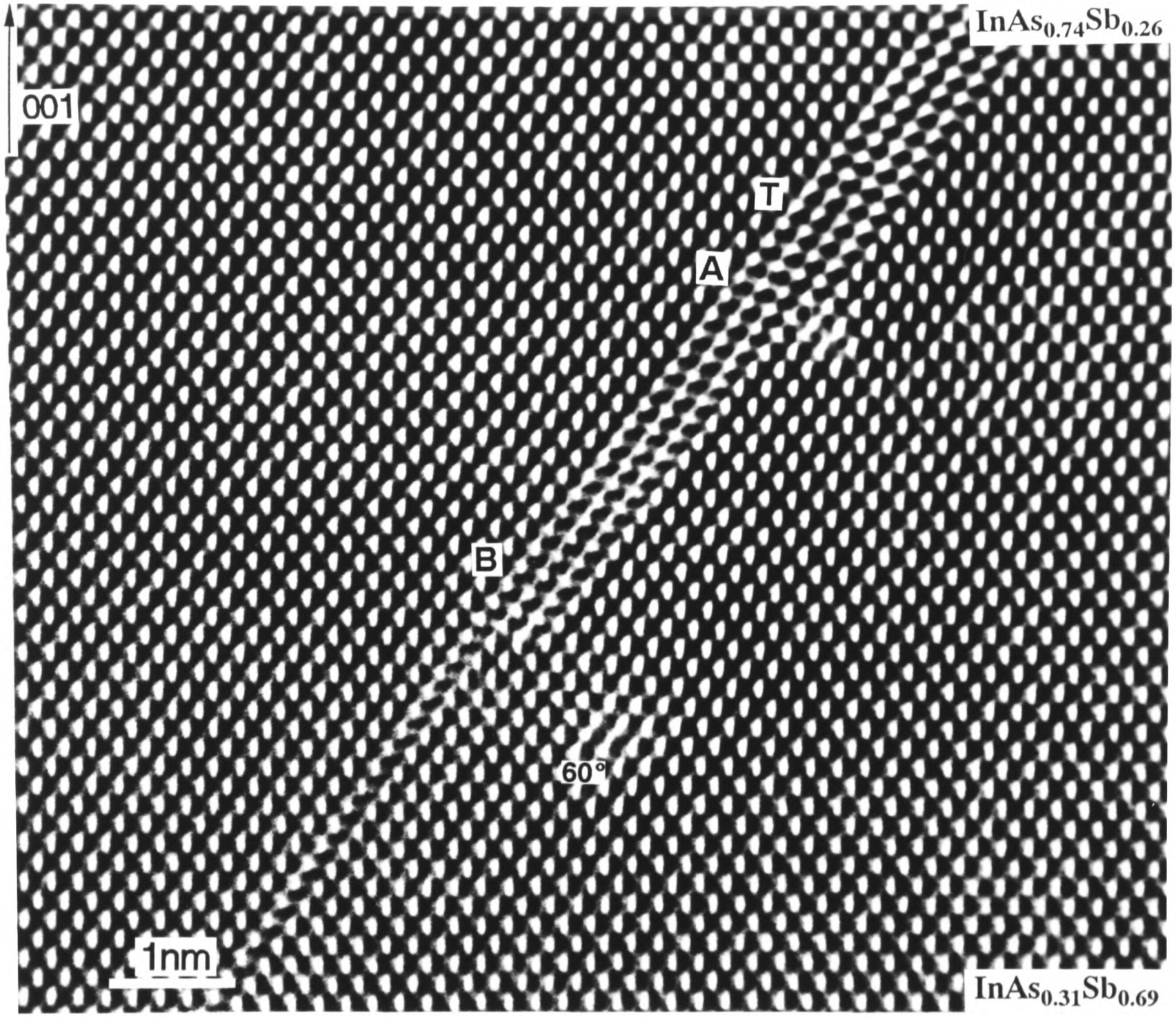

Fig. 7.8

Figure 7.9

[$\bar{1}$10] cross-section HREM lattice image of n-SLS of nominal composition $InAs_{0.6}Sb_{0.4}$ grown at 370°C (IC124), showing twin lamella (T) and Lomer dislocation (L) consisting of a pair of associated 60° perfect dislocations. Note deviation of {111} lattice fringes on crossing interface between $InAs_{0.31}Sb_{0.69}$ and $InAs_{0.74}Sb_{0.26}$.

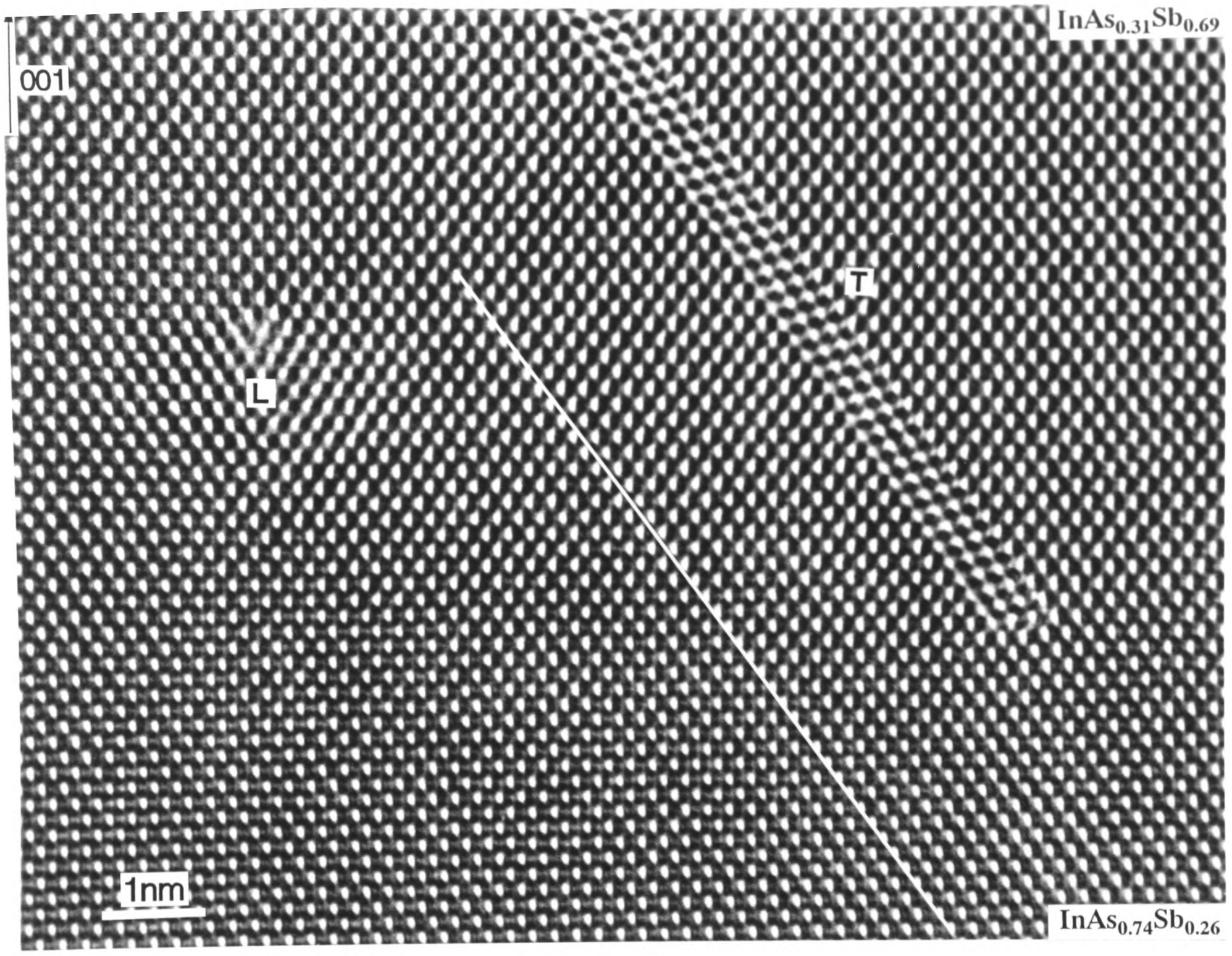

Fig. 7.9

Figure 7.10

Suggested atomic model of twin lamella shown in Fig. 7.9.

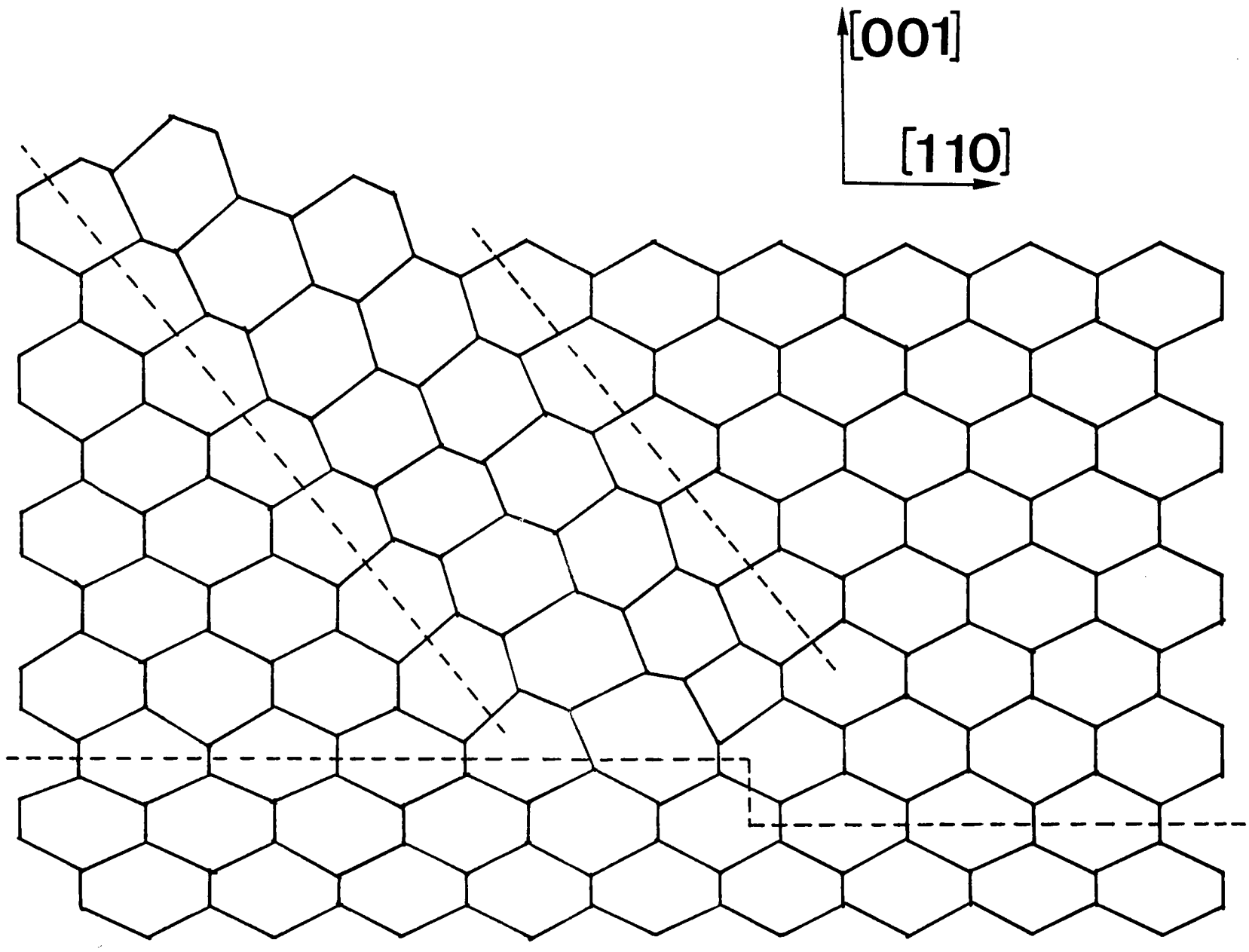

Fig. 7.10

Figure 7.11

[$\bar{1}$10] cross-section HREM lattice image of graded buffer layer (InSb to $InAs_{0.3}Sb_{0.7}$) of i-SLS of InAsSb grown at 430°C (IC257), showing end of twin lamella. Arrows indicate partial dislocations considered to be 90° Shockley (determined from higher magnification micrographs).

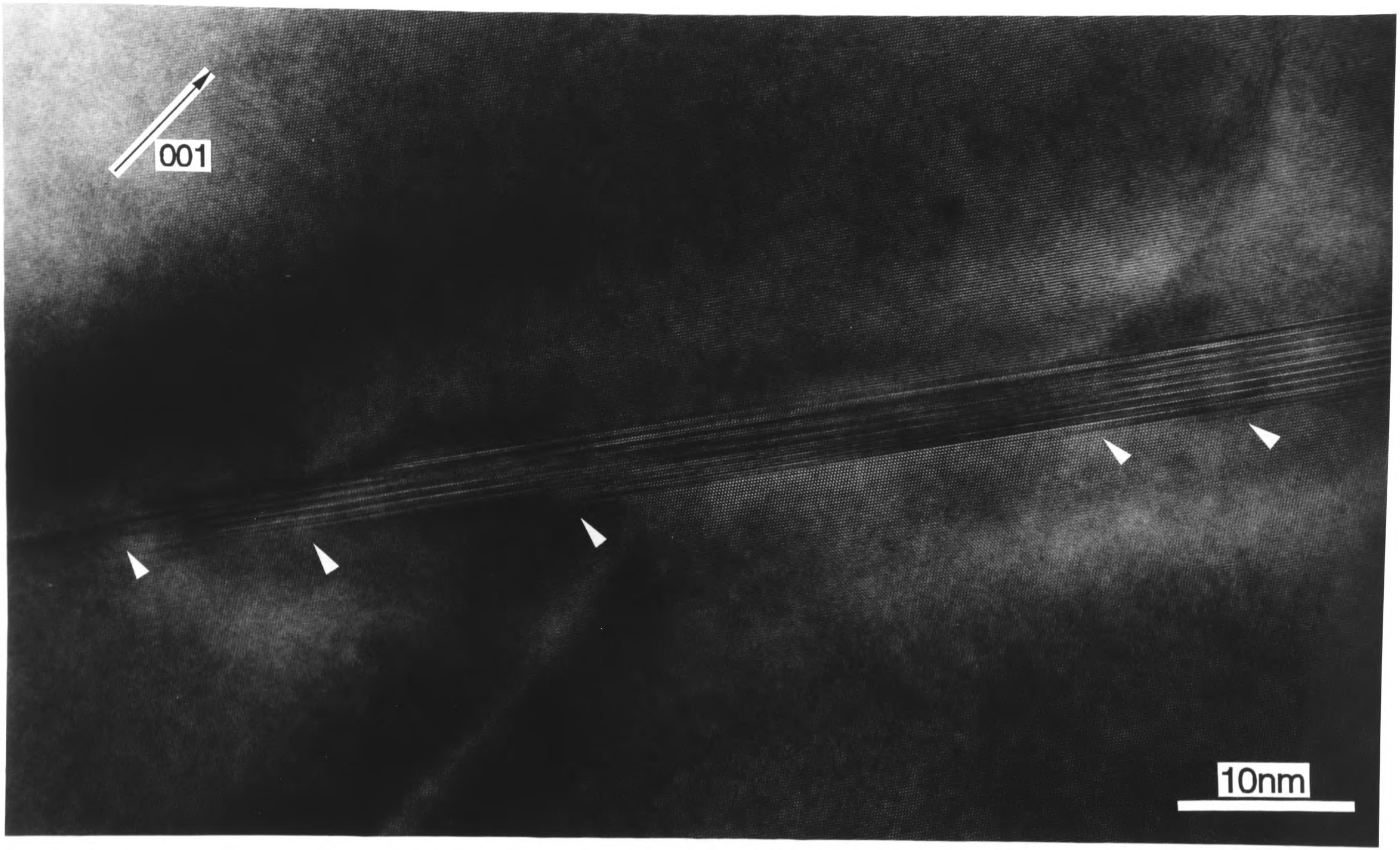

Fig. 7.11

marked by the arrows. This may indicate that the microtwins are responsible for strain relaxation. This mechanism is discussed in further detail in a later section.

7-4-1 Discussion: consideration of critical thickness in SLSs

For a coherently strained epitaxial layer, it is well known that there is a critical thickness, h_c, above which it is energetically favourable to relieve strain energy through the introduction of misfit dislocations. Several workers have calculated the critical thicknesses of strained epitaxial layers using different approaches, for example, i) involving a balance between strain and interfacial energy; ii) a balance between the line tension of a dislocation threading through the heterostructure with the force required to bend that dislocation over into a misfit dislocation; iii) a numerical approach following the logic of the energy balance criterion. There exist large differences in the measured critical thicknesses from workers to workers, even for the systems having the same lattice misfit, although the critical thickness could depend on the character of defects present and elastic properties of the strained layers. For example, for a lattice misfit of ~2.5%, the critical thickness predicted by Van de Merwe (28) is ~10Å. For the corresponding misfit, calculations by Dodson and Taylor (29), and Hockly (13) yield a critical thickness of ~40Å. However, People and Bean (30) calculated the critical thickness in Si/Si_xGe_{1-x} multilayers and gave much greater values of h_c than those of other workers, ~100Å. This discrepancy could be related to the different computational approaches used by these authors. Nonetheless, it is apparent that the critical thickness decreases exponentially with increasing lattice misfit strains, regardless of the physical properties of the alloy layers.

In the present work, the lattice misfit strain between the $InAs_{y1}Sb_{1-y1}$ and $InAs_{y2}Sb_{1-y2}$ for all four SLSs is ~2.5%. In spite of the disagreement between the various theories, the critical thicknesses of the SLSs (IC 118, IC 124, IC 237 and IC 257) appear to be less than 100Å. Beyond this thickness, the lattice misfit of 2.5% makes continued commensurate growth energetically unfavourable. Continued growth will result in the generation of lattice misfit defects.

7-5 Direct observation of lattice distortion in strained layers of $InAs_ySb_{1-y}$

A region of the strained layer of $InAs_{0.6}Sb_{0.4}$ (IC 124) grown at 370°C using MBE is shown in Fig. 7.3, and consists of a superlattice of 20-200nm thick $InAs_{0.31}Sb_{0.69}$ and 20-200nm thick $InAs_{0.74}Sb_{0.26}$ layers. As expected from the viewpoint of the critical thickness, many crystallographic defects are visible in the superlattice structures. Inset in Fig. 7.3 is a corresponding selected area TED pattern, clearly showing that there is a splitting of spots in the [001] direction but not in the [110] direction. This splitting reveals a degree of tetragonality in the strained layers. The magnitude of the splitting between the diffraction spots in the [001] direction reflects the difference in the lattice parameter parallel to the [001] growth direction. Lattice constants and calculated angles of deviation between {111} planes in the strained layer superlattice are listed in Table 7.2.

As the unit cells of superlattice structures of $InAs_ySb_{1-y}$ semiconducting layers are distorted into a tetragonal shape, the relative angles between various crystallographic planes change at the interface between regions of different compositions. It should be possible to see a change in the direction of the {111} lattice fringes as they cross the interfaces between the successive strained layers. These angle changes were calculated from the selected area TED results (Table 7.2) and changes ranging from 1.25° to 1.55° should be seen on the {111} lattice fringes. Angle changes were also directly measured from the HREM micrographs and found to vary from 1.5° to 1.9° as listed in Table 7.2.

A $[\bar{1}10]$ cross-section HREM lattice image of an $InAs_{0.31}Sb_{0.69}$-$InAs_{0.74}Sb_{0.26}$ superlattice is shown in Fig 7.9. The change of angles between the {111} lattice fringes is visualised on the micrograph by the extrapolation of lines drawn parallel to the (111) lattice fringes transversing the interface. The lattice distortion is clearly visible. The angular change was measured to be ~1.8°, which is in agreement with the calculated value of 1.55°, assuming the above composition.

The tetragonality of the strained layer superlattices also can be directly determined by the ratio of c/a using the spacings of the (002) and (220) lattice fringes of $InAs_{0.31}Sb_{0.69}$

Table 7.2 Deviation angles for {111} lattice planes on crossing the interface between adjacent tetragonally distorted layers in MBE $InAs_ySb_{1-y}$ superlattices.

Layer compositions	a_p (Å)	c_1 (Å)	c_2 (Å)	$\Delta\Phi_1$ (°)	$\Delta\Phi_2$ (°)
$InAs_{0.33}Sb_{0.67}$-$InAs_{0.69}Sb_{0.31}$ (IC 237)	6.28	6.40	6.11	1.5	1.25
$InAs_{0.33}Sb_{0.67}$-$InAs_{0.74}Sb_{0.26}$ (IC 118)	6.31	6.37	6.02	1.9	1.55
$InAs_{0.31}Sb_{0.69}$-$InAs_{0.74}Sb_{0.26}$ (IC 124)	6.26	6.44	6.08	1.8	1.55
$InAs_{0.40}Sb_{0.60}$-$InAs_{0.74}Sb_{0.26}$ (IC 257)	6.23	6.37	6.11	1.5	1.25

a_p = measured lattice parameter parallel to interface of phases 1 and 2; c_1 = measured lattice parameter in (001) direction of phase 1; c_2 = measured lattice parameter in (001) direction of phase 2; $\Delta\Phi_1$ = measured deviation angle for {111} lattice planes; $\Delta\Phi_2$ = calculated deviation angle for {111} lattice planes based on TED results.

and $InAs_{0.74}Sb_{0.26}$. The ratio of c/a in each layer was measured and found to be consistent with the values calculated from TED data.

It should be noted that for high growth temperatures, a small splitting of the spots in the [110] direction was detected by a close examination of the 440 spots. This splitting indicates that at higher growth temperatures, slightly more of the tetragonal strain is relieved and so more interface misfit dislocations are likely to be present.

7-6 Discussion on relaxation processes in $InAs_{y1}Sb_{1-y1}/InAs_{y2}Sb_{1-y2}$ SLSs

The lattice relaxation process of misfit in strained layers has been extensively studied in many systems (30-32). Crystallographic defects such as misfit dislocations play a major role in relaxing lattice strains. For the heteroepitaxial system such as silicon on sapphire, microtwins are usually observed in Si layers. It has been suggested that microtwins make a large contribution to the accommodation of lattice strains in this system (31), although the extent of the contribution of these defects to misfit relief is still a matter of some controversy. For example, Twigg et al.(33) have measured the volume fraction of microtwins in silicon on sapphire (SOS) to estimate the possible lattice strain relief due to twins and concluded that microtwins may not fully account for the observed relaxation. Recently, Wegscheider et al. (34) proposed a strain relaxation model of misfit defect formation in strained Si/Ge superlattices grown on (001) Ge. In this model, they attribute relaxation of lattice misfit-indueed strain to the formation of planar defects on {111} glide planes, which have been identified as microtwins.

In the present work, as described in section 7-3, the misfit relieving defects observed in naturally occurring and intentionally grown InAsSb SLSs were stacking faults and microtwins. We consider that the microtwins operate as plastic deformation twins acting to release strains in the layers. The configuration of the deformation twins is such that they are bounded by an array of partial dislocations with parallel Burgers vectors; each {111} plane of the twins is separated from the matrix by a partial dislocation.

In the IC 118 and IC 124 samples, the misfit-induced strain appears to be relaxed mainly through the introduction of stacking faults with an additional contribution from microtwins, which propagate through 3 or 5 periods of the superlattice. This observation indicates that stacking faults play a major role in the relaxation process in the IC 118 and IC 124 samples, which show poor quality superlattice structures. Additionally, a few microtwins also take part in the relaxation process. IC 237 and IC 257 samples show different characteristics: i.e. in these SLSs, misfit strains are relaxed mainly through the introduction of microtwins with minor contributions from stacking faults. Therefore, it is essential to characterise the detailed defect behaviour and structures of stacking faults and microtwins.

First, in order to understand the contribution to the relaxation process due to the occurrence of stacking faults and to determine the possible formation mechanism of misfit-induced defects, let us consider a pair of stacking faults as observed in IC 124, imaged using the HREM technique. As already discussed in section 7-4 (Figs.7.6 and 7.7), these stacking faults are bounded by 90° partial dislocations, namely, dipoles of 90° partials. Taking account of these results, we suggest a possible mechanism for the generation of these stacking faults. During deposition of the heteroepitaxial layers (IC124), the growth behaviour could occur as follows. Consider the growth of $InAs_{0.74}Sb_{0.26}$ on $InAs_{0.31}Sb_{0.69}$, such as that shown in Fig.7.6. The initial stages of $InAs_{0.74}Sb_{0.26}$ growth produce a defect-free layer. In this thin defect-free layer, misfit strain can be accommodated through elastic strain. When the layer thickness reaches the critical value of less than ~10nm, subsequent deposition of $InAs_{0.74}Sb_{0.26}$ requires that lattice relaxation processes operate, which results in the generation of misfit defects. In this system, the 90° Shockley partial dislocation nucleates probably at a surface step and glides down on a {111} plane towards the interface between $InAs_{0.74}Sb_{0.26}$ and $InAs_{0.31}Sb_{0.69}$ where it can lower the total strain energy, and results in the creation of a stacking fault. The interface between $InAs_{0.74}Sb_{0.26}$ and $InAs_{0.31}Sb_{0.69}$ might include a large number of surface steps. Since the lattice parameters of the two phases are different, it is expected that regions around the surface steps at the interface concentrate strain energy and are not energetically stable. Thus, it is likely,

with subsequent overgrowth of more monolayers of material, that when the local strain energy is large enough to overcome the defect formation barrier, a 90° partial dislocation nucleates at such a step at the surface and glides down on a {111} plane to the underlying interface, creating a stacking fault. As the layer continues to grow, the stacking fault grows upwards, always intersecting the surface. When the next $InAs_{0.31}Sb_{0.69}$ grows, the stacking fault may be grown over creating a 90° partial dislocation at the interface of opposite sign to the 90° partial dislocation at the underlying interface. In this way the intrinsic stacking faults consisting of two 90° partial dislocations having opposite signs to each other are formed. By this process, misfit strain within each superlattice period is relieved. Most of the defects are found to be intrinsic stacking faults bounded by either 90° or 30° Shockley partial dislocations. It should be mentioned that the character of Shockley partial dislocations associated with stacking faults depends on the character of the stresses in the layers, i.e. tensile or compressive. Under tensile stress, the 90° partial will be formed at the surface and then glide down on a {111} plane towards the interface, while under compression, the 30° partial will be formed first and then glide down towards the interface (35).

Secondly, to characterise the effects of stacking fault-induced microtwins on the relaxation process, which show minor contributions in IC 118 and IC 124 samples, we consider one of the microtwins observed in IC 124 (Fig.7.8). The presence of such microtwins may lead to some strain relaxation in the strained layers. Similar microtwins have been reported to be able to release strain in strained Si/Ge superlattices grown on (001)-oriented Ge by Wegschieder et al.(34). It was proposed that microtwins were formed by successive glide of 90° partial dislocations on adjacent {111} planes. As shown in Fig.7.8, similar relaxation processes may be applicable to this material system. In the present work it is likely that undissociated 60° dislocations are formed at the surface and then glide down towards the interface between $InAs_{0.74}Sb_{0.26}$ and $InAs_{0.31}Sb_{0.69}$. Such 60° dislocations, such as that at B, are often associated with the widening of {111} twin lamella.

In the IC 237 and IC 257 samples, the misfit-induced strains are found to be relieved mainly by microtwins with minor contributions from stacking faults (Fig 7.4(a,b)). The

microtwins were suggested to originate at the final surface of the SLS and propagate to the InAs buffer layer. The difference in the defect features between IC 237 and IC 257 samples is in the anisotropy of the generation of the two twin variants. The occurrence of this anisotropy is related to the surface steps caused by substrate tilting, as discussed in section 7.4. Some of the microtwins glide down to the interface between InAs and GaAs, indicating either that the InAs buffer layer is not fully relaxed or that there are a number of surface steps and contaminations at the interface, providing favourable sites for the formation of microtwins. TED examination revealed that the InAs buffer layer was to some extent tetragonally distorted, although significantly relaxed, so that further misfit strain may be relaxed by the generation of crystallographic defects such as stacking faults and twins.

In order to determine the formation mechanism of the crystallographic defects observed in IC 124, we examined the atomic structure of the observed microtwins using the HREM technique. In a HREM micrograph which is obtained with the electron beam parallel to the dislocation line, we can measure the magnitude of the Burgers vector. A $[\bar{1}10]$ cross-section HREM lattice image of the end of a twin observed in IC 257 (Fig.7.4(b)) is shown in Fig 7.11. We made a Burgers circuit around the entire defect to identify the nature of the defect. The Burgers vector to complete the Burgers circuit was measured to be 'zero'. The Burgers circuit analysis indicates that the bounding dislocation shown is a 90° Shockley partial and has a Burgers vector of $\mathbf{b}= (a/6)[1\,\bar{1}\,2]$. Therefore, the defect formation process can be described as follows. If the strain energy in the strained layer superlattice exceeds a critical value and the local strain energy is sufficiently large to overcome the defect formation barrier, misfit dislocations can nucleate at the surface. 90° partial dislocations, such as those shown in Fig.7.11, form probably at a surface step. These 90° partial dislocations glide down on {111} planes towards the strained layer superlattice and InAs buffer interface, which results in the formation of a dislocation half-loop. The structure resulting from this mechanism is clearly illustrated in Fig.7.11, which shows a stacking fault at the bottom end of a microtwin. The presence of such a stacking fault has also been reported in a Si layer on (001) GaP (35). Marée et al.(35) reported that a 30° Shockley partial dislocation follows the 90° partial dislocation on the same glide plane, which results in a perfect 60° dislocation with

the Burgers vector of a/2<110>. In contrast, we observe that after the generation of a stacking fault bounded by a 90° partial dislocation, another dislocation half-loop of 90° Shockley partial is created on a neighbouring glide plane and the 30° partials required to complete the 60° dislocation are some times not nucleated. This second 90° Shockley partial dislocation glides down towards the interface and stops at an energetically stable position, where the misfit-induced driving force reaches an equilibrium with the repulsive force between the two 90° partial dislocations with the same Burgers vector (34). Transformation of the intrinsic stacking fault to an extrinsic stacking fault takes place in such a manner. Finally, the successive glide of 90° partial dislocations results in the creation of a microtwin, as indicated by the arrows in Fig. 7.11. However, it is not yet clear why each successive partial dislocation forms and always glides down on adjacent {111} planes. The model described is only valid in the cases of hetero-epitaxial layers under a tensile stress, as pointed out by Marée et al.(35). This relaxation process seems to be consistent with the results of Wegscheider et al. (34) in the Si/Ge SLS system.

For all the SLSs, the growth rate and cooling rate were constant. The strain relief mechanism that occurred was not significantly dependent on alloy layer composition and growth temperature. However, the mechanism was dependent on the structures of the SLSs (Table 7.3). For thick individual strained layers having irregular and diffuse interfaces, individual layer relaxation played a major role in relieving misfit-induced strains, giving rise to 'short' stacking faults and 'short' microtwins. For thin individual strained layers having regular and abrupt interfaces, overall layer relaxation played a major role in relieving misfit strains, resulting in 'long' microtwins.

These behaviours can be qualitatively explained as follows. When the individual layers of the SLSs are thick, the critical layer thickness for the generation of defects such as dislocations, stacking faults and microtwins to relieve the layer strain is readily exceeded. Consequently, 'short' defects arise during the growth within the individual layers. The nucleation of such defects at the growing layer surface occurs more easily when irregularities such as surface steps are present, and there are many more such irregularities when the individual layers are non-uniform. Consequently, when SLSs such as those of specimens IC

Table 7.3 Defects relieving strain in SLSs of $InAs_ySb_{1-y}$ grown by MBE.

Sample number	Defects types	Morphology of individual layers within SLSs: Layer Thickness	Layer uniformity	Interface abruptness
IC 237	l-MT	thin	regular	abrupt
IC 118	s-SF, s-MT	thick	irregular	diffuse
IC 124	s-SF, s-MT	thick	irregular	diffuse
IC 257	l-MT	thin	regular	abrupt

s-SF = 'short' stacking fault, s-MT = 'short' microtwin, l-MT = 'long' microtwin.

118 and IC 124 are grown, much of the strain with respect to the underlying buffer layer and some of the strain between adjacent layers is relieved during the growth. Consequently, when the SLS cools down after growth, insufficient overall strain remains or develops, and so 'long' defects extending down from the SLS surface do not occur.

Conversely, when the individual layers of the SLSs are thin, the critical layer thickness for the generation of defects is less readily exceeded. Furthermore, the nucleation of such defects at the growing layer surface is more difficult when surface steps are not present, i.e. when the individual layers are more uniform. Consequently, when SLSs such as those of specimens IC257 and IC237 are grown, either of the strain is relieved during the growth. When the SLS cools down after growth, significant overall strain remains or develops, and so 'long' defects extending down from the SLS surface occur.

7-6 Conclusions

TEM and HREM studies were employed to investigate the defect structures in strained layer superlattices (SLSs) of $InAs_{y1}Sb_{1-y1}$ and $InAs_{y2}Sb_{1-y2}$ grown on InAs and InSb, the superlattices being either naturally or intentionally grown. In one case the main defects relating to misfit strains were 'short' stacking faults and 'short' microtwins, and in the other case were 'long' microtwins. Two possible mechanisms for relieving misfit-induced strains were proposed: one is related to individual layer relaxation and the other to overall layer relaxation (36). The relaxation mechanisms were dependant upon the morphology of the individual layers in the SLSs, i.e. the thickness, uniformity and abruptness of the layers. For thick irregular individual layers, the former mechanism occurred, while for thin regular individual layers, the latter mechanism occurred. These behaviours are qualitatively explained.

REFERENCES-CHAPTER 7

1. G.C. Osbourn, J. Vac. Sci. Tech. **B2** (1984) 176.
2. J.C. Woolley and J. Warner, Can. J. Phys. **42** (1964) 1879.
3. R.M. Bielfeld, J. Cryst. Growth **77** (1986) 369.
4. L.R. Dawson, J. Vac. Sci. Tech. **B4** (1986) 598.
5. S.R. Kurtz, G.C. Osbourn, R.M. Bielfeld, L.R, Dawson and H.J. Stein, Appl. Phys. Lett. **52** (1988) 831.
6. G.S. Lee, Y. Lo, Y.F. Flin, S.M. Bedair and W.O. Laidig, Appl. Phys. Lett. **47** (1988) 1219.
7. M.Y. Yen, B.F. Levine, C.G. Bethea, K.K. Choi and A.Y. Cho, Appl. Phys. Lett, **50** (1987) 927.
8. J.W. Matthews and E. Klokholm, Mater. Res. Bull. **7** (1972) 213.
9. G.H. Olsen, M.S. Abrahams, C.J. Buiocchi and T.J. Zamerowski, J. Appl. Phys. **46** (1975) 1643.
10. H. Kasano and S. Hosoki, J. Appl. Phys. **46** (1975) 394.
11. J.W. Matthews, J. Vac. Sci. Tech. **12** (1975) 126.
12. J.W. Matthews and A.E. Blakeslee, J. Cryst. Growth **32** (1976) 265.
13. M. Hockly, D.Phil. Thesis, Oxford University, 1983.
14. J. Petruzzello and M.R. Leys , Appl. Phys. Lett. **53** (1988) 2414.
15. G.R. Booker, J.M. Titchmarsh, J. Fletcher, D.B. Darby, M. Hockly and M. Al-Jassim, J. Cryst. Growth **45** (1978) 407.
16. F. Glas, C. Gruiile, P. Hénoc, and F. Houzay, Inst. Phys. Conf. Ser. **87** (1987) 71.
17. D.T. Eaglesham, R. Devenish, R.T. Fan, C.J. Humphreys, H. Morkoc, R. Bradley, P.P. Augustus, Inst. Phys. Conf. Ser. **87** (1987) 105.
18. J. Hirth and J. Lothe, "Theory of dislocations" 2nd ed. (Wiley, NewYork, 1982).
19. D. Hull and D.J. Bacon, Introduction to dislocations, 3rd ed. (Pergamon, Oxford, 1984).
20. J. Hornstra, J. Phys. Chem. Solids **5** (1958) 129.

21. M.P.A. Viegers, C.W.T. Bulle-Lieuwma, P.C. Zalm and P.M.J. Marée, MRS Symp. Proc. **37** (1985) 331.

22. N. Otsuka, C. Choi, Y. Nakamura, S. Nagakura, R. Fischer, C.K. Peng and H. Morkoc, Appl. Phys. Lett. **49** (1986) 277.

23. S. Marklund, Phys. Stat. Solid. **B100** (1979) 77.

24. M.N. Kabler, Phys. Rev. **131** (1963) 54.

25. K.C. Rajkumar, A. Madhukar, J.K. Liu and F.J. Grunthaner, Appl. Phys. Lett. **56** (1990) 1160.

26. Myung, Diplomarbeit, Göttigen, 1987, F.R. Germany.

27. D. Gerthsen, F.A. Ponce and G.B. Anderson, Phil. Mag. **A 57** (1989) 1045.

28. Van der Merwe, J. Appl. Phys. **34** (1963) 123.

29. B.W. Dodson and P.A. Taylor, Appl. Phys. Lett. **49** (1986) 642.

30. R. People and J.C. Bean, Appl. Phys. Lett. **47** (1985) 322.

31. M.S. Abrahams, J.C. Hutchison and G.R. Booker, Phys. Stat. Sol. **63** (1981) K3.

32. R.E. Mallard, D. Phil. Thesis, Oxford University, 1989.

33. M.E. Twigg, E.D. Richmond, J.G. Pellegrino, J. Appl. Phys. **67** (1990) 3706.

34. W. Wegscheider, K. Eberl, G. Abstreiter, H. Cerva and H. Oppolzer, Appl. Phys. Lett. **57** (1990) 1496.

35. P.M.J. Marée, J.C. Barbour, J.F. van der Veen, K.L. Kavanagh, C.W.T. Bulle-Lieuma and M.P.A. Viegers, J. Appl. Phys. **62** (1987) 4413.

36. R. Hull, J.C. Bean, F. Cerdeira, A.T. Fiory and J.M. Gibson, Appl. Phys. Lett. **48** (1986) 56.

CHAPTER 8

CONCLUSIONS AND SUGGESTIONS FOR FURTHER WORK

In this chapter, the major results from this thesis are summarized. Based on these findings, we draw conclusions and present suggestions for further work. In chapter 4, detailed TEM and TED examinations showed that phase separation occurs in (001) $InAs_ySb_{1-y}$ MBE layers when grown at and below 400°C. This gives rise to the formation of non-uniform plate-like structures of two phases with tetragonally distorted cubic lattices, ~5 to ~200nm thick, lying approximately parallel to the layer surface (corresponding to a naturally occurring strained layer superlattice (n-SLS)). An anisotropic geometry of the plate-like structures was observed when viewed in two orthogonal [110] and [$\bar{1}$10] directions. The phase separation was dependent on growth temperature and layer composition. The plate-like structure progressively increased in lateral size in both <110> directions and also in thickness as the growth temperature increased from 295 to 400°C. At a growth temperature of 370°C, phase separation occurred in $InAs_ySb_{1-y}$ layers for the composition range y = 0.4 to 0.8. It was concluded from annealing experiments that the phase separation arose at the (001) growing surface, rather than subsequently in the bulk. A model for the growth behaviour of the two phases was proposed based on the existence of a miscibility gap and using lateral and island growth mechanisms. The combination of the compositions of the two phases, the quantum effects associated with the superlattice, and the strains arising from the tetragonal distortions, resulted in an optical response out to wavelengths greater than 12μm, not previously obtained for $InAs_ySb_{1-y}$.

In order to extend this work to a more comprehensive investigation of phase separation, different growth methods should be employed. For example, analogous $InAs_ySb_{1-y}$ MOCVD layers grown at and below 400°C should be examined. Furthermore, a range of ternary alloy systems should be investigated. Preliminary results that we have recently obtained for MBE GaAsSb layers grown at 450°C (not described in this thesis) showed phase separation. Studies on the early stages of the layer growth should be performed to obtain more detailed information concerning the initial nucleation and growth mechanisms. It is expected that atomic mobility and sticking coefficients depend on the substrate crystallographic orientation and so $InAs_ySb_{1-y}$ layers grown on different orientation substrates such as (110), (111)A and (111)B should be investigated.

The MBE $InAs_ySb_{1-y}$ n-SLS grown in the present work with the most uniform plate-like structures was obtained using equally balanced As and Sb fluxes, rather than excess As. The dependence of the structures on the incident fluxes should be further investigated. Electrical and optical measurements need to be performed on more of the grown layers so as to make more detailed correlations with the experimentally determined structures, and infra-red detectors and opto-electronic devices need to be fabricated using the layers so as to assess possible practical applications.

In chapter 5, TEM results obtained from $In_xGa_{1-x}As$, InP_ySb_{1-y} and GaP_ySb_{1-y} MOCVD layers, grown under a wide range of conditions, exhibited a fine scale modulated contrast on a scale of ~8 to ~20nm and a fine scale speckle contrast on a scale of ~4 to ~5nm. The fine scale modulated contrast was attributed to alloy clustering, probably occurring by spinodal decomposition. This decomposition occurred two-dimensionally, i.e. only along the elastically soft [100] and [010] directions parallel to the (001) layer surface, but not in the [001] growth direction (1). The fine scale speckle contrast was related to lines of [110]-oriented diffuse intensity in [001] TED patterns and was attributed to static atomic displacements from the average lattice (2). For some as-grown and annealed InGaAs layers, fine scale modulated contrast and fine scale speckle contrast were simultaneously present. For InP_ySb_{1-y} layers, a fine needle-like contrast occurred on a scale of ~1.5 to ~2.2nm and was attributed to thin disc-shape segregations of atoms or an array of APBs due to surface dimerizations. A model to explain the formation of the fine needle-like contrast was proposed based on a (2x4) surface reconstruction unit cell (5). For GaP_ySb_{1-y} layers, TED patterns exhibited complicated features of diffuse intensity. Computer simulations using the valence force field (VFF) model (3,4) reproduced some of the diffuse intensity of the TED patterns, indicating that they are probably related to static atomic displacements.

Spinodal decomposition in these layers occurred at the layer surface. In order to understand the role of the surface structure in causing spinodal behaviour during epitaxial growth, the effects of dopants such as Si, Mn and Zn should be examined. Such dopants may change the surface thermodynamics and/or surface mobility so that different spinodal decomposition behaviour may occur. Spinodal decomposition in layers grown on different

orientation surfaces such as (110), (111)A and (111)B should be examined to see if the substrate orientations affect the behaviour. Norman (6) examined LPE $In_xGa_{1-x}As$ layers grown on the (111)B InP surface and reported strain modulations present along the elastically soft <100> directions. Different alloy systems grown on the {110} and {111} surfaces need to be examined to build up a more comprehensive understanding of spinodal decomposition behaviour at the growing layer surface.

Without direct experimental evidence, we proposed a model in chapter 5 to interpret the fine needle-like contrast observed for InPSb, assuming that the surface reconstruction was the same as for an InP layer. In order to confirm the model described and fully understand the surface structure of the InPSb layer, detailed surface studies using RHEED should be carried out on MBE InPSb.

In chapter 6, TED examinations showed that CuPt-type ordering occurs in many of the MOCVD $In_xGa_{1-x}As$, MOCVD and MBE $InAs_ySb_{1-y}$, and MOCVD InP_ySb_{1-y} layers grown under a wide range of conditions. Regardless of alloy systems and growth conditions, the ordering always occurred only on $(\bar{1}11)$ and $(1\bar{1}1)$ of the four possible {111} variants of the mixed Group III and V sublattices. The degree of ordering in InGaAs layers was deduced from the relative intensity of superlattice spots and was strongly dependent on growth temperature and growth rate. For the InGaAs layers, the ordered regions nucleated separately and occupied well defined areas. The ordered regions ranged from ~0.15 to ~0.6μm in width and extended throughout the full layer thickness. Their morphologies were dependent on growth temperature, growth rate and type of substrate. Further detailed studies of the morphology of the ordered structure should be carried out. Inclined planar defects such as APBs in the ordered regions are considered to be responsible for the inclination and elongation of superlattice spots. It was concluded from the results of annealing and doping experiments, and the presence of only two of the four possible {111} ordering variants, that the ordering occurs at the (001) growing surface during the epitaxial growth (6). The growth condition dependence of the ordering in InGaAs was interpreted as involving the two competing processes of surface-induced ordering and bulk diffusion-induced disordering within a near-surface transition region (7,8). The surface-induced ordering was considered to

be controlled by the two factors of the lifetime and relaxation time of the mixed Group III atoms both at the surface and in the transition region beneath the growing surface, whilst the bulk disordering was considered to be controlled by the two factors of the thermodynamic equilibrium degree of the surface-induced ordering and the diffusion time within the transition region. A model for the observed ordering was proposed based on surface reconstruction. It was suggested that crystallographic planes in the subsurface are bent due to the formation of surface dimers and that strains underneath the (001) growing surface give rise to site-specific lateral segregation in the layers (9,10). This leads to the subsurface consisting of alternating pairs of atoms along the $[\bar{1}10]$ direction.

It has been reported that the CuPt-type ordering correlated to a reduction of ~80meV in the energy band gap of $In_xGa_{1-x}P$ layers (11). The ordering is expected to lead to a lower electron scattering and better transport properties. This suggests that the CuPt-type ordering in InGaAs layers could also result in a similar reduction of bandgap and enhanced electrical properties. Therefore, optical and electrical measurements should be carried out to find the possible relationship between the degree of ordering and these properties. The CuPt-type ordering occurred on only $(\bar{1}11)$ and $(1\bar{1}1)$ of the four possible planes. This indicates that there may exist an asymmetry of the electron mobility in the [110] and $[\bar{1}10]$ directions. Therefore, it could be useful to understand an ordering-induced enhancement of electron mobility for device applications. In the present work, the degree of ordering was qualitatively measured using the relative intensity of superlattice spots obtained from TEM film negatives. In order to quantitatively determine the degree of ordering, further detailed investigations of the ordering should be performed. This may be achieved by direct measurement of the intensities of the main and superlattice spots using STEM. APBs are known to arise from two basic causes (12). First, they can represent the boundaries of different ordered domains. Secondly, they can be produced by dislocations within ordered regions. Therefore, detailed TEM examinations should be carried out to fully characterise the APBs. As demonstrated in this thesis, the CuPt-type ordering is unstable in the bulk layer. It is important to understand the bulk diffusion-induced disordering process. Doping and annealing lead to disordering. Therefore, systematic studies should be carried out to characterise the bulk disordering

process and to investigate the possible relationship between the introduction of APBs and disordering, i.e. to see if APBs act as nucleation sites of the disordered phase in ordered regions.

The proposed model for the ordering suggests that a change of the surface reconstruction unit cell may affect the degree of ordering and/or the type of ordering. Therefore, MBE $In_xGa_{1-x}As$ and $InAs_ySb_{1-y}$ layers grown on (001) substrates having different surface reconstructions should be investigated. Also, layers grown on (110), (111)A and (111)B substrates should be investigated and in-situ surface structure studies using RHEED should be carried out at the same time.

In chapter 7, naturally and intentionally grown SLSs of $InAs_ySb_{1-y}$ were examined by TEM and HREM. The main defects producing misfit relaxation were sometimes 'short' stacking faults and 'short' microtwins and in other cases 'long' microtwins. Two possible mechanisms for relieving misfit strain were proposed: i) an individual layer relaxation model; ii) an overall multilayer relaxation model (13). These relaxation mechanisms were dependant upon the morphology of the individual layers in the SLSs, i.e. the layer thickness, uniformity and abruptness. In order to fully understand the relaxation process, further experimental investigations of the critical thickness of the layers should be carried out. Detailed studies of the early stages of layer growth would also be important to characterise such relaxation mechanisms.

REFERENCES-CHAPTER 8

1. A.G. Norman and G.R. Booker, Inst. Phys. Conf. Ser. **76** (1985) 257.
2. F. Glas, C. Gors and P. Hénoc, Phil. Mag. **B62** (1990) 373.
3. P.N. Keating, Phys. Rev. **145** (1966) 637.
4. R.M. Martin, Phys. Rev **B1** (1970) 4005.
5. W. Weiss, R. Hornstein, D. Schmeisser and W. Göpel, J. Vac. Sci. Technol. **B8** (1990) 715.
6. A.G. Norman, D.Phil. Thesis, Oxford University, 1987.
7. S.R. Kurtz, J.M. Olson and A. Kibbler, Appl. Phys. Lett. **57** (1990) 1922.
8. P. Bellon, J.P. Chevalier, E. Augade, J.P. André and J.P. Martin, J. Appl. Phys. **66** (1989) 2388.
9. J.A. Appelbaum and D.R. Hamann, Surf. Sci. **74** (1978) 21.
10. F.K. LeGoues, V.P. Kesan, S.S. Iyer, J. Tersoff and R. Tromp, Phys. Rev. Lett. **64** (1990) 2038.
11. A. Gomyo, T. Suzuki, K. Kobayashi, S. Kawata, I. Hino and T. Yuasa, Appl. Phys. Lett. **50** (1987) 673.
12. T.S. Kuan, W.I. Wang and E.L. Wilkie, Appl. Phys. Lett. **51** (1987) 51.
13. R. Hull, J.C. Bean, F. Cerdeira, A.T. Fiory and J.M. Gibson, Appl. Phys. Lett. **48** (1986) 56.

APPENDIX

1) Calculated structure factor for $InAs_ySb_{1-y}$ and the (002) reflection for different values of y.

For III-V compound semiconductors with zinc-blende type structure the structure factor of the (002) reflection is given by*:

$$F_{002} = 4(f_{III} - f_V) \qquad (1)$$

where f_{III} and f_V are the atomic scattering factors of the Group III and Group V elements respectively, and random atomic mixing is assumed. For the ternary compound $InAs_ySb_{1-y}$, the scattering factor F_{002} is given by:

$$F_{(002)} = 4[(f_{In} - f_{Sb}) + y(f_{Sb} - f_{As})] \qquad (2)$$

The intensity (I) of the (002) TEM DF micrograph is proportional to F_{002}^2, i.e.

$$I \alpha F_{002}^2. \qquad (3)$$

The intensity in the (002) TEM DF micrographs thus simply depends on the value of y. Details are given in Table I. The results indicate that the (002) TEM DF micrograph becomes brighter as y increases from 0.2 to 0.8.

---

* P. M. Petroff, J. Vac. Sci. Technol. **14** (1977) 473.

Table I

$InAs_ySb_{1-y}$ (y)	a (Å)	$\sin\theta/\lambda$ ($Å^{-1}$)	Atomic scattering amplitude** In	As	Sb	F_{002}^2
0.2	6.395	0.156	6.88	5.31	7.07	0.65
0.3	6.353	0.157	6.86	5.29	7.04	1.38
0.4	6.311	0.159	6.81	5.25	6.99	2.06
0.6	6.226	0.161	6.76	5.21	6.94	3.43
0.8	6.142	0.163	6.71	5.17	6.89	4.78

** P.B. Hirsch, A. Howie, R.B. Nicholson, D.W Pashley. and M.J. Whelan, "Electron Microscopy of Thin Crystals" (Butterworths, London 1965).